

POLITECNICO DI TORINO

Department of Mechanical and Aerospace Engineering

Master's Degree in Automotive Engineering

Thesis title:

**Torque Vectoring Controls for Multi-architecture
Battery Electric Vehicles**



Politecnico di Torino

Supervisors:

Prof. Andrea Tonoli

Prof. Angelo Bonfitto

Candidate:

Riccardo Ninfa

October 2022

Abstract

This study investigates a method for enhancing Battery Electric Vehicle (BEV) longitudinal and lateral stability in a broad range of conditions. As with the state-of-the-art, a hierarchical control is developed: the upper layer uses vehicle state errors and predicted yaw acceleration in order to generate a corrective yaw moment using a sliding mode control (SMC); the lower layer distributes the total requested torque to the electric motors using a vertical-load-based torque distribution algorithm. The main contribution of this work is the additional term inside the yaw moment controller: the expected yaw acceleration of the vehicle is predicted, allowing a more effective action of the controller and thus reducing path errors. Another contribution of this work is the development of a sliding mode-based cruise control, featuring good responsiveness when the velocity error is high and robustness when it approaches zero. The proposed control system is verified in the MATLAB-Simulink environment, using a seven degree of freedom vehicle model (longitudinal, lateral, yaw and rotation of each wheel) and the bicycle model as reference model. Several simulations under different driving scenarios are run and the results are discussed, highlighting the merit of the proposed control strategy. Furthermore, the simulation environment that has been built allows the benchmarking of different BEV architectures. When changing the number and position of the electric motors, the developed integrated vehicle stability controller is able to split the required torque among the available motors in order to optimize available traction depending on the vehicle configuration.

To my family and my girlfriend Rebecca

Acknowledgements

First of all, I would like to express my sincere gratitude to my supervisor Dr. Bruce Minaker at the University of Windsor, whose guidance and suggestions have been fundamental throughout the development of this thesis. I remember our first meetings when I did not know where to start and where the research would have brought me, but he always believed in me. He also gave me the chance to present at the Canadian Society for Mechanical Engineering International Congress, which was an incredible and unique experience. I did learn a lot from him, especially the willingness to do things properly and constantly perfect them. One day I wish to be able to approach problems with his spirit and determination.

I wish to extend my special thanks to Dr. Andrea Tonoli and Dr. Angelo Bonfitto from Politecnico di Torino. Despite the distance between Canada and Italy, they supported me since the beginning and helped for the completion of this work. Their experience in the field has been really valuable when some development choices had to be made.

I am deeply grateful to Stellantis who sponsored this thesis and gave me the opportunity to take part in the Dual International Master Degree program with Politecnico di Torino and University of Windsor. Developing ideas that can contribute to the research and that can be helpful for the company made me more conscious of my potentiality. In particular, I would like to thank my industrial advisors Mr. Dru Mavalankar, Mr. Marco Tonetti and Dr. Chunjian Wang for their continuous interest in this thesis. They helped me understanding what the research areas could have been, and they allowed me to relate to the industrial world and the work environment for the first time. I would also like to thank the DIMD project coordinator from Stellantis Ms. Marie Mills. Her kindness and constant availability really helped in the success of this work.

I am also thankful to the academic supervisors of the DIMD project Dr. Maria Pia Cavatorta, Dr. Giovanni Belingardi and Dr. Jennifer Johrendt. The first two believed in me when I was interviewed for the DIMD program and they helped me with the paperwork for Politecnico di Torino. Dr. Johrendt assisted me especially in the initial phase of settling down at the University of Windsor.

I wish to show my appreciation to the thesis committee members Dr. Narayan Kar, and again Dr. Minaker, Dr. Johrendt and Dr. Wang, for their suggestions during the proposal and for their patience in the reading of this dissertation.

Words cannot express my gratitude to my family. I would like to thank my parents Enzo and Cinzia who imparted healthy values and always did everything possible to make me happy and to pursue my dreams. My upbringing and my mindset are their credits. My interests towards scientific subjects began when I was a child thanks to their inputs and likely I would not be here if my dad did not pass down to me his passion for cars and Formula 1. Then, I would like to thank my sister Serena for the love she always shows me and for her support during the most difficult periods. It has been amazing growing up together and becoming the people we are now. Also, I wish to thank my four beloved grandparents for their kindness and love. I could never forget the beautiful moments spent together, from the card games and the endless lunches during the holidays to the simplest daily life activities. I am so proud to be born and raised in this family that I could never be grateful enough.

I would also like to thank my girlfriend Rebecca from my heart. The last year and a half together has simply been extraordinary, I have no words to explain the love and the chemistry between us. Although we spend the last eleven months 7000 km away from each other, you cannot believe how close to me she was in this adventure overseas. She is my strength and the light of my life. In short, thank you for all the emotions you make me feel and for each single minute spent together.

I could not have undertaken this journey without my friends. I would like to thank them all for the amazing moments spent together. Special acknowledgements go to Mauro e Angelo, two brothers for me with which I spent many of the most beautiful and funny days of my life. Then I wish to thank Giorgio, with whom I shared the enjoyable experience in Canada, and Alberto, Edoardo and again Giorgio for the unforgettable moments in Politecnico. I would also like to thank Nick and Kieran who made me taste the Canadian lifestyle, and Mike for the help when I arrived in Canada and the evenings spent racing with the driving simulator.

I am deeply grateful to my math professor in high school Cesare Labianca. His dedication and passion for his job has been exemplary. He was able to impart the love for math and the study method that I still use. For these reasons, a consistent part of the credit of my successful educational career belongs to him.

Special thanks to Giampiero and Ivana, who welcomed me in their restaurant as a son and made me feel at home with the Italian cuisine.

Last but not least, I would like to express my deepest appreciation to the dearly departed Mr. Sergio Marchionne. I am extremely proud in saying that one of the most important business leaders in the world was born and raised in Chieti, my hometown. He was a self-made man whose charisma and managerial skills were out of the ordinary, and for these reasons he is my role model.

Contents

Abstract	iv
Dedication	v
Acknowledgements	vi
List of Figures	xi
List of Tables	xv
List of Abbreviations	xvi
List of Symbols	xviii
1 Introduction	1
1.1 Background	1
1.2 Motivation	3
1.3 Research Objectives	4
1.4 Methodology	5
1.5 Thesis Structure	5
2 Literature Review	6
2.1 Vehicle Dynamics	6
2.1.1 Coordinate Systems	6
2.1.2 Longitudinal Dynamics	7
2.1.3 Lateral Dynamics	9
2.1.4 Tire Models	14
2.2 Automotive stability enhancement systems	17
2.2.1 Antilock Braking System	17
2.2.2 Traction Control System	18
2.2.3 Electronic Stability Control	19
2.2.4 Torque Vectoring Control	20
3 Vehicle Model	26

3.1	Vehicle model in MATLAB-Simulink	26
3.1.1	Bicycle Model	26
3.1.2	7-DOF Non-linear Vehicle Model	27
3.2	Tire Model	29
3.3	Electric Motors Model	36
3.4	Driver Model	39
4	Integrated and Modular Vehicle Dynamics Controller	42
4.1	Torque Vectoring Control in MATLAB-Simulink	42
4.1.1	Sliding Mode Control for TVC	43
4.1.2	Derivative Feedback	50
4.1.3	TVC upper-layer layout	51
4.2	Cruise Control	53
4.3	Traction Control System	58
4.4	Torque Distribution Strategy	58
4.4.1	Motor Maximum Torque Curve	66
4.4.2	Regenerative Braking and Friction Brakes	69
5	Results and Discussion	71
5.1	Simulation environment setup	71
5.2	Sinusoidal steering angle input	72
5.3	ISO Double Lane-Change Maneuver	77
5.3.1	Double Lane-Change when coasting	79
5.3.2	Double Lane-Change at constant speed	89
5.4	Single Lane-Change Maneuver	95
5.5	Step-steer test	101
5.6	Standing start while cornering	106
5.7	Friction-split condition when driving straight	111
5.8	Electric Motor efficiency	115
5.9	Contributions of the different terms to the yaw acceleration prediction	119
5.10	Controller robustness	121
5.10.1	Double Lane-Change for off-design vehicle load conditions	121
5.10.2	Double Lane-Change under low road-adhesion conditions	126
6	Conclusions and recommendations	131
6.1	Summary	131
6.2	Conclusions	131
6.3	Limitations and recommendations	133
6.4	Research contributions	134
	References	139

Appendix A	Equations of the Sliding Mode Control for TVC	140
Appendix B	Equation of the yaw acceleration prediction for TVC	142
Appendix C	MATLAB scripts	144
C.1	Extract of the main script	144
C.2	Vehicle model functions	147
C.2.1	Three main DOF	147
C.2.2	Wheel dynamics	148
C.2.3	Tire vertical loads	148
C.2.4	Pacejka's Magic Formula	149
C.2.5	Tire side slip angles	151
C.2.6	Tire slip ratio and scaling factors	152
C.2.7	Steering angle correction from driver model	153
C.3	Controller functions	154
C.3.1	Reference values from bicycle model	154
C.3.2	Reference value limits	154
C.3.3	Yaw acceleration prediction formula	155
C.3.4	TVC upper-layer controller	156
C.3.5	Cruise Control	158
C.3.6	TVC lower-layer controller	159
	Torque distribution coefficient	159
	Torque distribution strategy	160
	Torque adjustment	161
	Electric motor torque limits	161
	Total limit torque	165
Vita Auctoris		167

List of Figures

2.1	Coordinate systems	6
2.2	Car free body diagram: forces in longitudinal and vertical direction	7
2.3	Wheel free body diagram	9
2.4	$F_x - \sigma$ characteristic of a 185/60 R14 tire for different vertical loads (experimental data from Tonoli[30])	10
2.5	$\mu_x - \sigma$ characteristic of a 185/60 R14 tire for $F_z = 4$ kN. It is representative of a dry tarmac road	11
2.6	Bicycle model	12
2.7	Important angles for tire lateral behaviour	13
2.8	$-F_y - \alpha$ characteristic of a 185/60 R14 tire for different vertical loads (experimental data from Tonoli[30])	14
2.9	$C_\alpha - F_z$ characteristic of a 185/60 R14 tire for different side-slip angles (experimental data from Tonoli[30])	15
2.10	$F_y - F_x$ friction ellipse characteristic of a 185/60 R14 tire for different side-slip angles at $F_z = 4$ kN (experimental data from Tonoli[30])	16
2.11	F_x error between experimental data (from Tonoli[30]) and Pacejka's Magic Formula of a 185/60 R14 tire for $F_z = 4$ kN	17
2.12	General control scheme for a hierarchical TVC based on Model Following Control	21
2.13	Schematic of a vehicle top view with ΔM_z and ΔF_x contributions	24
3.1	Three main DOF of the vehicle model implemented in a MATLAB function	28
3.2	Wheel model implemented in a MATLAB function	29
3.3	F_x as function of σ and α with the presented scaling approach	30
3.4	F_y as function of σ and α with the presented scaling approach	31
3.5	Tire saturation as function of σ and α with the presented scaling approach	32
3.6	F_x as function of σ and α without scaling approach	33
3.7	Tire saturation as function of σ and α without scaling approach	33
3.8	Pacejka's Magic Formula implemented in a MATLAB function	34
3.9	Computation of α in a MATLAB function	34
3.10	Computation of σ in a MATLAB function	34
3.11	Surface representing tire cornering stiffness as function of α and F_z , implemented in a look-up table	35

3.12	C_α trend for a Double-Lane Change maneuver when using the look-up table approach	35
3.13	EM efficiency map as function of angular velocity and torque at the wheel for a 4IWMEV (data from Maino[45])	37
3.14	Speed and acceleration trend at full throttle for a 4IWMEV with $\mu = 1$	38
3.15	Surface representing the EM efficiency map as function of angular velocity and torque at the wheel for a 4IWMEV	38
3.16	Electric motor dynamics in Simulink	38
3.17	Schematic of a vehicle with reference trajectory, cross-track error and heading error definitions	39
3.18	Driver model developed in MATLAB-Simulink	41
4.1	Sliding surface trend for a sinusoidal steering input in order to compare chattering solutions, for $\epsilon=4$ and $k_d=3$	48
4.2	Sliding surface and corrective yaw moment trend for a sinusoidal steering input in order to compare chattering solutions, for real time parameters	49
4.3	Evaluation of the yaw acceleration prediction in Simulink	51
4.4	Schematic of the TVC upper-layer developed in Simulink	52
4.5	Velocity trend under Test 1 conditions for the comparison among the three different parameters sets	55
4.6	Acceleration trend under Test 1 conditions for the comparison among the three different parameters sets	56
4.7	Velocity trend under Test 2 conditions for the comparison among the three different parameters sets	56
4.8	Cruise-control system developed in Simulink	57
4.9	Vehicle top view with corrective yaw moment ΔM_z and corresponding "motor torque" T_{yaw} for each wheel	60
4.10	Inputs to the torque distribution strategy in Simulink	61
4.11	Torque distribution coefficient k calculated in Simulink	62
4.12	Complete torque distribution strategy in Simulink	64
4.13	T_{yaw} trend for the comparison of the adjusted and non-adjusted torque distribution strategy on a step-steer test	65
4.14	T_{tot} trend for the comparison of the adjusted and non-adjusted torque distribution strategy on a step-steer test	66
4.15	EM torque limit comparison between given data and fitting procedure	68
4.16	Motor maximum torque curve in Simulink	68
4.17	Longitudinal speed and acceleration trend when fully braking on a straight road	70
5.1	Setup of simulation environment inputs in Simulink	72
5.2	Sinusoidal steering angle input	73
5.3	Sinusoidal steering angle input - Vehicle states for the three different cases	74

5.4	Sinusoidal steering angle input - Vehicle state errors and trajectory for the three different cases	75
5.5	Sinusoidal steering angle input - Vehicle state derivatives for the three different cases	76
5.6	Double Lane-Change possible reference trajectories	78
5.7	Double Lane-Change possible reference curvatures	78
5.8	Double Lane-Change at $v_{x0} = 84.1$ km/h - Trajectory for the three different cases and the three different BEV configurations	80
5.9	Double Lane-Change at $v_{x0} = 84.1$ km/h - Steering angle for the three different cases	81
5.10	Double Lane-Change at $v_{x0} = 84.1$ km/h - Vehicle states for the three different cases	82
5.11	Double Lane-Change at $v_{x0} = 84.1$ km/h - Vehicle state errors and corrective yaw moment for the three different cases	83
5.12	Double Lane-Change at $v_{x0} = 84.1$ km/h - Vehicle state derivatives for the three different cases	84
5.13	Double Lane-Change at $v_{x0} = 84.1$ km/h - Torque at the wheels for the three different cases	85
5.14	Double Lane-Change at $v_{x0} = 84.1$ km/h - Vertical loads at the wheels for the three different cases	86
5.15	Double Lane-Change at $v_{x0} = 84.1$ km/h - Vehicle states for the three different EV configurations	87
5.16	Double Lane-Change at $v_{x0} = 84.1$ km/h - Vehicle state errors and corrective yaw moment for three different EV configurations	88
5.17	Double Lane-Change with cruise control at $v_x = 79.4$ km/h - Trajectory for the three different cases and for the central motors configuration	90
5.18	Double Lane-Change with cruise control at $v_x = 79.4$ km/h - Steering angle for the three different cases and for the central motors configuration	91
5.19	Double Lane-Change with cruise control at $v_x = 79.4$ km/h - Vehicle states for the three different cases and for the central motors configuration	92
5.20	Double Lane-Change with cruise control at $v_x = 79.4$ km/h - Vehicle state errors and corrective yaw moment for the three different cases and for the central motors configuration	93
5.21	Double Lane-Change with cruise control at $v_x = 79.4$ km/h - Vehicle state derivatives for the three different cases and for the central motors configuration, and tire vertical loads for the uncontrolled vehicle	94
5.22	Single Lane-Change at $v_{x0} = 88$ km/h in braking condition - Trajectory for the three different cases	96
5.23	Single Lane-Change with at $v_x = 88$ km/h in braking condition - Vehicle states for three different EV configurations	97
5.24	Single Lane-Change at $v_{x0} = 88$ km/h in braking condition - Yaw rate error, longitudinal acceleration and steering angle for the three different cases	98

5.25	Single Lane-Change at $v_{x0} = 88$ km/h in braking condition - Yaw rate error, longitudinal acceleration and steering angle for the three different cases	99
5.26	Single Lane-Change at $v_{x0} = 88$ km/h in braking condition - Tire vertical loads for the uncontrolled vehicle	100
5.27	Step-steer test at $v_x = 65$ km/h in braking condition - Steering angle	102
5.28	Step-steer test at $v_{x0} = 65$ km/h in braking condition - Trajectory for the three different cases	102
5.29	Step-steer test at $v_x = 65$ km/h in braking condition - Vehicle states for the three cases	103
5.30	Step-steer test at $v_x = 65$ km/h in braking condition - Vehicle state errors and corrective yaw moment for the three different cases	104
5.31	Step-steer test at $v_x = 65$ km/h in braking condition - Yaw acceleration for the three cases and tire vertical loads for the uncontrolled vehicle	105
5.32	Standing start while cornering - Steering angle	107
5.33	Standing start while cornering - Trajectory for the three different cases	107
5.34	Standing start while cornering - Vehicle states for the three different cases	108
5.35	Standing start while cornering - Vehicle state errors and corrective yaw moment for the three different cases	109
5.36	Standing start while cornering - Vehicle state derivatives for the three different cases	110
5.37	μ -split condition when accelerating - Vehicle trajectories, velocities and allocated yaw moment for controlled and uncontrolled cases	113
5.38	μ -split condition when accelerating - Tire slip ratios and wheel torques for the controlled and uncontrolled vehicles	114
5.39	Sinusoidal steering angle input - Electric motor efficiencies for the three different cases	117
5.40	Double Lane-Change with cruise control at $v_x = 79.4$ km/h - Electric motor efficiencies for the three different cases	118
5.41	Contributions of the terms in the yaw acceleration prediction formula - Double Lane-Change when coasting, step-steer maneuver when braking and standing start while cornering	120
5.42	Double Lane-Change for off-design vehicle load conditions - Trajectories and steering angles	123
5.43	Double Lane-Change for off-design vehicle load conditions - Vehicle state errors and corrective yaw moment	124
5.44	Double Lane-Change for off-design vehicle load conditions - Yaw acceleration	125
5.45	Double Lane-Change under low road-adhesion conditions - Trajectories and steering angles	127
5.46	Double Lane-Change under low road-adhesion conditions - Vehicle state errors	128
5.47	Double Lane-Change under low road-adhesion conditions - Yaw acceleration	129

List of Tables

2.1	Comparison among Proportional Integral Derivative, Linear Quadratic Regulator, Linear Quadratic Gaussian Regulator, Model Predictive Control, Fuzzy logic and Sliding Mode Control	21
3.1	Vehicle specifications	27
4.1	Comparative recap of SMC and MPC	42
4.2	SMC constant parameters after trial-and-error procedure	45
4.3	SMC real-time adjustment of sliding surface dynamics parameters according to sliding surface values	46
4.4	Comparison of different SMC sliding surface dynamics parameters	47
4.5	k coefficients for the three sgn functions in Equation 4.16 according to Equation 4.18 (Solution 1)	47
4.6	Φ coefficients for the three sgn functions in Equation 4.16 according to Equation 4.19 (Solution 2)	48
4.7	TVC upper-layer inputs with reference to Figure 4.4	52
4.8	Comparison of different cruise-control parameters	54
4.9	Evaluation of the four k coefficients for each BEV configuration	60
4.10	Polynomial coefficients for the motor limit curve in the 4 IWM configuration	67
4.11	Braking performance when fully braking on a straight road from 100 km/h	69
5.1	Sinusoidal steering angle input - Results	77
5.2	Double Lane-Change at $v_{x0} = 84.1$ km/h - Results	89
5.3	Step-steer test at $v_{x0} = 65$ km/h in braking condition - Results	106
5.4	Standing start while cornering - Results	111
5.5	Electric motor efficiencies in percentage - Results	116
5.6	Vehicle mass and centre of gravity position for design and off-design conditions	121
5.7	Double Lane-Change for off-design vehicle load conditions - Results	126
5.8	Double Lane-Change under low road-adhesion conditions - Results	130

List of Abbreviations

All abbreviations used in this work are described in this section.

Abbreviation	Meaning
ABS	Anti-lock Braking System
AFS	Active Front Steering
ANN	Artificial Neural Network
ARS	Active Rear Steering
AS	Active Steering
ASC	Automotive Stability Control
ASR	Anti-Slip Regulator
BEV	Battery Electric Vehicle
CAFE	Corporate Average Fuel Economy
CG	Centre of Gravity
CM	Central Motor
DLC	Double Lane-Change
DoF	Degree of Freedom
DYC	Direct Yaw-moment Control
ECU	Electronic Control Unit
EKF	Extended Kalman Filter
EM	Electric Motor
ESC	Electronic Stability Control
ESP	Electronic Stability Program
EV	Electric Vehicle
FTSMC	Fast Terminal Sliding Mode Control
GHG	Green-House Gas
HEV	Hybrid Electric Vehicle
HiL	Hardware in-the-Loop
ICEV	Internal Combustion Engine Vehicle
ISO	International Organization for Standardization
ITSMC	Integral Terminal Sliding Mode Control
IVDC	Integrated Vehicle Dynamics Control

IWM	In-Wheel Motor
IWMDDEV	In-Wheel Motor Distributed Drive Electric Vehicle
LQGR	Linear Quadratic Gaussian Regulator
LQR	Linear Quadratic Regulator
MBD	Multi-Body Dynamics
MFC	Model Following Control
MPC	Model Predictive Control
PID	Proportional Integral Derivative
SAE	Society of Automotive Engineers
SiL	Software in-the-Loop
SLC	Single Lane-Change
SMC	Sliding Mode Control
TCS	Traction Control System
TVC	Torque Vectoring Control
VDC	Vehicle Dynamics Control
VSA	Vehicle Side-slip Angle
VSC	Vehicle Stability Control
YCS	Yaw Control Stability

List of Symbols

Symbol	Description	Unit
m	vehicle mass	kg
a_X	longitudinal acceleration in global reference frame	m s^{-2}
F_{xf}	longitudinal force on front axle	N
F_{xr}	longitudinal force on rear axle	N
F_{aero}	aerodynamic drag force	N
F_{roll}	rolling resistance	N
F_{slope}	longitudinal force to travel on an inclined road	N
ρ	air density	kg m^{-3}
S	frontal area of the vehicle	m^2
C_x	aerodynamic drag coefficient	-
v_{rel}	relative velocity of the air with respect to the vehicle	m s^{-1}
f	rolling resistance coefficient	-
F_z	vertical force	N
g	gravitational acceleration	m s^{-2}
θ	road slope angle	°
σ	tire slip ratio	-
R_e	tire effective rolling radius	m
ω_w	wheel angular velocity	rad s^{-1}
v_x	longitudinal velocity	m s^{-1}
J_w	wheel moment of inertia	kg m^2
$\dot{\omega}$	angular acceleration	rad s^{-2}
T_w	torque at the wheel	N m
F_x	tire longitudinal force	N
R_l	tire loaded radius	m
C_σ	tire longitudinal stiffness	N
μ_x	longitudinal force coefficient	-
ψ	yaw angle	°
a_Y	lateral acceleration in global reference frame	m s^{-2}
F_{yf}	lateral force on front axle	N
F_{yr}	lateral force on rear axle	N

a_y	lateral acceleration in vehicle reference frame	m s^{-2}
$\dot{\psi}$	yaw rate	$^\circ \text{s}^{-1}$
J_z	vehicle moment of inertia about the z-axis	kg m^2
$\ddot{\psi}$	yaw acceleration	$^\circ \text{s}^{-2}$
a	distance of the front axle from the vehicle CG	m
b	distance of the rear axle from the vehicle CG	m
β	vehicle side slip angle	$^\circ$
v_y	lateral velocity	m s^{-1}
α	tire side-slip angle	$^\circ$
x_i	distance between CG and i^{th} wheel in x direction	m
y_i	distance between CG and i^{th} wheel in y direction	m
δ	steering angle	$^\circ$
C_α	tire cornering stiffness	N rad^{-1}
C_f	front tires cornering stiffness	N rad^{-1}
C_r	rear tires cornering stiffness	N rad^{-1}
F_{x0}	maximum longitudinal force when α is null	N
F_{y0}	maximum lateral force when σ is null	N
B, C, D, E, S_H, S_V	factors for Pacejka's Magic Formula	
s	SMC sliding surface	
k, ϵ	SMC parameters	
ΔM_z	corrective yaw moment	N m
$v_{s,xi}$	longitudinal slip velocity at the i^{th} contact patch	m s^{-1}
ΔF_x	corrective longitudinal force from cruise control	N
l	wheelbase	m
h	height of the vehicle CG from ground	m
t_f	front track	m
t_r	rear track	m
r	yaw rate	$^\circ \text{s}^{-1}$
\dot{r}	yaw acceleration	$^\circ \text{s}^{-2}$
v_{sx}	longitudinal tire slip velocity	m s^{-1}
v_{sy}	lateral tire slip velocity	m s^{-1}
k_x	scaling factor for longitudinal tire force	-
k_y	scaling factor for lateral tire force	-
δ_e	steering angle error	rad
e_{ct}	cross-track error	m
e_h	heading error	rad
X_r	reference longitudinal position	m
Y_r	reference lateral position	m
ψ_r	reference yaw angle	rad

X_a	front axle longitudinal position	m
Y_a	front axle lateral position	m
X	CG longitudinal position	m
Y	CG lateral position	m
τ	time constant	s
$\rho, \Delta r _{max}, \Delta \beta _{max}$	SMC-based TVC parameters	
k_{us}	understeering coefficient	-
β_d	desired vehicle side slip angle	rad
r_d	desired yaw rate	rad s ⁻¹
\dot{r}_c	yaw acceleration commanded by SMC	rad s ⁻²
V	Lyapunov function	
v_{xd}	target speed	m s ⁻¹
E_v	cruise control performance indicator	m
\dot{r}_{pred}	predicted yaw acceleration	rad s ⁻²
$\dot{\delta}$	rate of change of steering angle	rad s ⁻¹
μ	road friction coefficient	-

Chapter 1

Introduction

1.1 Background

This study investigates a method for enhancing Battery Electric Vehicle (BEV) longitudinal and lateral stability in a broad range of conditions. Vehicle models and integrated vehicle dynamics controllers are studied and implemented. Furthermore, a simulation environment is built to run simulations and verify the merit of the proposed control strategy.

BEVs are gaining importance in the worldwide vehicle market share, as they contribute to the reduction of CO₂ and pollutant emissions. In many countries more stringent regulations are taking place in the transportation field to force carmakers to produce eco-friendly vehicles. In 2017, in Europe the transport sector was responsible for 27% of the total Green-House Gas (GHG) emissions, 71% of which came from road transport [1]. In 2019, the average CO₂ emitted by new passenger cars registered in Europe was 122.3 gCO₂/km. Starting from 1st January 2020, the European Union adopted Regulation (EU) 2019/631, setting a fleet-wide target of 95 gCO₂/km with 95€ penalty per each g of CO₂ exceeded [2], and a further 37.5% emissions reduction by 2030. In 2020, the US Corporate Average Fuel Economy (CAFE) set an average fleet-wide CO₂ emissions target of about 106 gCO₂/km [3]. European and American regulations are just two examples, since emission controls are now applied at the worldwide level. In this scenario, it is clear that BEVs, and to some extent Hybrid Electric Vehicles (HEVs), play a key role.

Aside from political and ecological discussions, BEVs intrinsically have important features that are not present or not so effective in a conventional vehicle. One of them is the so-called torque vectoring, meaning the direct control of electric motor torque at the wheels to improve traction and handling of the vehicle [4].

Automotive stability enhancement systems have become the object of research in the automotive field for more than 50 years and they have reached a maturity stage such that nowadays every vehicle sold is endowed with the above-mentioned systems. In 2017, the Society of Automotive Engineers (SAE) published an article [5] describing all the available systems on the market, namely Anti-lock Braking System (ABS), Traction Control System (TCS) and Electronic Stability Control

(ESC). ABS prevents the wheels from locking while braking, reducing the braking distance and improving stability even under emergency braking conditions. TCS avoids excessive wheelspin, which is very useful under low adhesion conditions or in off-road with a wheel suspended in the air. Lastly, the ESC improves vehicle lateral stability. The thesis will focus particularly on the development of the ESC, but having a special consideration for the longitudinal stability as well.

ESC are typically based on Direct Yaw-moment Control (DYC), that is the use of a difference in tire longitudinal forces to generate a corrective yaw moment. In Internal Combustion Engine Vehicles (ICEVs), this task is accomplished by applying a braking torque to the wheels or by reducing the engine torque. However, the latter method suffers from delays, as fuel metering and engine dynamics are far from being fast-responsive. By contrast, the former method guarantees low time constants but it is not efficient from an energetic point of view, as the engine keeps running at the same load while brakes are triggered. Most often, a combination of these two methods is implemented in actual DYC [4].

As mentioned before, BEVs feature a very powerful tool: electric motors (EM). Thanks to their fast dynamics (in the order of milliseconds), a very precise and effective torque control can be realized. As a comparison, an electric motor's torque response is almost 100 times faster than that of a conventional powertrain [6]. A further development is the use of two EMs on the same axle (one for each wheel) to exploit torque vectoring for DYC, leading to an improvement in responsiveness and efficiency compared to conventional DYC systems [7].

The state-of-the-art in torque vectoring controllers is represented by a hierarchical approach, where the upper layer evaluates the corrective yaw moment and the lower layer allocates the requested torque to the electric motors using a torque-distribution algorithm [8, 9, 10, 11]. Regarding the high-level controller, many control methods have been studied in the literature and collectively reviewed in Mousavinejad et al.[12]: Model Predictive Control (MPC), Sliding Mode Control (SMC), Proportional Integral Derivative (PID), fuzzy logic, H_∞ , gain scheduling and others. Although each of them has its own pros, most of the studies in recent years focused on MPC [4, 10, 13] and SMC [9, 11, 14]. MPC has become popular thanks to its intrinsic capability to handle system constraints and deal with non-linearities [4], while the second one owes its reputation to the robustness against non-linearities and disturbances [15]. Concerning the low-level controller, the torque allocation problem can be solved with simpler methods, i.e., average torque distribution and vertical-load-based torque distribution, or with optimization problems (either single-objective or multi-objective). In the last case, a distinction is made upon the objective function to minimize: longitudinal tire slip, electric motor losses, drivetrain losses, tire utilization, vehicle path tracking ability and others [16].

Nowadays, the most popular BEV configurations on the market have a single motor, a motor per each axle (front-rear independent) or four in-wheel independent motors. If the focus is on all-wheel drive capabilities, front-rear independent EVs are convenient compared to ICE-based vehicles because they get rid of the front-rear drive axle, thus reducing mechanical losses. Besides, this

configuration saves cost, space and control complexity with respect to the four in-wheel motors case [17]. However, the latter architecture has unique advantages, such as a simple and compact structure, high energy efficiency and independent control of the torque (also named electronic differential). Each in-wheel motor can be controlled individually and coordinated torque distribution strategies can enable very efficient ESC [16].

In the design phase of a vehicle, dynamic simulations are of paramount importance as they are the tool to study the vehicle behaviour even when the actual vehicle is not physically built yet. At this early stage, every change would imply the construction of a new prototype, thus design costs would exponentially increase. Having a solid and reliable simulation environment allows carmakers to run close-to-reality simulations and tune parameters and characteristics at almost no expense [18]. There are two methodologies to run virtual tests on vehicles: Software-in-the-Loop (SiL) and Hardware-in-the-Loop (HiL). SiL uses models of both controllers and vehicle, without the need of a real Electronic Control Unit (ECU), while HiL uses an actual ECU connected to a simulator to mimic the behaviour of a real car. SiL simulations are usually preferred, at least at an early stage, because they are faster to build and get rid of the problem of having an ECU [19]. For this purpose, many commercial softwares are available on the market: the well-known MATLAB-Simulink and Multi-Body Dynamics (MBD) tools like CarSim, ADAMS and MotionView. Usually, when dealing with complex systems as in the case of vehicle dynamics, a combination of simulators is used to enable a global simulation, leading to the so-called co-simulation (or collaborative simulation) [20]. Some studies in the literature have built a co-simulation using MATLAB-Simulink to develop a controller and CarSim for the vehicle model [9, 21, 22], while some others have used MATLAB-Simulink and ADAMS [23, 24, 25].

In conclusion, this project will focus on the development of a hierarchical controller to improve longitudinal and lateral behaviour of BEVs, as well as the development of a SiL simulation environment for virtual testing.

1.2 Motivation

BEVs are gaining popularity worldwide and projections of vehicle market shares clearly indicate that the future is far from the current concept of fossil fuels-propelled cars. The above-mentioned scenario opens the doors to interesting fields of research to improve the existent know-how. The focus of the current research is to study the electric motor controls at system level, i.e., the distribution of the total requested torque, without posing limitations on the BEV architecture. Multi-motor EVs have the potential to replace old ESC systems based on engine torque reduction or braking application with the precise, accurate and fast regulation of electric motors. It is clear that a solid and efficient torque allocation algorithm along with automotive stability enhancement systems improve vehicle dynamics and stability. An integrated controller is needed for this purpose, considering both vehicle stability and the driver's throttle and brake inputs. Besides, the

controller is intended to be modular, i.e., it can work for different vehicle architectures (in terms of the number and the position of the electric motors).

Simulation tools play a key role in the design and development phases of a vehicle. Understanding the virtual behaviour of a car in response to a certain maneuver helps the tuning of controller and vehicle parameters before the first prototype is built and tested on the road. Having an integrated simulation environment with a user-friendly interface speeds up the work. Furthermore, a smart design of the virtual testing tools, together with the integrated and modular controller, allows the benchmarking of different electric vehicle configurations.

1.3 Research Objectives

The first macro-objective of the present work is the development of an integrated and modular vehicle dynamics controller able to allocate torque to the wheels considering both longitudinal and lateral dynamics. In this way, a single control architecture will manage all the functionalities controlling torque to the wheels. Besides, the modularity will allow the controller to work for different BEV architectures. When changing the number and position of the electric motors, the developed controller will be able to split the required torque among the available motors according to a torque allocation algorithm. For instance, if the vehicle is equipped with four in-wheel motors, the so-called 4xE functionality will be enabled. An important topic associated with the controller is the vehicle stability: a proper DYC will be designed to keep the vehicle inside the stability limits and to reduce path errors with respect to a reference model. Furthermore, the controller will also include a properly designed cruise-control system, featuring good responsiveness when the velocity error is high and robustness when it approaches zero. Overall, the expected outcome is a unique vehicle dynamics controller distributing torque to the motors for several BEV configurations.

The second macro-objective is the development of a user-friendly simulation environment, where driver inputs can be tuned by using simple knobs and switches in a dashboard, and results in terms of vehicle states and trajectory are automatically shown at the end of the simulation. The proposed vehicle dynamics control strategy will be verified under different driving scenarios, with combinations of throttle, braking, steering angle, controller activation, initial vehicle velocity inputs and road adhesion conditions. Moreover, the simulation environment will allow the benchmarking of different BEV architectures.

The final objective of this thesis is the comparison of the implemented vehicle dynamics controller with current control strategies available in literature to prove its merit.

1.4 Methodology

The work will be based on a top-down approach: having the bigger picture in mind, the problem will be decomposed in smaller sub-problems, which are addressed and solved one at a time. First, the models and simulations will be build in MATLAB-Simulink. Beginning with the vehicle model, a good entry-level to start with is the well-known bicycle model. Afterwards, it will be refined adding more complexities for a higher-fidelity model with seven degrees of freedom, namely longitudinal, lateral, yaw and rotation of each wheel. Simple tire models will be also included, first considering a linear model and then the Pacejka's Magic Formula.

As with the state-of-the-art, a hierarchical control will be developed for DYC. The upper-layer will be based on a Sliding Mode Control applied to Model Following Control (MFC): the objective is to make the vehicle following a desired behaviour defined by a reference model, in this case the bicycle model. The lower-layer will implement a torque distribution strategy to strategically split the requested torque from both driver and upper-layer controller, ensuring performance and stability at the same time. Furthermore, a cruise-control system will be implemented and integrated in the vehicle controller.

The development of the integrated controller will be analyzed and its design choices will be thoroughly explained. Simulations will be run and the results benchmarked with the available control strategies to verify the merit of the proposed controller.

1.5 Thesis Structure

In Chapter 2, the available literature relevant to vehicle dynamics and controllers will be reviewed, with particular focus on longitudinal and lateral dynamics, and types of controllers for TCS and TVC .

Chapter 3 will present the vehicle model developed in MATLAB-Simulink, together with tire, electric motor and driver models.

Chapter 4 will explain the developed integrated controller and its design choices. At first, the Torque Vectoring Controller upper-layer will be presented, followed by the cruise control and the Traction Control System. Then, the torque distribution strategy allocating the torque from driver's inputs and controllers outputs will be explained.

Chapter 5 will show and discuss the obtained results for several driving scenarios and driver's inputs to verify the merit of the proposed integrated and modular vehicle dynamics controller.

Finally, Chapter 6 will include the conclusions, the recommendations and the limitations, along with a summary of the research contributions of the present thesis.

Chapter 2

Literature Review

2.1 Vehicle Dynamics

Vehicle dynamics is the study of the motion of vehicles to understand their behaviour [26]. At a general level, it can be subdivided into three interrelated branches: longitudinal dynamics, lateral dynamics and vertical dynamics. As the name suggests, the first one deals with the vehicle motion in its longitudinal direction, that is acceleration and braking, the second one refers to the lateral direction of the motion, i.e., when cornering, and the third one studies ride quality. As said before, there is no demarcation line among them since longitudinal, lateral and vertical dynamics interact together in most practical cases (e.g. braking and accelerating while cornering) [27].

2.1.1 Coordinate Systems

Before exploring the equations for longitudinal and lateral dynamics, it is important to introduce the two main coordinate systems that will be used in the present work. Looking at Figure 2.1, XYZ is the global inertial reference frame while xyz is the ISO standard vehicle coordinate system. It is worthwhile to mention that SAE defined another vehicle coordinate system, considering the positive y-axis toward the right and the positive z-axis pointing down.

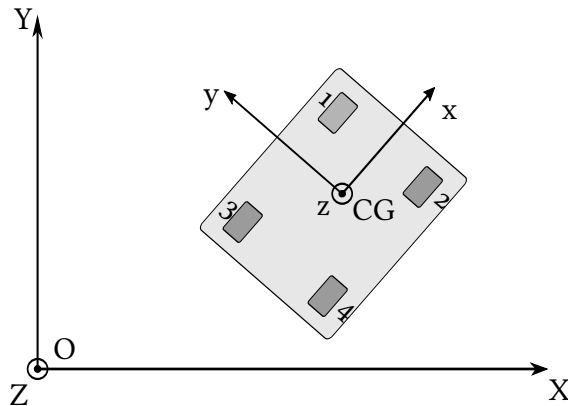


FIGURE 2.1: Coordinate systems: global inertial reference frame XYZ and standard vehicle coordinate system xyz

2.1.2 Longitudinal Dynamics

With reference to Rajamani[28], consider a vehicle with mass m moving on a sloped road with acceleration a_X , as shown in Figure 2.2 . Writing Newton's Second Law for this system results in the following:

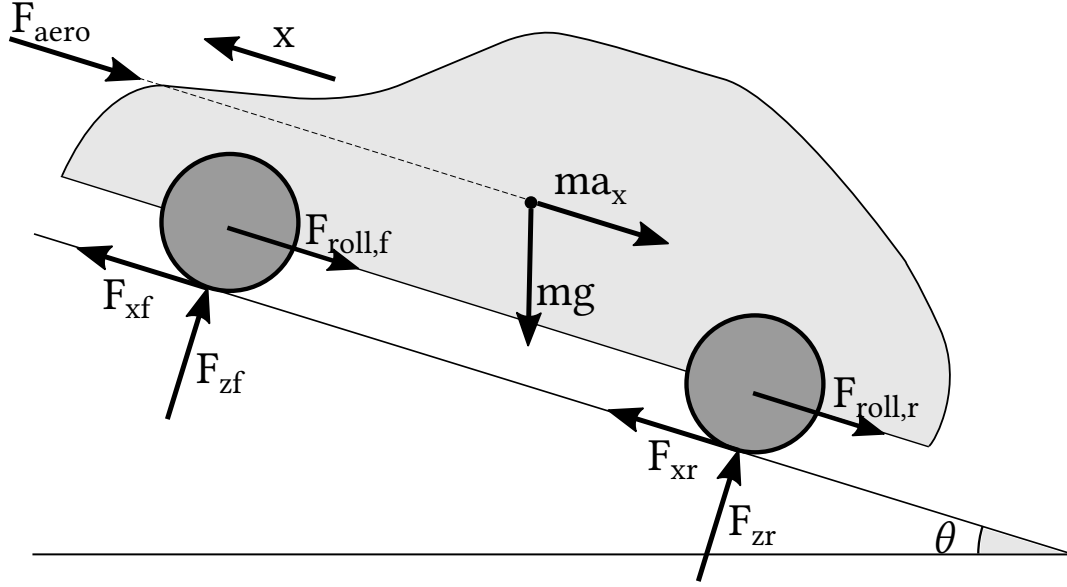


FIGURE 2.2: Car free body diagram: forces in longitudinal and vertical direction

$$ma_X = F_{xf} + F_{xr} - F_{aero} - F_{roll} - F_{slope} \quad (2.1)$$

The aerodynamic drag force F_{aero} is obtained as:

$$F_{aero} = \frac{1}{2} \rho S C_x v_{rel}^2 \quad (2.2)$$

where ρ is the air density, S is the frontal area of the vehicle, C_x is the aerodynamic drag coefficient (obtained in wind tunnel tests) and v_{rel} is the relative velocity of the air with respect to the vehicle (assuming that there is no wind, it simply becomes the vehicle speed).

The term F_{roll} is the total tire rolling resistance. This is a complex phenomenon due to hysteresis and deformation at tire-road contact patch that results in a loss of energy. With reference to a generic i tire, the rolling resistance can be modelled with the following formula:

$$F_{i,roll} = fFz_i \quad (2.3)$$

where Fz_i is the vertical load acting on the tire and f is the rolling resistance coefficient, which can be approximated with a quadratic function of the longitudinal speed:

$$f = f_0 + f_1 v^2 \quad (2.4)$$

where f_0 and f_1 are constants.

By summing Equation 2.3 for the four tires, the total tire rolling resistance becomes:

$$F_{roll} = fmg \cos \theta \quad (2.5)$$

The force required to travel on a θ -inclined road F_{slope} is equal to:

$$F_{slope} = mg \sin \theta \quad (2.6)$$

The front and rear tire forces in the x direction are F_{xf} and F_{xr} respectively. Since only longitudinal dynamics is considered, the vehicle can be collapsed along its longitudinal symmetry axis without introducing accuracy losses. With this assumption, the wheels on the same axle have the same forces and therefore it is simple to get rid of axle forces and deal with forces acting on each single wheel.

Longitudinal forces depend on several factors, such as vertical load, road-tire friction coefficient and slip ratio. The last mentioned parameter is defined as:

$$\sigma_x = \frac{R_e \omega_w - V_x}{V_x} \quad (2.7)$$

where ω_w is the wheel angular velocity, V_x is the longitudinal velocity of the wheel hub and R_e is the tire effective rolling radius, which is defined as the radius of a rigid wheel that has the same longitudinal and angular velocity of the pneumatic wheel. It differs with respect to the unloaded and loaded radii due to tire deformation, and for a radial tire it is usually about 98% of the unloaded radius [29].

The equation describing wheel dynamics is a simple moment balance around its spin axis:

$$J_w \dot{\omega} = T_w - F_x R_l \quad (2.8)$$

where J_w is the wheel moment of inertia, $\dot{\omega}$ is the angular acceleration, T_w is the applied torque, F_x is the longitudinal tire force and R_l is the tire loaded radius (for a radial tire, it is usually about 94% of the unloaded radius [29]). The associated free body diagram is shown in Figure 2.3.

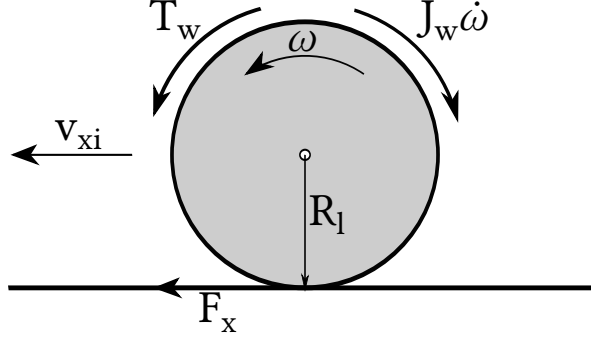


FIGURE 2.3: Wheel free body diagram

Figure 2.4 represents a classic tire longitudinal behaviour. At first approximation, the characteristic curve can be considered linear for small σ values. The longitudinal force can be then expressed as:

$$F_x = C_\sigma \sigma \quad (2.9)$$

where C_σ is the tire longitudinal stiffness, defined as $C_\sigma = \left(\frac{\partial F_x}{\partial \sigma} \right)_{\sigma=0}$.

Another important variable is the longitudinal force coefficient $\mu_x = \frac{F_x}{F_z}$, plotted in Figure 2.5 as function of σ . It mainly depends on road adhesion conditions, type of tire and presence of lateral forces.

2.1.3 Lateral Dynamics

Lateral dynamics is intrinsically more complex than longitudinal dynamics because more variables are involved. The simplest model to study vehicle lateral dynamics is the so-called bicycle model [28] (also known as the yaw plane model), reported in Figure 2.6. It features two Degrees of Freedom (DoF), namely vehicle lateral position, y , and yaw angle, ψ (rotation about the vertical axis), and its distinguishing characteristic is that the two front and the two rear wheels are collapsed together such that the vehicle width is neglected. Moreover, the steering angle is assumed to be small such that it can be neglected, and the longitudinal velocity is a constant parameter.

Newton's Second Law applied to this system in the y direction gives the following equation:

$$ma_Y = F_{yf} + F_{yr} \quad (2.10)$$

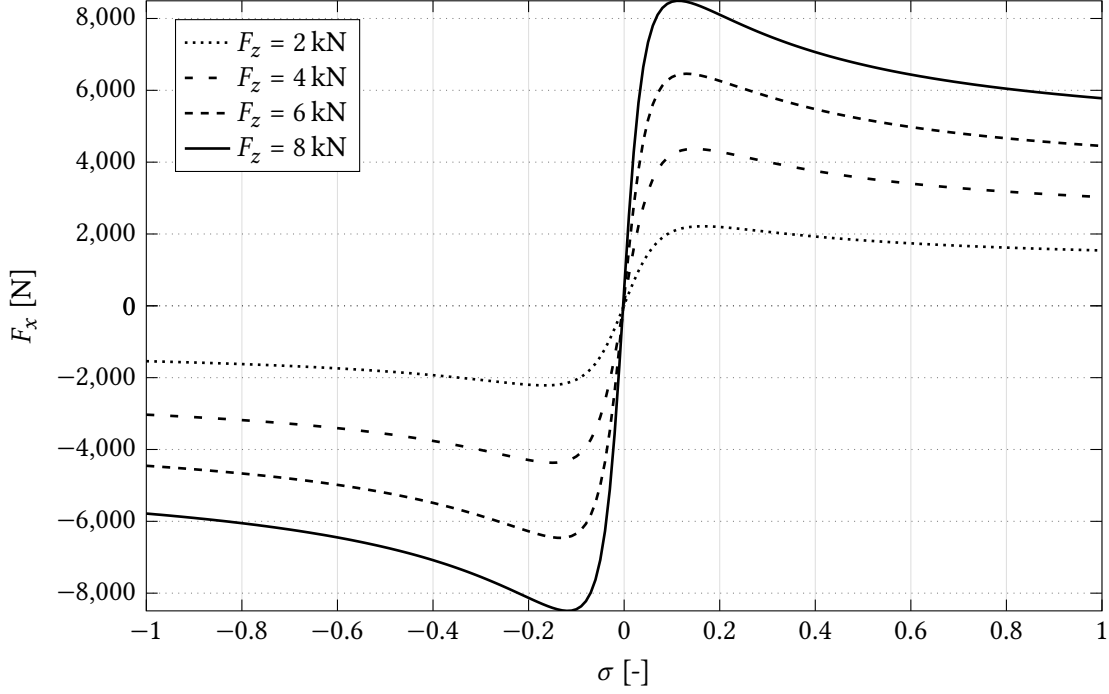


FIGURE 2.4: $F_x - \sigma$ characteristic of a 185/60 R14 tire for different vertical loads (experimental data from Tonoli[30])

where a_Y is the vehicle lateral acceleration in the global inertial reference frame OXY (see the definition of coordinate systems in Figure 2.1), and F_{yf} and F_{yr} are respectively the front and rear side forces at tire level (see the free body diagram in Figure 2.6). It is more convenient to write the acceleration with respect to the vehicle coordinate system $CGxy$:

$$a_Y = a_y + v_x \dot{\psi} \quad (2.11)$$

a_y is the lateral acceleration in the non-inertial reference frame, v_x is the vehicle longitudinal speed and $\dot{\psi}$ is the yaw rate (very often also referred as r). Substituting Equation 2.11 into Equation 2.10, the equation describing vehicle motion in y direction is obtained:

$$m(a_y + v_x \dot{\psi}) = F_{yf} + F_{yr} \quad (2.12)$$

Assuming that v_x is constant and known, Equation 2.12 still has two unknowns, i.e., a_y and $\dot{\psi}$. The moment balance about the z -axis is introduced:

$$J_z \ddot{\psi} = F_{yf} a + F_{yr} b \quad (2.13)$$

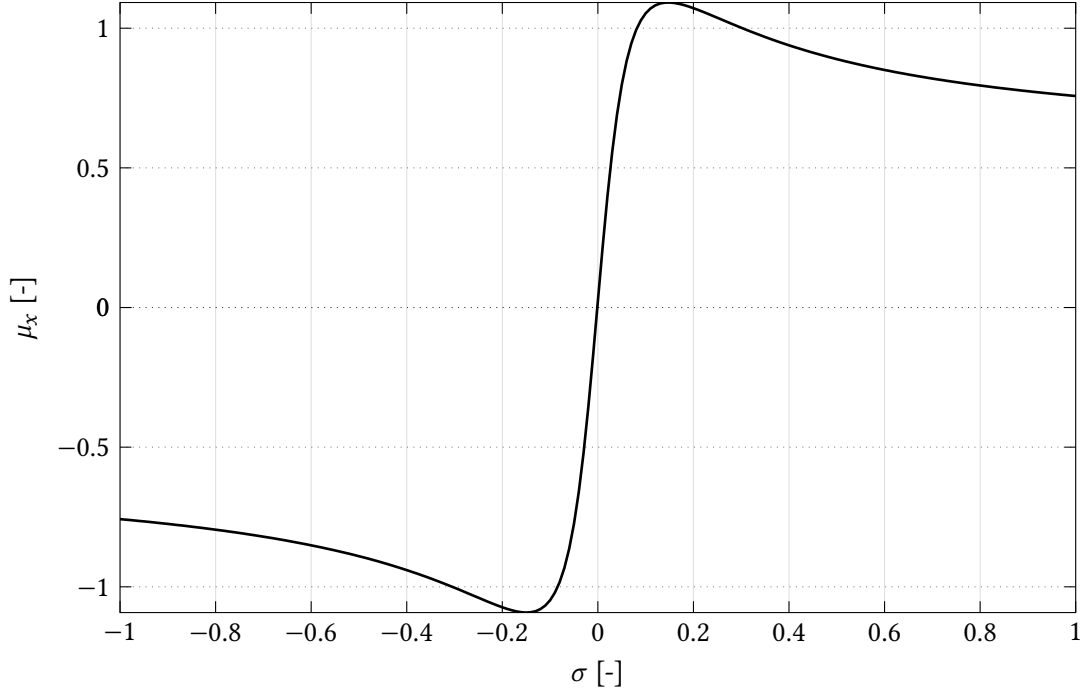


FIGURE 2.5: $\mu_x - \sigma$ characteristic of a 185/60 R14 tire for $F_z = 4$ kN. It is representative of a dry tarmac road

where J_z is the vehicle moment of inertia about the z -axis, $\ddot{\psi}$ is the yaw acceleration, and a and b are respectively the distances of the front and rear axle from the centre of gravity of the vehicle.

An important vehicle state that will be thoroughly discussed in Section 2.2.3 is the Vehicle Side-slip Angle (VSA) β , defined as:

$$\beta = \arctan \frac{v_y}{v_x} \quad (2.14)$$

Figure 2.7 explains the origin of tire lateral forces: whenever the velocity of the i^{th} wheel hub is at an angle α_i with respect to the wheel vertical middle plane, the tire produces a lateral force. That angle is called tire side-slip angle and it is evaluated as:

$$\alpha_i = \beta_i - \delta = \arctan \left(\frac{v_y + \dot{\psi} x_i}{v_x - \dot{\psi} y_i} \right) - \delta \quad (2.15)$$

where β_i is the angle between the wheel hub velocity and the longitudinal vehicle axis, δ is the wheel steering angle, v_y is the lateral vehicle speed, x_i and y_i are the distances between the Centre of Gravity (CG) and the i^{th} wheel in x and y direction respectively (the sign convention is consistent with the CGxy reference frame in Figure 2.6) [29]. In the particular case of the bicycle

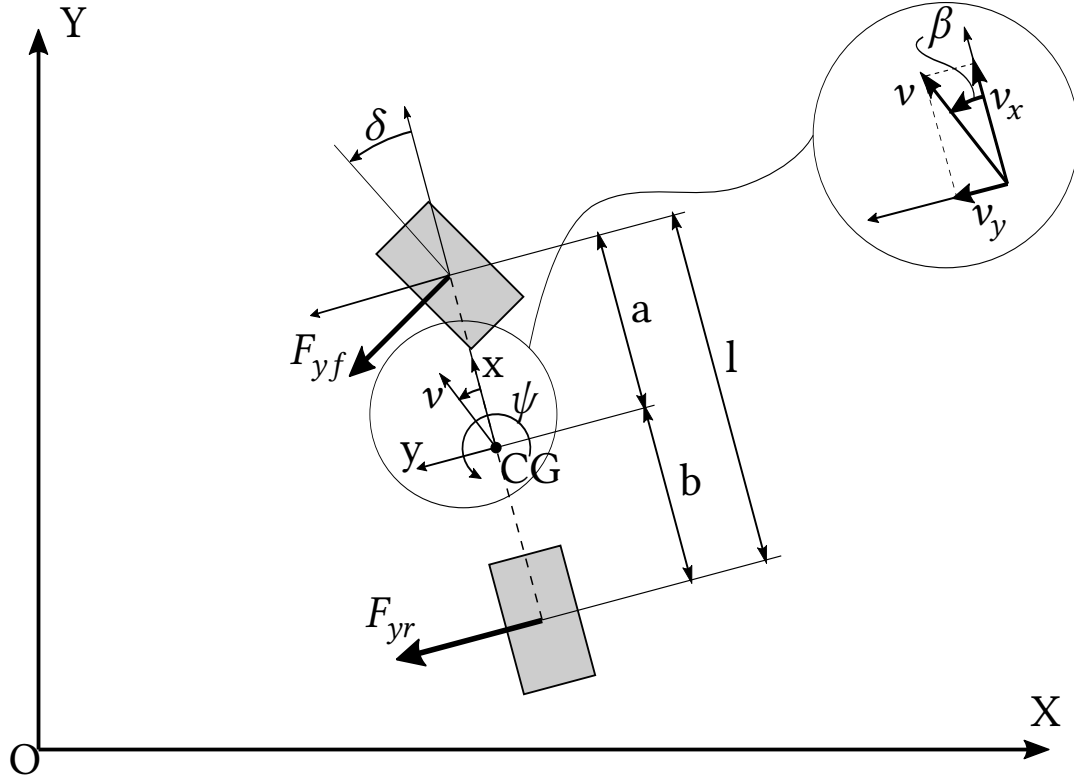


FIGURE 2.6: Bicycle model

model y_i is zero. Besides, α_i is positive when it goes counter-clockwise from x_{ti} to y_{ti} and negative in the other case (the one reported in Figure 2.7).

From experimental data in Tonoli[30], the tire lateral force as a function of its side-slip angle is represented by a curve as the one in Figure 2.8. The convention assumes that a negative value of α generates a positive F_y . For this reason, in order to have the plot in the first and third Cartesian plane quadrants, the tire lateral characteristic is usually plotted for $-F_y$.

For small tire side-slip angles, the characteristic can be considered linear:

$$F_y = -C_\alpha \alpha \quad (2.16)$$

The tire cornering stiffness C_α is defined as $C_\alpha = \left(\frac{\partial F_y}{\partial \alpha} \right)_{\alpha=0}$. Once more, the minus sign in the equation is to be consistent with the F_y and α sign convention, since the cornering stiffness is defined as an always-positive value. Figure 2.9 shows its trend with respect to vertical load when varying side-slip angles values. Cornering stiffness increases for higher vertical loads until a limit value which depends on α , then it remains constant or slightly decreases. Besides, for the same vertical load it decreases by increasing the side-slip angle. It is also a common practice to express cornering stiffness values in N/rad, while keeping α in degree.

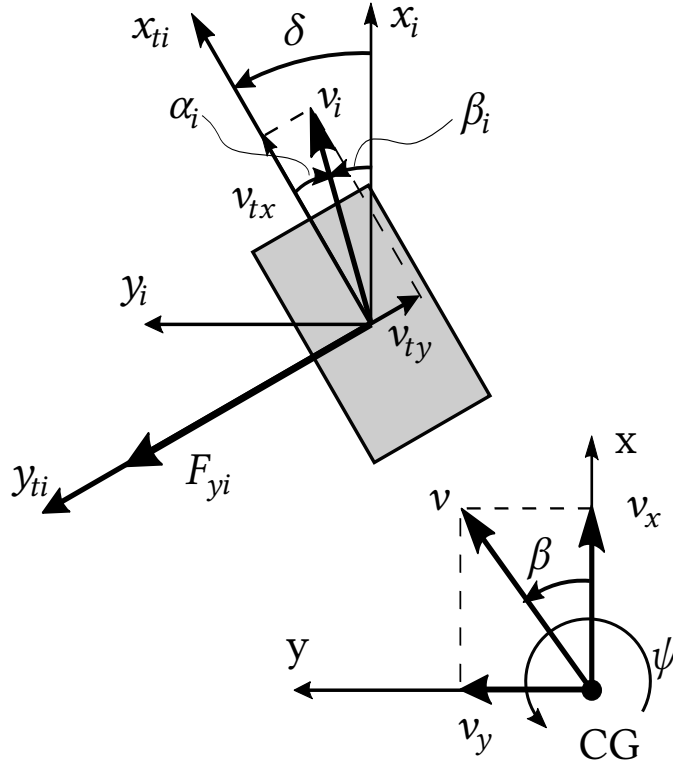


FIGURE 2.7: Important angles for tire lateral behaviour

Under the assumption of small angles, Equation 2.15 is linearized and substituted into Equation 2.16 to get the lateral tire force written in an expanded form:

$$F_y = -C_\alpha \left(\frac{v_y + \dot{\psi} x_i}{v_x} - \delta \right) \quad (2.17)$$

Equations 2.12 and 2.13 represent the basis of the bicycle model. Substituting Equation 2.17 into them and rearranging the terms, the final result is a system of two equations [15]:

$$m(\dot{v}_y + v_x \dot{\psi}) = -(C_f + C_r) \frac{v_y}{v_x} - (aC_f - bC_r) \frac{\dot{\psi}}{v_x} + C_f \delta \quad (2.18)$$

$$J_z \ddot{\psi} = -(aC_f - bC_r) \frac{v_y}{v_x} - (a^2 C_f + b^2 C_r) \frac{\dot{\psi}}{v_x} + aC_f \delta \quad (2.19)$$

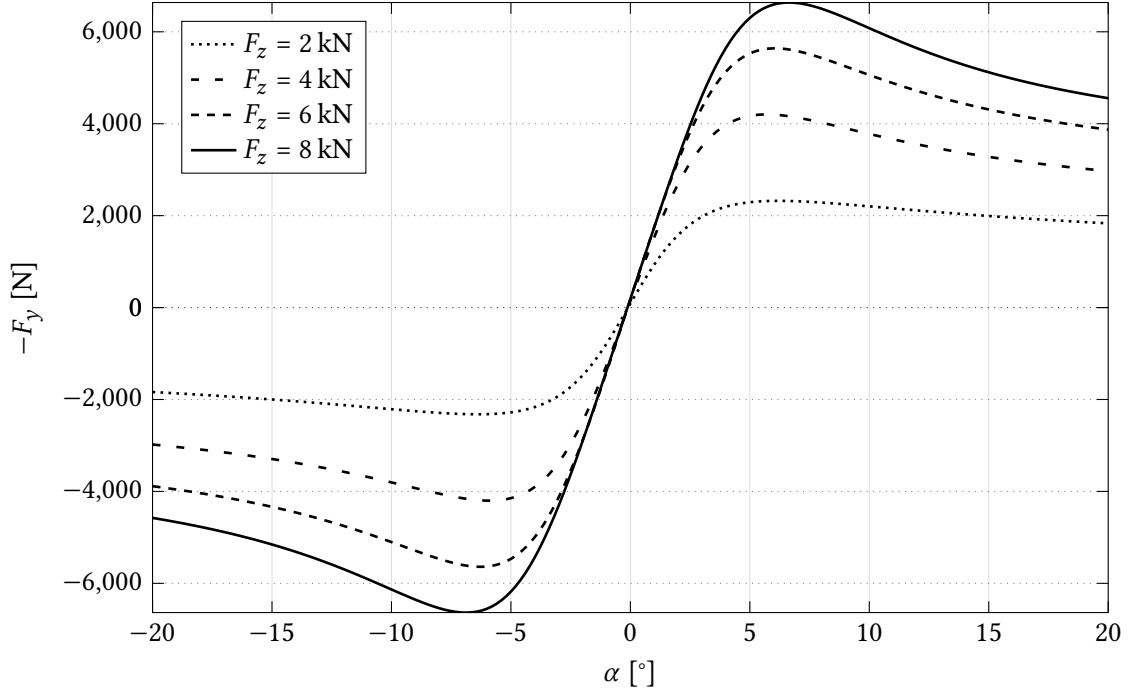


FIGURE 2.8: $-F_y - \alpha$ characteristic of a 185/60 R14 tire for different vertical loads (experimental data from Tonoli[30])

Extracting \dot{v}_y from the first and $\ddot{\psi}$ from the second, the bicycle model equations can be written in matrix form as:

$$\begin{bmatrix} \dot{v}_y \\ \ddot{\psi} \end{bmatrix} = \begin{bmatrix} -\frac{C_f + C_r}{mv_x} & -\frac{aC_f - bC_r}{mv_x} - v_x \\ -\frac{aC_f - bC_r}{J_z v_x} & -\frac{a^2 C_f + b^2 C_r}{J_z v_x} - v_x \end{bmatrix} \begin{bmatrix} v_y \\ \dot{\psi} \end{bmatrix} + \begin{bmatrix} \frac{C_f}{m} \\ \frac{aC_f}{J_z} \end{bmatrix} \delta \quad (2.20)$$

2.1.4 Tire Models

A high-fidelity tire model is fundamental in vehicle dynamics simulations, as the accuracy of the vehicle model itself is significantly affected by the tire model [11]. Equations 2.9 and 2.16 introduced respectively in Sections 2.1.2 and 2.1.3 are too simple and accurate enough only in the linear tire range. Besides, they treat longitudinal and lateral dynamics as separate, even though experimental studies demonstrated that there is a coupling between the two: if the tire produces forces in both directions, the traction used in one direction somehow limits that available in the other [29]. This behaviour is modelled with the so-called friction ellipse:

$$\left(\frac{F_x}{F_{x0}} \right)^2 + \left(\frac{F_y}{F_{y0}} \right)^2 = 1 \quad (2.21)$$

$F_{x0} = \mu_{xp} F_z$ is the maximum longitudinal force that can be developed (when side-slip angle is null) and $F_{y0} = C_0 \alpha$ is the maximum lateral force when no longitudinal traction is exploited.

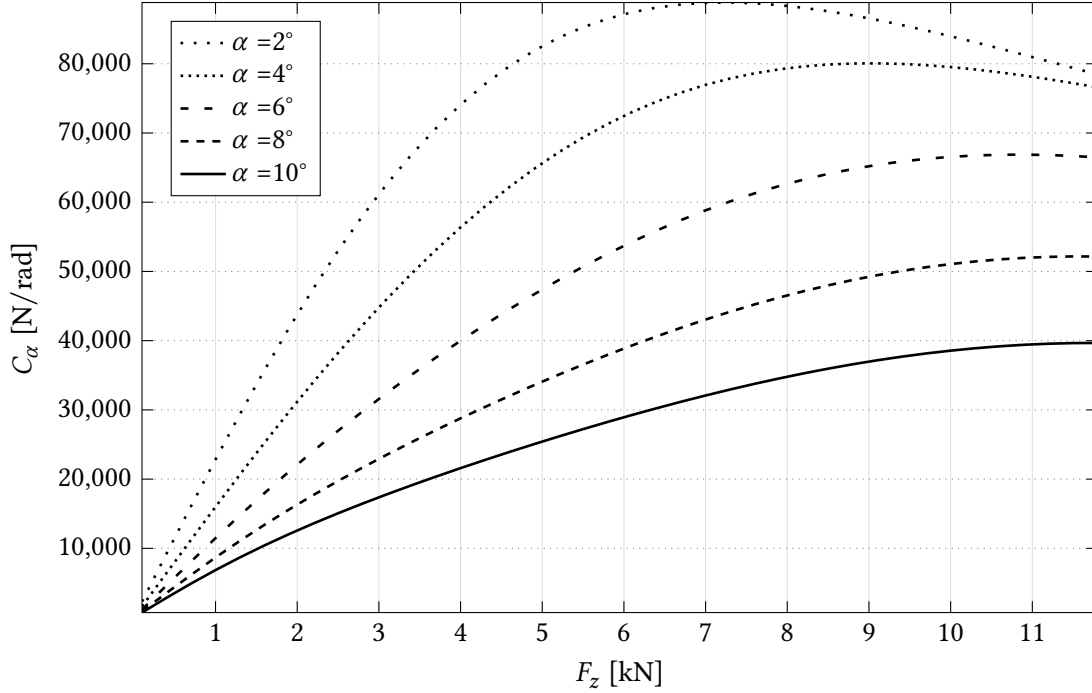


FIGURE 2.9: $C_\alpha - F_z$ characteristic of a 185/60 R14 tire for different side-slip angles (experimental data from Tonoli[30])

Figure 2.10 plots the friction ellipses for several values of tire side-slip angles.

Several tire models have been studied over the years. Dugoff's and Burckhard's tire models are both empirical, with the second one being more accurate as it describes tires non-linearities and longitudinal-lateral characteristics coupling. They fulfill both good model accuracy and fast computational time for real-time implementations. Conversely, some other models have been developed to represent tire behaviour at its best, like Pacejka's Magic Formula. It is probably the most widespread model in vehicle dynamics simulations; it is excellent in accuracy but it is heavier from the computational point of view [10].

Pacejka[31] contains an accurate description of the semi-empirical Magic Formula's tire model. Its general form is:

$$y = D \sin\{C \arctan[Bx - E(Bx - \arctan(Bx))]\} \quad (2.22)$$

y and x are defined as:

$$y(x) = Y(x) - S_V \quad (2.23)$$

$$x = X + S_H \quad (2.24)$$

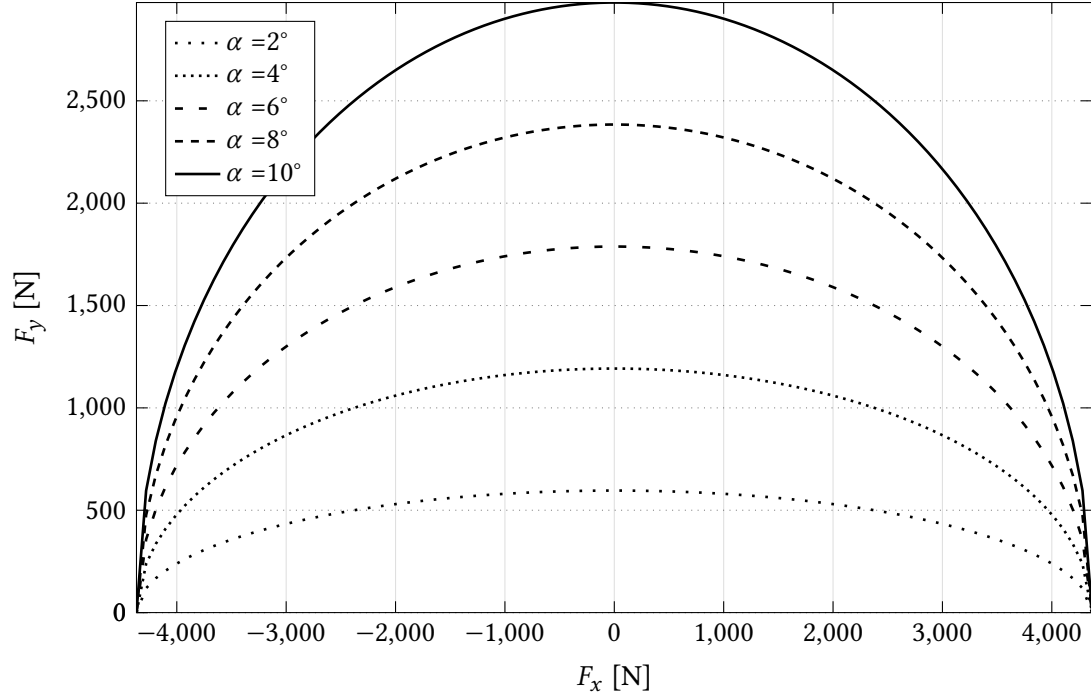


FIGURE 2.10: $F_y - F_x$ friction ellipse characteristic of a 185/60 R14 tire for different side-slip angles at $F_z=4$ kN (experimental data from Tonoli[30])

where Y and X are respectively the output and the input, S_V is the vertical shift, S_H is the horizontal shift, and D, C, B, E are factors. For instance, in the case of longitudinal tire force, the input is σ (defined as in Equation 2.7) and the output is F_x . The complete equations for longitudinal and lateral forces are reported below for sake of clarity:

$$F_x = D \sin\{C \arctan[B(1 - E)(\sigma + S_H) + E \arctan[B(\sigma + S_H)]]\} + S_V \quad (2.25)$$

$$F_y = D \sin\{C \arctan[B(1 - E)(\alpha + S_H) + E \arctan[(B(\alpha + S_H))]]\} + S_V \quad (2.26)$$

The B, C, D, E factors are clearly different in the two cases, being a function of vertical load in the first, and of vertical load and camber angle in the second.

The output curves from Magic Formula's tire model look exactly the same as the tire characteristics obtained from experimental data. Figure 2.11 shows the longitudinal force error introduced with Pacejka's model as function of slip rate. Even though the plot may look noisy, the important thing to notice is that the error is in the order of magnitude of tens of N, demonstrating the accuracy of such a model.

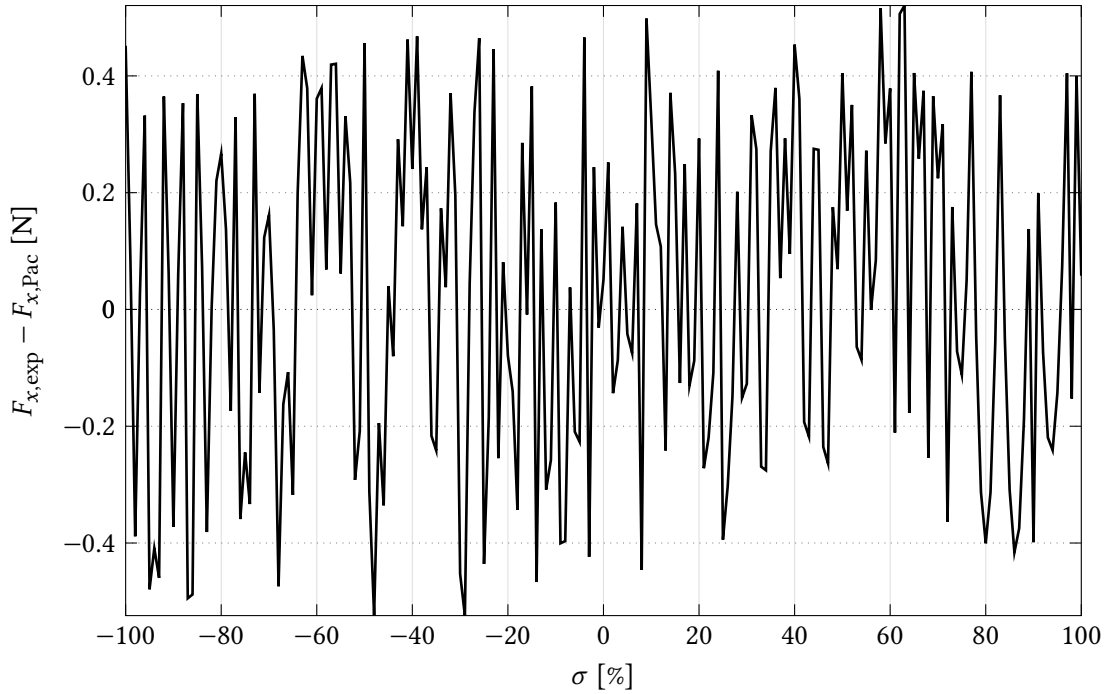


FIGURE 2.11: F_x error between experimental data (from Tonoli[30]) and Pacejka's Magic Formula of a 185/60 R14 tire for $F_z=4$ kN

2.2 Automotive stability enhancement systems

Automotive stability enhancement systems have been studied, developed and tested over the last decades. Although some manufacturers have renamed their products to highlight unique features, the Society of Automotive Engineers (SAE) classifies primary systems in Antilock Braking System (ABS), Traction Control System (TCS) and Electronic Stability Control (ESC) [5]. ESC characteristics and controller implementations will be thoroughly discussed in Section 2.2.3, since this study will mainly focus on its development. Nevertheless, a quick description of ABS and TCS will be also provided in Sections 2.2.1 and 2.2.2.

2.2.1 Antilock Braking System

ABS regulates the braking torque to control wheel slip with the aim of improving vehicle stability under braking conditions. Indeed, monitoring the wheel speeds and triggering ABS intervention prevents the wheels from locking and this is beneficial for the vehicle steering capability. Keeping in mind the tire friction ellipse discussed in Section 2.1.4, if the wheel locks, i.e., $\sigma = -1$, the tire is completely saturated in the longitudinal direction and there is no other available traction to be exploited in the lateral direction, thus the vehicle loses steering capability. Besides, ABS reduces braking distance under most road conditions when compared to a vehicle without it [5].

2.2.2 Traction Control System

Traction Control Systems are used to regulate wheel slip rate to prevent the wheel from excessive spinning under high acceleration and low road-adhesion conditions, with the aim to improve vehicle stability and steer-ability. Other common names to refer to TCS are Automotive Stability Control (ASC) and Automatic Stability Regulation (ASR, sometimes also called Anti-Slip Regulator) [5].

Estimation of the road friction coefficient, real-time slip rate value and control algorithm are the key aspects in the implementation of a TCS. Its performance is highly dependent on the merit of the tire-road adhesion coefficient estimation, which is a fundamental parameter to evaluate the reference slip rate [32]. Road friction estimation methods are usually based on extended Kalman filters, neural networks or statistical methods, while Zhang and Göhlich[33] applied Bayes' theorem-based iteration algorithm.

Conventional ICE vehicles utilize TCS by controlling the engine torque and/or brake torques. However, these methods intrinsically feature slow response and poor control accuracy of the actuators [32]. Zhang and Göhlich[33] studied a traction control strategy applied to a 4 In-Wheel Motor Distributed Drive Electric Vehicle (4IWMDDEV), exploiting quick and accurate torque response from electric motors. On high adhesion roads, the torque is distributed to maximize motor efficiency, while on low adhesion roads a sliding mode control is implemented to keep the wheel slip ratio around the optimal point. However, since the definition of σ (see Equation 2.7) can lead to numerical issues when the vehicle velocity is small, the study considered the wheel rotational speed as control variable, defining the following sliding surface:

$$s = (\omega - \omega_0) + c \int (\omega - \omega_0) dt \quad (2.27)$$

where ω is the current wheel angular speed, ω_0 is the angular speed corresponding to the optimal slip ratio and c is a constant.

The dynamics of the sliding surface is given as:

$$\dot{s} = -ks - \epsilon \operatorname{sgn}(s) \quad (2.28)$$

with k and ϵ constant parameters.

Eventually, Equation 2.27 is differentiated and combined with Equation 2.28, and the obtained $\dot{\omega}$ is substituted into Equation 2.8 (representing the wheel dynamics) to get the torque that has to be allocated on each wheel to reach the optimal slip ratio:

$$T = -J_z[\epsilon \operatorname{sgn}(s) + ks + c(\omega - \omega_0)] + F_x R_l \quad (2.29)$$

Zhai et al.[21] implemented a wheel slip controller for a 4IWMDDEV based on the fuzzy logic control method. The input of the controller is the slip ratio error between the actual value and the desired one (set equal to 0.2), and its output is the adjustment torque for each in-wheel motor.

Some other studies have focused on anti-slip control strategies in combination with torque distribution algorithms for multi-motor EVs. In a conventional torque distribution strategy there is no direct control over tire slip rate, meaning that if the allocated output torque leads to a driving force higher than tire adhesion conditions, there must be an ABS/ASR intervention. This anti-slip control strategy is said to be passive. Conversely, in the torque distribution strategy proposed by Cao et al.[17] for a dual-motor EV, the anti-slip control is active: the maximum driving torque complying with tire adhesion conditions is set as the limit value when applying the torque distribution strategy:

$$T_{k,\text{lim}} = \mu F_{zk} R_l \quad (2.30)$$

where $T_{k,\text{lim}}$ is the limit torque that can be applied on the k^{th} axle to stay within the maximum admissible tire slip rate, μ is the road friction coefficient, F_{zk} is the vertical load on that axle and R_l is the tire loaded radius.

Even though the above-mentioned control is not a proper TCS by definition because it does not control wheel slip directly, it is still a valuable countermeasure to avoid undesired wheel slipping.

2.2.3 Electronic Stability Control

An Electronic Stability Control system monitors vehicle states and driver's commands in order to improve vehicle stability and maneuverability with yaw moment adjustments. By definition, it is a computer controlled system with a closed-loop algorithm that measures or estimates yaw velocity, vehicle side slip angle and driver's steering input, and induces a yaw moment correction to the vehicle. The hardware needed to accomplish this task includes wheel speed sensors, steering angle sensors, velocity sensors and accelerometers [5]. The reader may sometimes find ESC also referred as ESP (Electronic Stability Program), Yaw Control Stability (YCS) or under the general terms of Vehicle Stability Control (VSC) or Vehicle Dynamics Control (VDC).

Vehicle side slip angle is a key state for stability purposes, but sensors to measure it are too expensive and cannot be used in practical applications for normal cars. Besides, optical transducers require a precise alignment for a reliable measurement and a stiff structure to avoid vibrations [34]. For this reason, state estimation methods are required. They can be classified into observer-based and neural-network based: the first one uses a vehicle reference model for state estimators, the second one is based on Artificial Neural Networks (ANN) [35]. Examples of observer-based are the Extended Kalman Filter (EKF), developed in Gadola et al.[34], and the Luenberger observer, implemented in Lu et al.[7].

VSC systems can be classified in two categories: Active Steering (AS), in which the steering input from the driver is adjusted, and Direct Yaw-moment Control (DYC), in which an additional yaw moment is generated by using driving or braking torques on the wheels. AS systems are further subdivided into Active Front Steering (AFS), Active Rear Steering (ARS) and 4 Wheel Steering (4WS). These systems use an electric motor as actuator to generate active steering torque. In the case of AFS and 4WS, the steering angle on the wheels is the sum of the steering angle from the driver and the rotary actuator. As a rule of thumb, ARS is for low speed maneuvers and AFS is better for high speed maneuvers. However, Active Steering systems in general have important limitations when the tire enters in the lateral saturation region. By contrast, DYC systems also work in the tire lateral non-linear range, as they exploit longitudinal forces. In ICE-based vehicles such systems work by controlling the four brakes individually and/or the engine torque. However, if braking is applied then the vehicle longitudinal performance is reduced, and if driving torque is applied then the yaw moment correction could be insufficient at high speeds. Sometimes, the combination of AS and DYC is implemented, leading to the so-called Integrated Vehicle Dynamics Control (IVDC): AFS is activated before the tire saturation region, DYC in the other case [12].

The activation of DYC affects the mechanical power of the wheels and the cornering resistance, defined as the projection of the lateral forces on the vehicle side slip angle. In short, it is the resistance in longitudinal direction due to lateral forces [36, 37].

Overall, several kinds of VCS systems have been implemented in the last two decades. Although the list of names is long, their common target is the enhancement of vehicle stability. DYC is the most suitable system under a broader range of conditions because it removes the lateral tire saturation problem. Section 2.2.4 will focus on DYC systems for BEV, where the electric motors' exploitation does make the difference with respect to engine-based and friction brakes-based methods.

2.2.4 Torque Vectoring Control

Torque Vectoring Control (TVC) consists of the direct control of electric motor torque at the wheels in order to improve traction and handling of the vehicle. In particular, different longitudinal forces are applied on the wheels of the same axle in order to produce a yaw moment correction that can be used to control vehicle's lateral dynamics [38].

Torque vectoring controllers in the literature are usually based on a hierarchical approach: the upper-layer evaluates the corrective yaw moment and the lower-layer allocates the requested torque to the electric motors using a torque distribution algorithm [8, 9, 10, 11]. Zhai et al.[21] presented a TVC with a further layer on top of the other two, called stability judgment controller, whose aims are the generation of desired yaw rate and side slip angle, and the choice of the control mode (normal driving or ESC activated). Eventually, the third possibility is to have a one-layer controller which directly computes the torques on each wheel. However, in this case the vehicle model has to be simplified [10].

The stability controllers are mainly based on MFC: the objective is to make the vehicle follow a desired behaviour defined by a reference model, which is usually the well-known bicycle model for its simplicity and acceptable accuracy at the same time [7]. Figure 2.12 represents a typical torque vectoring control scheme. The vehicle state x and the reference vehicle state x_{ref} are used to compute the state error e_x . The upper-layer controller exploits this error for the computation of the corrective yaw moment ΔM_z that is then transformed by the lower-layer controller into a total torque value to be split among the motors according to a torque-allocation algorithm.

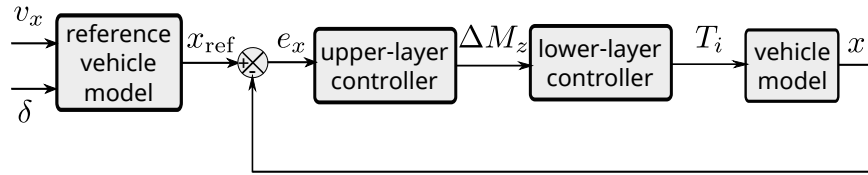


FIGURE 2.12: General control scheme for a hierarchical TVC based on Model Following Control

Undoubtedly, several automatic control strategies are available in the literature for the high-level controller. Medina et al.[39] compared them and the results are summarized in Table 2.1.

TABLE 2.1: Comparison among Proportional Integral Derivative, Linear Quadratic Regulator, Linear Quadratic Gaussian Regulator, Model Predictive Control, Fuzzy logic and Sliding Mode Control

	Pros	Cons
PID	easy implementation low computational requirements	plant linearization required missing complete vehicle knowledge
LQR	minimize state error and control action	sensitive to perturbations plant linearization required
LQGR	minimize state error and control action disturbances modelled as Gaussian noises	plant linearization required
MPC	optimization between error and control action non-linearities included	computationally heavy
Fuzzy logic	effective control strategy for DYC	designer's expertise required
SMC	robust against modelling uncertainties	risk of extremely active controller

Zhai et al.[21] implemented a fuzzy logic PID whose inputs are the side slip angle and yaw rate errors. The same state variables were used in Zhang et al.[4] and Zhou et al.[10] for an MPC strategy, and in Lu et al.[7] for a gain scheduling controller with feedforward and feedback terms.

As opposed to the upper-layer controller, the lower one depends on the EV configuration, i.e., number and position of electric motors. Eight possible drive system patterns were individuated

by Himeno et al.[40]: 4 IWMs, 1 motor in the front and 2 IWMs in the rear, 2 IWMs in the front and 1 motor in the rear, 2 IWMs in the rear, 2 IWMs in the front, 1 motor in the front and 1 motor in the rear, 1 motor in the front, 1 motor in the rear. The DYC cannot be applied to the last three configurations because there is no way to generate a difference in driving force between left and right wheels. However, a smart control strategy could be implemented when the vehicle is endowed with one motor per each axle. In that case, a proper torque distribution between front and rear axle could correct understeering and oversteering behaviour, giving more torque to the rear in the former case and more torque to the front in the latter one.

The objective of the low-level controller is the distribution of the requested torque from driver's inputs and high-level controller to the electric motors according to a torque allocation algorithm. In the case of multiple motors EVs, this is the so-called over-actuated problem, i.e., the control outputs (torques to the motors) are more than the states to be controlled [10]. In over-actuated systems the control allocation algorithm is of paramount importance [22]. In Li et al.[16], torque distribution strategies are classified into vehicle economy-based and vehicle stability-based: the first ones consider motor losses, motor efficiency, friction power and energy feedback; the second ones account for maneuverability and stability, surface adhesion consumption rate and vehicle path tracking ability. However, since the torque distribution has an effect on both economy and stability of the vehicle, they should be considered together in a multi-objective torque distribution strategy for the improvement of the overall vehicle performance.

Optimization-based torque distribution strategies have been widely studied over the past years. Zhai et al.[21] considered tire utilization applied to a 4IMDEV, defined as:

$$\min J = \sum_{i=1}^4 \frac{F_{xi}^2 + F_{yi}^2}{(\mu F_{zi})^2} \quad (2.31)$$

Tire longitudinal friction work is introduced in Yamakawa and Watanabe[6]:

$$\min J = \sum_{i=1}^4 F_{xi} \cdot v_{s,xi} \quad (2.32)$$

where $v_{s,xi}$ is the tire longitudinal slip velocity at the contact patch of the i^{th} tire.

A similar study was carried out in Kobayashi et al.[37] considering the total tire dissipation power at the contact patch:

$$\min J = \sum_{i=1}^4 \vec{F}_i \cdot \vec{v}_{si} \quad (2.33)$$

Other studies have focused on EM power losses or drivetrain power losses minimization [13, 41]. A very similar solution is the maximization of motor efficiency or vehicle driving efficiency, proposed in Hu et al.[11] for a 4 in-wheel motors EV and in Cao et al.[17] for a one-motor-per-axle configuration:

$$\max J = \frac{P_{\text{out}}}{P_{\text{EM}}} = \frac{\sum T_i \omega_i}{\sum \frac{T_i}{\eta_i} \omega_i} \quad (2.34)$$

Constraints on the control outputs, i.e., motor torques, are applied to deal with longitudinal and lateral dynamics requirements. Considering a 4IMDEV, the control output ξ is a vector containing the four torques to the motors and w is the constraint vector:

$$B\xi = w \quad (2.35)$$

$$\begin{bmatrix} \frac{1}{R_l} & \frac{1}{R_l} & \frac{1}{R_l} & \frac{1}{R_l} \\ -\frac{t}{2} \frac{1}{R_l} & \frac{t}{2} \frac{1}{R_l} & -\frac{t}{2} \frac{1}{R_l} & \frac{t}{2} \frac{1}{R_l} \end{bmatrix} \begin{bmatrix} T_1 \\ T_2 \\ T_3 \\ T_4 \end{bmatrix} = \begin{bmatrix} \Delta F_x \\ \Delta M_z \end{bmatrix} \quad (2.36)$$

where t is the vehicle track and R_l is the tire loaded radius.

The minimization of one of the cost functions introduced before with the addition of the control output constraints leads to a multi-objective torque distribution strategy, which can be summarized with the following sequential least square problem [21]:

$$\begin{cases} u = \arg \min \|W_\xi \xi\|_2 & \xi \in \Omega \\ \Omega = \arg \min \|W_w(B\xi - w)\|_2 & \xi_{\min} \leq \xi \leq \xi_{\max} \end{cases} \quad (2.37)$$

The problem can be converted into a weighted sum least squares problem to integrate the two-steps algorithm of Equation 2.37 into the following one-step algorithm [7, 21, 42, 43]:

$$u = \arg \min \left(\|W_\xi \xi\|_2^2 + \epsilon \|W_w(B\xi - w)\|_2^2 \right) \quad u_{\min} \leq u \leq u_{\max} \quad (2.38)$$

Zhai et al.[21] introduced other two simpler control strategies for a 4IMDEV, i.e., the average-based torque allocation algorithm and the tire-dynamic-load-based torque allocation algorithm. In the first one, the longitudinal force ΔF_x set by the cruise control and the yaw moment ΔM_z set by the TVC are evenly distributed among the wheels, while in the second one they are distributed proportionally to the vertical load on that wheel. The general equations for both strategies are:

$$T_1 = k_1 \left(\Delta F_x R_l - \frac{\Delta M_z}{\frac{t}{2}} R_l \right) \quad (2.39)$$

$$T_2 = k_2 \left(\Delta F_x R_l + \frac{\Delta M_z}{\frac{t}{2}} R_l \right) \quad (2.40)$$

$$T_3 = k_3 \left(\Delta F_x R_l - \frac{\Delta M_z}{\frac{t}{2}} R_l \right) \quad (2.41)$$

$$T_4 = k_4 \left(\Delta F_x R_l + \frac{\Delta M_z}{\frac{t}{2}} R_l \right) \quad (2.42)$$

In the average torque distribution strategy $k_i = 0.25$, while in the vertical load-based one $k_i = \frac{F_{zi}}{F_z}$. The subscript 1 refers to the front left wheel, 2 to the front right one, 3 to the rear left one and 4 to the rear right one.

Figure 2.13 shows a schematic of a vehicle top view to visualize the contributions of ΔM_z and ΔF_x in the torque distribution strategy of Equations 2.39 – 2.42.

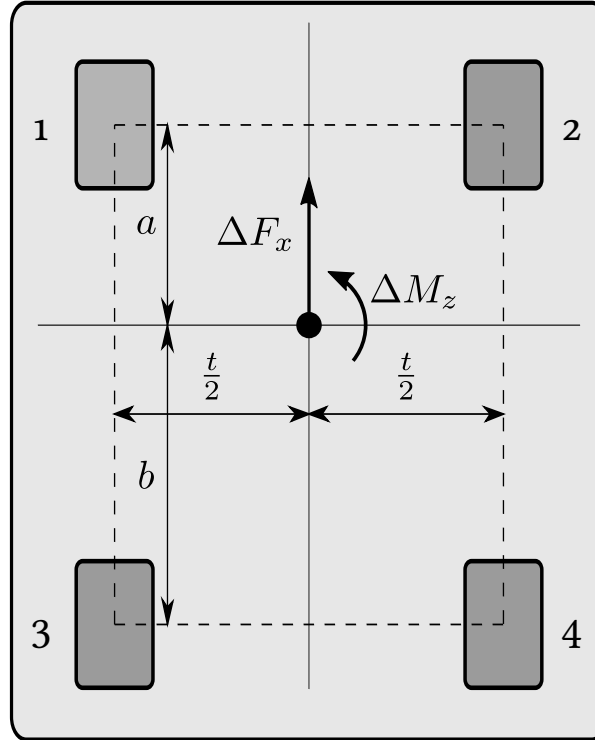


FIGURE 2.13: Schematic of a vehicle top view with ΔM_z and ΔF_x contributions

The tire-dynamic-load-based torque distribution strategy is developed to account for the fact

that the adhesion force increases with the increase of vertical load, under the assumption of a constant friction coefficient. In other words, a more loaded wheel is able to generate a higher traction or braking force without slipping. Tire vertical forces are calculated considering both longitudinal and lateral load transfer due to accelerations:

$$F_{z1} = \frac{mg}{2} \frac{b}{l} - \frac{ma_x}{2} \frac{h}{l} - ma_y \frac{b}{l} \frac{h}{t} \quad (2.43)$$

$$F_{z2} = \frac{mg}{2} \frac{b}{l} - \frac{ma_x}{2} \frac{h}{l} + ma_y \frac{b}{l} \frac{h}{t} \quad (2.44)$$

$$F_{z3} = \frac{mg}{2} \frac{b}{l} + \frac{ma_x}{2} \frac{h}{l} - ma_y \frac{a}{l} \frac{h}{t} \quad (2.45)$$

$$F_{z4} = \frac{mg}{2} \frac{b}{l} + \frac{ma_x}{2} \frac{h}{l} + ma_y \frac{a}{l} \frac{h}{t} \quad (2.46)$$

where a is the distance of the front axle from the vehicle CG, b is the distance of the rear axle from the vehicle CG, l is the wheelbase, h is the height of the CG and t is the vehicle track (assumed to be equal between front and rear axle). Those equations lack the effect of the roll stiffnesses of suspensions and anti-roll bars, which clearly modify the load transfers.

In Zhai et al.[21], the previous two methods were compared with the tire utilization-based torque distribution strategy of Equation 2.31 under different tests. The best strategy was found to be the optimization-based one because the torque of each wheel can be controlled considering dynamic vertical load transfer and tire saturation together.

Chapter 3

Vehicle Model

Vehicle models have always been one of the main focuses in vehicle dynamics because they enable virtual simulations. These get rid of the problem of building a physical prototype during the early development stages, when design changes would require a new prototype every time. When coupling a vehicle model with a controller model, the so-called Software-in-the-Loop (SiL) method is obtained. This chapter focuses on the vehicle model, while Chapter 4 will explain the controller design. The commercial software MATLAB-Simulink was chosen in this project for its flexibility and capability to easily integrate parameters definition, models and results in just one environment.

3.1 Vehicle model in MATLAB-Simulink

In this section, the vehicle model developed in MATLAB-Simulink environment will be presented. Since building a full-vehicle model is quite complex, a top-down approach is chosen for the development of a model step-by-step: starting from the bicycle model, more degrees of freedom are added in order to better represent dynamic phenomena of different vehicle components.

Most of the vehicle specifications used for this project were found in a database available online (see [44]). However, some parameters (e.g. position of the centre of gravity and vehicle moment of inertia) cannot be directly measured and car manufacturers may internally evaluate them. Whenever specifications were not available, they were chosen based on engineering common sense to make them all consistent with respect to each other and resemble real data. Table 3.1 sums up the main vehicle data. It is worthwhile to mention that the vehicle mass used for the simulations will be the curb weight plus 80 kg representative of the driver and their luggage (respectively 70 kg and 10 kg).

3.1.1 Bicycle Model

The bicycle model is the simplest vehicle model featuring only 2 DOF, i.e., lateral direction and yaw rotation. The variables representing the lateral motion are v_y (lateral speed measured at the centre of gravity) and β (vehicle side slip angle). Since the two are directly linked by v_x

TABLE 3.1: Vehicle specifications

Parameter	Value	Parameter	Value
curb weight	1430 kg	wheelbase	2.6 m
front wheelbase	1.130 m	rear wheelbase	1.470 m
front track	1.575 m	rear track	1.584 m
CG height	0.511 m	vehicle yaw moment of inertia	2045 kg m ²
C _x	0.290	frontal area	1.85 m ²
tire	185/60 R14	rolling resistance coeff.	0.010
wheel radius	0.2891 m	wheel moment of inertia	0.6 kg m ²

(longitudinal vehicle speed), just one of them will represent a vehicle state (in this dissertation v_y has been preferred). The second state variable is the yaw rate r . The bicycle model will be used in Chapter 4 as reference for the Torque Vectoring controller.

One of the main limitations of the bicycle model is that all the angles are assumed to be small with the aim of linearizing non-linear functions. For instance, in the tire side slip angle equation (Equation 2.15), the arctan function is replaced with just its argument. In that case the model loses accuracy when moderate/severe cornering conditions occur. Besides, the assumption of constant vehicle speed in the bicycle model does not allow one to simulate accelerating or braking conditions. For these reasons, v_x is introduced as third degree of freedom.

3.1.2 7-DOF Non-linear Vehicle Model

A 7-DOF non-linear vehicle model has been developed to better represent the vehicle behaviour. The three main DOF are v_x , v_y and r , and the other four DOF are the angular velocities ω_i of each wheel. This approach has been widely used in literature since it is a compromise between model accuracy and complexity [4, 10, 14].

From the equations introduced in Chapter 2, writing Equation 2.1 in the vehicle reference frame and coupling it with Equations 2.12 and 2.13, the following system of equations is obtained:

$$\dot{v}_x = v_y r - \frac{1}{m} \left(\left(\frac{1}{2} \rho S C_x v_x^2 + f m g \right) - \left((F_{x1} + F_{x2}) \cos \delta - (F_{y1} + F_{y2}) \sin \delta + F_{x3} + F_{x4} \right) \right) + \Delta F_x \quad (3.1)$$

$$\dot{v}_y = -v_x r + \frac{1}{m} \left((F_{y1} + F_{y2}) \cos \delta + (F_{x1} + F_{x2}) \sin \delta + F_{y3} + F_{y4} \right) \quad (3.2)$$

$$\begin{aligned} \dot{r} = \frac{1}{J_z} & \left((F_{x1} + F_{x2}) \sin \delta \cdot a + (F_{y1} + F_{y2}) \cos \delta \cdot a - (F_{y3} + F_{y4}) \cdot b + (F_{x2} - F_{x1}) \cos \delta \cdot \frac{t_f}{2} + \right. \\ & \left. + (F_{x4} - F_{x3}) \cdot \frac{tr}{2} + (F_{y1} - F_{y2}) \sin \delta \cdot \frac{t_f}{2} \right) + \Delta M_z \quad (3.3) \end{aligned}$$

The term ΔF_x is the additional longitudinal force from cruise control and ΔM_z is the corrective yaw moment from TVC. Their meaning will be clearer in Sections 4.1.1 and 4.2.

Since the objective is to build a non-linear vehicle model, the tire forces are decomposed along the x and y axes using trigonometry with the steering angle δ . However, some important assumptions are made:

- aerodynamics is accounted for in longitudinal direction only (no cross-wind, no lift/down-force);
- air is still, therefore the relative velocity between vehicle and air is simply the vehicle longitudinal speed;
- although the tire rolling resistance depends on the square of the longitudinal speed by the law $f = f_0 + kv^2$, only a constant factor is considered in this dissertation. Given $k = 6.5 \times 10^{-6} \text{ s}^2/\text{m}^2$ [29], moderate vehicle speeds would increase the rolling resistance coefficient by few thousandths and the overall effect on longitudinal dynamics would be very small;
- no sloped roads are considered.

The other four DOF are represented by the angular velocities of the four wheels. Equation 2.8 can be rewritten as:

$$\dot{\omega}_i = \frac{1}{J_w} (T_{wi} - F_{xi} R_l) \quad (3.4)$$

The states variable is defined as:

$$x = [v_x \quad v_y \quad r \quad \omega_1 \quad \omega_2 \quad \omega_3 \quad \omega_4]^T \quad (3.5)$$

and it is obtained from the integration of Equations 3.1 – 3.5, given the initial conditions x_0 . Eventually, v_y is translated into β using Equation 2.14, as this is the control variable inside the TVC.

Figures 3.1 and 3.2 show respectively the vehicle and the wheel model in Simulink environment.

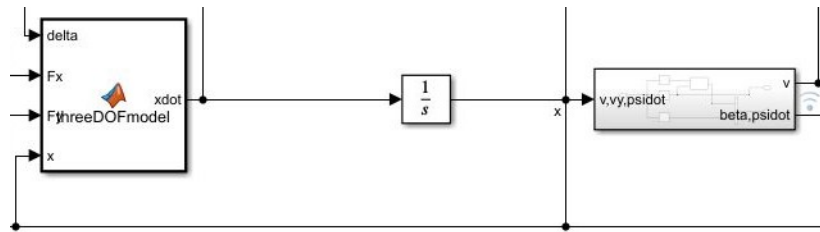


FIGURE 3.1: Three main DOF of the vehicle model implemented in a MATLAB function

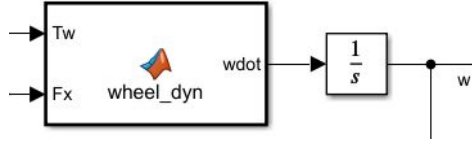


FIGURE 3.2: Wheel model implemented in a MATLAB function

Throughout the vehicle and controller modelling, vertical loads on each wheel are evaluated according to Equations 2.43 – 2.46.

3.2 Tire Model

The well-established Pacejka's Magic Formula is chosen to represent the tire behaviour for its high accuracy. From Equations 2.25 and 2.26, the model direct inputs are the tire slip rate σ and the side slip angle α . In addition, vertical load F_z and camber angle γ are other inputs hidden in the B, C, D, E factors.

The problem of this Magic Formula definition is that it does not take into account longitudinal/lateral tire coupling. For this reason, the model has been further refined over the years introducing the so-called combined slip conditions [31]. However, those model parameters are not available in the literature and therefore in this dissertation the pure longitudinal and pure side slip conditions are adopted for the forces computation. Nevertheless, a scaling factor is introduced in order to replicate the friction ellipse behaviour. Before explaining it in detail, some preliminary considerations have to be done. First of all, the wheel hub speed \vec{v}_i has different direction and magnitude with respect to the vehicle speed \vec{v} (reference to Figure 2.7):

$$\vec{v}_i = \begin{bmatrix} v_{xi} \\ v_{yi} \end{bmatrix} = \begin{bmatrix} v_x - r y_i \\ v_y + r x_i \end{bmatrix} \quad (3.6)$$

From Figure 2.7, \vec{v}_i can be written in the tire reference frame $0'x_{ti}y_{ti}$ using $\sin \delta$ and $\cos \delta$ to get the two components v_{tx} and v_{ty} . At this point, the longitudinal and lateral tire slip velocities can be computed as:

$$v_{sx} = |\omega R_e - v_{tx}| \quad (3.7)$$

$$v_{sy} = |v_{ty}|; \quad (3.8)$$

The two variables can be normalized with respect to the total slip velocity vector:

$$k_x = \frac{v_{sx}}{\sqrt{v_{sx}^2 + v_{sy}^2}} \quad (3.9)$$

$$k_y = \frac{v_{sy}}{\sqrt{v_{sx}^2 + v_{sy}^2}} \quad (3.10)$$

where k_x and k_y are the scaling factors for longitudinal and lateral forces that pre-multiply the Magic Formula equations to take into account the tire coupling behaviour.

This empirical approach has led to the results shown in Figures 3.3 and 3.4, where the tire forces are plotted as function of longitudinal slip ratio and side slip angle, given $v_{xi} = 20$ m/s and $F_z = 3700$ N. The choice of that particular force value is not random, since it corresponds to the average static load on each wheel. In both plots it is possible to underline that the 3-D surface has negative gradients when the combined effect $\sigma - \alpha$ increases, which is exactly what happens in a real tire. Since the longitudinal velocity slip is the prevalent term in the σ and α range, F_y is expected to decay more rapidly than F_x .

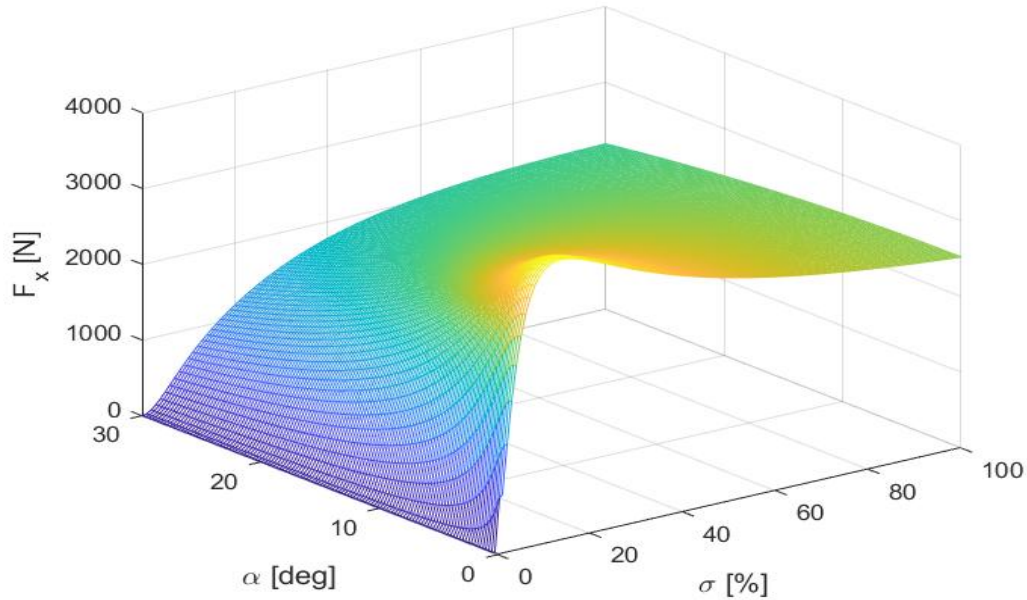


FIGURE 3.3: F_x as function of σ and α with the presented scaling approach: F_x decreases when the combined effect of σ and α increases

Figure 3.5 shows the friction ellipse (computed as in Equation 2.21) as function of σ and α . The results predict the expectations:

- the limit (represented by $z = 1$) is never exceeded;
- the tire is globally working at its saturation limits in the range $\sigma = 0 - 15\%$ and $\alpha = 0 - 8^\circ$ where both F_x and F_y have their peak values;
- when the slip velocities increase, i.e., when σ and α increase, their “pure slip” contributions decrease and as a result the combined effect $F_x - F_y$ is reduced too.

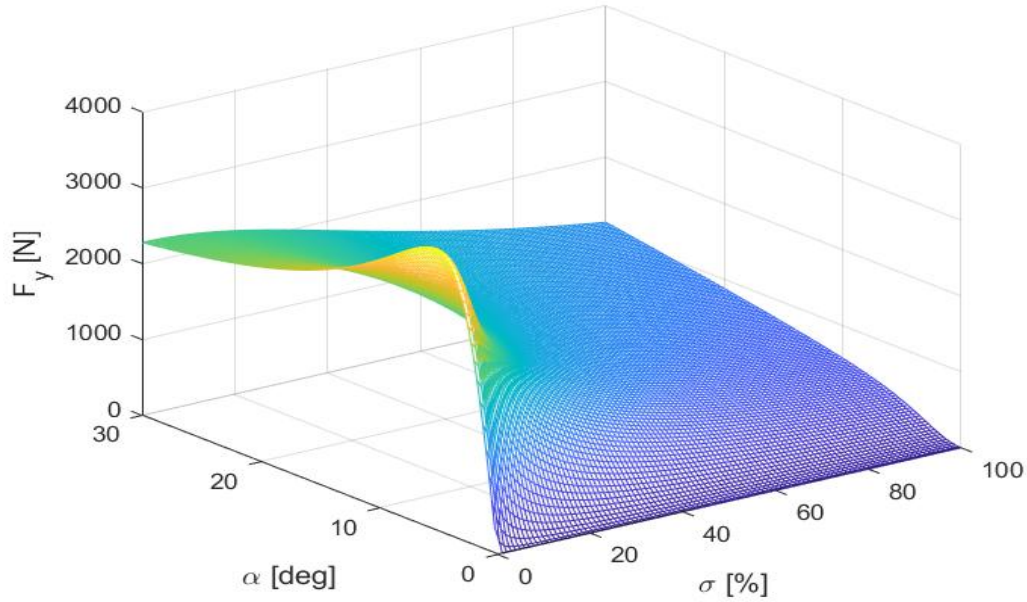


FIGURE 3.4: F_y as function of σ and α with the presented scaling approach: F_y rapidly decreases when the combined effect of σ and α increases

Just as a comparison, Figure 3.6 plots F_x against σ and α when the scaling procedure introduced in this project is not considered. Longitudinal and lateral forces are totally decoupled, as F_x is not affected by α . A similar trend would be observed when plotting F_y as function of α . The use of the Magic Formula without the longitudinal-lateral coupling leads to a sort of “friction rectangle” instead of the friction ellipse: considering Figure 3.7, it is clear that the z-axis fails to stay below 1 and thus this tire model would exceed the physical limits.

Figure 3.8 shows the Magic Formula implemented in a MATLAB function in Simulink, while Figures 3.9 and 3.10 exhibit the computation of tire side slip angle and longitudinal slip ratio respectively.

Although Pacejka’s model well describes the tire behaviour, the linear approach already presented in Section 2.1.3 finds a good application in the vehicle reference model for the TVC. As it will be discussed in Section 4.1.1, cornering stiffness is an important parameter for the definition of the desired vehicle states. Here, two methods are proposed for its calculation. The first one considers a constant value, assuming that the vehicle weight is equally distributed among the four wheels. The final value is obtained by averaging the cornering stiffness computed as tangent of the F_y - α curve at the origin (short range of α) with the one representing the slope connecting $F_{y,\max}$ and $F_{y,\min}$ (long range of α) [10]:

$$C_\alpha = \frac{C_{\alpha,sr} + C_{\alpha,lr}}{2} \approx 60\,000 \text{ N/rad}$$

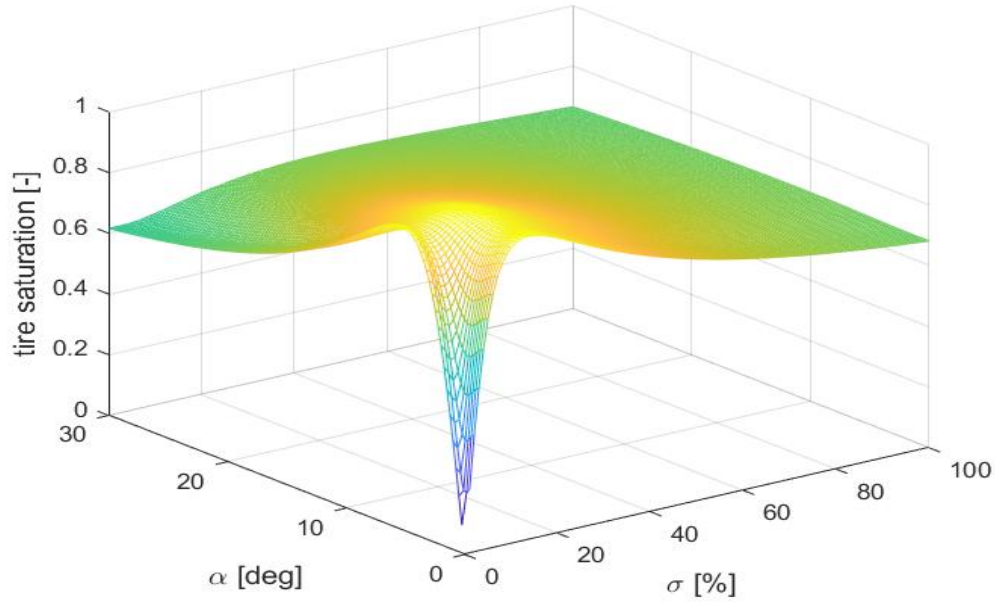


FIGURE 3.5: Tire saturation as function of σ and α with the presented scaling approach: as expected, the limit represented by $z=1$ is never exceeded

At this point, the cornering stiffness of each axle is equal to 120 000 N/rad.

The second method considers a real-time calculation of the cornering stiffness. For this purpose, a look-up table has been built and the cornering stiffness values are obtained by double linear interpolation, given vertical load and tire side slip angle. This method easily overcomes the problem of F_y measurement or estimation, as it only requires F_z (considering load transfers due to longitudinal and lateral acceleration) and α (knowing vehicle states and steering angle). The surface representation of the look-up table is reported in Figure 3.11. With respect to the first approach, cornering stiffness values do change as function of tire parameters and this resembles the real behaviour. However, this solution causes undesired action of the controller when cornering stiffness values are really low due to high side slip angles and low vertical loads, or side slip angles close to zero. Figure 3.12 shows the estimated cornering stiffness trend for front and rear axle during a Double-Lane Change maneuver.

The first approach has been preferred in this project: the obtained values may not be accurate outside the tire linear range, but at least a good controller action is preserved.

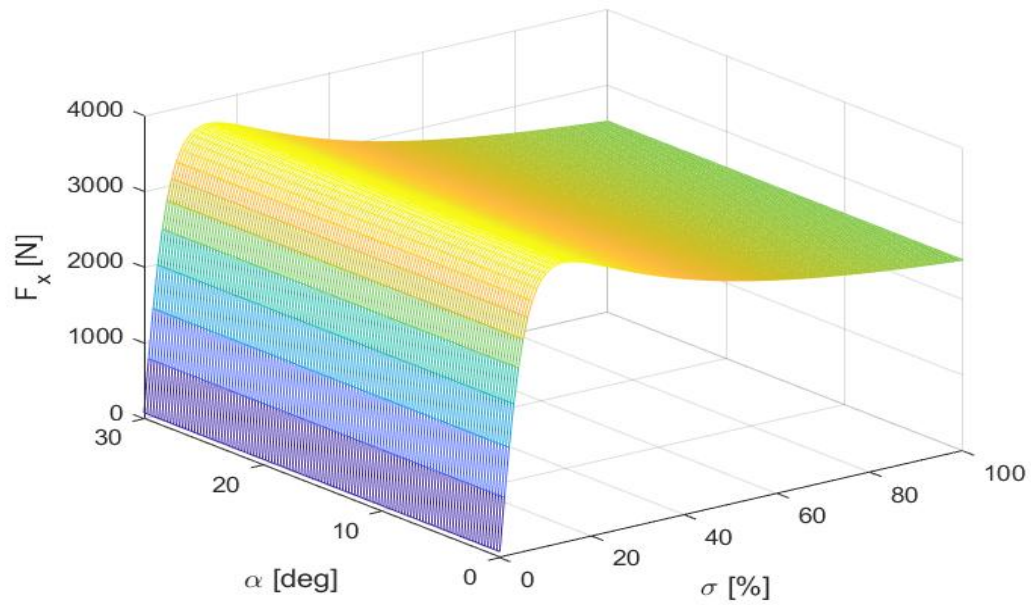


FIGURE 3.6: F_x as function of σ and α without scaling approach: F_x is not affected by α , i.e., F_x and F_y are totally decoupled

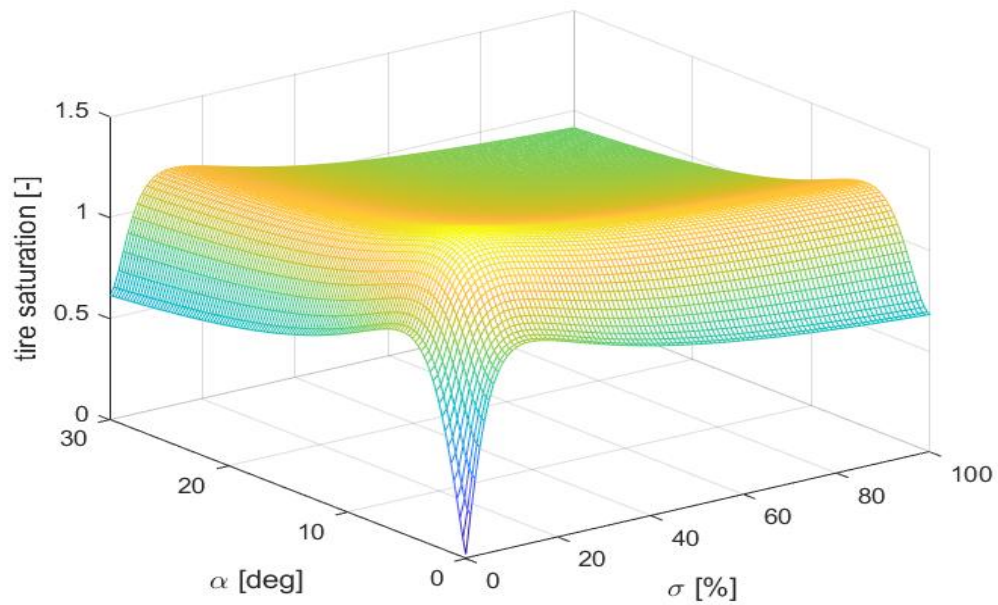


FIGURE 3.7: Tire saturation as function of σ and α without scaling approach: the model would exceed the tire physical limits when $z > 1$

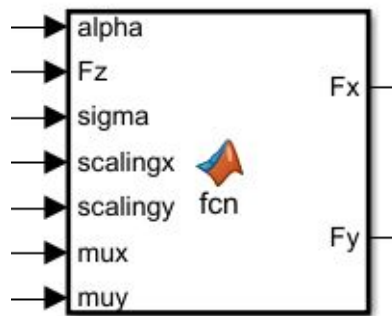
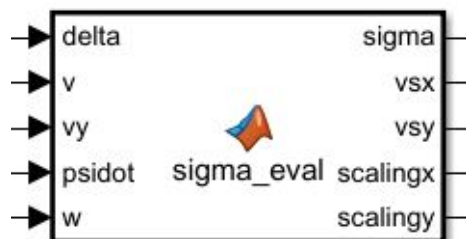


FIGURE 3.8: Pacejka's Magic Formula implemented in a MATLAB function

FIGURE 3.9: Computation of α in a MATLAB functionFIGURE 3.10: Computation of σ in a MATLAB function

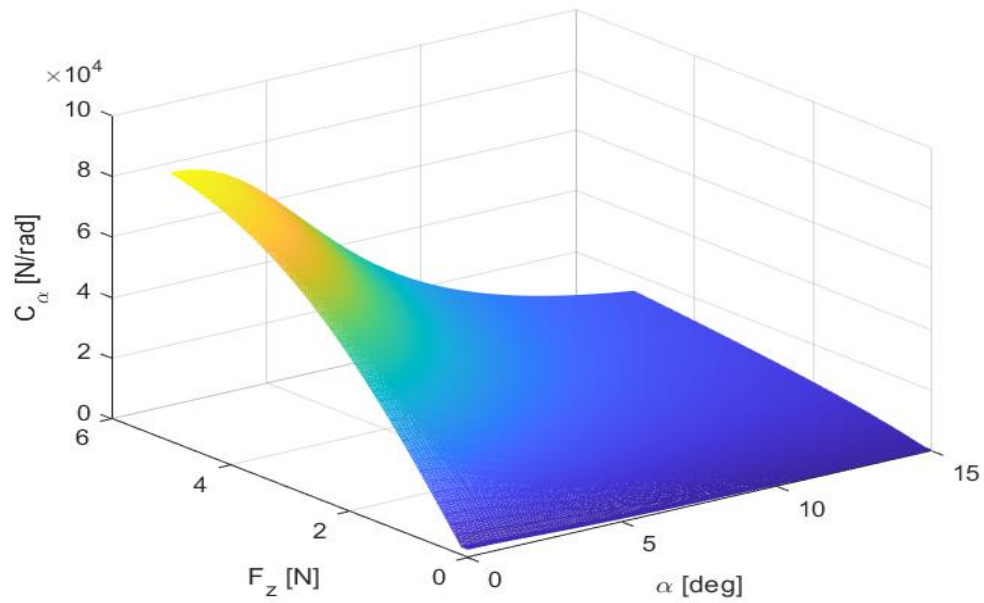


FIGURE 3.11: Surface representing tire cornering stiffness as function of α and F_z , implemented in a look-up table

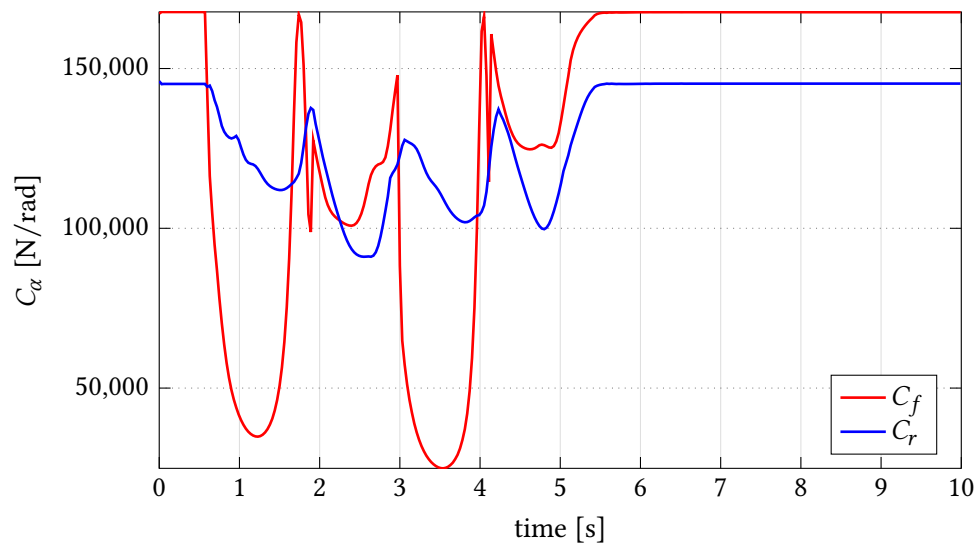


FIGURE 3.12: C_α trend for a Double-Lane Change maneuver when using the look-up table approach: small cornering stiffness values, due to high side slip angles for example, would cause an undesired action of the controller

3.3 Electric Motors Model

Electric Motors (EMs) are the powertrain components that propel BEVs. The common approach for EM modelling consists of the efficiency map as function of angular speed and torque. Since one of the objectives of this dissertation is development of a controller able to work for different BEV architectures, the choice of the EMs' characteristics for each configuration play an important role.

First of all, the numbers and positions of electric motors have to be decided. Four different cases are considered:

- 4 In-Wheel Motors (4IWM), one per each wheel
- 2 In-Wheel Motors on the front axle
- 2 In-Wheel Motors on the rear axle
- 2 Central Motors (CM), one per each axle

Although there are several other combinations of BEV architectures, the four chosen cases are the most representative ones to highlight the differences in TVC exploitation.

It is clear that the motors need different sizes in order to keep the same vehicle longitudinal performance among the BEV configurations. For this reason, the total torque at the wheels must be the same. This means that, for instance, the torque on each wheel for the 4 IWM case will be half of the torque on each front wheel for the 2IWM on the front axle case. In practical applications there is typically a fixed transmission ratio between the motor and the wheel in order to increase the torque at the wheels and at the same time allowing the motor to operate at higher angular speed with respect to the wheels. The efficiency map reported in Figure 3.13 can be interpreted as the motor efficiency points given torque and speed at the wheels (with motor torque and speed scaled respectively down and up by the gear ratio). However, the motors operating conditions are not a concern since the sizing of the motor, inverter and battery is not the focus of this project.

From Figure 3.13, some important parameters can be drawn:

- constant torque region = 441.5 N m at the wheels
- total maximum torque at the wheels = 1766 N m
- motor base speed for 48 km/h
- maximum vehicle speed = 160 km/h

Four of these motors allow the vehicle to accelerate 0 – 100 km/h in 8.66 s with a peak acceleration of 4 m/s^2 , as shown in Figure 3.14. It is important to underline that the vehicle acceleration capabilities are reduced when the motor base speed is overcome.

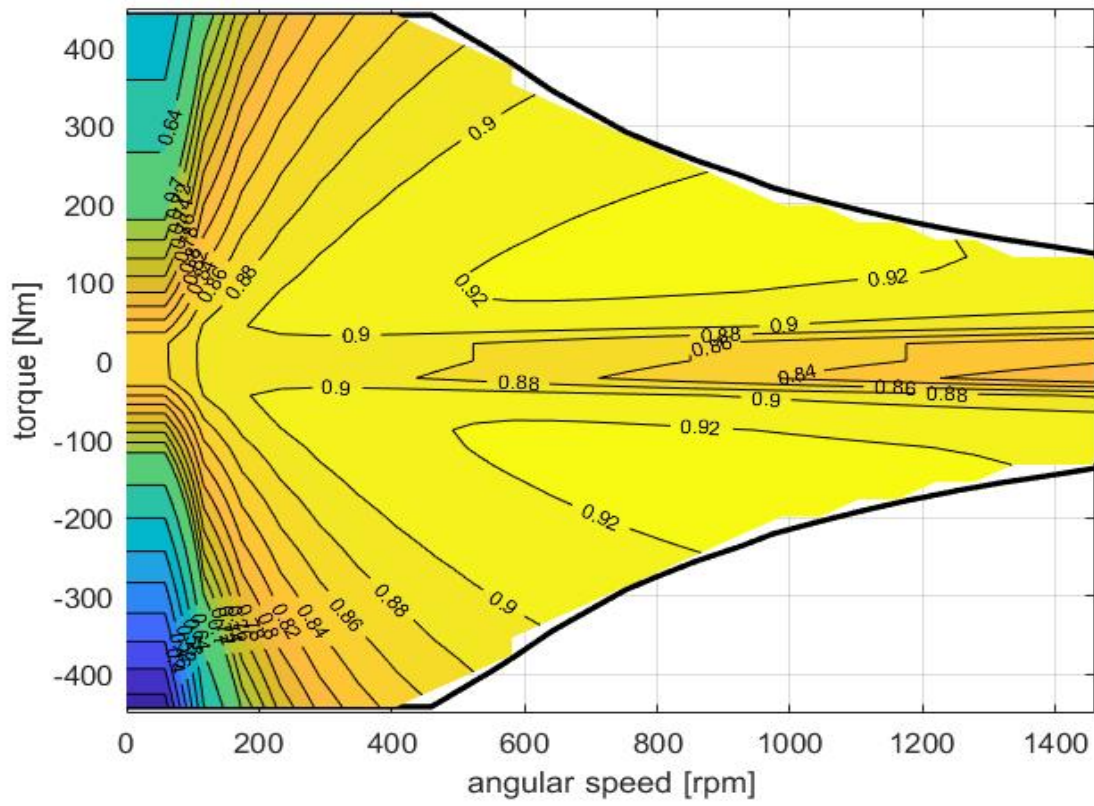


FIGURE 3.13: EM efficiency map as function of angular velocity and torque at the wheel for a 4IWMEV (data from Maino[45])

In the other three BEV configurations considered here, the vehicle is equipped with just two motors. In order to keep the same total torque, each motor has to double its torque output (assuming the same transmission ratio in both cases). The new efficiency map is obtained by simply stretching the one in Figure 3.13 with respect to the vertical axis, keeping untouched the efficiency values.

A 2-D look-up table is built to calculate the motor efficiency points in real time as function of torque and angular speed at the wheels. Figure 3.15 shows the obtained surface for the electric motor applied to the 4IWMEV.

The electric motor dynamics is modelled as a first-order low-pass filter with a 50 ms time constant. Its implementation in Simulink is reported in Figure 3.16: the commanded torque for each motor is saturated between the EM limit curves and then the four low-pass filters account for their transient delays. This is a general configuration also valid for the 2-motors EVs (in those cases two torques would simply be equal to zero).

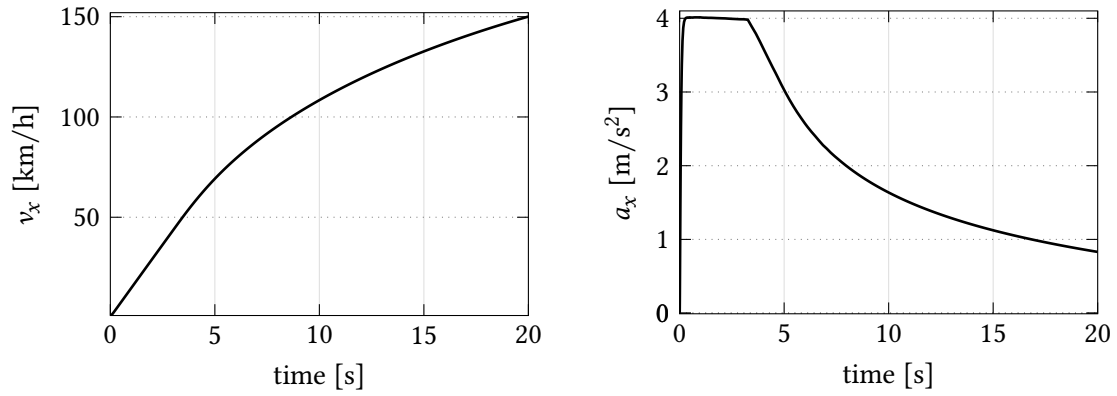


FIGURE 3.14: Speed and acceleration trend at full throttle for a 4IWMEV with $\mu = 1$

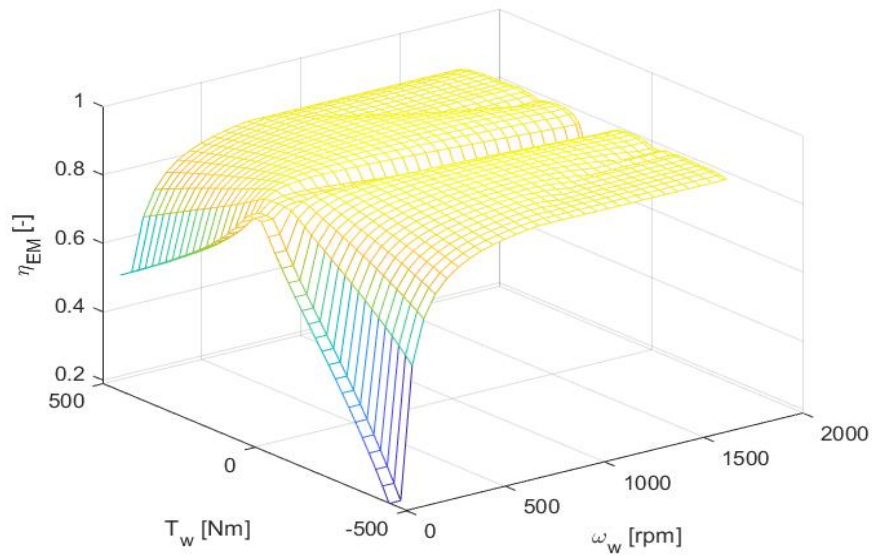


FIGURE 3.15: Surface representing the EM efficiency map as function of angular velocity and torque at the wheel for a 4IWMEV

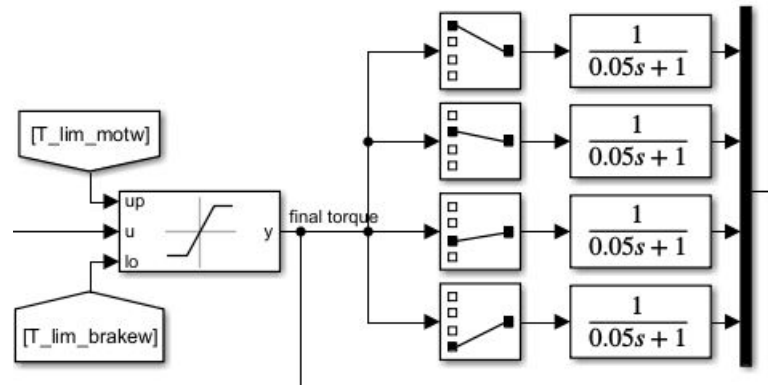


FIGURE 3.16: Electric motors dynamics in Simulink: the commanded torques are saturated between the limit curves and then delayed by the low-pass filters

3.4 Driver Model

A driver model needs to be considered for closed-loop steering maneuvers simulations such as Single-Lane Change (SLC) and Double-Lane Change (DLC). The objective of the model is to replicate the driver attitude to follow a desired vehicle trajectory applying a steering correction.

A typical approach considers cross-track error and heading error. Cross-track error is the distance from the centre of the front axle to the closest point on the reference trajectory, while the heading error is the yaw angle difference between reference trajectory and vehicle [46]. Figure 3.17 shows a schematic of a vehicle with its desired path, cross-track error, and heading error.

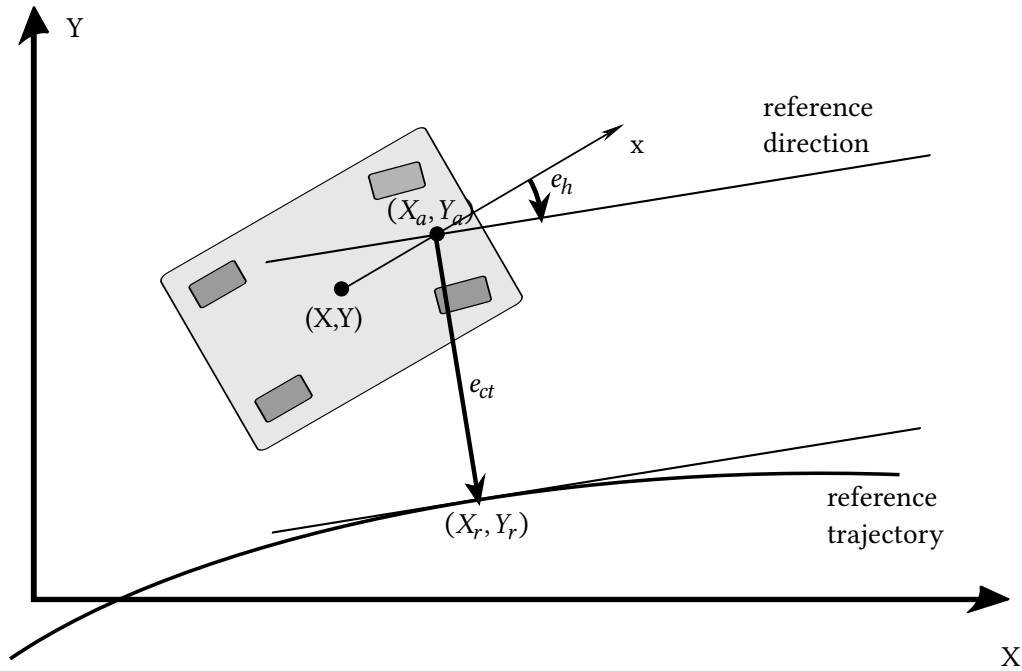


FIGURE 3.17: Schematic of a vehicle with reference trajectory, cross-track error and heading error definitions

Since the core research of this project is really something else, a deep literature review regarding driver models has not been carried out. The developed driver model computes the steering angle error δ_e as a weighted sum of cross-track error e_{ct} , heading error e_h and curvature gain for a neutral-steer vehicle [47]:

$$\delta_e = 0.1e_{ct} + 1.1e_h + l\frac{1}{R} \quad (3.11)$$

One of the key factors in Equation 3.11 is the presence of the curvature $\frac{1}{R}$ (where R is the corner

radius), which allows the model to better follow the planned trajectory. Given the reference vehicle states X_r , Y_r and ψ_r , and given the vehicle states referred to the front axle X_a , Y_a and ψ , the cross-track error and the heading error are calculated as follows:

$$e_{ct} = (Y_r - Y_a) \cos \psi_r - (X_r - X_a) \sin \psi_r \quad (3.12)$$

$$e_h = \psi_r - \psi \quad (3.13)$$

The front axle position is calculated as:

$$X_a = X + a \cos \psi \quad (3.14)$$

$$Y_a = Y + a \sin \psi \quad (3.15)$$

As suggested in Novara[48], ψ and ψ_r are bounded in the interval $[0, 2\pi]$, while e_h is bounded in the interval $[-\pi, \pi]$.

The equation linking the steering angle error δ_e found in Equation 3.11 with the actual steering angle δ is the following:

$$\dot{\delta} = k(\delta_e - \delta) \quad (3.16)$$

Using the Laplace variable s , the desired steering angle is obtained as:

$$\delta = \frac{1}{\tau s + 1} \delta_e \quad (3.17)$$

with $\tau = \frac{1}{k} = 0.01$ s.

Figure 3.18 shows how the driver model with all the above-mentioned components appears in MATLAB-Simulink. The complete reference trajectory and the front axle position are used to find the closest trajectory point to the vehicle, which is then used to compute the cross-track error and the heading error. At this point, the steering error is computed according to Equation 3.11 and the final steering angle is calculated using the low-pass filter in Equation 3.17. An almost null constant (1×10^{-10} rad) is added to the steering angle to avoid numerical problems in the simulation if δ ever starts from zero.

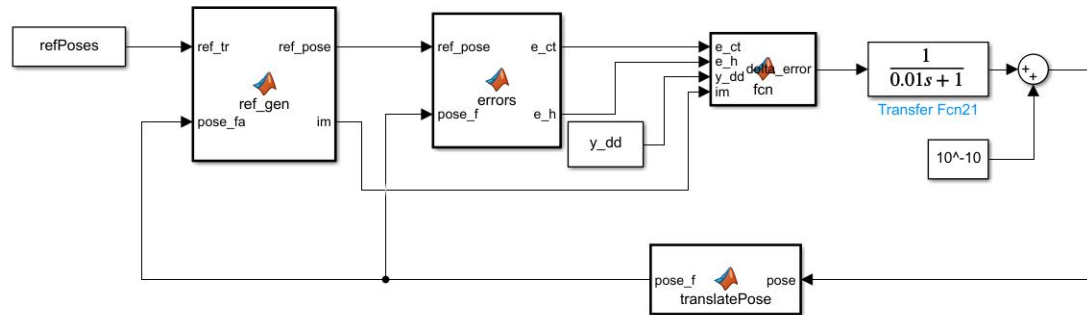


FIGURE 3.18: Driver model developed in MATLAB-Simulink: from left to right there are the evaluation of the closest trajectory point to the vehicle, the computation of cross track and heading error, the calculation of the steering error and eventually of the final steering angle

Chapter 4

Integrated and Modular Vehicle Dynamics Controller

This section focuses on the development of the integrated and modular vehicle dynamics controller based on a hierarchical approach. The upper layer is composed of three different parts: TVC, TCS and cruise control. The fact that the three systems are included in one main controller suggests the word “integrated”. Besides, the torque allocation algorithm, representing the lower layer, has been designed to make the controller suitable for the four BEV architectures introduced in Section 3.3, hence the name “modular”. Each developed control system will be analyzed in detail and their design choices will be thoroughly discussed.

4.1 Torque Vectoring Control in MATLAB-Simulink

Torque Vectoring Control systems exploits electric motor control on both vehicle sides for the generation of a corrective yaw moment in order to properly adjust vehicle’s lateral dynamics. As already discussed in Section 2.2.4, several control strategies have been studied in literature. This study focuses on SMC, as it is very effective in terms of disturbance rejections and management of model uncertainties, it is very robust to non-linearities and it is not computationally intensive [9, 12, 15]. Table 4.1 shows a comparative recap of SMC and MPC.

	SMC	MPC
deal with non-linearities	✓	✓
disturbances rejection	✓	✗
handle system constraints	✗	✓
computationally light	✓	✗

TABLE 4.1: Comparative recap of SMC and MPC

4.1.1 Sliding Mode Control for TVC

The objective of this section is the explanation of the main characteristics of the SMC in order to better understand the design procedure that has been followed in this study.

The first step is the definition of a sliding surface s , which is presented in a general form as:

$$s = c(x - x_d) \quad (4.1)$$

where x_d is the desired state at each time instant. The aim of the controller is to make s converge to zero, which can be written in a mathematical form as:

$$\lim_{t \rightarrow \infty} s = 0 \quad (4.2)$$

The term $s(x, x_d) = 0$ is a time-varying surface in the state space, since $x = x(t)$ and $x_d = x_d(t)$ [15].

The second step is the definition of the sliding surface dynamics with a reaching condition. The simplest case is a constant velocity reaching law [9, 43, 49]:

$$\dot{s} = -k \operatorname{sgn}(s) \quad (4.3)$$

A more complex exponential law can be considered [11, 15, 33, 50]:

$$\dot{s} = -k_p s - k_s \operatorname{sgn}(s) \quad (4.4)$$

where k_p determines the convergence rate of s and k_s is tuned according to bound of uncertainties and disturbances.

Two main SMC categories are reported in Mousavinejad et al.[51]: Integral Terminal SMC (ITSMC), which fits first order systems, and Fast Terminal SMC (FTSMC), which can deal with second or higher order systems. Below, the FTSMC applied to DYC for an IVDC is reported :

$$s_\beta = (\beta - \beta_d) + a|\beta - \beta_d|^{y_1} \operatorname{sgn}(\beta - \beta_d) + b|\dot{\beta} - \dot{\beta}_d|^{y_2} \operatorname{sgn}(\dot{\beta} - \dot{\beta}_d) \quad (4.5)$$

By converse, a classic form of ITSMC [9, 43, 52] is:

$$s = r - r_d + k \int (r - r_d) dt \quad (4.6)$$

An even simpler SMC definition, introduced in Kang et al.[49] and Nam et al.[50], is shown below :

$$s = r - r_d \quad (4.7)$$

$$\dot{s} = -k \operatorname{sgn}(s) \quad (4.8)$$

Without considering Equation 4.5, which refers to a DYC in combination with AFS, the other proposed equations do not control vehicle side slip angle. The vehicle side slip angle β , also known as attitude or drift angle, is a key parameter in automotive active safety systems; it is an indication of the misalignment between vehicle orientation and trajectory [35]. The yaw rate, which reflects vehicle maneuverability when side slip angle is close to zero, is a good control variable. However, when β is large this is the best parameter to consider, as the vehicle is drifting and yaw rate is no longer representative of the vehicle behaviour. In other words, it is possible to state that the yaw rate reflects the driver's intention and the vehicle side slip angle reflects the vehicle's stability. In conclusion, both yaw rate and side slip angle should be controlled [14].

Hu et al.[11] and Zhang et al.[14] proposed the following equations:

$$s = \frac{\rho}{|\Delta r|_{\max}} |r - r_d| + \frac{1 - \rho}{|\Delta \beta|_{\max}} |\beta - \beta_d| \quad (4.9)$$

$$\dot{s} = -\epsilon \operatorname{sgn}(s) - k_d s \quad (4.10)$$

in which the sliding surface is a weighted sum of yaw rate error and vehicle side slip angle error. ρ , $|\Delta r|_{\max}$, $|\Delta \beta|_{\max}$, ϵ and k_d are controller parameters, and r_d and β_d are the desired values computed from the bicycle model (see Minaker[26]) as :

$$\beta_d = \frac{b - \frac{amv_x^2}{C_r l}}{l + k_{us} \frac{v_x^2}{g}} \delta \quad (4.11)$$

$$r_d = \frac{v_x}{l + k_{us} \frac{v_x^2}{g}} \delta \quad (4.12)$$

where k_{us} is the understeering coefficient defined as:

$$k_{us} = \frac{mg}{l} \frac{bC_r - aC_f}{C_f C_r} \quad (4.13)$$

The previously reported reference values from the bicycle model are bounded by the following constraints found in Hu et al.[11] and Mousavinejad et al.[51] to avoid possible high values that would hinder the performance of the controller:

$$|r_d| \leq 0.85 \frac{\mu g}{v_x} \quad (4.14)$$

$$|\beta_d| \leq \arctan(0.02 \mu g) \quad (4.15)$$

Equations 4.9 and 4.10 are the starting point for the development of the TVC presented in this study. From those equations, differentiating the first and coupling it with the second, the yaw acceleration commanded by the SMC \dot{r}_c is found as function of the other variables:

$$\dot{r}_c = \dot{r}_d - \frac{|\Delta r|_{max}}{\rho} \{ \epsilon \operatorname{sgn}[(r - r_d)s] + k_d s \operatorname{sgn}(r - r_d) \} - \frac{1 - \rho}{\rho} \frac{|\Delta r|_{max}}{|\Delta \beta|_{max}} \operatorname{sgn}[(r - r_d)(\beta - \beta_d)](\dot{\beta} - \dot{\beta}_d) \quad (4.16)$$

At this point, substituting \dot{r}_c into Equation 3.3 (representing the yaw DOF in the vehicle model), the corrective yaw moment ΔM_z is obtained as:

$$\Delta M_z = J_z \dot{r}_c - M_z \quad (4.17)$$

where M_z represents the yaw moment coming from the different tire forces components. For more mathematical details, please see Appendix A.

The term ΔM_z is the required yaw moment correction in order to minimize the surface in Equation 4.9. The parameters of that equation play a key role and unfortunately in literature there is little indication on how to tune them. A first attempt has been done treating them as constants. Considering a sinusoidal steering input of amplitude $A = 5^\circ$ starting from 50 km/h and a Double Lane-Change starting from 80 km/h, a trial-and-error procedure is followed to find the coefficients in Table 4.2.

TABLE 4.2: SMC constant parameters after trial-and-error procedure

Parameter	Value	Parameter	Value
ρ	0.6		
$ \Delta r _{max}$	0.1 rad/s	$ \Delta \beta _{max}$	0.01 rad
ϵ	4	k_d	3

A second option is the real-time adjustment of the coefficients of the sliding surface dynamics, i.e., ϵ and k_d , according to the sliding surface value. The other three coefficients are kept as they

are because instability has been observed when changing them. After running several other simulations considering the same maneuvers, i.e., sinusoidal steering input and Double Lane-Change, the parameters in Table 4.3 are found.

TABLE 4.3: SMC real-time adjustment of sliding surface dynamics parameters according to sliding surface values

ϵ	$1.5 s $	k_d	$1 s $
------------	-----------	-------	---------

Table 4.4 recaps some results obtained when changing the parameters of the sliding surface dynamics for the two maneuvers. Three different set of parameters are considered and will be identified respectively as “Case 1”, “Case 2” and “Case 3”, where the first represents the real-time adjustment while the other two consider constant values. The norm-2 and the norm- ∞ of the sliding surface s and of the control action ΔM_z are considered for the first maneuver, while norm-2 of cross-track error, norm-2 of heading error and maximum speed to pass the test are taken into account for the second maneuver. From the first maneuver, it is possible to see that Case 3 has the smaller sliding surface magnitude but the highest maximum amplitude. Case 2 seems to be better from that point of view, but the required corrective yaw moment is the biggest in terms of magnitude. Considering a compromise between sliding surface and control action, Case 1 is the best because the magnitude of the sliding surface is very close to the other two cases and the controller action is much lower. Eventually, the Double Lane Change maneuver shows that the cross-track error is minimized in Case 1 and heading error in Case 3, even though the important data is the speed at which the test is passed. Reminding that e_{ct} and e_h reported in the table refer to the initial condition of 80 km/h, the last column in the table shows the maximum speed at which the vehicles are able to pass the test. The result is that in Case 3 the test is passed with just a 0.1 km/h higher speed with respect to Case 1. In conclusion, the real-time adjustment of the coefficients of the sliding surface dynamics (Case 1) has been preferred for the above-mentioned reasons, considering a compromise between sliding surface values, controller action and Double Lane-Change maximum admissible speed. Nevertheless, Case 3 with $\epsilon = 4$ and $k_d = 3$ would have been another possible and reasonable choice. For a fair comparison among the different parameters, all the simulations are run at the same fixed time step of 0.5×10^{-2} s.

Another important point is the chattering due to the sgn functions in Equation 4.16. The sgn function gives ± 1 when its argument swings around zero and this worsen the controller action. Please note that the results shown in Table 4.4 refer to a condition in which the chattering issue has been already solved using the second approach shown below in Equation 4.19.

Given a generic function $f(t)$, a first countermeasure that can be taken is the one suggested in Karnopp[15], referred here as “Solution 1”:

$$\text{sgn}(f(t)) \rightarrow \frac{f(t)}{|f(t)| + k} \quad (4.18)$$

TABLE 4.4: Comparison of different SMC sliding surface dynamics parameters: Case 3 is preferred as a compromise between sliding surface values, controller action and maximum admissible speed in the Double Lane-Change test

		Sinewave steering input				Double Lane Change		
		$\ s\ _2$ [-]	$\ s\ _\infty$ [-]	$\ \Delta M_z\ _2$ [Nm]	$\ \Delta M_z\ _\infty$ [Nm]	$\ e_{ct}\ _2$ [m]	$\ e_h\ _2$ [rad]	max speed [km/h]
Case 1	$\epsilon = 1.5 s , k_d = s $	8.9261	0.3081	1775.1	290.5633	6.2148	0.9584	81.7
Case 2	$\epsilon = 3, k_d = 2$	8.7214	0.3451	6417.77	297.4834	6.4284	0.9438	81.4
Case 3	$\epsilon = 4, k_d = 3$	8.8698	0.3709	4835.0	302.6884	6.6435	0.9308	81.8

with k positive and small constant.

A more refined solution is presented in Zhao and Zang[43] and consist of replacing the sgn with a saturation function:

$$\text{sgn}(f(t)) \rightarrow \text{sat}\left(\frac{f(t)}{\Phi}\right) = \begin{cases} \frac{f(t)}{\Phi} & \text{if } |f(t)| \leq \Phi \\ \text{sgn}(f(t)) & \text{if } |f(t)| > \Phi \end{cases} \quad (4.19)$$

where Φ is a small positive constant. This approach is referred as “Solution 2”.

Equation 4.16 contains three sgn functions, therefore either three k coefficients for Equation 4.18 or three Φ coefficients for Equation 4.19 have to be determined. A trial-and-error procedure has been used for both approaches and the resulting coefficients are reported in Tables 4.5 and 4.6. For sake of brevity, the three sgn functions are called $\text{sgn} 1$, $\text{sgn} 2$, $\text{sgn} 3$ and are respectively defined as:

$$\text{sgn} 1 = (r - r_d)s \quad (4.20)$$

$$\text{sgn} 2 = r - r_d \quad (4.21)$$

$$\text{sgn} 3 = (r - r_d)(\beta - \beta_d) \quad (4.22)$$

TABLE 4.5: k coefficients for the three sgn functions in Equation 4.16 according to Equation 4.18 (Solution 1)

$\text{sgn} 1$	$\text{sgn} 2$	$\text{sgn} 3$
0.1	0.1	0.1

Figure 4.1 shows the sliding surface s trend for the comparison among the two above-mentioned solutions, i.e., Solution 1 and Solution 2, and the “Standard case”, i.e., without countermeasures against chattering. The reported maneuver is a sinusoidal steering input of amplitude $A = 5^\circ$

TABLE 4.6: Φ coefficients for the three sgn functions in Equation 4.16 according to Equation 4.19 (Solution 2)

sgn 1	sgn 2	sgn 3
0.1	0.05	0.1

starting from 50 km/h (same test of the SMC parameters tuning) and the sliding mode parameters correspond to Case 3 in Table 4.4 for a reason that will be explained in the next paragraph. As it is possible to see, the Standard case has huge spikes and this would lead to an extremely poor control action. By converse, Solution 1 and Solution 2 have similar trends as they both prevent chattering.

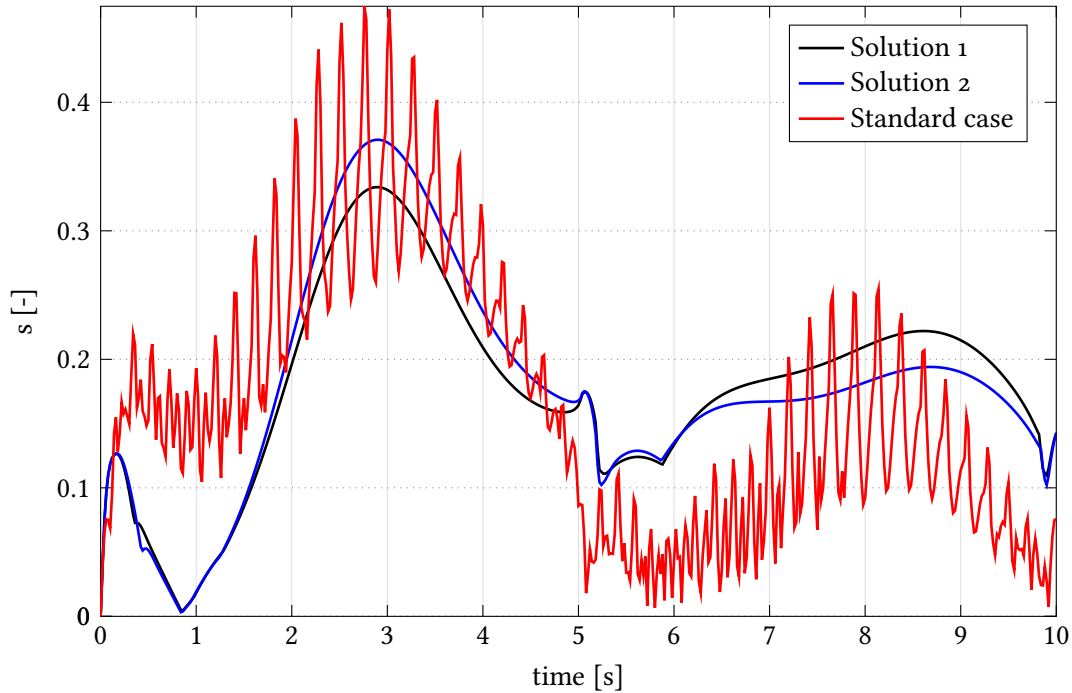


FIGURE 4.1: Sliding surface trend for a sinusoidal steering input in order to compare chattering solutions, for $\epsilon=4$ and $k_d=3$: Solution 1 and Solution 2 are both effective

However, as described previously, the results reported in Figure 4.1 refer to the case in which the SMC parameters are constant and not tuned in real-time. Under the last condition, the chattering effect is partially attenuated by itself since ϵ and k_d multiplying the first two sgn functions in Equation 4.16 modulate the sgn functions themselves when their argument is small. Figure 4.2 shows the sliding surface and the yaw moment correction for a step-steer maneuver of amplitude 5° starting from 60 km/h, considering the real-time SMC parameters of Case 1. The comparison is among chattering Solutions 1 and 2, and the Standard case. Note that the Standard Case has some small spikes in the sliding surface trend which in turn reflect important oscillations in the corrective yaw moment. Solution 1 also has some very small and almost imperceptible oscillations

when the surface is converging to the steady state value. By contrast, Solution 2 has the smoother trend and at the end it is what has been chosen for the controller.

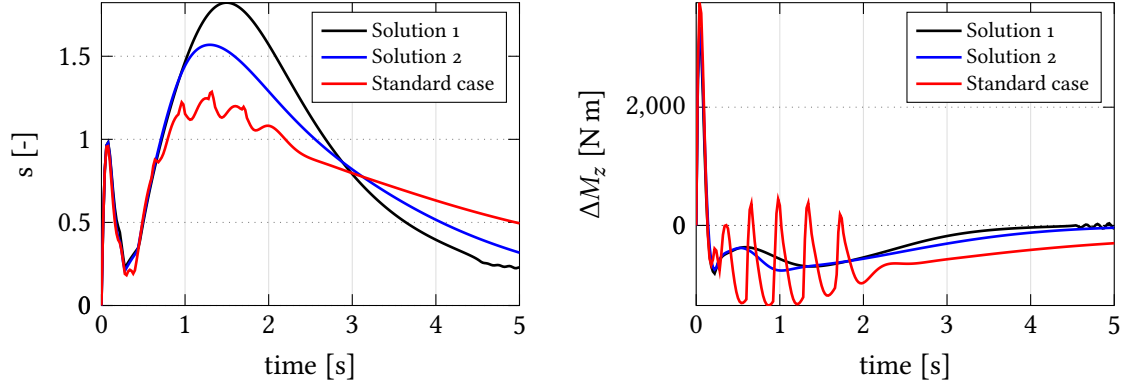


FIGURE 4.2: Sliding surface and corrective yaw moment trend for a sinusoidal steering input in order to compare chattering solutions, for real time parameters: Solution 2 has the smoother trend and for this reason it has been implemented in the controller

As a recap, the real-time parameter tuning reported in Table 4.3 and the saturation approach for the chattering prevention introduced in Equation 4.19 with coefficients in Table 4.6 are chosen as the best compromise for all the above-mentioned reasons. It is worthwhile to point out that the whole procedure has been carried out considering the 4IWM EV configuration, which is the major focus of this project. However, since the controller is designed to be unique and able to work for all four configurations presented in Section 3.3, it may not be optimized for the other three architectures.

A last important concept that needs to be discussed when dealing with SMC is represented by the so-called Lyapunov stability. Defining the Lyapunov function V as in Equation 4.23, the always negative derivative of such function is a sufficient condition for the system states to converge on the sliding surface [43, 49, 51, 53].

$$V = \frac{1}{2}s^2 \quad (4.23)$$

At this point, the choice of the sliding surface dynamics in Equation 4.10 can be justified:

$$\dot{V} = s \cdot \dot{s} = s \cdot (-\epsilon \operatorname{sgn}(s) - k_d s) = -\epsilon |s| - k_d s^2 < 0 \quad (4.24)$$

Equation 4.24 guarantees that the derivative of the Lyapunov function is always negative, given ϵ and k_d positive values. Since those two parameters are function of the sliding surface, it is important to use the absolute value of s when computing them. In the case in which the parameters were negative, the Lyapunov theorem would be no more valid but the system could still be stable, since $\dot{V} < 0$ is a sufficient but not necessary condition.

4.1.2 Derivative Feedback

The Torque Vectoring Controller developed so far is in line with the state-of-the-art. Indeed, it is well known that the combined control of yaw rate and vehicle side slip angle is one of the most effective ways to improve vehicle lateral stability. Starting from this solid base, the objective has been the extension and improvement of the controller effectiveness having in mind some typical real-life driving scenarios such as accelerating/braking while cornering.

The control action developed in Equations 4.16 and 4.17, together with the reference values in Equations 4.11 and 4.12, does not directly consider any vehicle longitudinal acceleration in the loop. Here, the idea is to find a direct link between longitudinal and yaw acceleration, and add this information inside the TVC. In principle, knowing the reference yaw acceleration would allow the knowledge of the yaw acceleration error which in turn would allow a better control of the yaw rate error, since the first is the derivative of the second.

The starting point is the equation linking longitudinal vehicle velocity v_x , yaw rate r and radius of curvature R , as found in Minaker[26]:

$$v_x = rR \quad (4.25)$$

Differentiating Equation 4.25, the following is obtained:

$$\dot{v}_x = \dot{r}R + r\dot{R} \quad (4.26)$$

Now, the curvature gain equation from the bicycle model is introduced in order to substitute the radius of curvature and its derivative into Equation 4.26:

$$\frac{1}{R\delta} = \frac{1}{l + k_{us} \frac{v_x^2}{g}} \quad (4.27)$$

where k_{us} is the understeering coefficient defined in Equation 4.13.

The final result showing the yaw acceleration prediction is reported below:

$$\dot{r}_{pred} = \frac{\dot{v}_x \delta \left(l + k_{us} \frac{v_x^2}{g} \right) - v_x \left(-\dot{\delta} \left(l + k_{us} \frac{v_x^2}{g} \right) + \delta \frac{2v_x \dot{v}_x}{g} \right)}{\left(l + k_{us} \frac{v_x^2}{g} \right)^2} \quad (4.28)$$

A curious reader can find all the mathematical computations in Appendix B. Here, the really interesting part is the result in Equation 4.28 with the relationship among the variables. The yaw

acceleration is a function of longitudinal vehicle acceleration \dot{v}_x , steering angle δ , longitudinal vehicle speed v_x and rate of change of steering angle $\dot{\delta}$. In particular, the appearance of the steering angle derivative in the formula was unexpected. Besides, the yaw acceleration also depends on vehicle constructive parameters such as mass, cornering stiffness, longitudinal position of the centre of gravity (all hidden inside the understeering coefficient) and wheelbase.

Figure 4.3 shows the implementation of the above-mentioned calculations in Simulink. A low-pass filter with $\tau = 0.05$ s is added to cut the possible high-frequency components and smooth the curve.

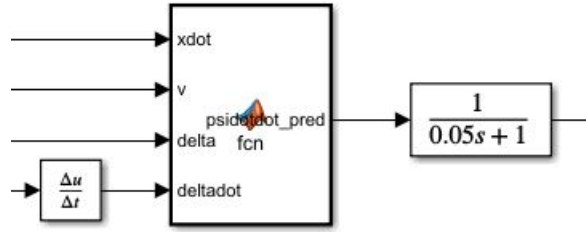


FIGURE 4.3: Evaluation of the yaw acceleration prediction in Simulink

At this point, the yaw acceleration in Equation 4.28 is added as derivative feedback term inside the corrective yaw moment calculation in Equation 4.17.

$$\Delta M_z = J_z(\dot{r}_c + (\dot{r}_{\text{pred}} - \dot{r})) - M_z \quad (4.29)$$

The control action has now become the sum of two terms:

- \dot{r}_c that comes from the Sliding Mode Control in Equation 4.16
- $(\dot{r}_{\text{pred}} - \dot{r})$ that is the derivative feedback term obtained as the error between the yaw acceleration prediction in Equation 4.28 and the actual vehicle yaw acceleration

Since the term “yaw acceleration prediction” may be misleading if wrongly interpreted, for sake of clarity a brief explanation is included. The “prediction” has nothing to do with Model Predictive Control techniques, but it has to be intended as the calculation of the reference yaw acceleration that allows the prediction or anticipation of the reference yaw rate trend.

4.1.3 TVC upper-layer layout

The steps followed until now have shown the corrective yaw moment calculation according to the developed control strategy. In particular, with reference to the TVC general control scheme in Figure 2.12, the vehicle model has been presented in Chapter 3 and the upper-layer together with the reference vehicle model in Chapter 4.

For sake of completeness, the schematic of the TVC upper-layer developed in Simulink is reported in Figure 4.4. Table 4.7 highlights the controller inputs and their source.

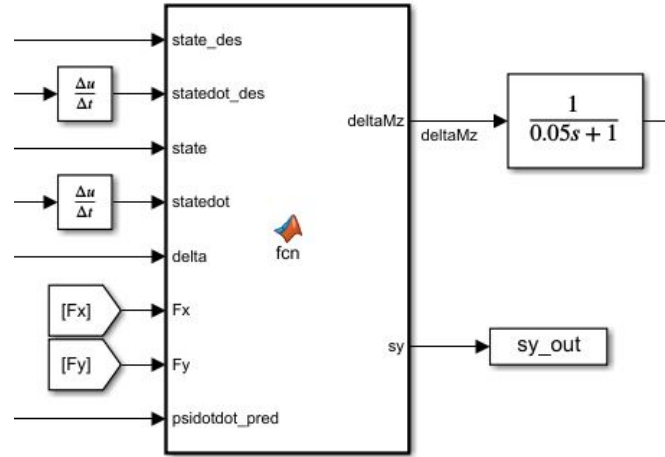


FIGURE 4.4: Schematic of the TVC upper-layer developed in Simulink

TABLE 4.7: TVC upper-layer inputs with reference to Figure 4.4

Input	Origin
reference states	bicycle model
reference states derivative	derivative block
vehicle states	vehicle model
vehicle state derivatives	derivative block
steering angle	simulation input / driver model
longitudinal and lateral tire forces	Pacejka's Magic Formula
yaw acceleration prediction	Equation 4.28

The controller is designed taking into account its feasibility in a real application. All the variables listed in Table 4.7 can be measured or estimated in a real vehicle: reference states with their derivatives and tire forces can be computed by the Electronic Control Unit (ECU) exploiting respectively the bicycle model and the Magic Tire Formula. The steering angle, together with its rate of change (needed for the yaw acceleration prediction), can be measured with a steering angle sensor, as the one developed by Bosch Motorsport[54]. The vehicle states and their derivatives can be dealt with in the following way:

- longitudinal vehicle speed is usually computed considering a pure average of all wheels speeds (although this approach suffers from inaccuracy), see Bonfitto[55];
- vehicle side slip angle is really expensive to measure, therefore estimation methods already discussed in Section 2.2.3 are preferred;
- yaw rate, longitudinal and lateral acceleration are measured with an accelerometer installed at the vehicle's centre of gravity.

However, one of the main limitations of this project is that the vehicle side slip angle is assumed to be precisely known, i.e., no estimation methods have been developed. Besides, vehicle yaw acceleration is obtained as derivative of the measured yaw rate. In practical cases, taking derivatives could be challenging because they tend to amplify the noise in the measurements. For this reason, filters or other measures may be necessary.

4.2 Cruise Control

Cruise-control systems allow the automatic control of vehicle speed set by the driver without using the accelerator pedal. Indeed, they allow the reduction of driver's fatigue and they improve riding comfort and powertrain efficiency [56].

The implementation of a cruise-control system has been necessary to enable simulations at nearly constant vehicle speed. Two of the main control methods available in the literature are PID and SMC. Since the former struggles with non-linearities, the latter has been preferred in this work. The implemented SMC uses the vehicle speed error between the actual and the target values for the calculation of the corrective longitudinal force [11, 43, 49]. The sliding surface and its dynamics are defined as:

$$s_v = v_{xd} - v_x \quad (4.30)$$

$$\dot{s} = -\epsilon \operatorname{sgn}(s_v) - k_d s \quad (4.31)$$

where v_{xd} is the target speed set by the driver and v_x is the actual longitudinal vehicle speed. The controller parameters are ϵ and k_d .

Differentiating Equation 4.30 and combining it with Equation 4.31, the longitudinal acceleration \dot{v}_x is obtained as:

$$\dot{v}_x = \dot{v}_{xd} + \epsilon \operatorname{sgn} s_v + k_d s_v \quad (4.32)$$

Now, substituting \dot{v}_x from Equation 4.32 into Equation 3.1 (vehicle model longitudinal DOF), the corrective longitudinal force is computed as:

$$\Delta F_x = m(\dot{v}_{xd} + \epsilon \operatorname{sgn} s_v + k_d s_v) - m v_y r - F_x \quad (4.33)$$

The term ΔF_x in Equation 4.33 represents the required additional force in longitudinal direction to guarantee the desired constant speed. By contrast, F_x is intended as the sum of actual tire forces in longitudinal direction, rolling resistance and aerodynamic drag.

Two different parameters tuning approaches have been studied and compared. The first one considers them as constants, the second one tunes them according to the velocity error, i.e., the sliding surface in Equation 4.30. For sake of shortness, the two sets of constant parameters will be referred to as “Case 1” and “Case 2”, while the real-time tuning will be called “Case 3”. A tuning procedure considering a vehicle driving on a well-paved road ($\mu = 1$) is conducted for two different velocity sets and steering conditions: in the first one (called “Test 1”), the initial speed is 70 km/h, the target one is 80 km/h and the vehicle is driving straight; in the second one (called “Test 2”), the vehicle has to drive constantly at its initial speed of 60 km/h under a sinusoidal steering angle input of amplitude $A = 5^\circ$ and period $T = 5$ s with the TVC activated. Table 4.8 shows the results of the two tests for the three different parameters cases. In order to fairly compare them, the simulations are run at the same fixed time-step of 0.5×10^{-2} s. The comparative metric is E_v , a performance indicator of the cruise control system that is defined as the norm-1 of the velocity error:

$$E_v = \int_{t_0}^{t_f} |v_{xd} - v_x| dt \quad (4.34)$$

TABLE 4.8: Comparison of different cruise-control parameters: Case 1 minimizes the velocity error in both tests

		Test 1 E_v [m]	Test 2 E_v [m]
Case 1	$\epsilon = 7, k_d = 6$	1.5332	0.0146
Case 2	$\epsilon = 0.8, k_d = 0.7$	2.1873	0.1723
Case 3	$\epsilon = 0.9 s_v + 1, k_d = 0.8 s_v $	1.6278	0.1426

Table 4.8 indicates that Case 1 minimizes the velocity error in both tests, Case 2 is the worst and Case 3 seems to be a good compromise. However, these numbers do not give information about the driving comfort in terms of velocity and acceleration profile.

Figures 4.5 and 4.6 show the velocity and acceleration trend under the Test 1 condition for the three different parameters sets. As it is possible to see, in conditions in which the cruise speed is not coincident with the vehicle initial speed, the controller is either too aggressive (overshoot when reaching constant speed) in Case 1, or too slow (significant amount of time to reach constant speed) in Case 2. By contrast, the parameters modulation according to the velocity error in Case 3 combines a fast and a robust controller together. Besides, the acceleration trend in Case 1 is highly undesirable because passengers would feel accelerations and decelerations when approaching the target speed, while the difference between Case 2 and Case 3 is just in the responsiveness of the controller.

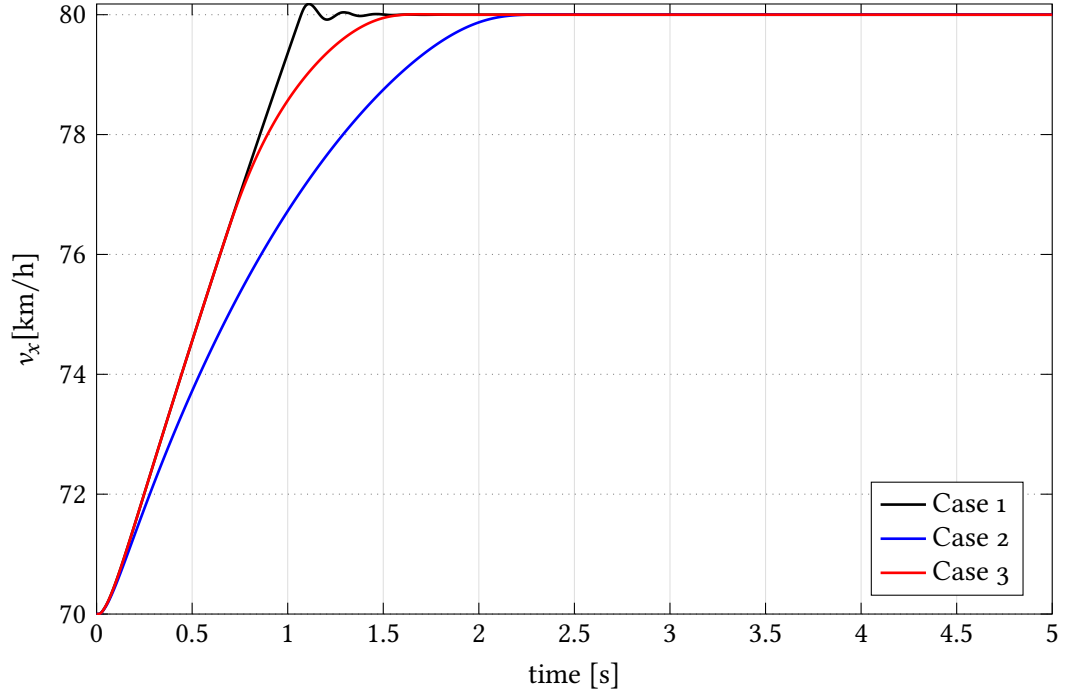


FIGURE 4.5: Velocity trend under Test 1 conditions for the comparison among the three different parameters sets: Case 3 is the best compromise between a fast and a robust controller

Figure 4.7 shows the velocity trend under Test 2 conditions, with the objective to show the cruise control effectiveness when longitudinal-lateral dynamics coupling is present. It is possible to notice that the controller well-works in all three cases, since the velocity errors at the steering angle peaks are within 0.3 km/h. Although Case 1 manages to keep a really small velocity error, this solution is not acceptable for the reasons discussed before. The developed real-time tuning procedure is the one chosen for the cruise-control, since it has proven to be the best compromise between fast response and good vehicle riding comfort. The chattering issue typical of the Sliding Mode Control has been solved with the approach in Equation 4.18 considering $k = 0.1$.

The cruise-control system developed in Simulink is shown in Figure 4.8. The MATLAB function receives inputs for the computation of the corrective longitudinal force ΔF_x . The absolute value and the integral blocks are used to evaluate the performance indicator E_v .

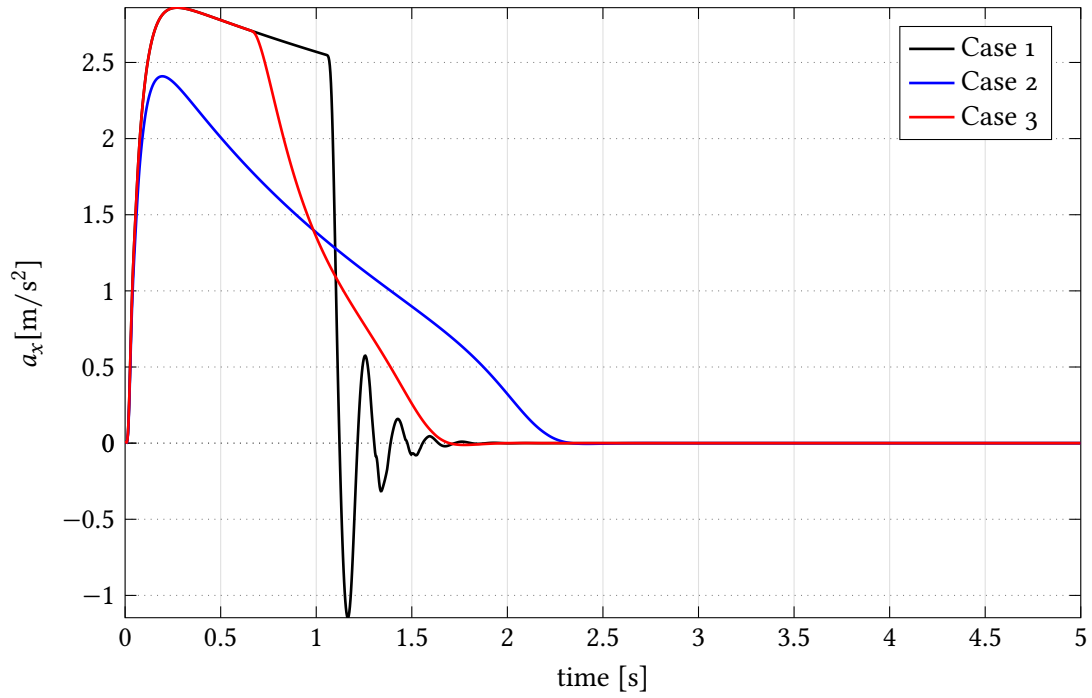


FIGURE 4.6: Acceleration trend under Test 1 conditions for the comparison among the three different parameters sets: Case 1 would cause discomfort to passengers when approaching the target speed

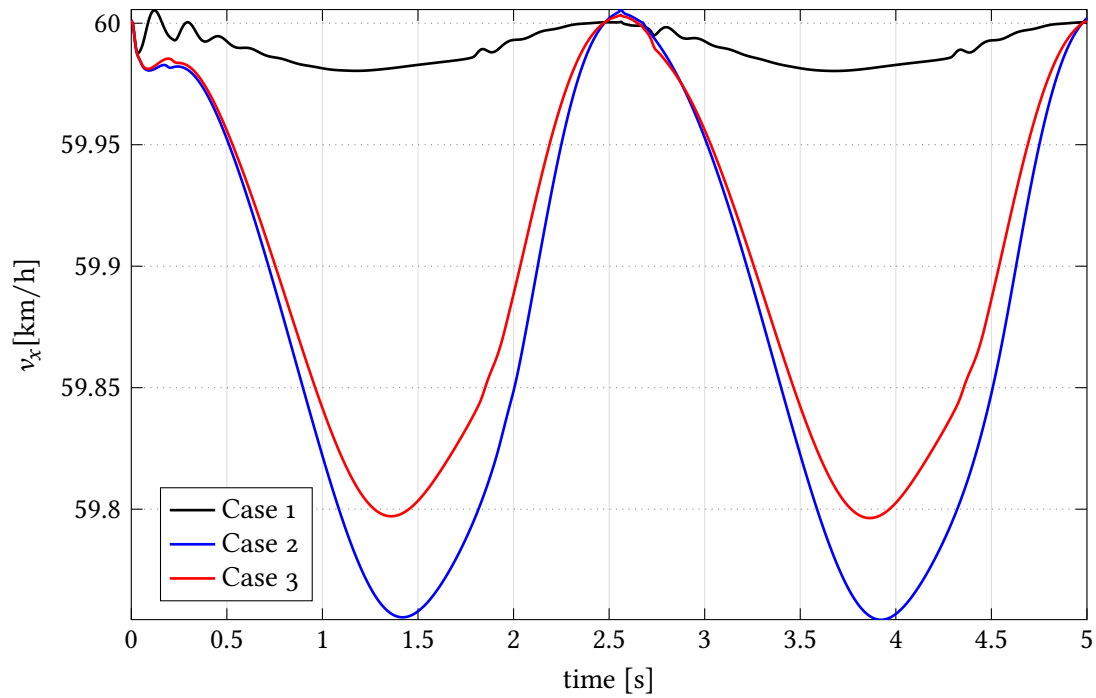


FIGURE 4.7: Velocity trend under Test 2 conditions for the comparison among the three different parameters sets: Case 1 keeps a really small velocity error but generates undesired oscillations

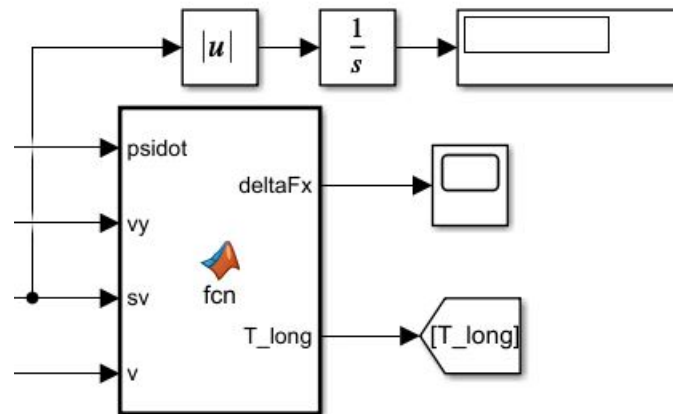


FIGURE 4.8: Cruise-control system developed in Simulink: the MATLAB function computes the corrective longitudinal force and the blocks above evaluate the performance indicator E_v

4.3 Traction Control System

Traction Control Systems regulate the wheel slip rate to prevent excessive wheel spinning. Their intervention is most likely to occur under high accelerations and low road-adhesion conditions. As already discussed in Section 2.2.2, several approaches are available in the literature. However, the main reason for which a TCS has been implemented here is to enable effective simulations in low adhesion conditions. Indeed, when the friction coefficient μ is small the wheels would spin and the result would be a less controllable vehicle. The TCS is used as a tool to study the behaviour of the TVC in poor road adhesion conditions.

That being said, the simple anti-slip control strategy discussed in Equation 2.30 is implemented. Essentially, the maximum torque to comply with tire adhesion conditions is set as the limit torque, and the overall motor limit curve is the minimum between the characteristic limit curve and the one from the anti-slip controller. Although this implementation in a real vehicle would require the real-time estimation of the road friction coefficient, it is worthwhile to remember once more that the TCS here is used to enable simulations without excessive wheel slip ratios for testing the TVC itself.

4.4 Torque Distribution Strategy

The torque distribution strategy is the core of multi-motor EVs. The driver's inputs in terms of throttle and brake, and controller's inputs in terms of yaw moment and longitudinal force corrections are split among the motors according to a torque allocation algorithm. This represents the lower-layer controller in the hierarchical-approach-based TVC.

Although the high-level controller is “universal”, meaning that the corrective yaw moment from TVC and the longitudinal force from cruise control are independent of the EV configuration, this is not the case for the low-level controller, which does depend on the BEV architecture. In the literature, no articles with torque distribution strategies for multiple EV configurations are found. Optimization problems and average/vertical-load-based torque allocation algorithms could be properly modified to account for different numbers and positions of electric motors.

The objective of this section is the explanation of the design choices of the low-level controller. Facing a complex situation in which the same strategy has to work for the four BEV configurations introduced in Section 3.3, a simpler but effective solution has been chosen: it is the vertical-load-based approach already reported in Equations 2.39 – 2.42 for a 4IWMEV case. Extending it to a general case, the torque to each motor is distributed proportionally to the vertical load on that wheel (if it is an in-wheel motor) or on that axle (in the case of a central motor). This is a smart strategy because more torque is given to the most loaded wheels, which are the ones that can better exploit traction. Optimization-based algorithms have been rejected for their complexity, since the solution of least squares problems is not straightforward, and because they require computational time.

The torques that the allocation algorithm accounts for are throttle, regenerative braking, yaw moment correction and possible corrective longitudinal force from cruise control. It is assumed that the throttle opening position is proportional to the total motor output torque. Considering a 50% throttle for example, the sum of motor torques corresponds to 1/2 of the sum of each motor maximum torque at that angular speed. This approach has been used to link the throttle pedal input with the total desired torque, which will be split among the motors. The motor maximum torque curve will be better explained in Section 4.4.1. The second driver's input is the brake pedal position. Here the situation is a little bit more complicated since both regenerative braking and friction brakes play a role but just the first one has to be considered in the torque distribution strategy. The friction brakes intervention will be discussed in Section 4.4.2. Back to the point, the same approach used for the throttle is also applied for the regenerative braking. However, this time the braking torque is proportional to the product of brake pedal position and desired regenerative braking percentage. The latter is another simulation input and it is defined as the ratio $\frac{T_{RG}}{T_{lim}}$, where T_{RG} is the regenerative braking torque and T_{lim} is the sum of each motor's maximum braking torque at that angular speed. The possible additional longitudinal force from cruise control is converted into a torque that is bounded between the sum of each motor maximum torque. This is a first step to avoid unreasonable torque values inside the torque distribution strategy. Eventually, the corrective yaw moment ΔM_z from the TVC upper-layer is transformed into "motor torque" T_{yaw} using the following relationship:

$$T_{yaw} = \frac{\Delta M_z}{\frac{\frac{t_f}{2} + \frac{t_r}{2}}{2}} R_l \quad (4.35)$$

By looking at Figure 4.9, T_{yaw} represents the total torque that has to be allocated in order to generate the corrective yaw moment ΔM_z . More specifically, the following relationship holds:

$$\left(T_{yaw,2} \frac{t_f}{2} + T_{yaw,1} \frac{t_f}{2} + T_{yaw,3} \frac{t_r}{2} + T_{yaw,4} \frac{t_r}{2} \right) \frac{1}{R_l} = \Delta M_z \quad (4.36)$$

It is also worthwhile to note that the sum of torque wheel contributions on the longitudinal direction should be in principle equal to zero to avoid undesired longitudinal forces.

The situation described until now is reported in Figure 4.10, which shows the four possible torque inputs to the torque allocation algorithm.

In the implemented vertical-load based torque distribution strategy, the evaluation of the normal load on each wheel plays a significant role. To this aim, Equations 2.43 – 2.46 have been used. Note that longitudinal and lateral load transfer, respectively responsible for pitch and roll, are taken into account in the calculation even though those degrees of freedom are not directly considered in the vehicle model. Since suspension models are omitted, one limitation is that the roll stiffnesses of suspensions and anti-roll bars have not been considered. Depending on the BEV

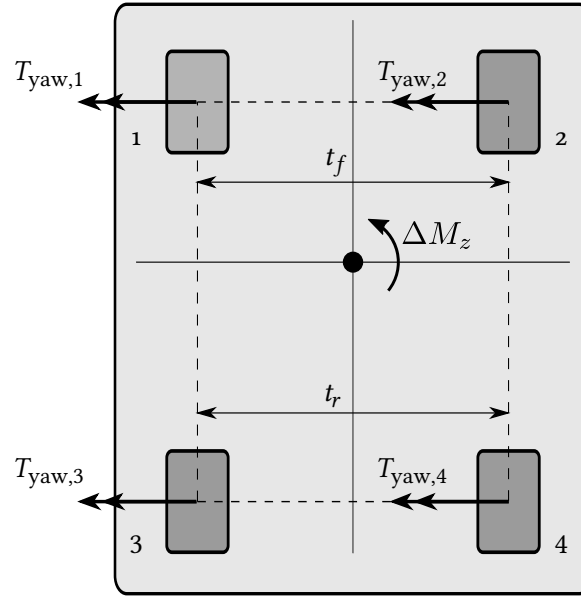


FIGURE 4.9: Vehicle top view with corrective yaw moment ΔM_z and corresponding "motor torque" T_{yaw} for each wheel: $T_{yaw,i}$ is the torque that has to be allocated to each motor in order to generate ΔM_z

configuration, which is a simulation input parameter, a torque distribution coefficient k is defined for each wheel. Figure 4.11 shows its calculation in a MATLAB function where if-else statements are implemented.

Table 4.9 exhibits the four k coefficients computed for each BEV configuration, i.e., 4IWM, 2IWM front axle, 2IWM rear axle and 2 Central Motors (CM). Please note that 1 refers to the front left wheel, 2 to the front right wheel, 3 to the rear left wheel and 4 to the rear right wheel. In the in-wheel motors case, it is clear that the wheel torque is directly linked to the motor torque, as discussed in Section 3.3. In the 2CM case, the front/rear torque distribution is proportional to the vertical load on that axle, and then the torque is split in half between the left and right wheels.

TABLE 4.9: Evaluation of the four k coefficients for each BEV configuration

Config.	k_1	k_2	k_3	k_4
4IWM	$k_1 = \frac{F_{z1}}{F_{z1}+F_{z2}+F_{z3}+F_{z4}}$	$k_2 = \frac{F_{z2}}{F_{z1}+F_{z2}+F_{z3}+F_{z4}}$	$k_3 = \frac{F_{z3}}{F_{z1}+F_{z2}+F_{z3}+F_{z4}}$	$k_4 = \frac{F_{z4}}{F_{z1}+F_{z2}+F_{z3}+F_{z4}}$
2IWMf	$k_1 = \frac{F_{z1}}{F_{z1}+F_{z2}}$	$k_2 = \frac{F_{z2}}{F_{z1}+F_{z2}}$	$k_3 = 0$	$k_4 = 0$
2IWMr	$k_1 = 0$	$k_2 = 0$	$k_3 = \frac{F_{z3}}{F_{z3}+F_{z4}}$	$k_4 = \frac{F_{z4}}{F_{z3}+F_{z4}}$
2CM	$k_1 = \frac{0.5(F_{z1}+F_{z2})}{F_{z1}+F_{z2}+F_{z3}+F_{z4}}$	$k_2 = k_1$	$k_3 = \frac{0.5(F_{z3}+F_{z4})}{F_{z1}+F_{z2}+F_{z3}+F_{z4}}$	$k_4 = k_3$

The longitudinal additional torque from the cruise control, the throttle torque and the regenerative braking torque are split proportionally to the k coefficient:

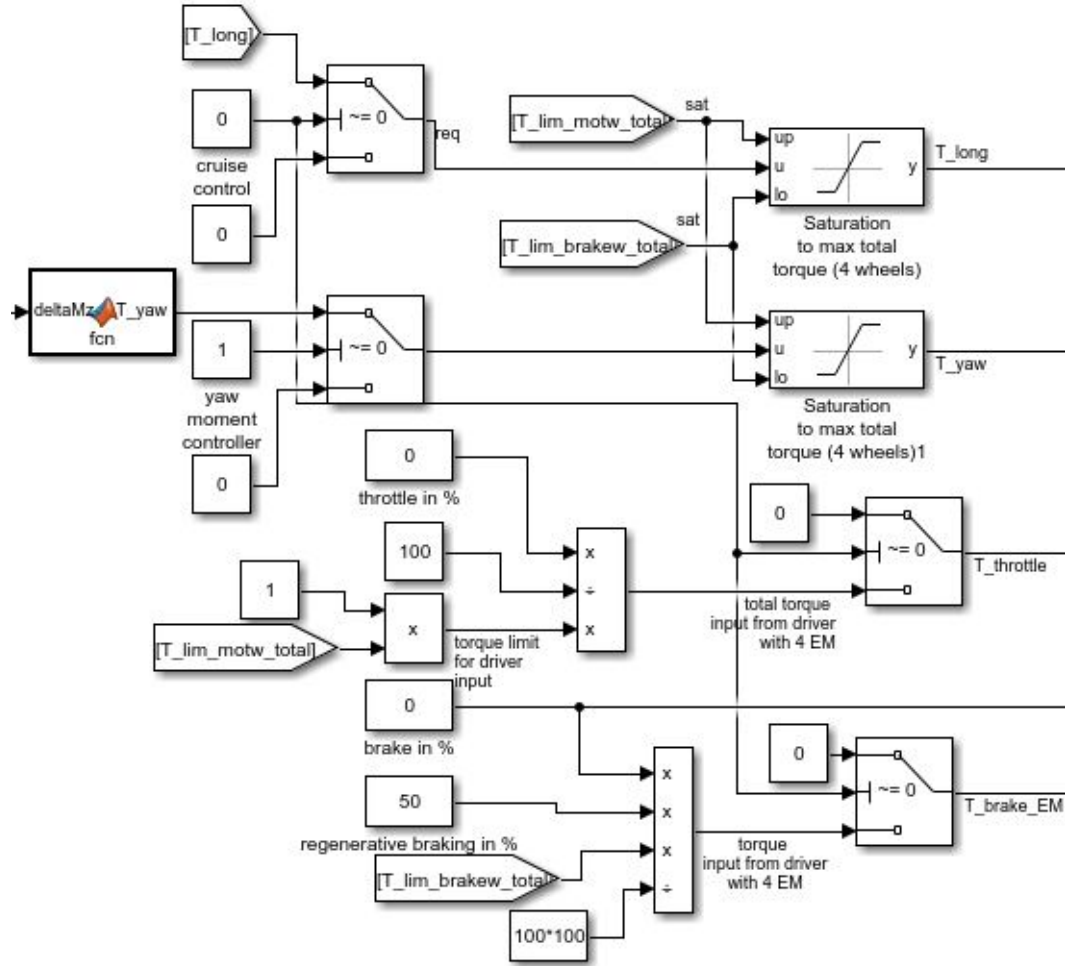


FIGURE 4.10: Inputs to the torque distribution strategy in Simulink: from top to bottom there are corrective longitudinal force from cruise control, corrective yaw moment from TVC, torque from throttle and torque from regenerative braking

$$T_i = k_i(T_{long} + T_t + T_{RG}) \quad (4.37)$$

Since the k coefficients already have the information about the BEV configuration, the equations for the torque distribution to the motors are “universal”. For instance, in the case of the 2IWM on the front axle, T_3 and T_4 evaluated with Equation 4.37 will be equal to zero.

A separate discussion has to be done for the yaw moment torque contribution. Looking at Equation 4.37, it is clear that the torques on the two vehicle sides may be different if the respective k coefficients are different, which is usually what happens in cornering conditions. The only exception is represented by the 2CM configuration, in which the left and right wheels always have the same torque by definition from Table 4.9. Back to the point, when the left and right vehicle sides have different torques, the vehicle itself generates a yaw moment and this has to

FIGURE 4.11: Torque distribution coefficient k calculated in Simulink

be accounted for when distributing the corrective yaw moment from the TVC. The effective total torque due to yaw moment $T_{\text{yaw,eff}}$ is calculated as:

$$T_{\text{yaw,eff}} = T_{\text{yaw}} - (T_2 + T_4 - T_1 - T_3) \quad (4.38)$$

where T_{yaw} is the one evaluated in Equation 4.35, and T_1 – T_4 are evaluated according to Equation 4.37.

The new torques to each wheel, adding the yaw moment contribution, become:

$$T_1 = k_1(T_{\text{long}} + T_t + T_{RG} - T_{\text{yaw,eff}}) \quad (4.39)$$

$$T_2 = k_2(T_{\text{long}} + T_t + T_{RG} + T_{\text{yaw,eff}}) \quad (4.40)$$

$$T_3 = k_3(T_{\text{long}} + T_t + T_{RG} - T_{\text{yaw,eff}}) \quad (4.41)$$

$$T_4 = k_4(T_{\text{long}} + T_t + T_{RG} + T_{\text{yaw,eff}}) \quad (4.42)$$

The torque values coming from Equations 4.39 – 4.42 are bounded by the motor maximum torque curves reported at the wheels. For sake of clarity, two examples are now provided. Considering the 2CM configuration, the motor limit curve reported at each wheel is half of the actual motor limit curve (assuming no transmission in between motor and wheel), as the k coefficients of the two wheels on the same axle are equal (meaning that half of the motor torque goes to the left wheel and half to the right one). In the case of 4IWMDEV, the motor limit curve reported at the wheel is the same as the actual motor one, assuming no transmission ratio in between (the concept has been already explained in Section 3.3). The motor maximum torque curve will be further explained in Section 4.4.1.

However, the approach developed until now has problems in the effective yaw moment allocation when motors are close to their saturation limits. The following numerical example tries to explain the issue: imagine that the total required torque from throttle is 1080 N m and the one from yaw moment correction is –140 N m (clockwise), and that each motor's limit torque for that working point is 265 N m. Also, imagine that the following torques at the wheels are allocated by Equations 4.39 – 4.42:

	left	right
front	350 N m	280 N m
rear	260 N m	190 N m

The value on the top left refers to the front left wheel, on the top right to the front right wheel and so on. The sum of the four values is 1080 N m and the torque for yaw moment correction is -140 N m. Later this situation will be called “unsaturated”. However, the saturation block has to be applied in order to comply with the 265 N m limit. Therefore, the allocated torques become:

	left	right
front	265 N m	265 N m
rear	260 N m	190 N m

Now, the effective torque for yaw moment is only -70 N m. This situation will be referred as the “saturated” condition. The effect of TVC on the front wheels is totally lost due to the electric motor torque limit. In this case, the front right wheel torque should be decreased by an amount such that the total torque producing yaw moment is -140 N m. The following condition is the desired one in terms of TVC effectiveness:

	left	right
front	265 N m	195 N m
rear	260 N m	190 N m

In this way, the TVC is fully exploited (desired -140 N m for yaw moment generation are obtained), but the longitudinal performance is penalized (a total of 910 N m is obtained in the longitudinal direction instead of 1080 N m). Keeping in mind the two definitions of “unsaturated” and “saturated” defined before, the following equations are introduced:

$$T_2 = T_{2,\text{sat}} + ((T_{2,\text{unsat}} - T_{2,\text{sat}}) - (T_{1,\text{unsat}} - T_{1,\text{sat}})) \quad (4.43)$$

$$T_4 = T_{4,\text{sat}} + ((T_{4,\text{unsat}} - T_{4,\text{sat}}) - (T_{3,\text{unsat}} - T_{3,\text{sat}})) \quad (4.44)$$

With the required computations, the output torques now are exactly the desired ones, that is the ones that allows the full exploitation of the Torque Vectoring Controller in terms of yaw moment correction. Equations 4.43 and 4.44 have general validity for the cases in which the corrective yaw moment is negative.

A similar example could be introduced in the case of a positive corrective yaw moment (counter-clockwise). Using the same total longitudinal torque of the previous example (1080 N m) and the same torque for yaw moment with opposite sign (140 N m), a symmetric situation with respect to the vehicle longitudinal axis would be obtained. In order to meet the corrective yaw moment

requirement, the front left wheel torque has to be adjusted. A general correction applicable for positive yaw moments conditions is reported in Equations 4.45 and 4.46:

$$T_1 = T_{1,sat} - ((T_{2,unsat} - T_{2,sat}) - (T_{1,unsat} - T_{1,sat})) \quad (4.45)$$

$$T_3 = T_{3,sat} - ((T_{4,unsat} - T_{4,sat}) - (T_{3,unsat} - T_{3,sat})) \quad (4.46)$$

Equations 4.43 – 4.46 have validity under braking conditions (negative torques) as well. These values are then saturated at the motor maximum torque curves to be sure to not exceed them.

Figure 4.12 shows the whole TVC lower-layer, i.e., the torque distribution strategy, in the Simulink environment. The first MATLAB function on the left implements Equations 4.39 – 4.42 and the second one implements the adjustments introduced in Equations 4.43 – 4.46. The two saturation blocks bound the torque to the motor limit curves, and eventually the four transfer functions model the EM delays as introduced in Section 3.3.

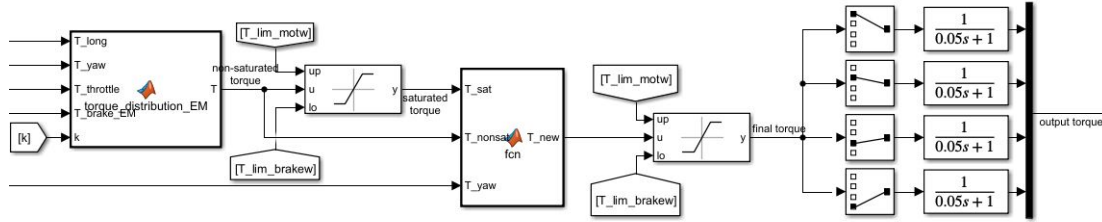


FIGURE 4.12: Complete torque distribution strategy in Simulink: the first MATLAB function on the left implements the torque distribution strategy, the second one makes the torque adjustments in Equations 4.43 – 4.46

The final allocated torque for yaw moment $T_{yaw,fin}$ is computed as:

$$T_{yaw,fin} = -T_1 + T_2 - T_3 + T_4 \quad (4.47)$$

The final longitudinal torque $T_{tot,fin}$ is simply the sum of the torques at the wheels:

$$T_{tot,fin} = T_1 + T_2 + T_3 + T_4 \quad (4.48)$$

Figures 4.13 and 4.14 compare $T_{yaw,fin}$ and $T_{tot,fin}$ with the desired T_{yaw} from TVC and the desired T_{tot} coming from cruise control, throttle or regenerative braking for two different cases: one with the adjusted torque distribution strategy presented before and one without it. A step-steer test with amplitude $A = 5^\circ$ is conducted starting from an initial speed of 40 km/h with a 70% throttle to trigger the motors saturation problem. The adjusted torque allocation algorithm is TVC-oriented, meaning that the final torque for yaw moment matches the desired one perfectly,

as seen in Figure 4.13. However, a lower torque may be available for traction, as shown in Figure 4.14. The two small torque steps are due to the electric motor curve that has been provided.

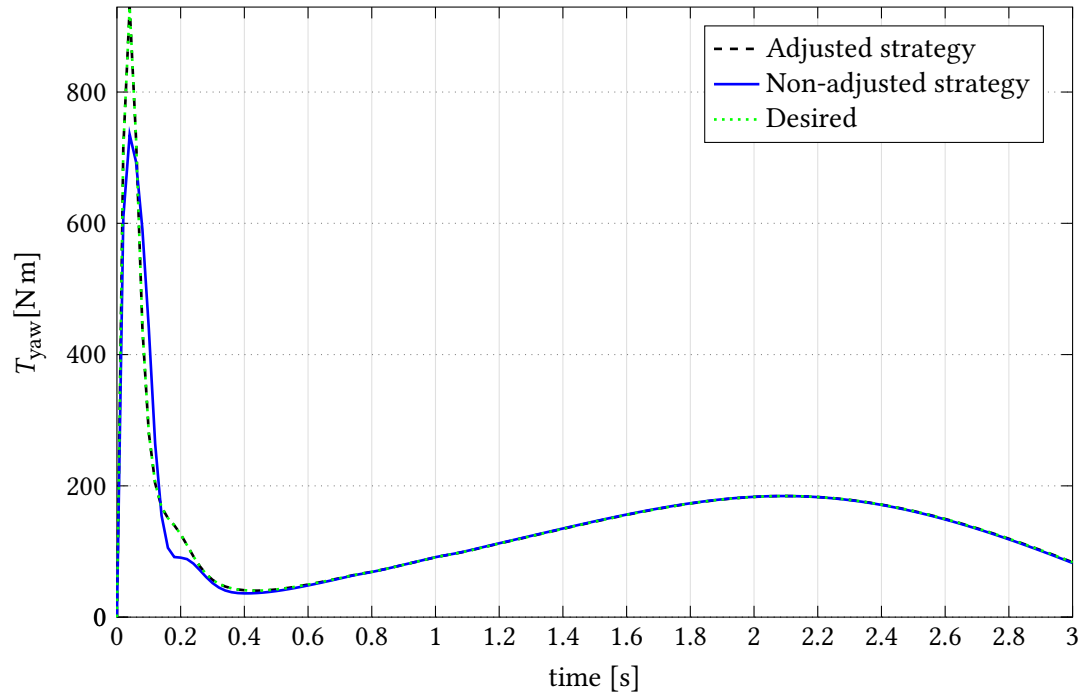


FIGURE 4.13: T_{yaw} trend for the comparison of the adjusted and non-adjusted torque distribution strategy on a step-steer test: the final torque for yaw moment perfectly matches the desired one in the adjusted strategy

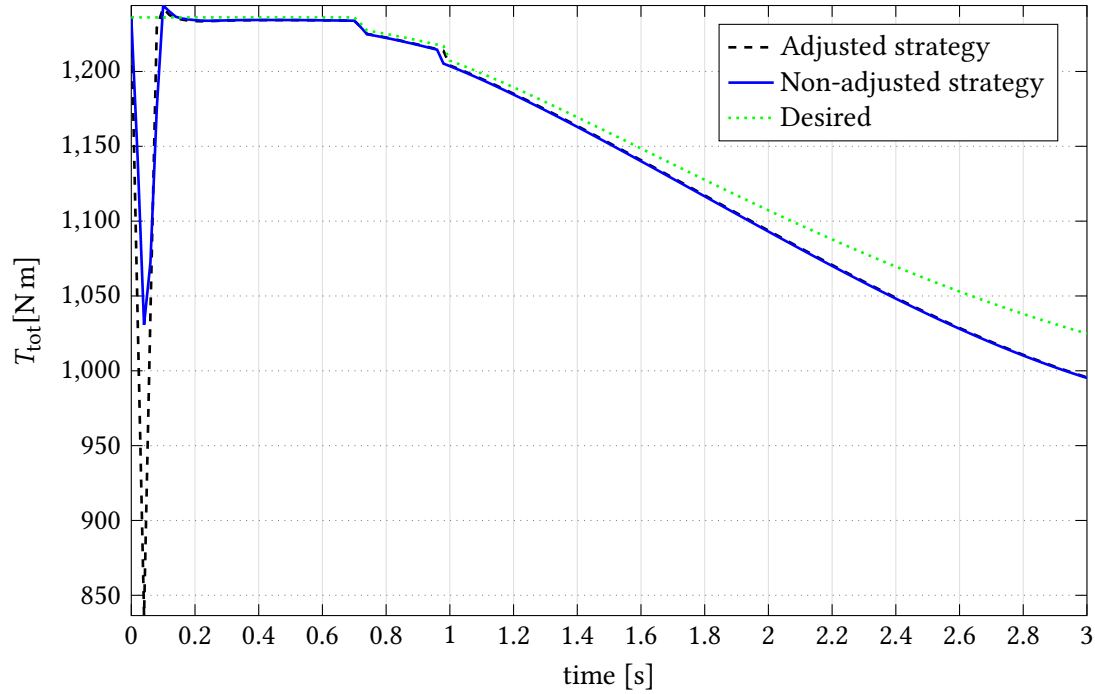


FIGURE 4.14: T_{tot} trend for the comparison of the adjusted and non-adjusted torque distribution strategy on a step-steer test: a lower torque is available for traction in the adjusted strategy

4.4.1 Motor Maximum Torque Curve

The electric motor efficiency map has been provided in Figure 3.13. The objective of this section is the explanation of the motor maximum torque curve meaning and its implementation in Simulink.

First of all, the motoring and braking limit curves are considered, as they are the physical motor limits. Each time step, the EM limit torque has to be evaluated in order to bound the allocated torque from the lower-layer controller. Since the points given to construct the curves are not enough in number, a direct interpolation of angular speed to get a torque value would lead to inaccuracies. Besides, the procedure would be inefficient from a computational point of view since each simulation time-step would require an interpolation. For these two reasons, a different approach based on curve fitting is implemented. A denser angular velocity vector is constructed for the range beyond the EM base speed and the corresponding torque values are obtained by linear interpolation of the given data. A polynomial is chosen to fit the obtained points:

$$T = k_0 + k_1\omega + \frac{k_2}{\omega} + \frac{k_3}{\omega^2} + \frac{k_4}{\omega^3} \quad (4.49)$$

Equation 4.49 can be written in a shorter form as:

$$T = \mathbf{A}\mathbf{k} \quad (4.50)$$

where $\mathbf{k} = [k_0 \ k_1 \ k_2 \ k_3 \ k_4]^T$ and \mathbf{A} is defined as:

$$\mathbf{A} = \begin{bmatrix} 1 & \omega(1) & \frac{1}{\omega(1)} & \frac{1}{\omega(1)^2} & \frac{1}{\omega(1)^3} \\ \dots & \dots & \dots & \dots & \dots \end{bmatrix} \quad (4.51)$$

The least squares problem is solved in order to find the coefficients [57]:

$$\mathbf{k} = \text{inv}(\mathbf{A}^T \mathbf{A}) \mathbf{A}^T \mathbf{T} \quad (4.52)$$

The obtained coefficients for the motor in the 4IWM BEV configuration are reported in Table 4.10.

TABLE 4.10: Polynomial coefficients for the motor limit curve in the 4 IWM configuration

k_0	k_1	k_2	k_3	k_4
76.82	-0.21	5.43e3	1.692e6	-5.232e7

A straight horizontal line is coupled with Equation 4.49. The motor limit curve is therefore defined by the following piecewise function:

$$T_{\text{lim,mot}} = \begin{cases} T_{\text{peak}} & \omega \leq \omega_{\text{base}} \\ T = k_0 + k_1\omega + \frac{k_2}{\omega} + \frac{k_3}{\omega^2} + \frac{k_4}{\omega^3} & \omega > \omega_{\text{base}} \end{cases} \quad (4.53)$$

This whole procedure is done offline and Equation 4.53 allows the direct computation of the EM limit torque once knowing the angular speed in rad/s at the i^{th} time instant. Figure 4.15 shows the accuracy of the fitting procedure: the obtained curve totally overlaps with the given data. Besides, this statement is supported by the calculation of the correlation coefficient, resulting to be equal to 0.999957.

As already discussed in Section 4.3, the maximum torque to comply with tire adhesion conditions represents another torque constraint to avoid excessive wheel slip:

$$T_{\text{lim,slip}}(i) = F_z(i)\mu_x(i)R_l \quad (4.54)$$

The overall motor maximum torque curve is set as the minimum between the physical motor limits from Equation 4.53 and the anti-slip constraint from Equation 4.54. The motor braking curve

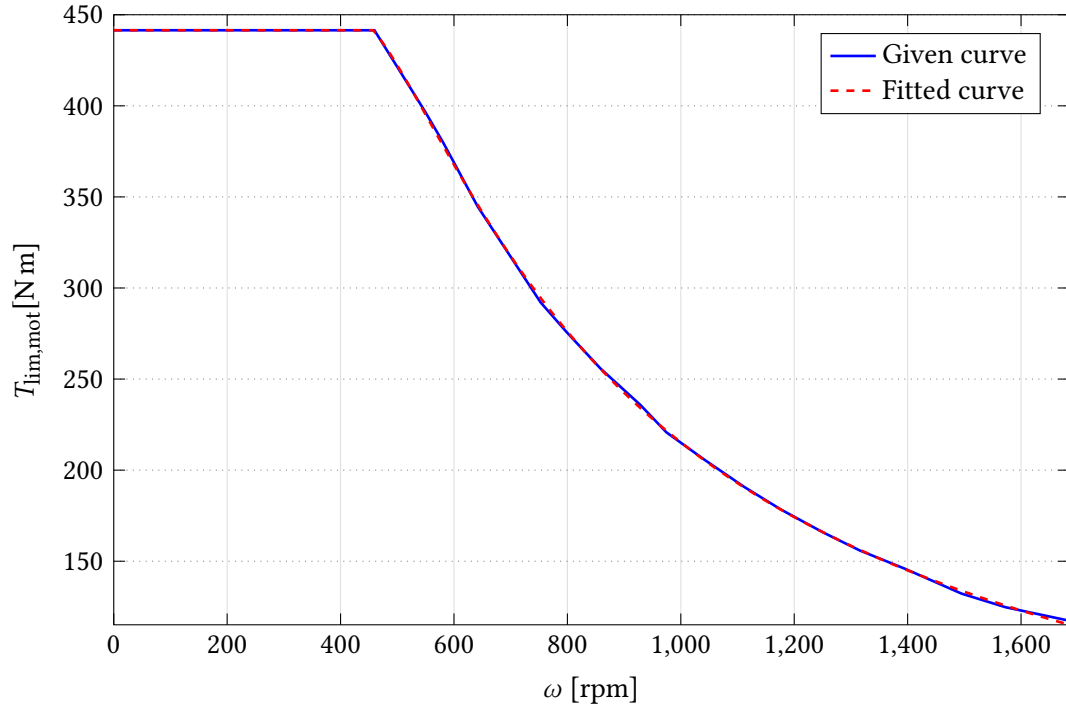


FIGURE 4.15: EM torque limit comparison between given data and fitting procedure: the obtained curve totally overlaps with the given one

is obtained by simply mirroring the motoring one with respect to the x-axis. The procedure can be repeated in the exact same way for the other BEV configurations.

Figure 4.16 shows the calculation of the motor maximum torque curve in Simulink. The first MATLAB function implements Equations 4.53 and 4.54, the second one calculates the sum of each motor maximum torque. The latter value is used to calculate throttle and regenerative braking torque and to limit cruise-control and TVC demands, as explained in Section 4.4.

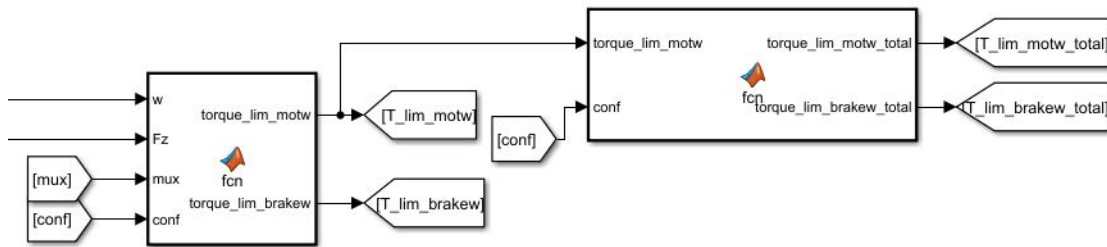


FIGURE 4.16: Motor maximum torque curve in Simulink: the first MATLAB function calculates the overall motor maximum torque curve while the second one evaluates the sum of each motor maximum torque

4.4.2 Regenerative Braking and Friction Brakes

Torque management in braking conditions is a delicate situation, since both conventional friction brakes and regenerative braking are involved. In this work, the ratio between regenerative braking and conventional brakes torque can be regulated, emulating what the ECU can do in a real vehicle. The feature is known as brake blending and allows the control and optimization of conventional and electric braking system [58].

The regenerative braking torque and its allocation among the different motors has been explained in Section 4.4. In addition to EM braking, EVs should also be equipped with conventional disc brakes in order to guarantee the minimum braking performance for the required driving safety. In this project, the front - rear brake balance is set proportional to the static load distribution:

$$f = \frac{b}{l} = 56.5 \%$$

$$r = \frac{a}{l} = 43.5 \%$$

Given a maximum total braking torque of 1600 N m and assuming that the two wheels on the same axle receive the same braking torque, the conventional brakes torque distribution is:

$$T_{b1} = T_{b2} = T_{b,tot} \frac{f}{2} \quad (4.55)$$

$$T_{b3} = T_{b4} = T_{b,tot} \frac{r}{2} \quad (4.56)$$

The above-mentioned total torque value has been chosen to guarantee a certain braking performance when regenerative braking is not available. Figure 4.17 shows longitudinal velocity and acceleration when fully braking on a straight road from an initial speed of 100 km/h.

Table 4.11 shows the vehicle braking performance in terms of stopping time, peak deceleration and braking distance.

TABLE 4.11: Braking performance when fully braking on a straight road from 100 km/h

stopping time	peak deceleration	braking distance
7.17 s	4.02 m/s ²	100.15 m

The development of a proper brake blending strategy is out of the scope of this project. Brake management is considered with the sole purpose of simulating maneuvers with braking while cornering. To this aim, the regenerative braking percentage, here defined as the percentage of

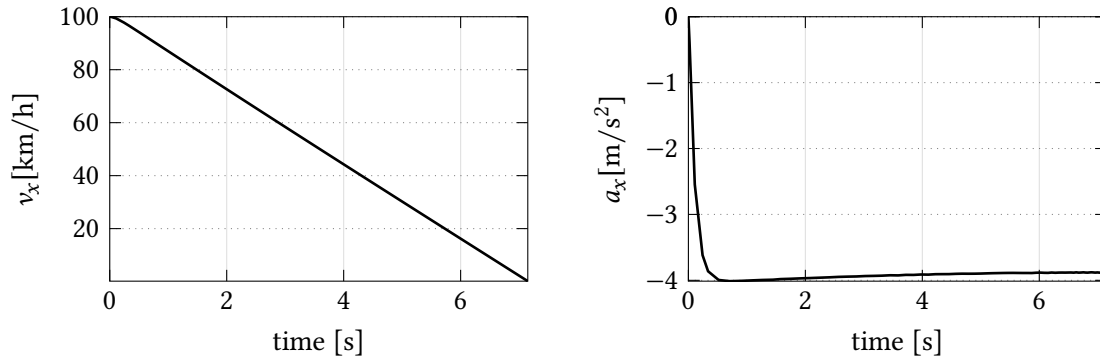


FIGURE 4.17: Longitudinal speed and acceleration trend when fully braking on a straight road

electric motor braking limit curve, is considered. When the driver asks for a certain amount of braking torque, part of it comes from the EMs according to the regenerative braking ratio, and the rest is provided by the disc brakes. When changing that percentage, the total braking torque is still kept the same so as to obtain the same braking performance (with small variations due to the fact that the torque distribution strategies are different between conventional brakes and electric motors).

Chapter 5

Results and Discussion

This chapter reports the main results obtained from several simulations. The objective is the verification of the proposed integrated and modular vehicle dynamics controller, featuring Torque Vectoring Controller, Traction Control System and Cruise Control, under a broad range of driving scenarios.

5.1 Simulation environment setup

Most of the simulation inputs can be directly chosen inside the Simulink environment, as shown in Figure 5.1. Rotary switches, slider switches and knobs are used to create a more user-friendly environment. As discussed in Section 3.3, four different BEV architectures are considered: 4 in-wheel motors, 2 in-wheel motors on the front axle, 2 in-wheel motors on the rear axle and 2 central motors, one per each axle. Besides, four different macro scenarios can be selected: straight condition, sinusoidal steering input, step steer and closed loop steering maneuver. In particular, the last case enables the driver model presented in Section 3.4, where a Single and a Double Lane-Change are implemented. Cruise Control and Torque Vectoring Control (using Direct Yaw-moment control) can be enabled or disabled, and possible cruise speed can be selected. Eventually, throttle, brake and regenerative braking percentages can be chosen using the last three knobs. Other than that, the initial vehicle speed and the road friction coefficient for each single wheel can be chosen in the main MATLAB script. Further details are reported in Appendix C.

There are 64 different combinations of vehicle configuration, driving maneuver and controllers enabled or disabled, and an infinite number of them if considering also all the percentages of throttle, braking and regenerative braking. It is clear that including all those driving conditions would simply be impossible. Therefore, the most representative ones are chosen and will be reported in the following sections. In order to trigger the expected effectiveness of the developed TVC, several maneuvers will consider acceleration or braking while cornering and abrupt steering angles changes.

Three different vehicles will be compared: one endowed with the controller developed in this thesis, i.e., considering both Sliding Mode Control and derivative feedback as in Equation 4.29,

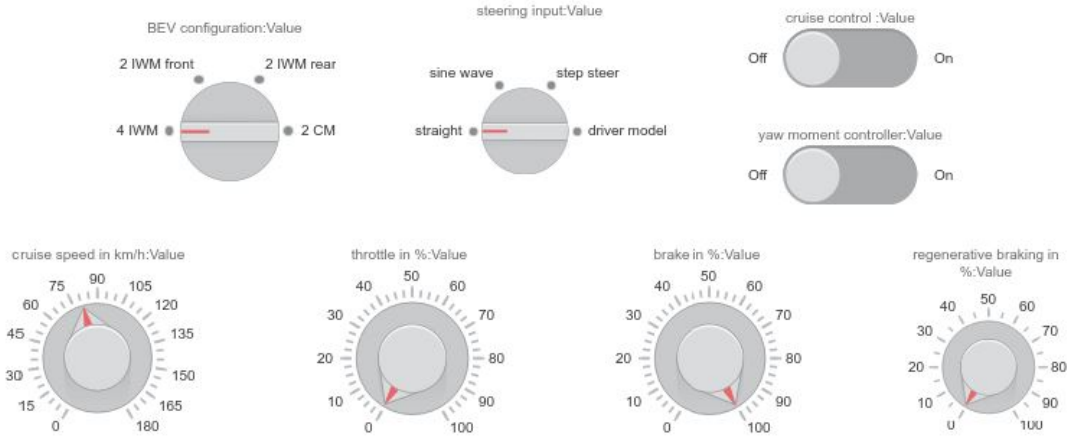


FIGURE 5.1: Setup of simulation environment inputs in Simulink

one with the controller available in literature, i.e., with just the Sliding Mode Control term (Equation 4.17) and one without any controller. They will be respectively referred as “TVC on”, “TVC old” and “TVC off”. Additionally, the output vector’s norm-2 will be used in many cases as a direct comparison among the vehicles. For this reason, all simulations are run at a fixed time-step of 0.5×10^{-2} s in order to obtain the same vectors lengths.

5.2 Sinusoidal steering angle input

The first maneuver implemented considers a sinusoidal steering angle input to understand the controller behaviour and the vehicle reaction under a smooth dynamic condition. The sinewave has an amplitude $A = 5^\circ$ and a period $T = 10$ s, as shown in Figure 5.2. The vehicle is equipped with four in-wheel motors and drives on a well-paved road ($\mu = 1$) at an initial speed $v_0 = 30$ km/h with throttle = 40%.

Figure 5.3 shows the vehicle states for the three different cases mentioned in Section 5.1. Considering that the peak steering angle is 5° and that the speed increases beyond 60 km/h, this is a quite aggressive maneuver. The vehicle without any TVC completely loses stability in the second part of the sinewave, as β and r increase exponentially. The other two cases are really similar, with the “TVC on” case anticipating and slightly reducing the yaw rate oscillations in the most severe part. Figure 5.4 presents the state errors with respect to the reference, and the vehicle trajectory. From the first plot, the TVC does not manage to keep a low vehicle side slip angle error in the second part, but it eventually manages to bring it back to an almost null value. The second plot shows the yaw rate error, which has an undesired ripple of about 20 % of the yaw rate value in both TVC cases. However, the proposed controller mitigates the effect since the oscillations have lower amplitudes. A possible explanation has been found in the aggressiveness of the maneuver; the controller has to be extremely active to keep the vehicle close to the reference case. Eventually, the third plot shows the resulting vehicle trajectory. The same oscillations are also present

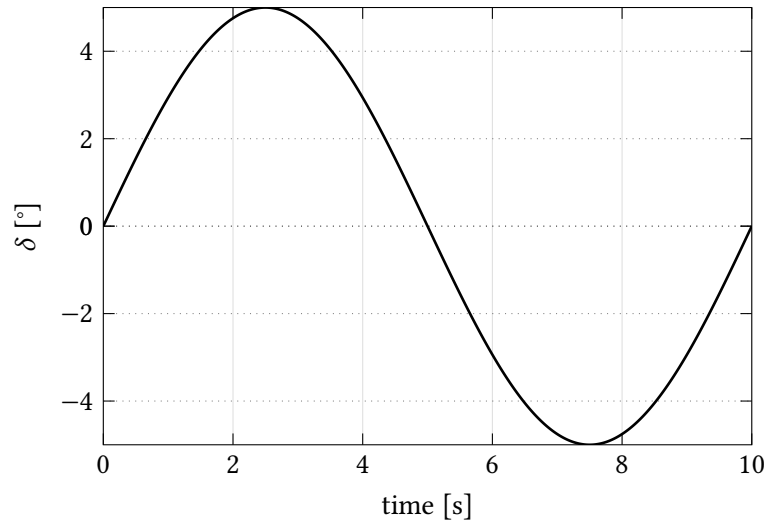


FIGURE 5.2: Sinusoidal steering angle input of amplitude $A = 5^\circ$ and period $T = 10$ s

in Figure 5.5 regarding the vehicle state derivatives. In particular, the third plot presents the yaw acceleration: its predicted value matches well with the actual ones for both vehicles with TVC in the first 8 s of simulation; after that, the actual yaw acceleration oscillates around the predicted value.

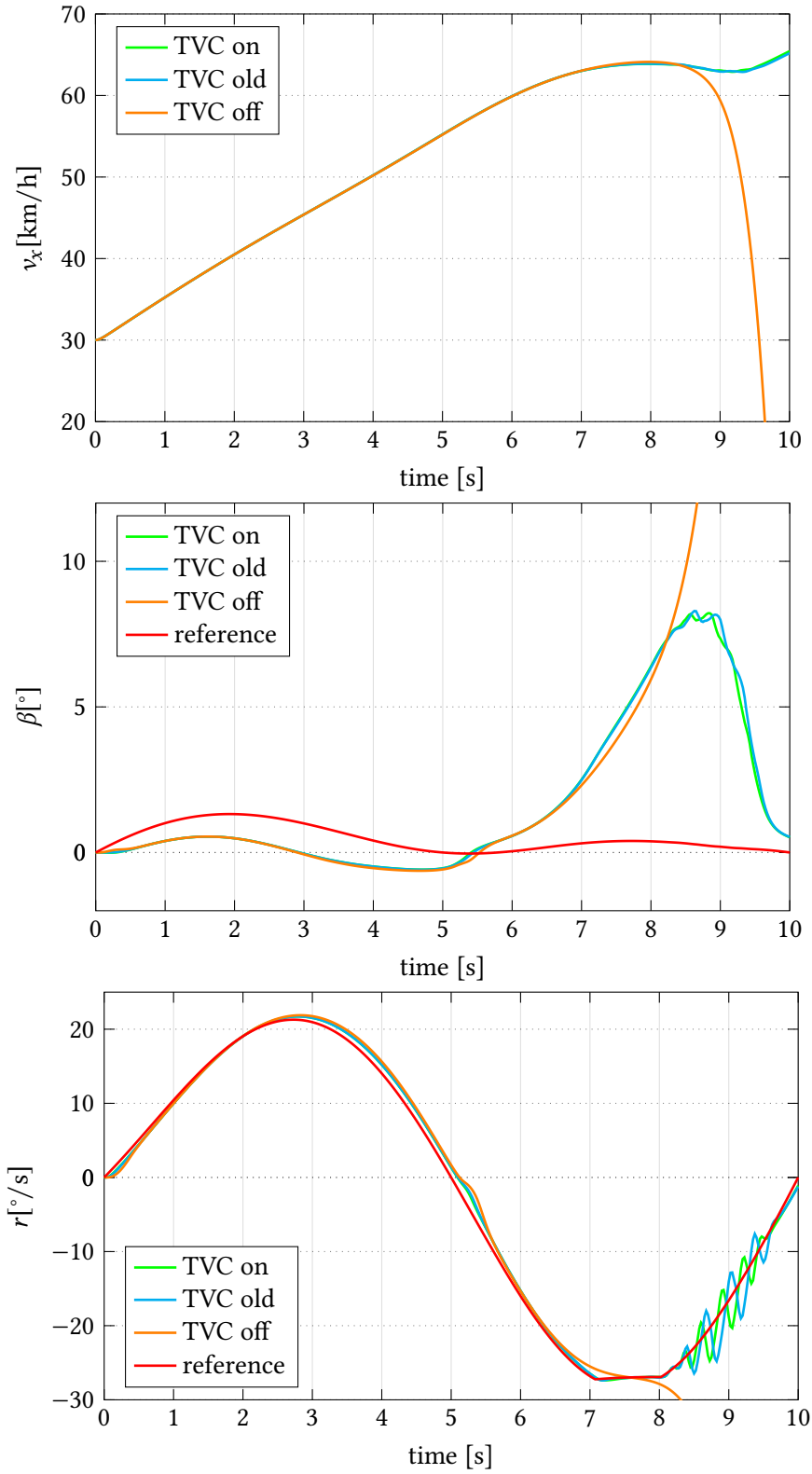


FIGURE 5.3: Sinusoidal steering angle input - Vehicle states for the three different cases: the uncontrolled vehicle is clearly unstable, while the proposed controller slightly reduces the yaw rate oscillations in the last part

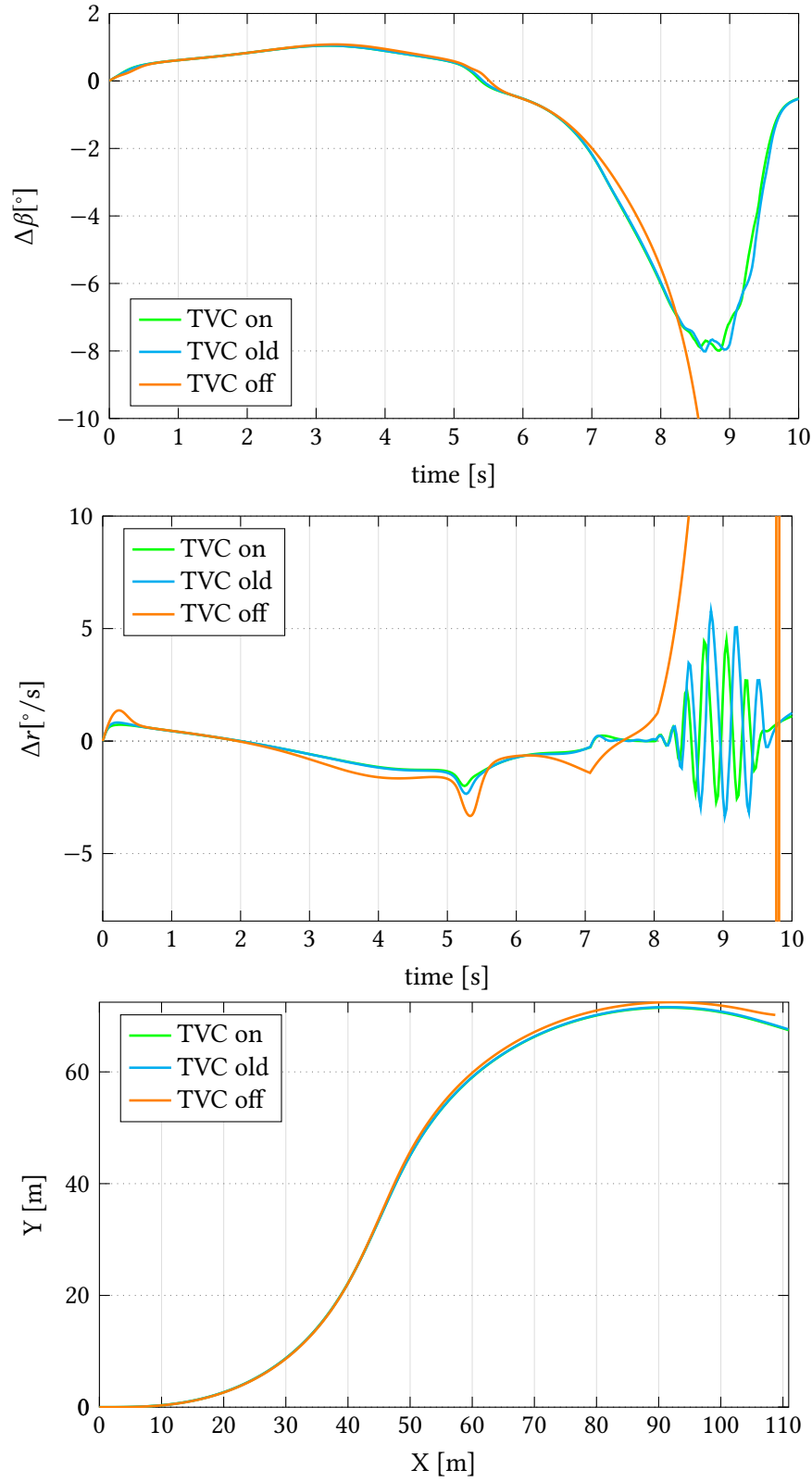


FIGURE 5.4: Sinusoidal steering angle input - Vehicle state errors and trajectory for the three different cases: quite large side slip angle error and yaw rate error ripple are due to the aggressiveness of the maneuver; the proposed controller mitigates the yaw rate error oscillations

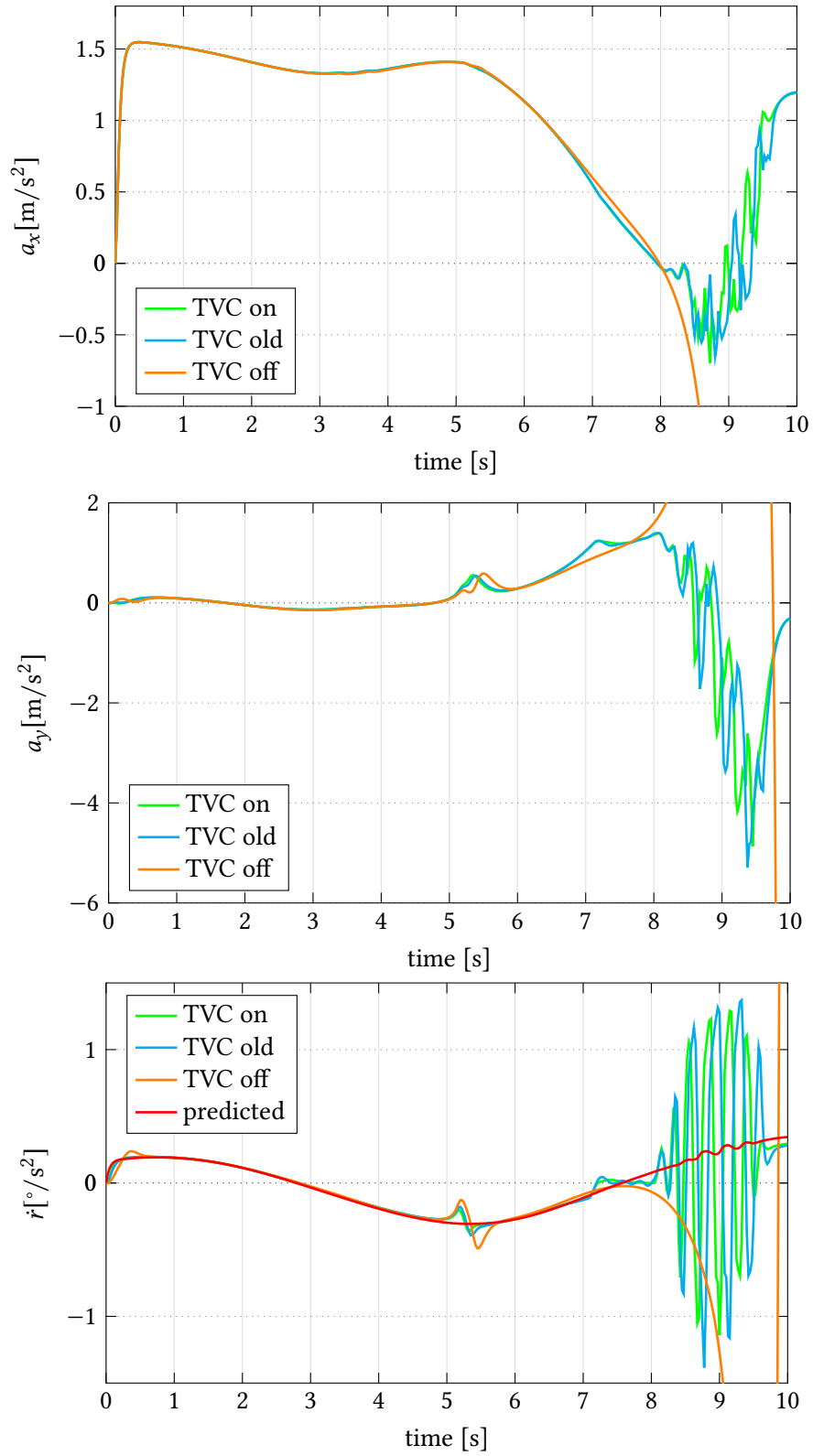


FIGURE 5.5: Sinusoidal steering angle input - Vehicle states derivatives for the three different cases: oscillations are clearly visible at the end of the maneuver; the yaw acceleration swings around the predicted value

Table 5.1 reports the norm-2 of vehicle side slip angle error and yaw rate error. The vehicle endowed with the proposed TVC manages to reduce the overall yaw rate error magnitude and also the β error to a smaller extent. The vehicle without controller does not manage to pass the test because its states are far beyond the stability region.

TABLE 5.1: Sinusoidal steering angle input - Results: the proposed controller significantly reduces the yaw rate error magnitude

TVC	$\ \Delta\beta\ _2$ [rad]	$\ \Delta r\ _2$ [rad/s]	Result
on	2.3762	0.8117	pass
old	2.4029	0.9641	pass
off	17.9368	44.7138	fail

5.3 ISO Double Lane-Change Maneuver

The Double Lane-Change Maneuver is a standardized procedure to subjectively assess road-holding ability of passenger cars and light commercial vehicles up to a gross vehicle mass of 3.5 t. The ISO 3888 standard specifies the dimensions of the test track that is divided in six sections. Their lengths are fixed while their widths are a function of vehicle width (without considering rear view mirrors) [59]. Although the standard provides the track bounds, there is no indication of the reference trajectory, whose knowledge is needed by the driver model for the computation of the steering angle. A combination of two symmetrical Bezier curves and a straight line are used for this purpose in Korzeniowski and Ślaski[60]. Here, a different approach has been used, considering MATLAB interpolation functions: *spline*, which performs a cubic spline interpolation; *makima*, which is the modified Akima piecewise cubic Hermite interpolation; *pchip*, which is the acronym of Piecewise Cubic Hermite Interpolating Polynomial. The common base among the three is that they can use values y at sample points x to find interpolated values at the query points. Besides, they can also return a piecewise polynomial structure. Remembering that the driver model discussed in Section 3.4 needs curvature values, the MATLAB command *fnder* is used to return another piecewise polynomial representing the second-order derivative of the piecewise polynomial linked to the reference trajectory. At this point, *ppval* is used to evaluate the second-order derivative piecewise polynomial at the query points, giving exactly the curvature. Although the above-mentioned approach could be used for all three interpolation functions, the resulting curves differ quite substantially, as shown in Figure 5.6. The reference points (x, y) are chosen at the extremity of the centre line of each track section defined by ISO 3888. It is clearly visible that *makima* and *spline* are not suitable because of their wavy behaviour that would cause undesired steering angle even when the vehicle should go straight. Besides, the curvatures for the three different functions are shown in Figure 5.7. Although larger curvature changes are present with *pchip*, this is the only solution that allows a reasonable reference trajectory and for this reason it is the implemented one.

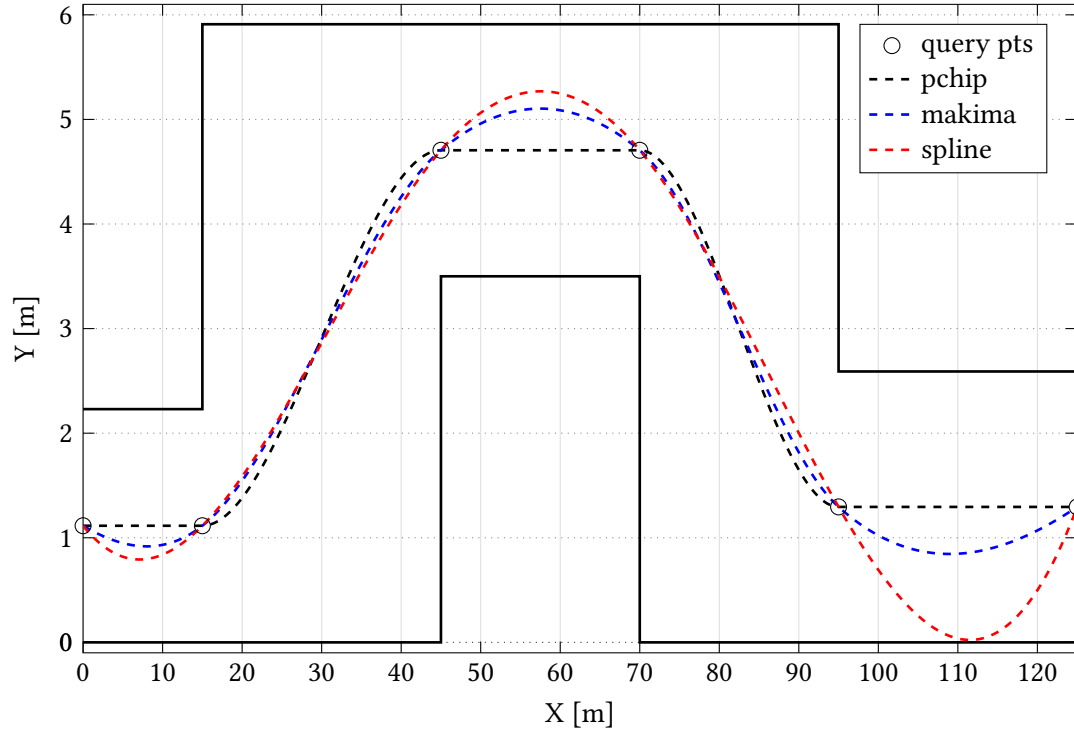


FIGURE 5.6: Double Lane-Change possible reference trajectories: the wavy behaviour of *makima* and *spline* would cause undesired steering angle when the vehicle should go straight

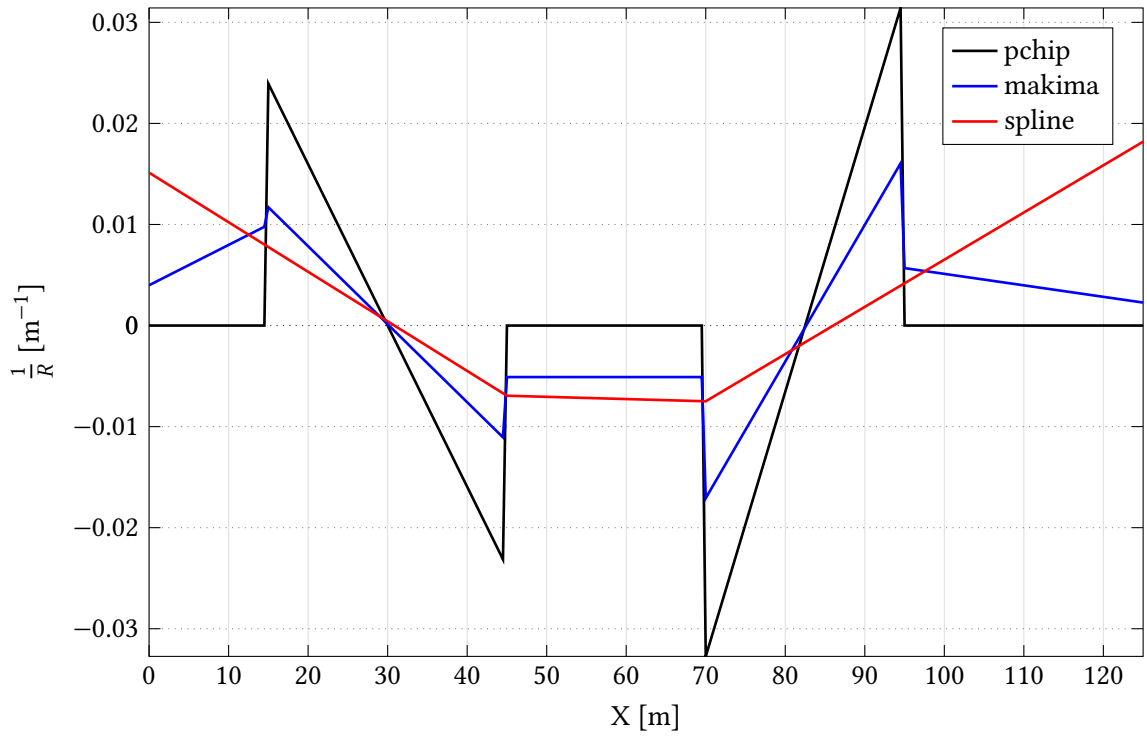


FIGURE 5.7: Double Lane-Change possible reference curvatures: *pchip* features the largest curvature changes

5.3.1 Double Lane-Change when coasting

A first set of Double Lane-Change tests is conducted to understand the maximum initial allowable speed at which the 4IWM EV with the proposed TVC passes the test when coasting down on a well-paved road ($\mu = 1$). After a trial-and-error procedure, the maximum speed is found to be 84.1 km/h. At this point, the test is repeated for the other two controller cases and also for the two 2IWM configurations, always considering the same speed. Figure 5.8 reports the vehicles trajectories and shows that the 4IWM vehicle endowed with the proposed controller is the only one passing the test at that speed together with the uncontrolled vehicle, while the old controller does not manage to keep the vehicle within the bounds of the second lane change. Surprisingly, the uncontrolled vehicle passes the test but its speed is significantly lower, as it will be discussed in the next paragraph, and thus a fair comparison cannot be done. The 2IWM front and rear cases fail also in the first lane change, with the latter configuration resulting the worse one. The two-central-motors architecture has not been considered here because the TVC does not work in this case and thus the vehicle behaves exactly the same as the uncontrolled one. As expected, the test bottleneck has been the second lane change since the longitudinal space allowed to complete that maneuver is shorter than the first one. Given the vehicle width of 1.8 m, it is worthwhile to specify that the centre of gravity bounds are the limits within which the vehicle CG has to stay in order to let the external sizes stay within the track limits.

Figures 5.9 – 5.14 exhibit vehicle variables of the the 4IWM configuration for the three different controller cases. Figure 5.9 shows the steering angle from the driver model: in all cases the trend is very similar except for the last steering correction, where the vehicle without controller needs much more steering angle. Vehicle states are reported in Figure 5.10. A first important observation is that the vehicle with TVC deactivated carries a lower speed throughout the maneuver since its side slip angle and yaw rate values are larger, thus enhancing drift. Secondly, r values are closer to the reference than β because the sliding mode parameter ρ of the TVC is more yaw rate-oriented, as reported in Table 4.2. The reference yaw rate has saturation regions due to stability constraints imposed by Equation 4.14. Besides, the proposed TVC with yaw acceleration feedback allows the reduction of yaw rate lag with respect to the old controller. The small velocity difference (less than 0.5 km/h) between the “TVC on” and “old” cases does not taint the improvements brought by the new controller. The same considerations can be done for the first two plots in Figure 5.11, showing the vehicle state errors. The third plot represents the corrective yaw moment, which is the TVC control output. Since the maneuver is very aggressive and the vehicle drives at its limit, the controller has to be extremely active in order to keep the vehicle close to the reference behaviour. Figure 5.12 reports states derivatives. The longitudinal acceleration has some oscillatory behaviour due to the torque distribution strategy that favours the yaw moment correction rather than longitudinal forces, as pointed out in Figures 4.13 and 4.14. The lateral acceleration reaches an impressive 1g peak for both controlled vehicles and even almost 1.5g for the uncontrolled one (the two left wheels are almost lifting from the ground and an extra large vertical load is transferred on the right side). Eventually, the third plot shows the yaw acceleration values, which are very

close to the reference one. The wheel torques are reported in Figure 5.13. The small changes in distributed torque between the “on” and the “old” controller cases do make the difference in the vehicle trajectory and state errors. Clearly, no torque is allocated for the uncontrolled vehicle. Eventually, Figure 5.14 shows the tire vertical loads. The oscillations are due to heavy longitudinal and lateral load transfers, which are more pronounced for the uncontrolled vehicle.

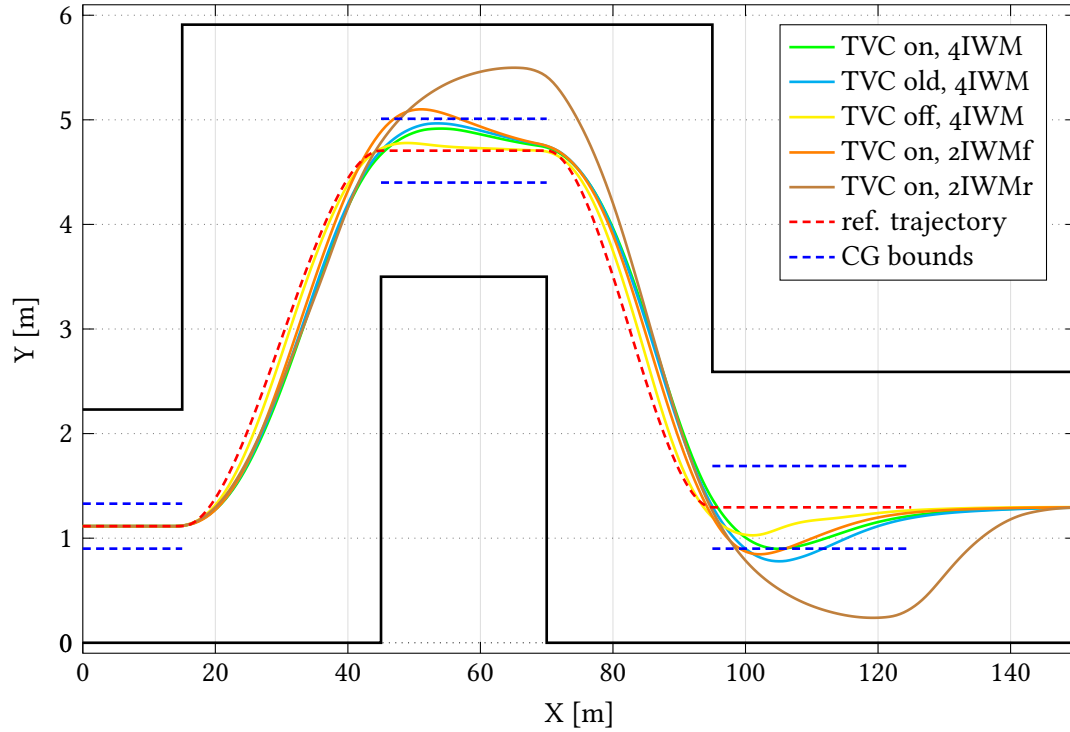


FIGURE 5.8: Double Lane-Change at $v_{x0} = 84.1$ km/h - Trajectory for the three different cases and the three different BEV configurations: the proposed controller makes the vehicle passing the test, while in the other cases the vehicles fail; the uncontrolled vehicle passes the test but carrying a lower speed, thus a fair comparison cannot be done

Figures 5.15 and 5.16 want to compare the vehicle states and yaw moment correction among the three different BEV configurations featuring the new TVC. Looking at the first plot of Figure 5.15, it is clear that the 2IWM front configuration carries a lower speed throughout the maneuver with respect to the 4IWM one (nearly 2 km/h difference). This aspect, together with the natural understeering behaviour of a front wheel drive vehicle, reflects in lower side slip angle and yaw rate, and in turn in lower state errors too. The 2IWM rear configuration has a strange behaviour ascribable to the intrinsic oversteering nature typical of rear wheel drive vehicles. Large β values and controller parameters tuned for the 4IWM configuration badly reflects the TVC effectiveness for this architecture. Same considerations can be done for the first two plots in Figure 5.16, reporting the state errors. The third plot shows the corrective yaw moment trend, with the 2IWM front resulting to have the overall lowest control action and the 2IWM rear the highest one.

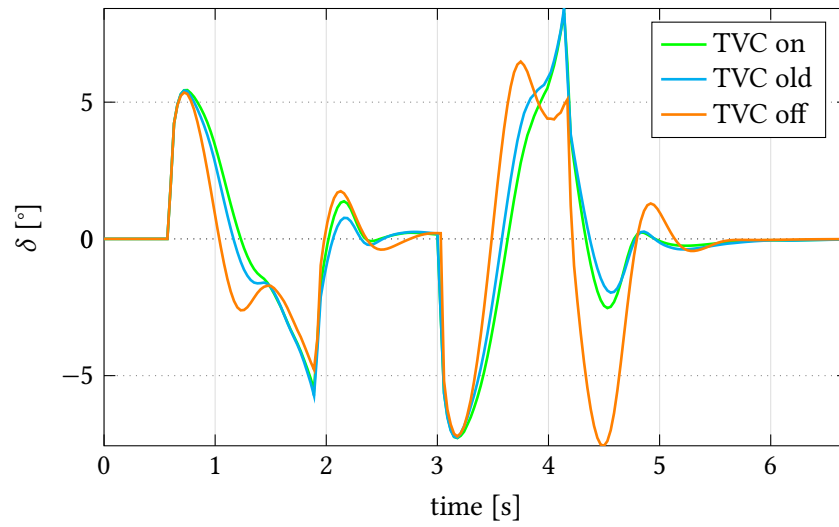


FIGURE 5.9: Double Lane-Change at $v_{x0} = 84.1$ km/h - Steering angle for the three different cases: very similar trends except for the last steering correction, where the uncontrolled vehicle needs much more steering angle

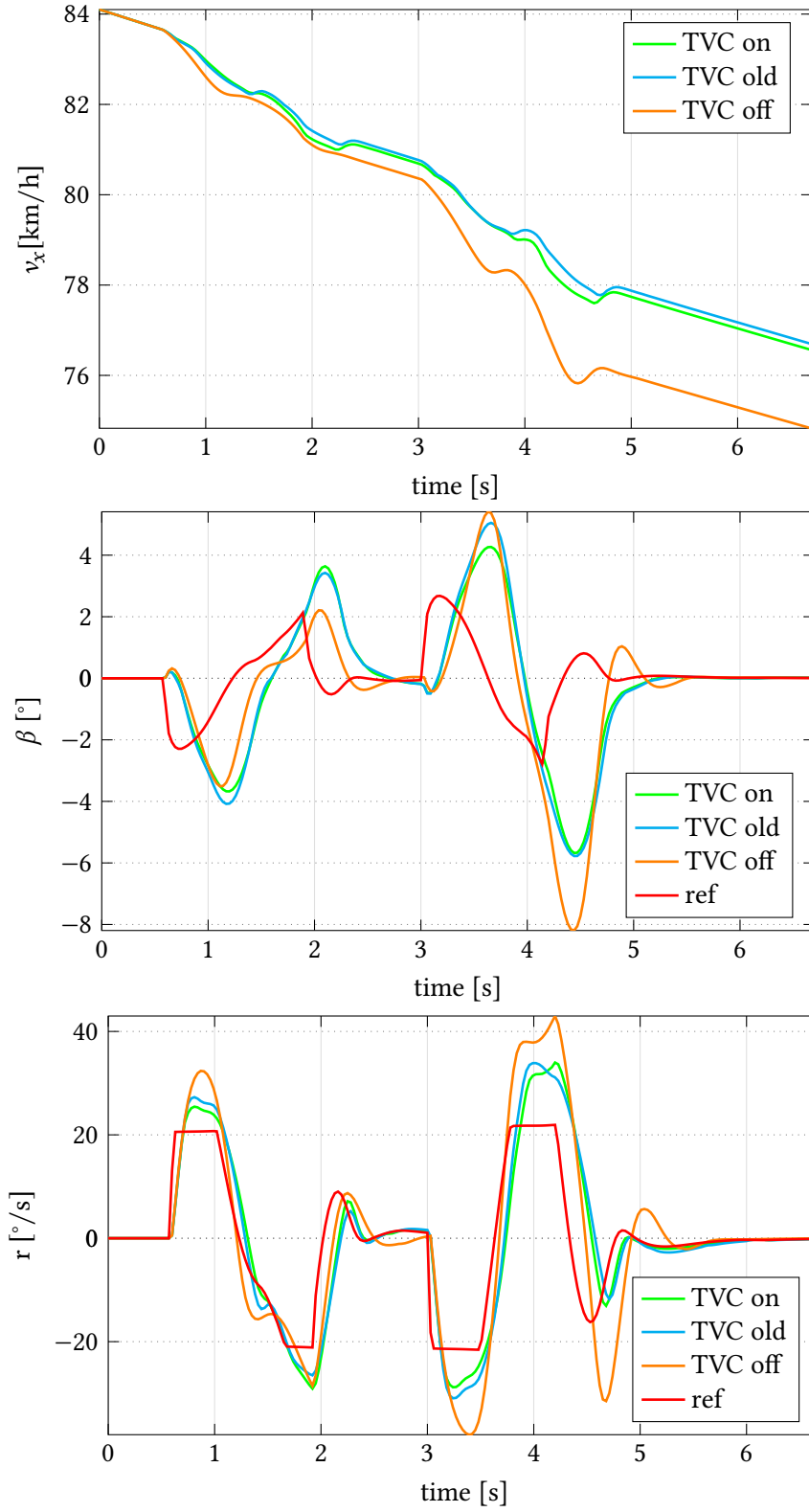


FIGURE 5.10: Double Lane-Change at $v_{x0} = 84.1$ km/h - Vehicle states for the three different cases: the uncontrolled vehicle carries a lower speed because of large β and r values; the proposed controller reduces the yaw rate lag with respect to the old controller

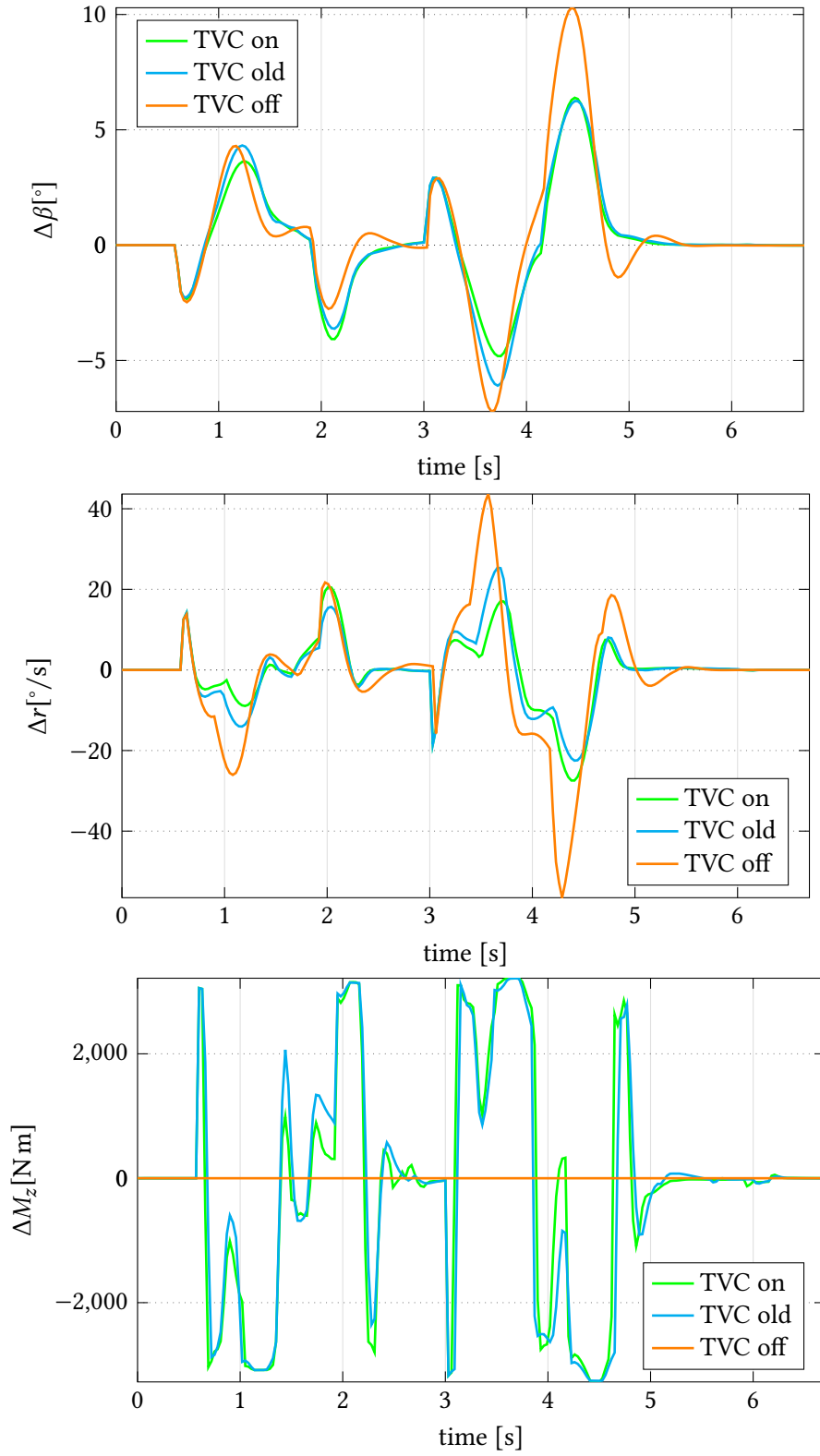


FIGURE 5.11: Double Lane-Change at $v_{x0} = 84.1 \text{ km/h}$ - Vehicle state errors and corrective yaw moment for the three different cases: the controller has to be extremely active to keep the vehicle close to the reference behaviour

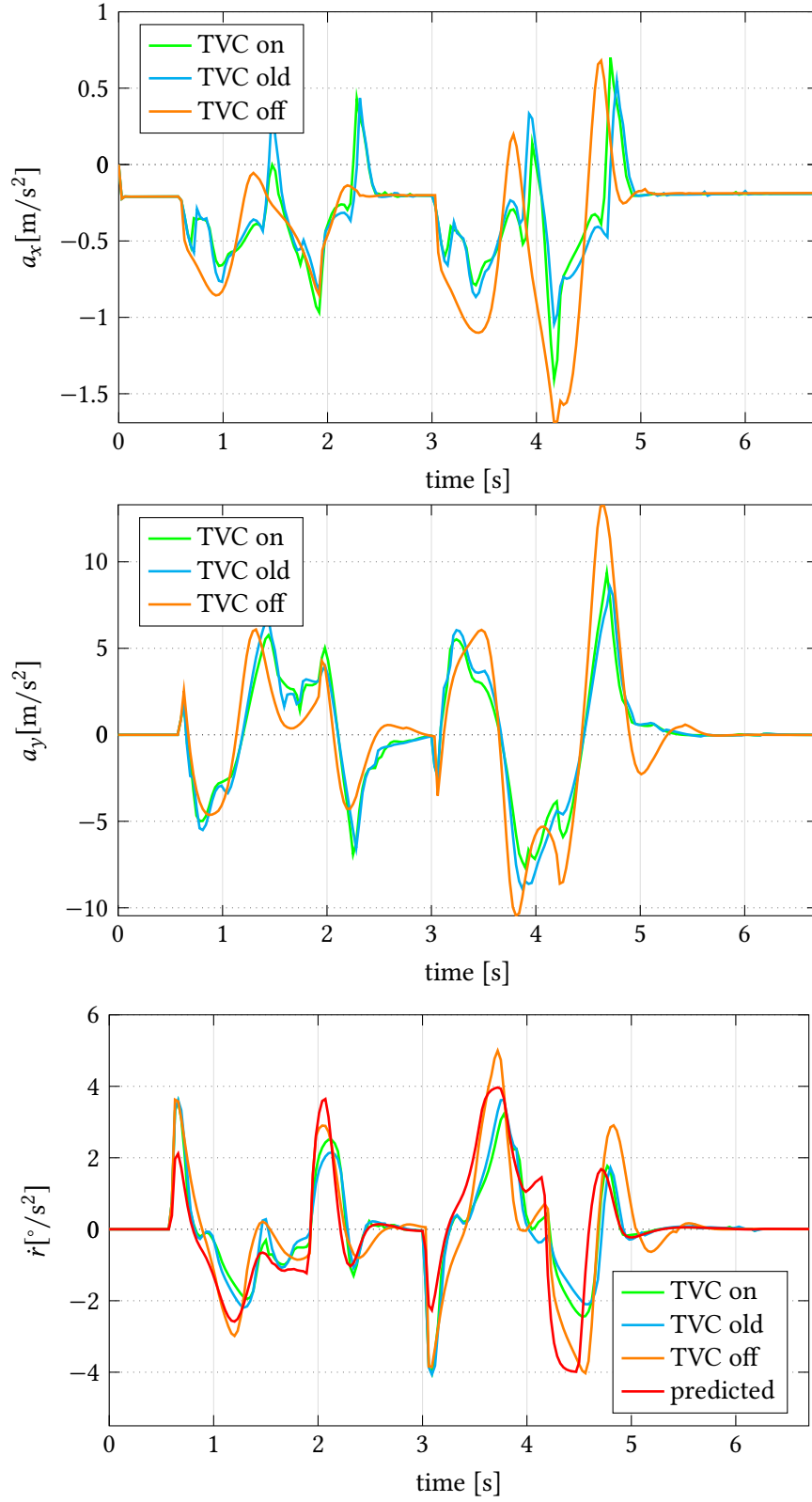


FIGURE 5.12: Double Lane-Change at $v_{x0} = 84.1$ km/h - Vehicle state derivatives for the three different cases: a_x has some oscillatory behaviour due to the torque distribution strategy; a_y reaches 1g peak for both controlled vehicles; \dot{r} values are very close to the predicted ones

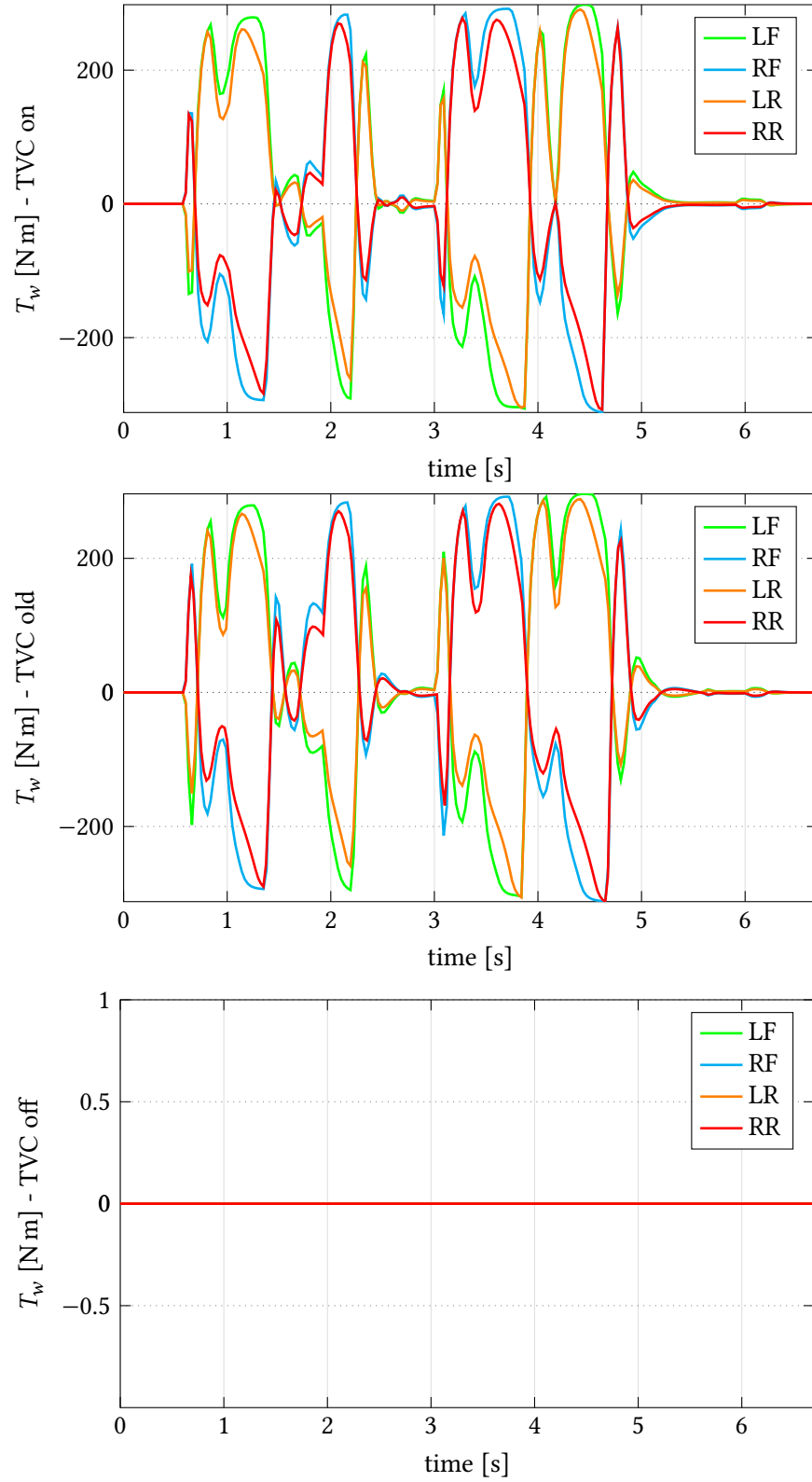


FIGURE 5.13: Double Lane-Change at $v_{x0} = 84.1$ km/h - Torque at the wheels for the three different cases: the small changes between the two controlled vehicles make the difference; clearly no torque is allocated for the uncontrolled vehicle

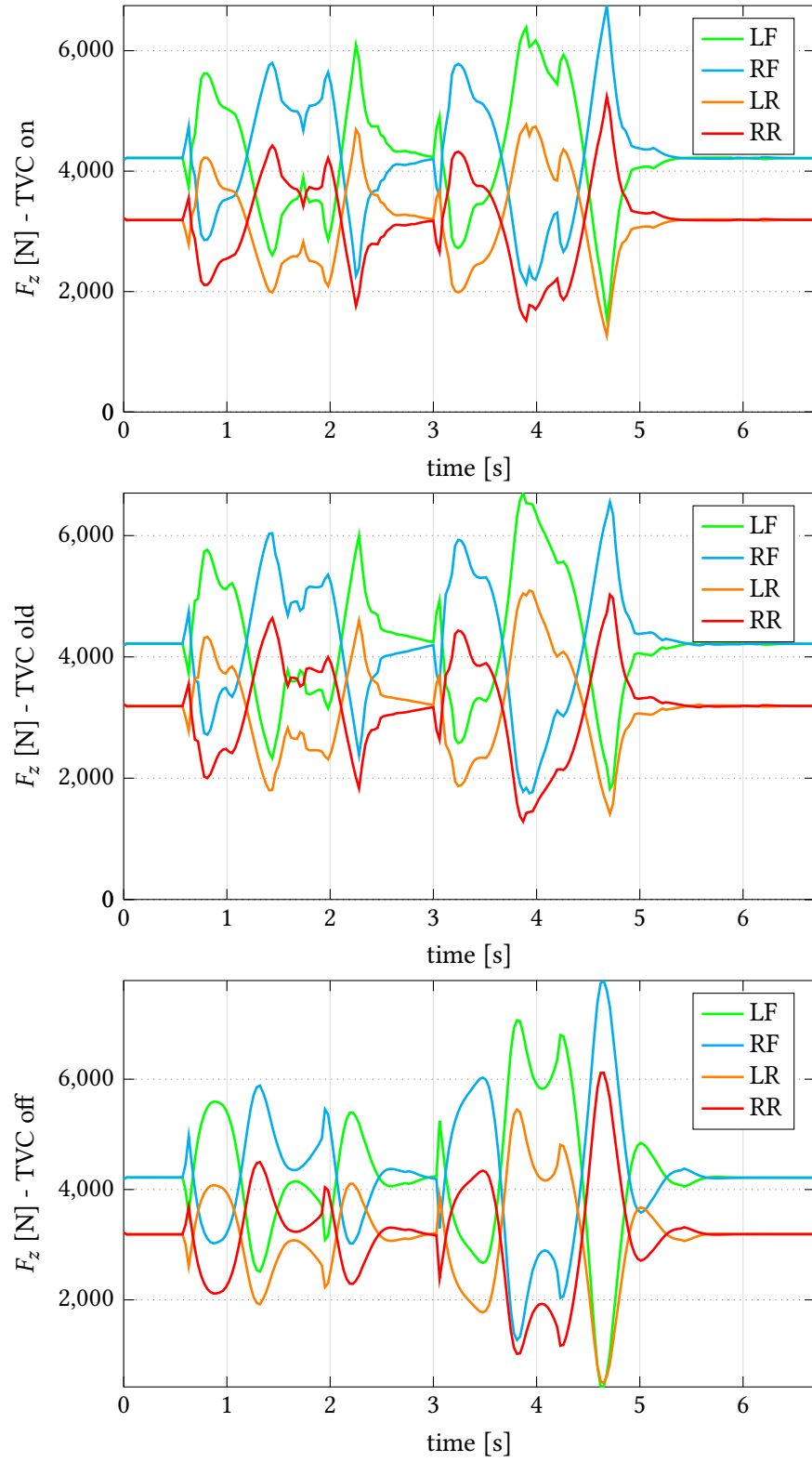


FIGURE 5.14: Double Lane-Change at $v_{x0} = 84.1$ km/h - Vertical loads at the wheels for the three different cases: the oscillations are due to heavy longitudinal and lateral load transfers

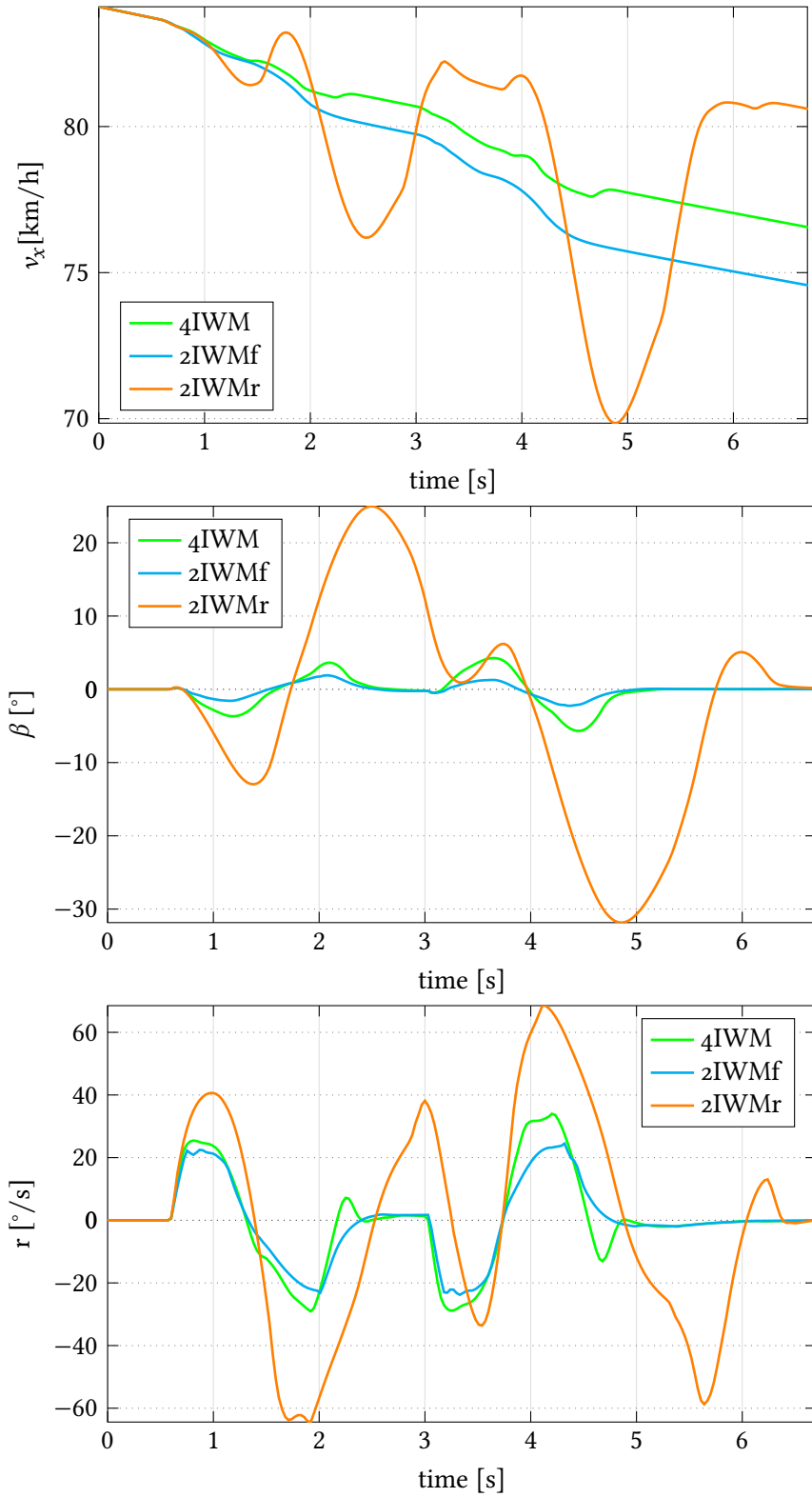


FIGURE 5.15: Double Lane-Change at $v_{x0} = 84.1$ km/h - Vehicle states for the three different EV configurations: the 2IWM front axle configuration has low β and r values because of the lower v_x ; the 2IWM rear axle configuration features the typical oversteering behaviour

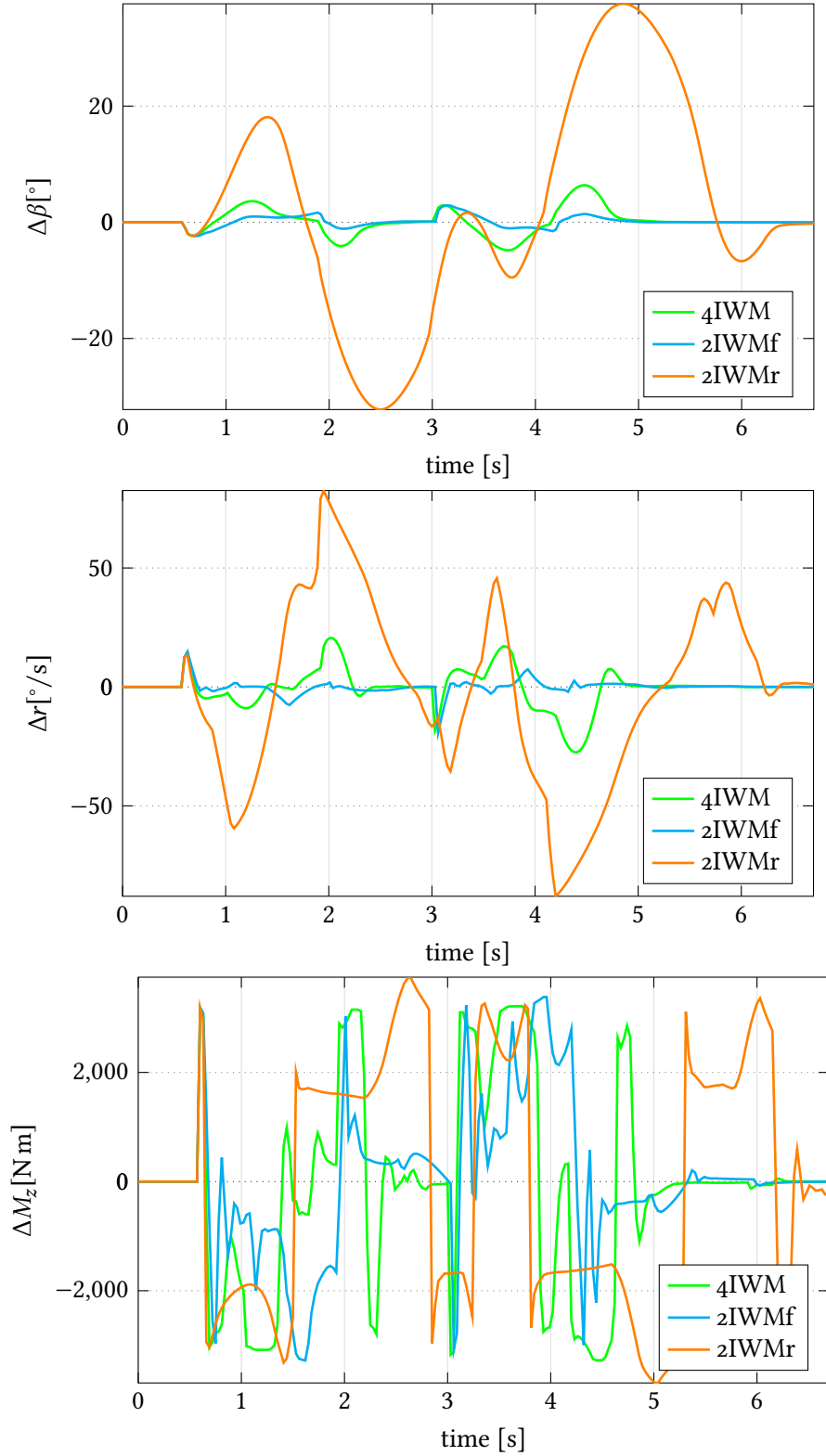


FIGURE 5.16: Double Lane-Change at $v_{x0} = 84.1$ km/h - Vehicle state errors and corrective yaw moment for three different EV configurations: the 2IWM front axle configuration has the lowest control action, followed by the 4IWM case and the 2IWM rear axle one

Table 5.2 presents the norm-2 values of vehicle side slip angle, yaw rate, cross track error and heading error resulting from the Double Lane-Change maneuver performed at 84.1 km/h. First, the proposed control strategy allows the overall minimization of vehicle side slip angle and yaw rate for the 4IWM architecture. The controller is quite effective for the 2IWM front configuration, even though the vehicle fails the test. However, its numbers in terms of β and r may be misleading: the lower magnitudes with respect to the 4IWM vehicle are simply because in the latter case the speed throughout the test is considerably higher. Furthermore, the 2IWM rear drive with the developed controller fails the test because two wheels lift from the ground. Eventually, a trial-and-error procedure is conducted to find the maximum speed at which the vehicle with the old controller is capable of passing the test. The result is a speed of 81.7 km/h, which is 2.4 km/h lower than that with the updated controller.

TABLE 5.2: Double Lane-Change at $v_{x0} = 84.1$ km/h - Results: the proposed controller minimizes side slip angle and yaw rate magnitudes for the 4IWM architecture

	$\ \beta\ _2$ [rad]	$\ r\ _2$ [rad/s]	$\ e_{ct}\ _2$ [m]	$\ e_h\ _2$ [rad]	note
TVC on, 4IWM	1.3256	9.4854	8.4394	1.2282	pass at 84.1 km/h
TVC old, 4IWM	1.4371	9.7589	8.6899	1.3093	pass at 81.7 km/h
TVC off, 4IWM	1.5002	11.6745	2.8452	1.4102	lower speed
TVC on, 2IWMf	0.5465	7.6012	8.3974	1.1341	fail
TVC on, 2IWMr	9.3565	21.6085	12.446	8.9358	2 wheels lift-off

5.3.2 Double Lane-Change at constant speed

A second set of Double Lane-Change tests is conducted at constant speed to verify both the Torque Vectoring Controller and the Cruise Control behaviour for the 4IWM BEV on a $\mu = 1$ road. After a trial-and-error procedure, a velocity of 79.4 km/h is selected, as it is the maximum allowable speed at which the vehicle with the new TVC can pass the test. Given this reference, the tests are repeated for the vehicle with the old controller and for the uncontrolled one, and also for the two-central-motors configuration. Figure 5.17 plots the four different trajectories: just like the Double Lane-Change when coasting, the new controller is the only one allowing the vehicle to fairly pass the test at that speed, while the vehicle with the old controller fails by few cm only. By contrast, the 4IWM EV without TVC and the 2CM EV do not pass the test because two wheels lift from the ground (see Figure 5.21 for the 4IWM case) and it is not clear whether the vehicle overturns or not. For this reason, from that point on the results cannot be trusted and the trajectory plot is interrupted. The steering angle trends are reported in Figure 5.18.

Figure 5.19 plots the three vehicle states. The first graph shows the velocity trend and highlights the merit of the cruise control, which is able to keep the velocity really close to the target even though severe lateral dynamics is involved. The uncontrolled vehicle loses stability and there is nothing the cruise control can do. The same applies for the two-central-motors configuration,

which can be considered as an uncontrolled vehicle too: the central motors do not allow torque vectoring, and the only adjustment that the controller can do is the torque split from cruise control in the torque distribution strategy. For sake of shortness, from now on the 4IWM with TVC off and the 2CM with TVC on will be both referred as “uncontrolled” vehicles. Side slip angle and yaw rate for the two controlled vehicles are not far from the reference, with the yaw rate being closer. State errors are reported in Figure 5.20: the uncontrolled vehicles are clearly unstable, as vehicle side slip angle error almost reaches 30° ; the two controlled vehicles have similar error trends, with the old controller even resulting in an overall lower yaw rate error. The corrective yaw moment in the third plot shows a little bit more control action for the new controller. The proposed TVC loses effectiveness a little bit because the longitudinal acceleration linked with the yaw acceleration is close to zero, as shown in the first plot of Figure 5.21. In the second plot, the yaw acceleration values for the controlled vehicles track the prediction well, with just some delay introduced. Lastly, the third plot shows that two wheels of the uncontrolled vehicle lift from the ground, first the right and then the left ones. This is the result of really large side slip angle and yaw rate values, which lead to vehicle instability.

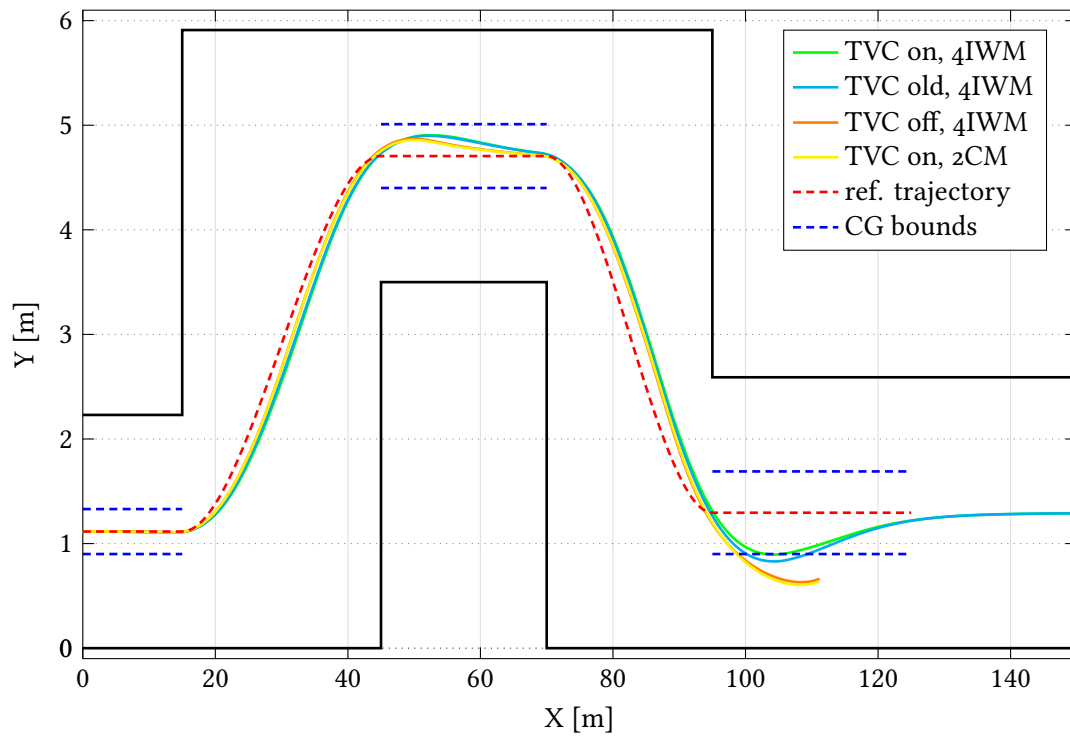


FIGURE 5.17: Double Lane-Change with cruise control at $v_x = 79.4$ km/h - Trajectory for the three different cases and for the central motors configuration: the vehicle with 4IWM and the proposed controller is the only one passing the test; the uncontrolled and the 2CM vehicles do not pass it because two wheels lift from the ground

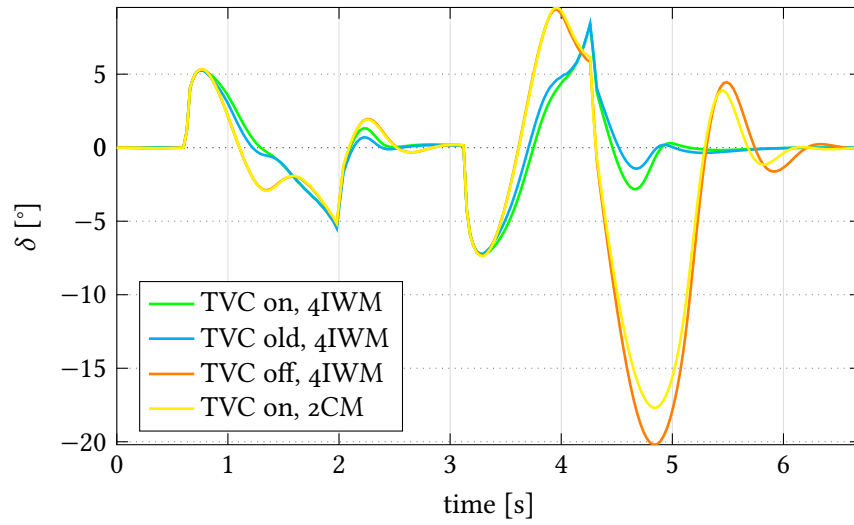


FIGURE 5.18: Double Lane-Change with cruise control at $v_x = 79.4$ km/h - Steering angle for the three different cases and for the central motors configuration

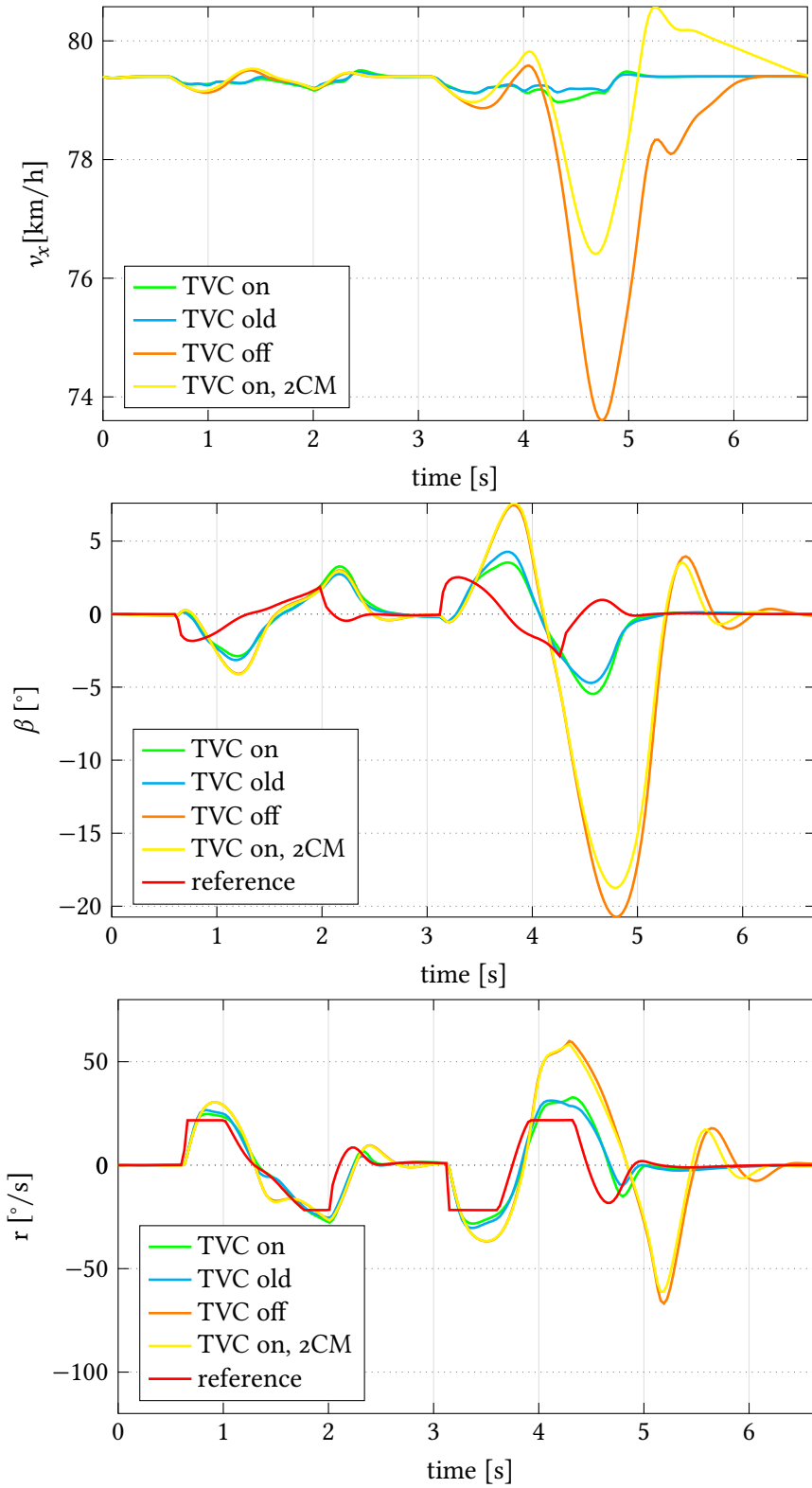


FIGURE 5.19: Double Lane-Change with cruise control at $v_x = 79.4$ km/h - Vehicle states for the three different cases and for the central motors configuration: the uncontrolled 4IWM and the controlled 2CM configurations are clearly unstable; side slip angle and yaw rate are close to the reference for both controlled vehicles

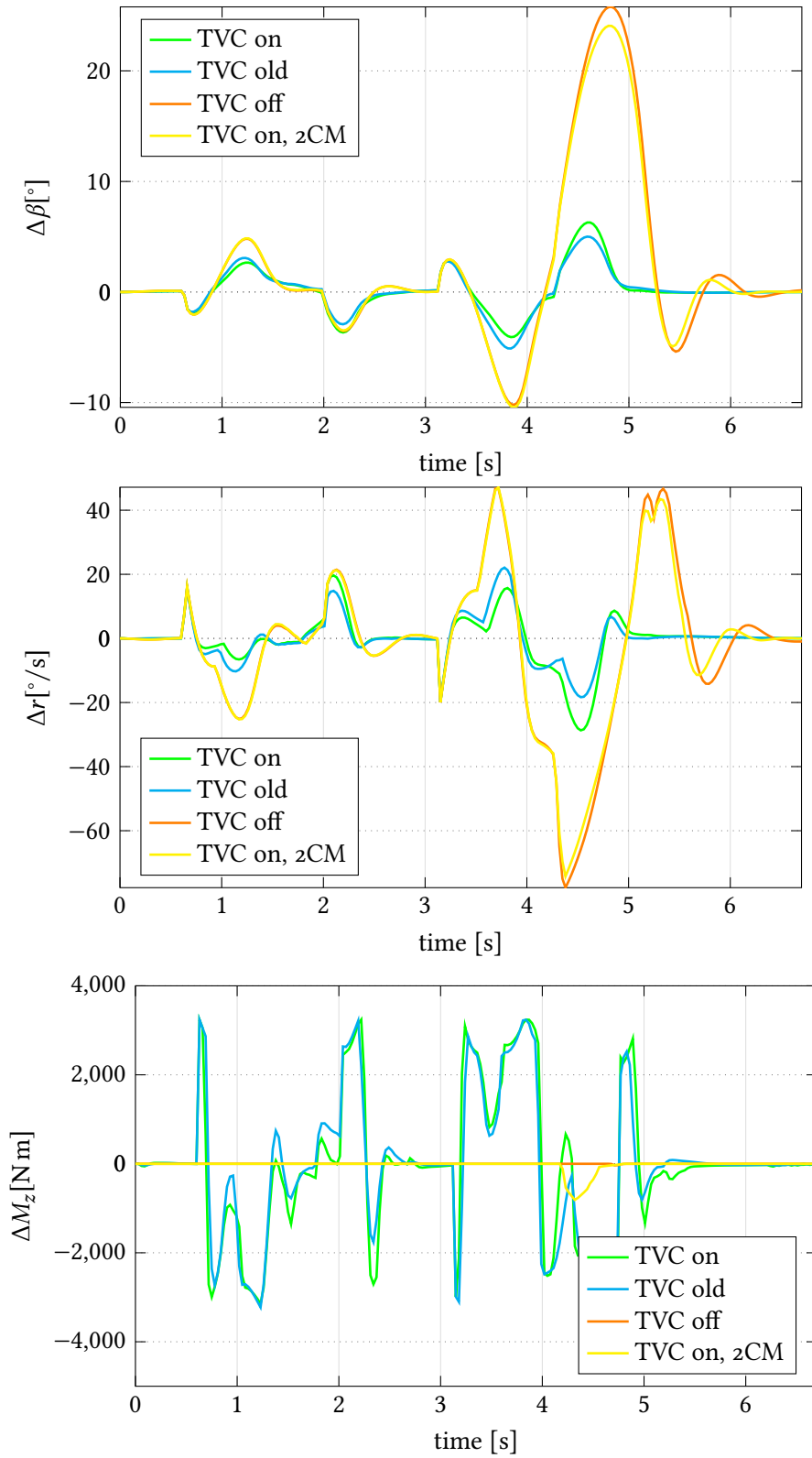


FIGURE 5.20: Double Lane-Change with cruise control at $v_x = 79.4$ km/h - Vehicle state errors and corrective yaw moment for the three different cases and for the central motors configuration: the old controller overall allows an even lower yaw rate error and also features a slightly lower corrective yaw moment with respect to the proposed controller

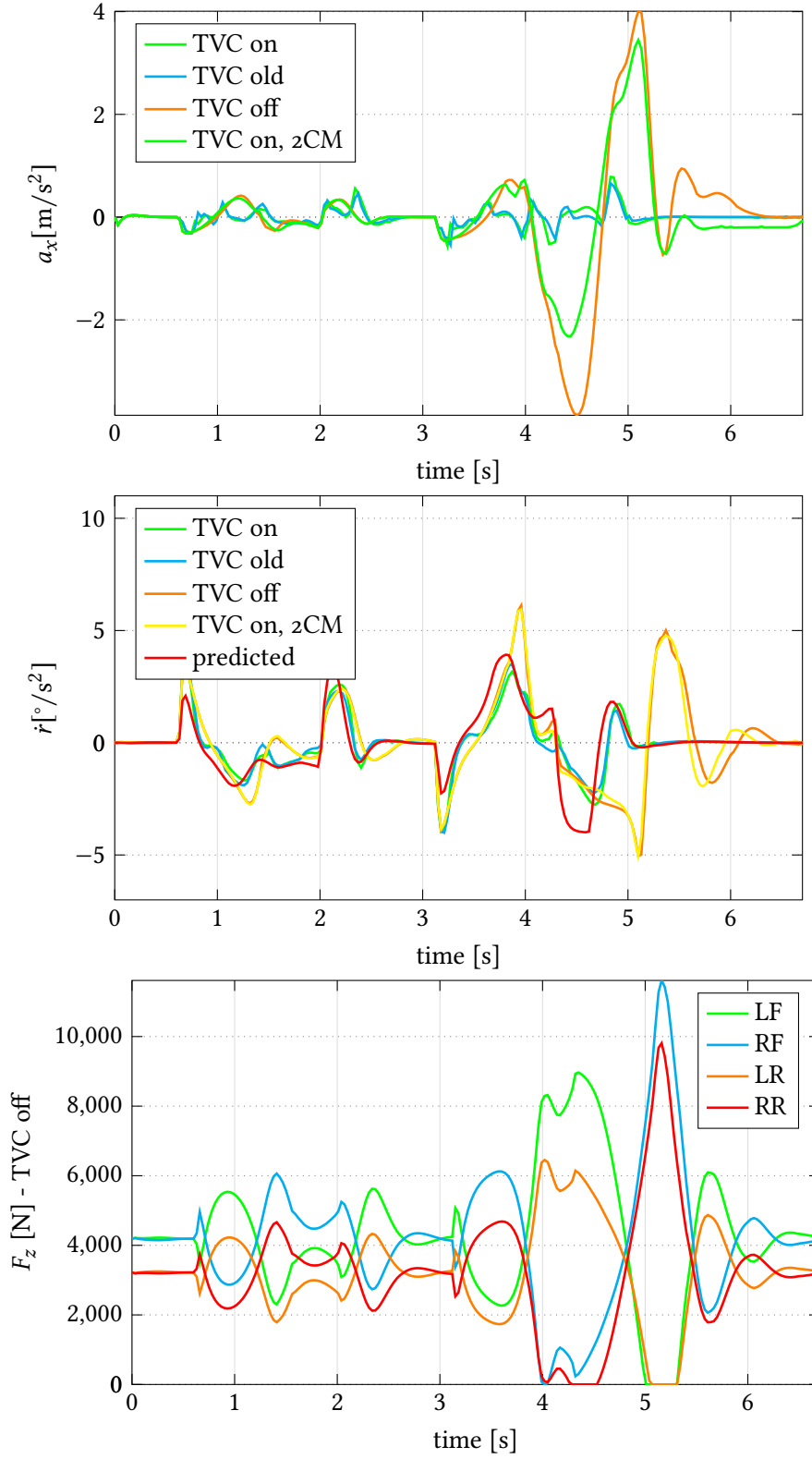


FIGURE 5.21: Double Lane-Change with cruise control at $v_x = 79.4$ km/h - Vehicle states derivatives for the three different cases and tire vertical loads for the uncontrolled vehicle: the longitudinal acceleration is close to zero for both controlled vehicles; the yaw acceleration tracks the predicted value well, with a small delay; the uncontrolled vehicle is unstable since two wheels lift from the ground (first the right and then the left ones)

5.4 Single Lane-Change Maneuver

The Single Lane-Change Maneuver is another well-known test to assess vehicles' handling capabilities. The track specifications are the same as the Double Lane-Change but the distance is of course shorter since the second lane change is not present. In this work, the test is conducted under severe braking conditions to simulate a real-case scenario of obstacle avoidance on the track. The vehicle with the proposed controller is taken as reference to understand the initial limit speed at which the vehicle passes the test. After the usual trial-and-error procedure, the initial speed is set equal to 88 km/h with a braking action of 60% and 50% of regenerative braking (as defined in 4.4.2). Figure 5.22 shows the three vehicles trajectories. Quite surprisingly, the vehicles with the two different controllers behave the same, meaning that the new TVC has lost effectiveness in this condition. The uncontrolled vehicle trajectory is reported in the same graph until the point in which two wheels lift from the ground. Given the unstable condition and the impossibility to determine whether roll-over occurs or not, the test is said to be failed.

Figure 5.23 shows the vehicle states over the entire maneuver. The uncontrolled vehicle is clearly unstable, as β peak values of 32° and r peak values of $75^\circ/\text{s}$ are far beyond stability. The two controlled vehicles have the same trends and just imperceptible differences in terms of values. Longitudinal and yaw acceleration are reported in Figure 5.24. The two controlled vehicles are braking almost constantly, with the small a_x oscillations attributed to the TVC intervention. The yaw acceleration tries to follow the reference but it slightly lags behind it. The explanation for the loss in effectiveness for the proposed controller can be seen in Figure 5.25, where corrective yaw moment, and allocated torque and limit torque for each wheel are plotted for the new TVC on the left and the old TVC on the right. The aggressiveness of the maneuver does require a significant yaw moment, and since the motors are already close to saturation because of the regenerative braking, the electric motor torques are fully exploited by the vehicle equipped with the old controller. The new controller loses effectiveness when the derivative feedback contribution positively adds up to the SMC one, since no more corrective yaw moment can be allocated due to motor saturation. Tire vertical loads for the uncontrolled vehicle are shown in Figure 5.26: first the two left wheels and then the two right ones clearly lift from the ground.

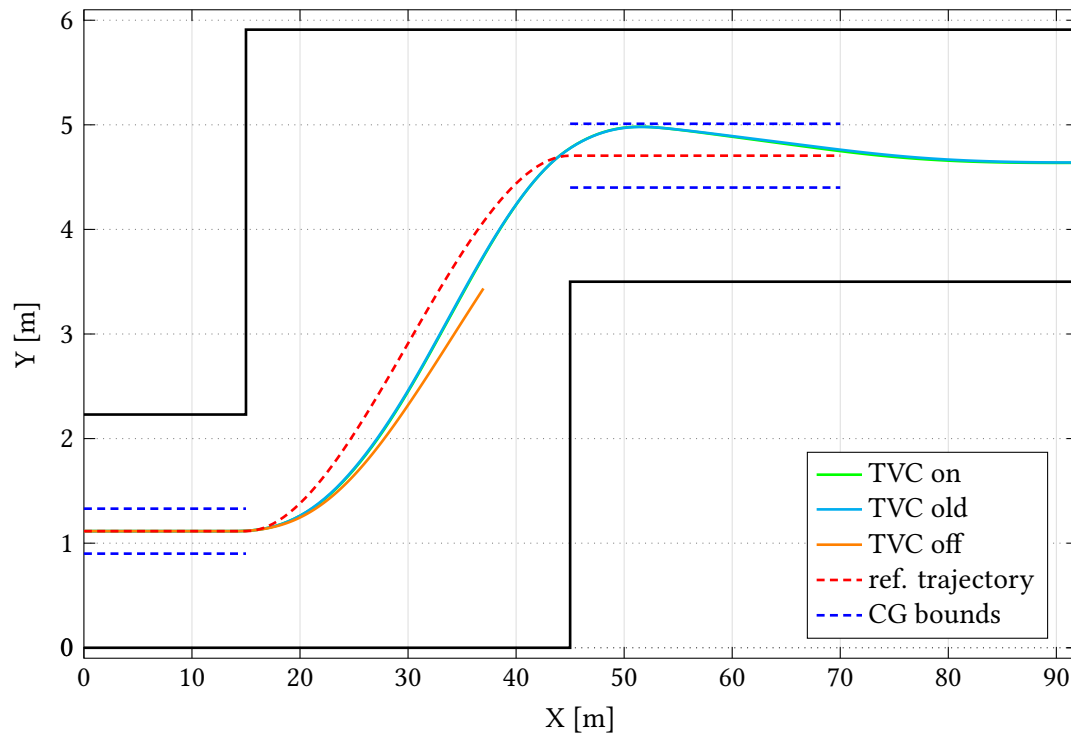


FIGURE 5.22: Single Lane-Change at $v_{x0} = 88$ km/h in braking condition - Trajectory for the three different cases: the proposed TVC loses effectiveness, since the two controlled vehicles behave in the same way; the uncontrolled one fails because two wheels lift from the ground

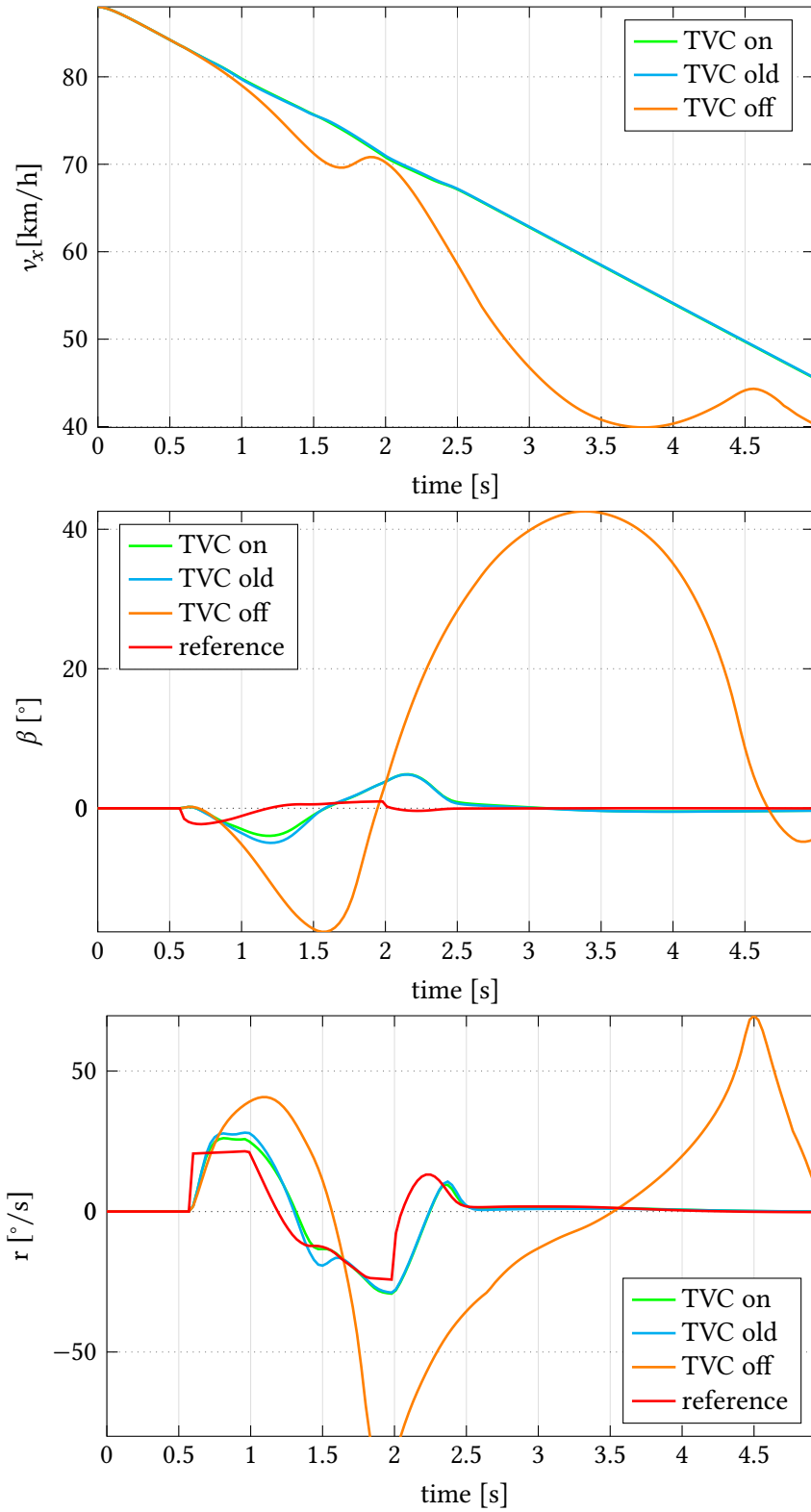


FIGURE 5.23: Single Lane-Change with $v_x = 88$ km/h in braking condition - Vehicle states for three different EV configurations: the two controlled vehicles have the same trends with imperceptible differences; the uncontrolled vehicle is unstable, as β and r peak values are far beyond stability

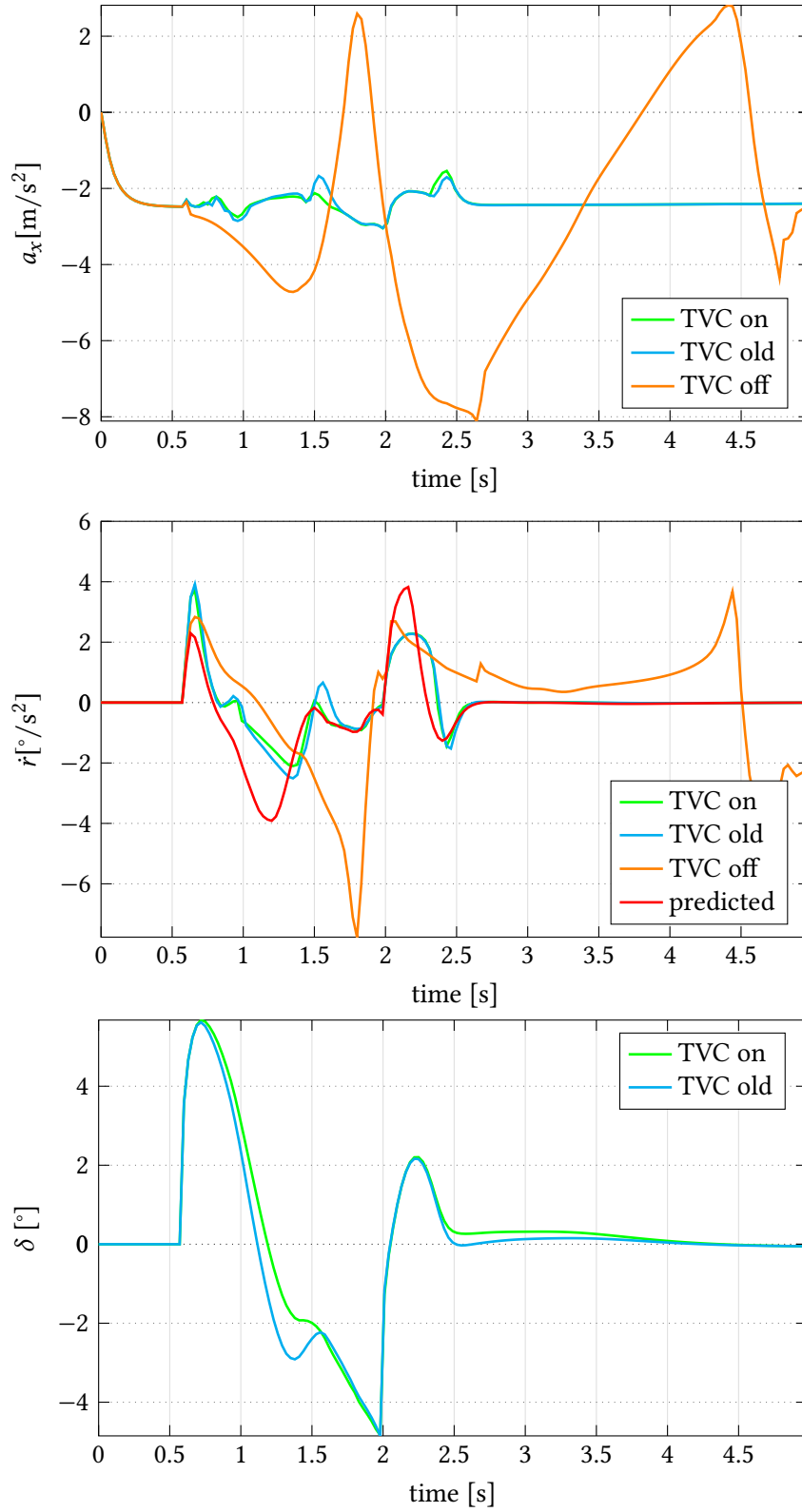


FIGURE 5.24: Single Lane-Change at $v_{x0} = 88 \text{ km/h}$ in braking condition - Yaw rate error, longitudinal acceleration and steering angle for the three different cases: the small oscillations in the longitudinal acceleration of the two controlled vehicles are due to the TVC intervention; the yaw acceleration of the two controlled vehicles lags behind the predicted value but the overall trend is followed well

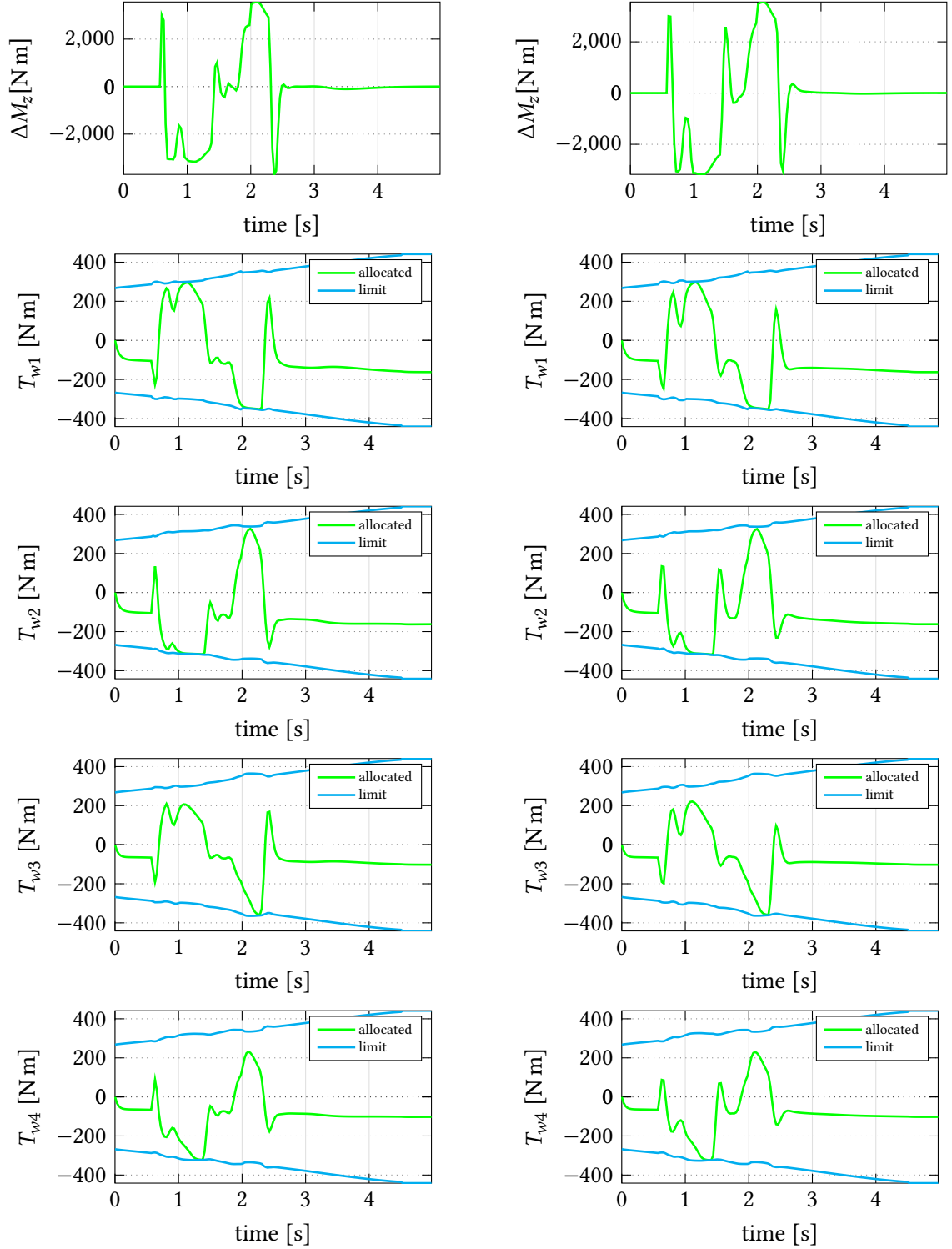


FIGURE 5.25: Single Lane-Change at $v_{x0} = 88$ km/h in braking condition - Corrective yaw moment, and allocated and limit torque for each motor. On the left the vehicle equipped with the proposed controller, on the right the vehicle with the old one. The new controller loses effectiveness when its contribution adds up to the SMC one, since the motors are already at their saturation limits due to the regenerative braking and the significant required yaw moment

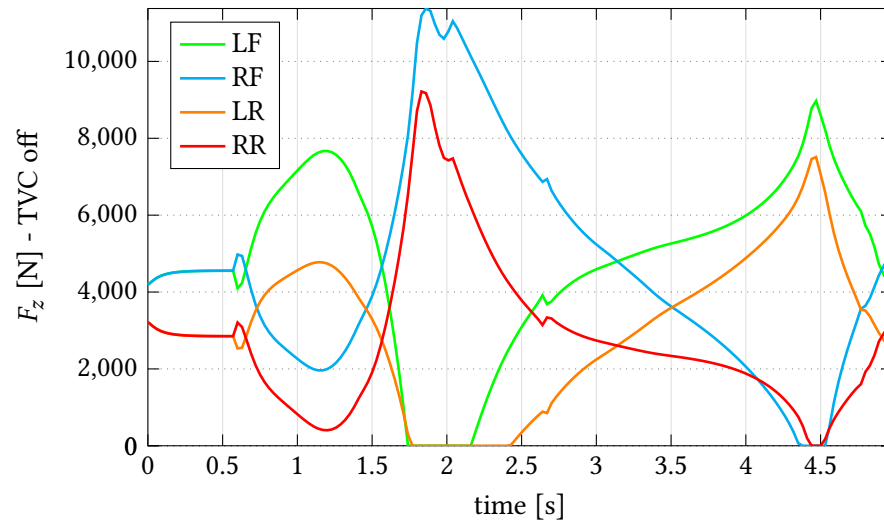


FIGURE 5.26: Single Lane-Change at $v_{x0} = 88 \text{ km/h}$ in braking condition - Tire vertical loads for the uncontrolled vehicle: first the two left wheels and then the two right ones lift from the ground

5.5 Step-steer test

The step-steer maneuver is an established method for testing vehicle response in both transient and steady-state conditions. A step steering angle of 5° is applied while the 4IWM electric vehicle is travelling at $v_x = 65$ km/h and starts braking. The brake pedal is at 40% of its travel and the regenerative braking is at 50% of the motor limit. Figure 5.27 shows the steering angle as function time: the input step is smoothed by a first-order low-pass filter to simulate a realistic steering condition.

The obtained trajectories in Figure 5.28 are almost 100% overlapping for the two controlled vehicles. The trajectory of the vehicle without TVC is plotted up to the point in which the vehicle itself becomes unstable, as it is seen in its states reported in Figure 5.29: β and r values enormously increase and do not converge to steady-state anymore, therefore those simulation results become meaningless. The two controlled vehicles have very similar states, with the side slip angle far from the reference at the very beginning and then slowly converging to it. Their yaw rate trends are really close to the reference and the proposed control strategy manages to reduce the light oscillations after the steering step. From Figure 5.30, it is clear that both controllers are effective in reducing state errors: the vehicle side slip angle error slowly converges towards zero and the yaw rate error already reaches zero before the end of the maneuver. Eventually, the third plot in the same figure shows the commanded corrective yaw moment. In this test, the proposed strategy also reduces control action as the four ΔM_z oscillations of the old controller are totally smoothed. Besides, the controllers generate a negative yaw moment correction, i.e., clockwise, that contrasts the commanded sharp left turn in order to reduce vehicle side slip angle and yaw rate, and also to prevent vehicle from overturning. The last mentioned situation happens for the uncontrolled vehicle, since the tire vertical loads in the second plot of Figure 5.31 are entirely unrealistic. The first plot shows the yaw acceleration: both controlled vehicles manage to perfectly follow the predicted value, but the proposed TVC flattens the oscillations and thus improves passenger comfort.

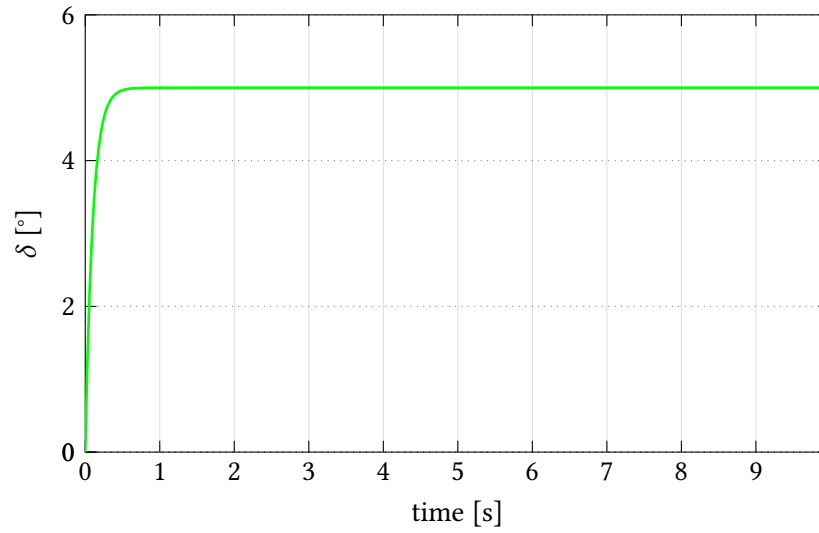


FIGURE 5.27: Step-steer test at $v_x = 65$ km/h in braking condition - Steering angle: a first order low-pass filter is added to smooth the steering step and simulate a realistic input

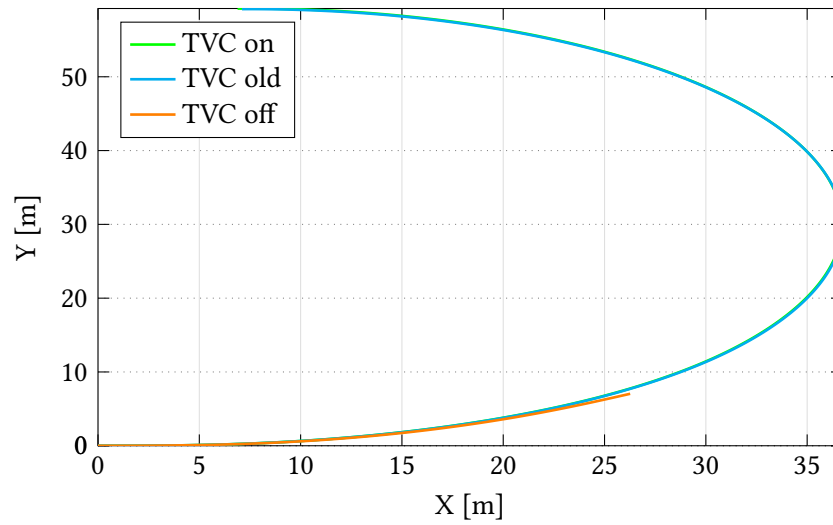


FIGURE 5.28: Step-steer test at $v_{x0} = 65$ km/h in braking condition - Trajectory for the three different cases: the two controlled vehicles behave in the same way; the uncontrolled vehicle is completely unstable and thus the trajectory plot is interrupted at a certain point

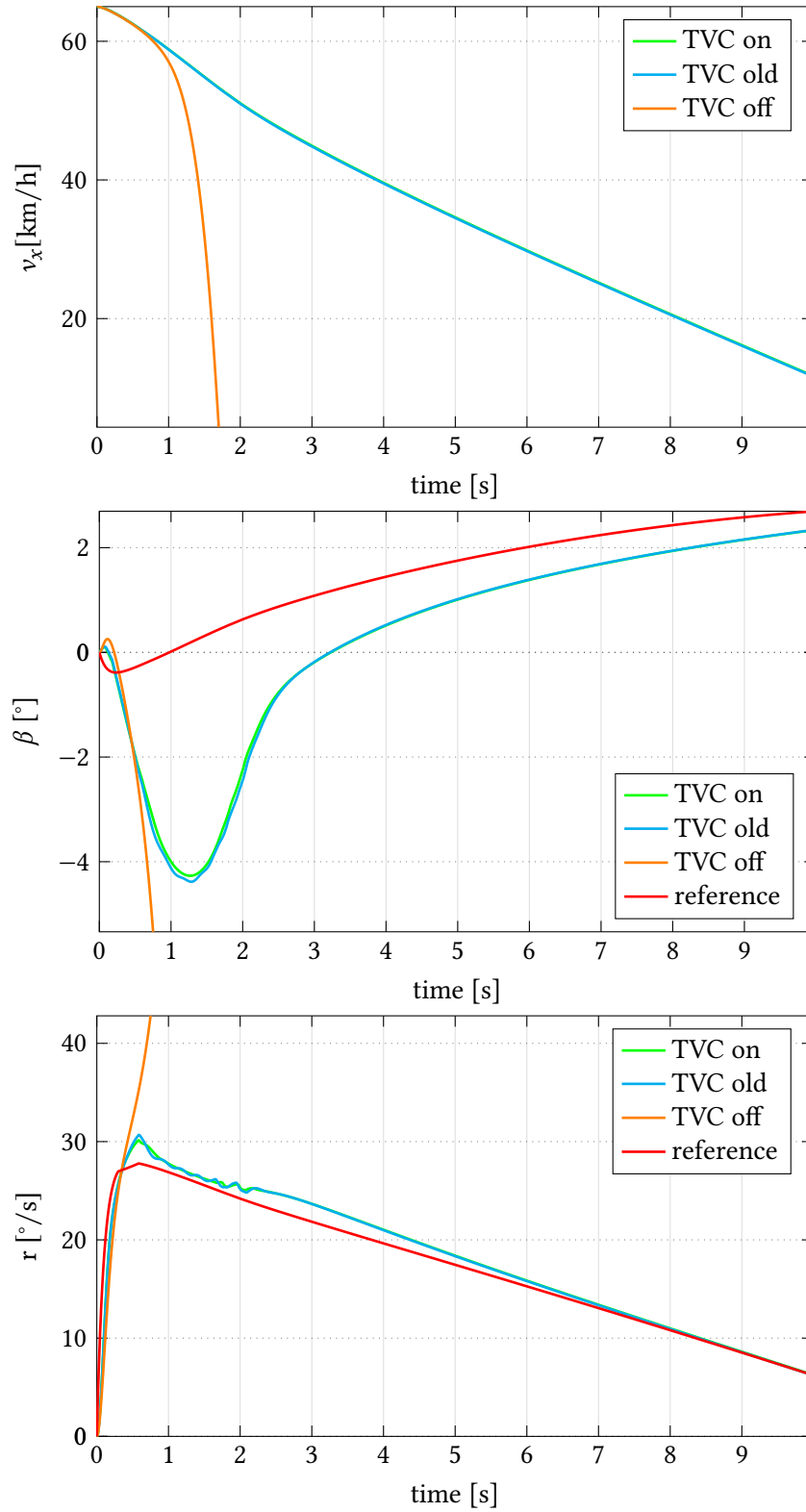


FIGURE 5.29: Step-steer test at $v_x = 65$ km/h in braking condition - Vehicle states for the three cases: the side slip angles of the controlled vehicles slowly converges towards the reference; the proposed controller reduces the light yaw rate oscillations after the steering step

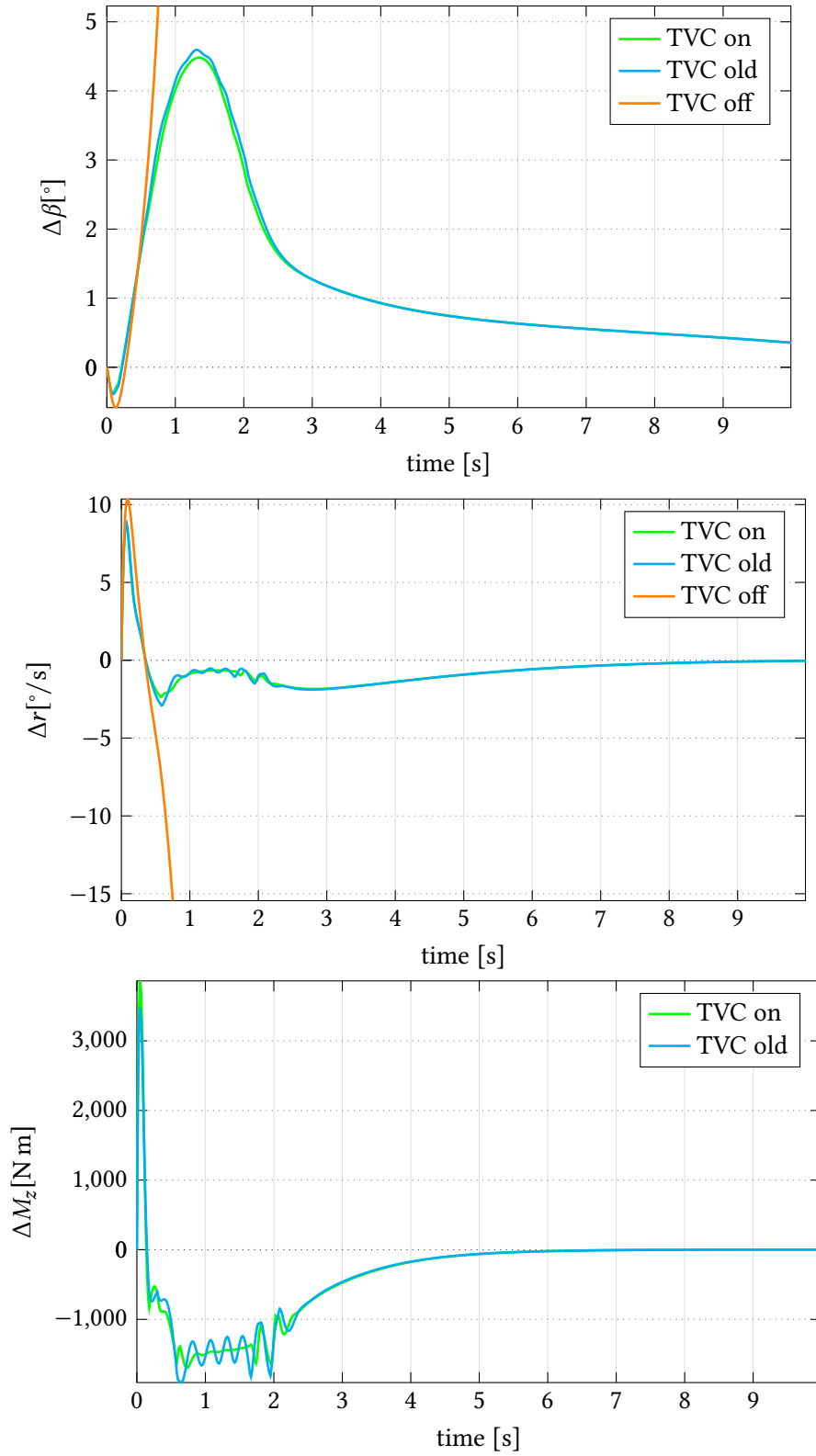


FIGURE 5.30: Step-steer test at $v_x = 65$ km/h in braking condition - Vehicle state errors and corrective yaw moment for the three different cases: the controllers make the state errors converge towards the steady state values; the proposed TVC reduces the ripple after the steering step, as well as the corrective yaw moment oscillations

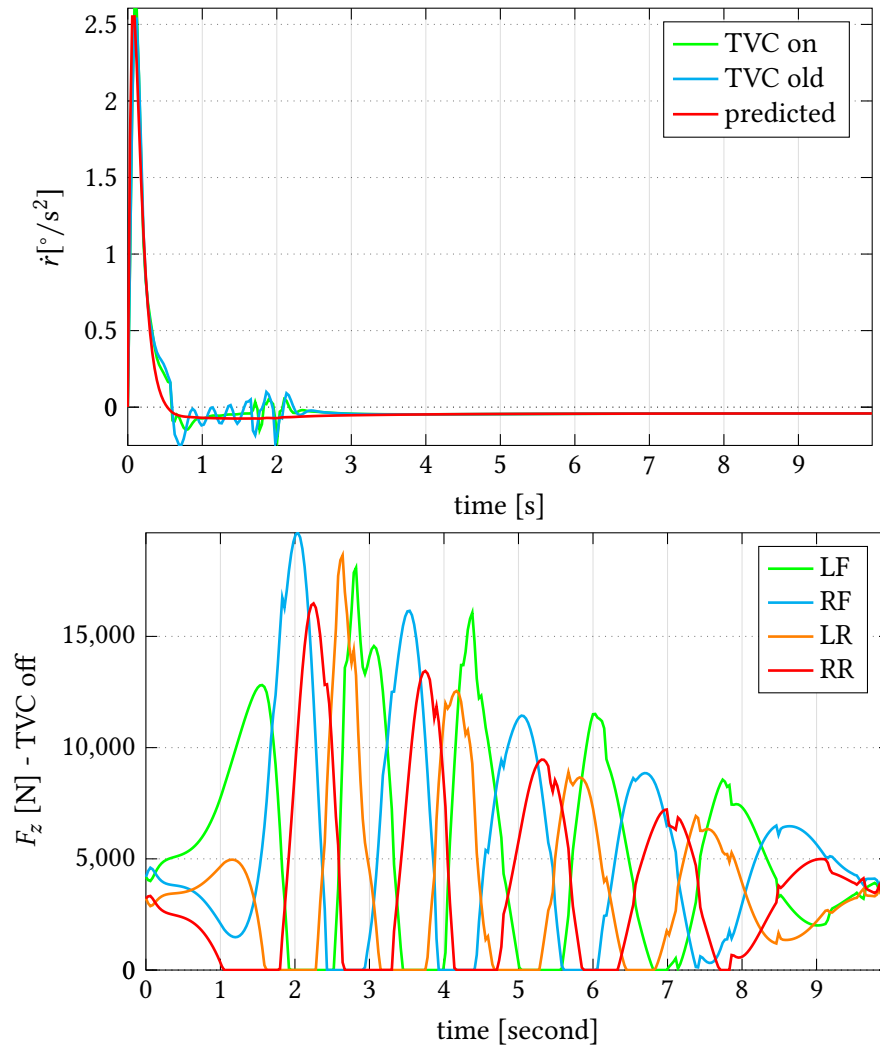


FIGURE 5.31: Step-steer test at $v_x = 65$ km/h in braking condition - Yaw acceleration for the three cases and tire vertical loads for the uncontrolled vehicle: the "TVC on" case reduces the yaw acceleration oscillations; the uncontrolled vehicle is obviously unstable from the tire vertical load plot

Table 5.3 gives numerical results in terms of vehicle side slip angle and yaw rate error magnitudes. Although the uncontrolled vehicle is clearly unstable as its values are incredibly high, overall the two controlled vehicles behave the same, with the proposed strategy able to reduce the vehicle side slip angle and yaw rate error magnitudes by a couple of cents.

TABLE 5.3: Step-steer test at $v_{x0} = 65$ km/h in braking condition - Results: the proposed TVC slightly reduces the overall vehicle side slip angle and yaw rate errors

TVC	$\ \Delta\beta\ _2$ [rad]	$\ \Delta r\ _2$ [rad/s]	note
on	1.3109	1.0704	pass
old	1.3490	1.0873	pass
off	78.8566	869.2830	2 wheels lift-off

5.6 Standing start while cornering

The objective of this test is to replicate a real driving scenario in which a vehicle pulls away turning left or right. This common situation can be found for instance at a traffic light or at a stop sign. The maneuver is conducted starting from $v_x = 1$ km/h with throttle = 75% and steering angle reported in Figure 5.32. More precisely, the steering input is a half sine-wave with amplitude $A = 10^\circ$ and period $T = 5$ s. The choice of the initial speed has been done to avoid numerical issues in the simulations for speeds around zero. The usual three different vehicles are compared: the one endowed with the proposed controller, the one with the sliding mode controller only and the uncontrolled one.

The vehicle trajectories are reported in Figure 5.33 and as it is possible to see there is almost no difference among the three cases. Figure 5.34 shows the vehicle states: the velocity profiles are exactly the same, while vehicle side slip angle and yaw rate have almost imperceptible changes. Figure 5.35 shows that the proposed controller does not affect β errors but slightly reduces r errors throughout the whole maneuver, at the expense of a higher control action. From the third plot, which shows exactly the corrective yaw moment, it is possible to understand that both controllers enhance oversteering at the beginning (counter-clockwise yaw moment, in the same direction of turning) and understeering after $t = 3.5$ s (clockwise yaw moment). The accelerations are reported in Figure 5.36: a_x has the same trend for the three cases, a_y has some minor differences for the second part of the maneuver and \dot{r} values are very close to the reference. In particular, the yaw acceleration prediction is tracked well for the first part of the test but then a small error is introduced and kept until the end.

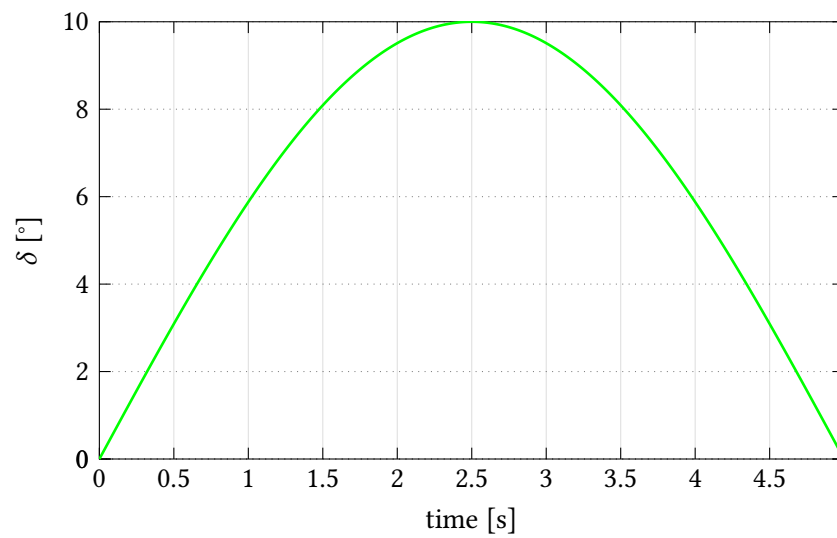


FIGURE 5.32: Standing start while cornering - Steering angle

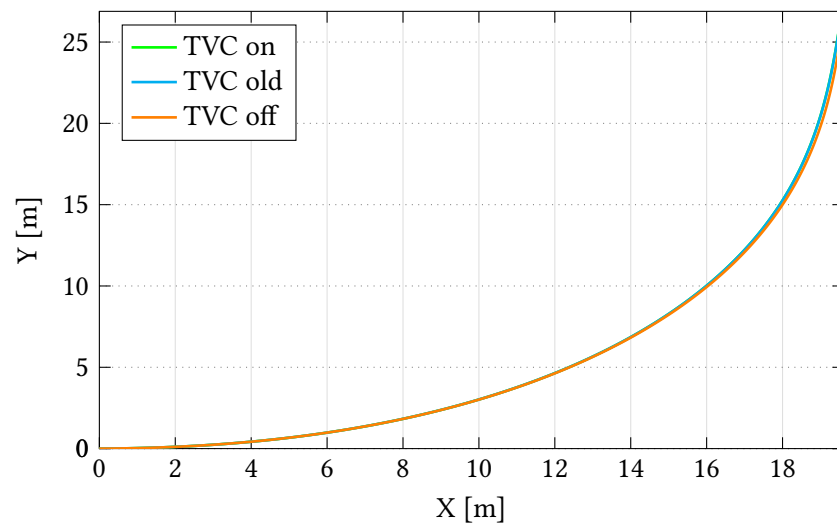


FIGURE 5.33: Standing start while cornering - Trajectory for the three different cases: there is almost no difference between the three curves

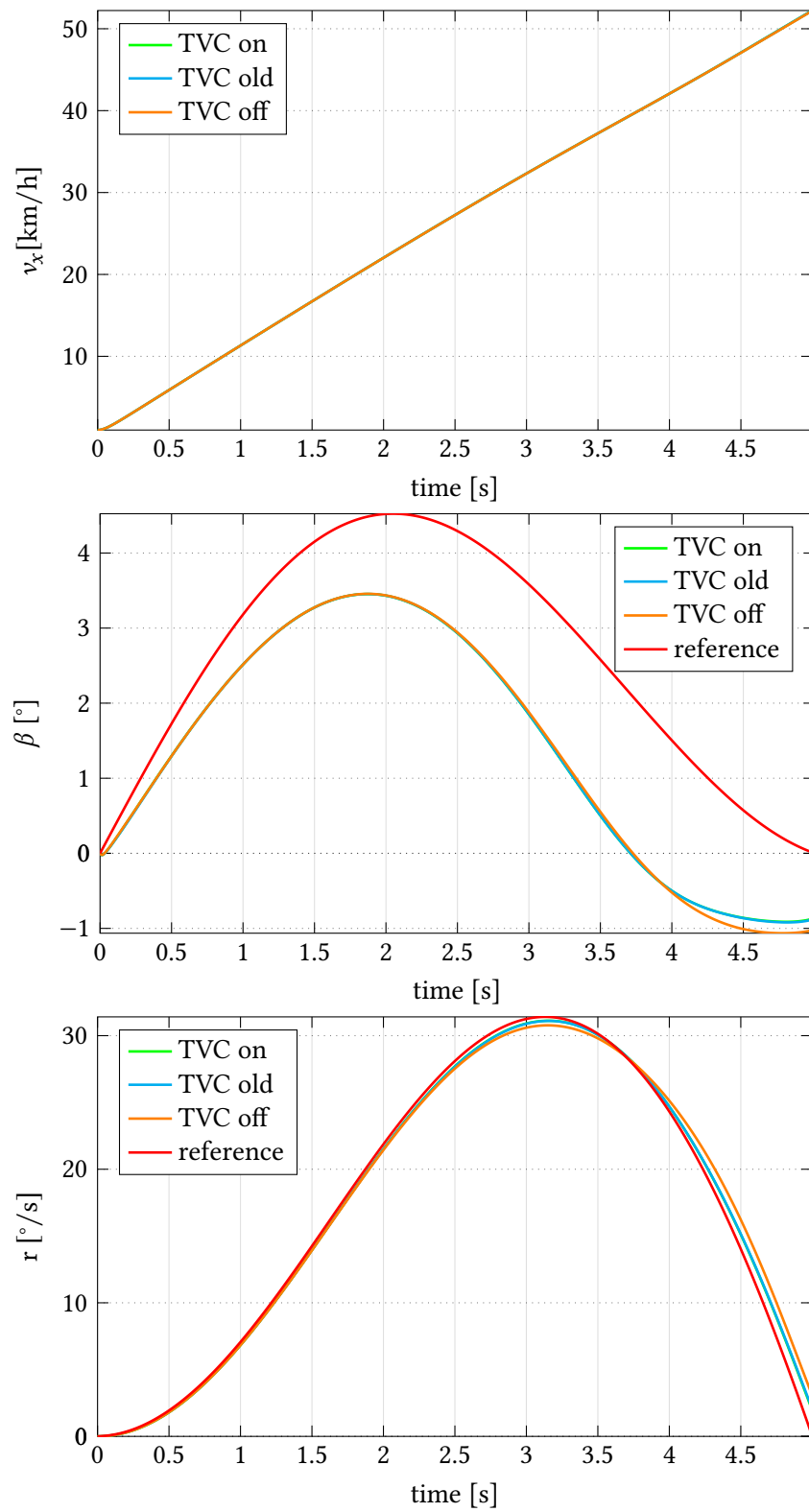


FIGURE 5.34: Standing start while cornering - Vehicle states for the three different cases: there are imperceptible differences between the two controlled vehicles

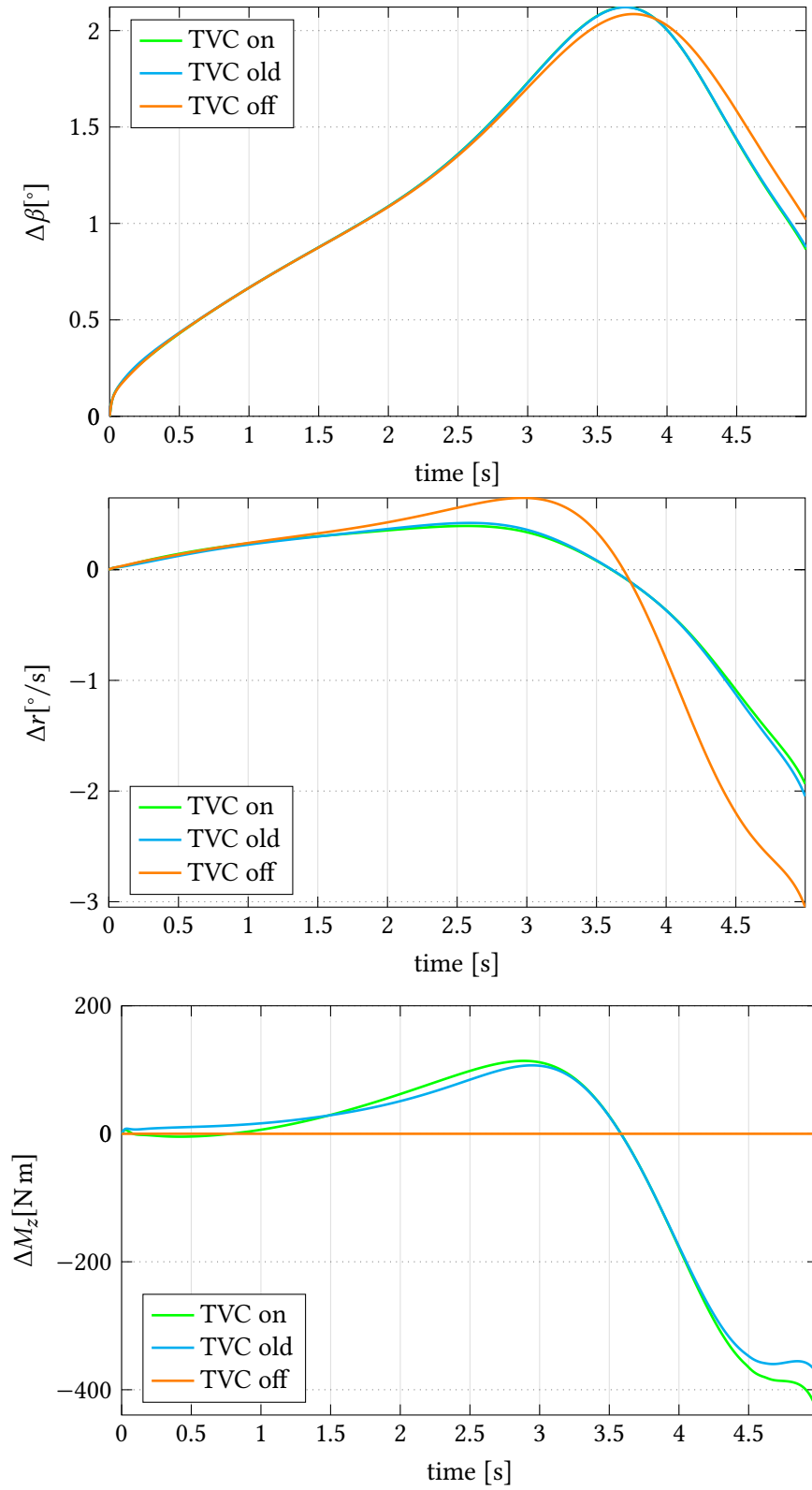


FIGURE 5.35: Standing start while cornering - Vehicle state errors and corrective yaw moment for the three different cases: the proposed controller does not affect β errors but slightly reduces r errors; the corrective yaw moment is higher in this case

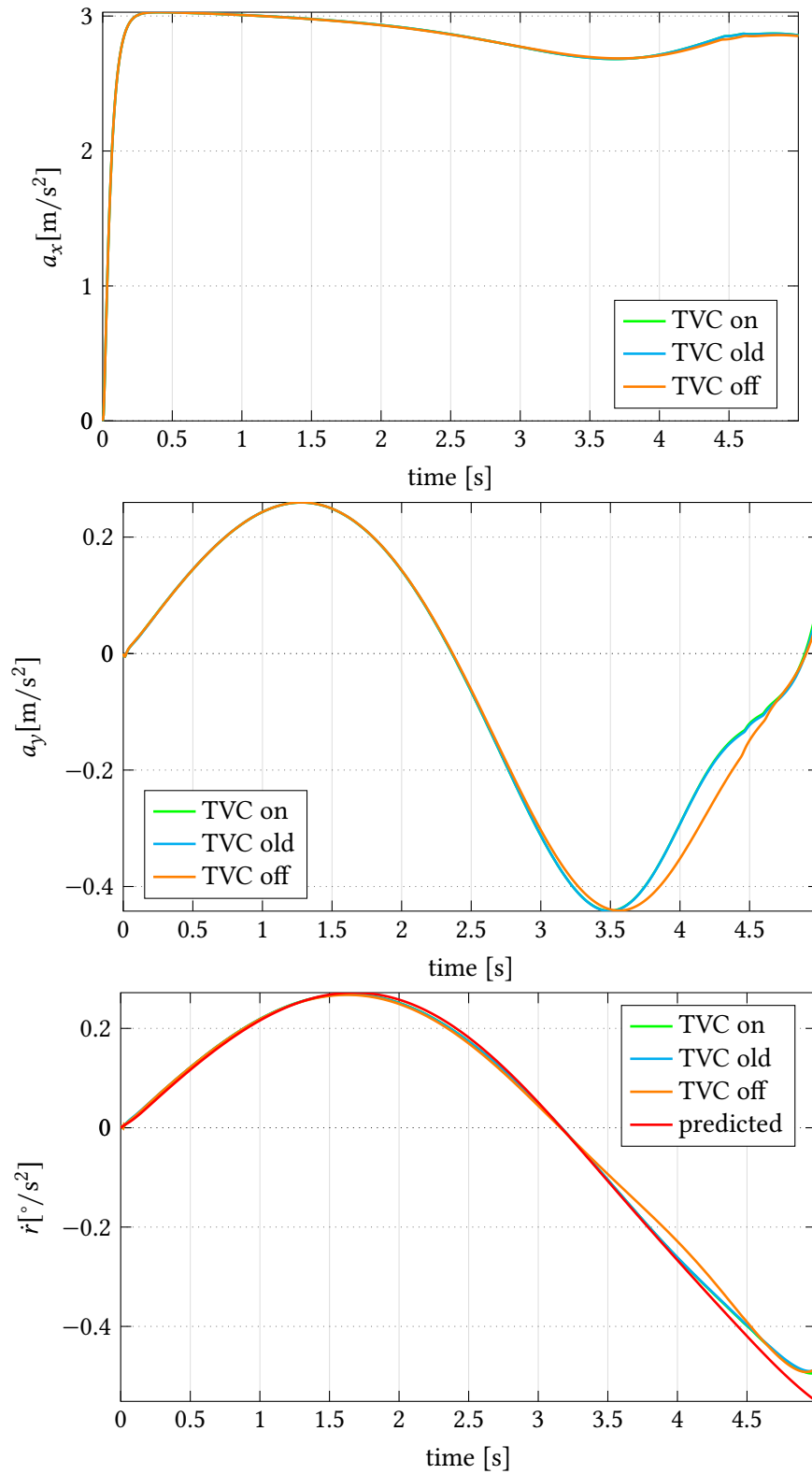


FIGURE 5.36: Standing start while cornering - Vehicle state derivatives for the three different cases: a_x has the same trend; a_y has some minor differences for the second part of the maneuver; \dot{r} values are very close to the reference

Table 5.4 contains the magnitudes of vehicle side slip angle and yaw rate, and also their respective errors with respect to the reference. For all the four norms-2, the values of the two controlled vehicles are very similar. However, the yaw rate error is reduced with respect to the old controller and is almost halved if compared to the uncontrolled vehicle. Although the developed TVC does not significantly improve the vehicle trajectory, the graphs shown before and the numbers in the table demonstrate that it is capable of reducing the yaw rate error.

TABLE 5.4: Standing start while cornering - Results: the proposed TVC reduces the yaw rate error magnitude

TVC	$\ \beta\ _2$ [rad]	$\ r\ _2$ [rad/s]	$\ \Delta\beta\ _2$ [rad]	$\ \Delta r\ _2$ [rad/s]
on	2.5932	25.2283	1.6686	0.7220
old	2.5937	25.2237	1.6689	0.7508
off	2.6135	25.2675	1.6853	1.2784

5.7 Friction-split condition when driving straight

The so-called friction split (or μ -split) condition occurs when the left and right wheels have different friction coefficients. A simulation is performed considering a four in-wheel motor BEV driving straight, i.e., no steering angle is applied, with the left wheels on a high adhesion road ($\mu = 1$) and the right ones on a low friction terrain ($\mu = 0.2$). The initial speed is 10 km/h and the vehicle accelerates with 60% throttle. In this case, TCS and TVC play an important role in keeping vehicle stability: the expected behaviour of the vehicle when there is no steering angle would be driving straight, but due to the μ -split condition presented here the vehicle would go on the right when accelerating and on the left when braking. As already explained in Section 4.3, the primary scope of the project has been the development of the Torque Vectoring Controller. The Traction Control System is of paramount importance in off-road conditions and in low road-adhesion situations in general, and for this reason it has been included in the controller. When simulating a condition like the μ -split, the TCS becomes fundamental to avoid excessive wheel spinning that would also compromise the TVC behaviour. Two different vehicles are compared: the first one is endowed with both the developed TVC and TCS, while the second one does not have any of the above ones and features only the torque distribution strategy based on tire vertical load.

The trajectories in Figure 5.37 clearly show that the uncontrolled vehicle tends towards the lower traction side, while the controlled vehicle keeps the desired straight trajectory. The second plot reports the vehicle speed: the TCS allows higher traction and thus the vehicle manages to accelerate faster. The allocated yaw moment in the third plot explains the reason for which the controlled vehicle manages to run straight: since the driver is not turning the steering wheel, the only way the vehicle could run straight would be having the same torque on the left and right

wheels, and this is allowed by the combination of TVC and TCS. Indeed, the TCS saturates the two right wheel torques according to the friction coefficient value, thus avoiding over-spinning, and the torque distribution strategy reduces the torque on the left wheels to match the right ones, thus avoiding undesired right turning behaviour. More precisely, at the very beginning the TVC upper-layer does not require any corrective yaw moment, as the vehicle is going to start tending on the right but it has not yet; in this condition the torque distribution strategy, and in particular Equations 4.45 and 4.46, corrects the left wheel torques to keep the generated yaw moment equal to zero. By contrast, the uncontrolled vehicle allocates torques generating a counter-clockwise yaw moment that is responsible for vehicle's left turning behaviour: as the right wheels excessively spin, their limit torque is in the high rpm region and therefore it is a lower torque than the left wheels that do not slip; this, in combination with the absence of torque correction (Equations 4.45 and 4.46), intrinsically generates an unwanted yaw moment. The tire slip ratios and the wheel torques are reported in Figure 5.38. It is clear that the combination of TVC and TCS activated allows the control of tire longitudinal slip rate, whose values are still kept in the linear region. Besides, in this case the allocated torques on the left and on the right wheels are the same, as already discussed. By contrast, the uncontrolled vehicle exhibits incredibly high slip rates and the torque distribution unavoidably leads to a right-tending behaviour.

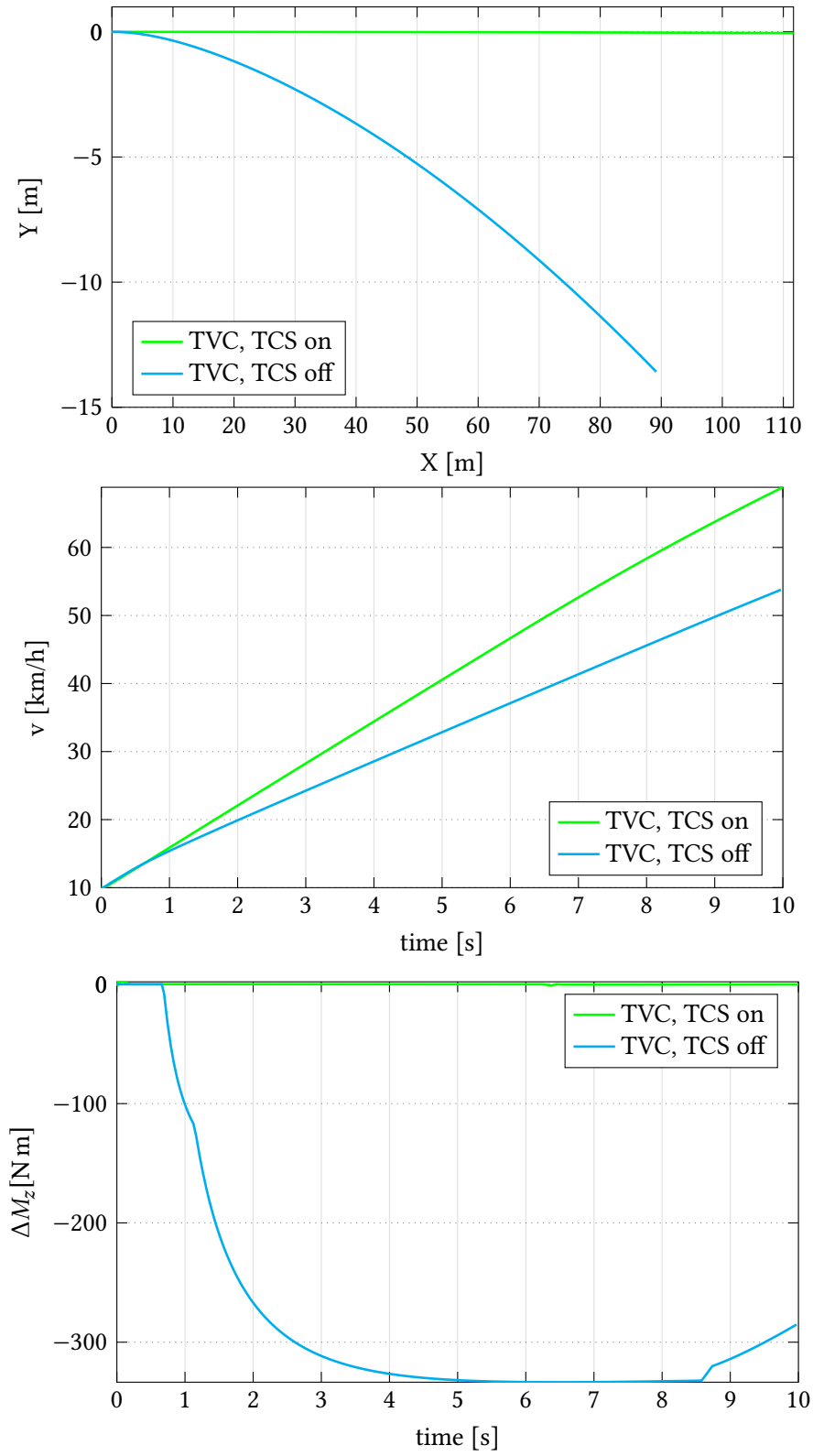


FIGURE 5.37: μ -split condition when accelerating - Vehicle trajectories, velocities and allocated yaw moment for controlled and uncontrolled cases: the controlled vehicle is kept on the desired straight trajectory and manages to get a higher acceleration; the allocated yaw moment for the controlled vehicle is zero, as this is the only way the vehicle could run straight without any steering angle

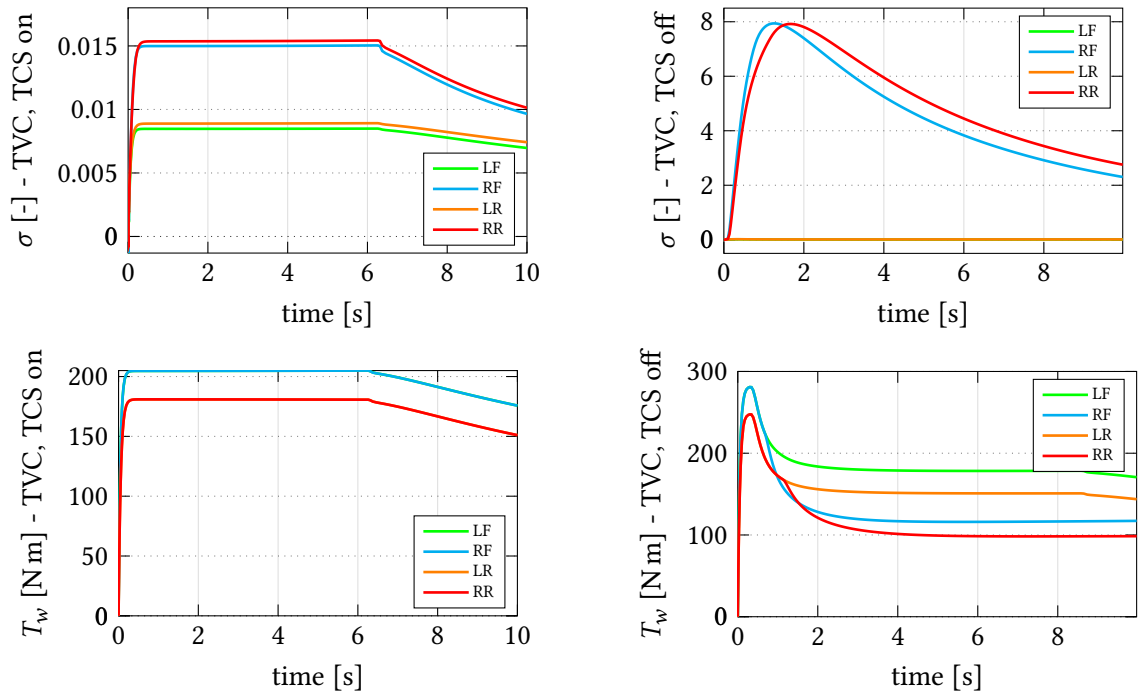


FIGURE 5.38: μ -split condition when accelerating - Tire slip ratios and wheel torques for the controlled and uncontrolled vehicles: the controller keeps the slip ratios within the linear tire range

5.8 Electric Motor efficiency

Powertrain efficiency is a key aspect, especially for electric vehicles, since loss reduction can significantly increase the driving range. Although this project does not focus on the electric powertrain, i.e., electric motor, inverter and battery, an efficiency assessment is conducted with the aim to understand whether the proposed TVC strategy penalizes the electric motor efficiency.

Table 5.5 summarizes the average electric motor efficiencies for the three different cases, i.e., vehicle equipped with the proposed TVC, vehicle with the controller in literature and uncontrolled vehicle, considering the 4IWM configuration. The results refer to the same maneuvers introduced in this chapter, i.e., sinusoidal steering angle input in Section 5.2, Double Lane-Change at constant speed in Section 5.3.2, Single Lane-Change when braking in Section 5.4, step-steer test in Section 5.5 and standing start while cornering in Section 5.6. The efficiency values are calculated using the mean value theorem for integrals applied to a discrete function (time steps are 0.005 s). The last column reports the simple average efficiency value of the four motors. In all the cases except for the standing start while cornering the proposed controller improves the overall average efficiency. In the standing start, in the step-steer maneuver and in the Single Lane-Change the differences are really small since the additional torque due to yaw moment is quite small. However, the proposed controller significantly improves the efficiency in the sinusoidal steering input and in the Double Lane-Change. The uncontrolled vehicle generally has a lower EMs average efficiency than the controlled ones, likely because in the latter case the TVC makes the motors work in the high angular speed region, which is the most efficient one (see the electric motor map in Figure 3.13). The results of the uncontrolled vehicle for the step-steer test are unreliable because the vehicle is completely unstable, as seen in Section 5.5.

Figures 5.39 and 5.40 show the efficiency trends as function of time for the sinusoidal steering angle input and the Double Lane-Change at constant speed, considering the three different controller cases. In both figures it is possible to notice that when the TVC intervenes, the efficiency trends have an oscillatory behaviour due to the commanded torque for yaw moment. The slight changes in efficiency among the different motors can also be noticed. Although a clear difference among the different cases cannot be appreciated, the results in Table 5.5 have confirmed that the proposed Torque Vectoring Controller does not penalize the electric motor efficiencies.

TABLE 5.5: Electric motor efficiencies in percentage - Results: the proposed controller significantly improves the average efficiency in the sinusoidal steering input and in the Double Lane-Change at constant speed; in the other scenarios the differences are really small

Test	TVC	LF	RF	LR	RR	average
Sinusoidal steering angle input when accelerating	on	91.0101	91.0465	91.2771	91.3078	91.1604
	old	90.4649	90.1312	90.3453	90.2367	90.2945
	off	88.7942	89.1585	89.1332	89.936	89.2555
DLC at constant speed	on	88.8884	88.3747	88.4932	88.1672	88.4809
	old	88.5427	88.3934	88.2329	88.1053	88.3386
	off	88.5436	88.5951	88.1305	88.0328	88.3255
SLC when braking	on	91.5655	91.5263	91.6543	91.6895	91.6089
	old	91.5572	91.5214	91.6540	91.6106	91.5858
	off	90.0737	91.7900	88.4149	89.8352	90.65815
Step-steer when braking	on	89.3763	89.6017	89.6676	90.5228	89.7921
	old	89.3425	89.5817	89.6705	90.5055	89.7751
	off	83.2080	70.2213	78.5465	67.1744	74.7876
Standing start while cornering	on	79.8309	80.5810	80.1641	80.7936	80.3424
	old	79.8427	80.5701	80.176	80.8828	80.3679
	off	79.8598	80.5531	80.1916	80.8688	80.3683

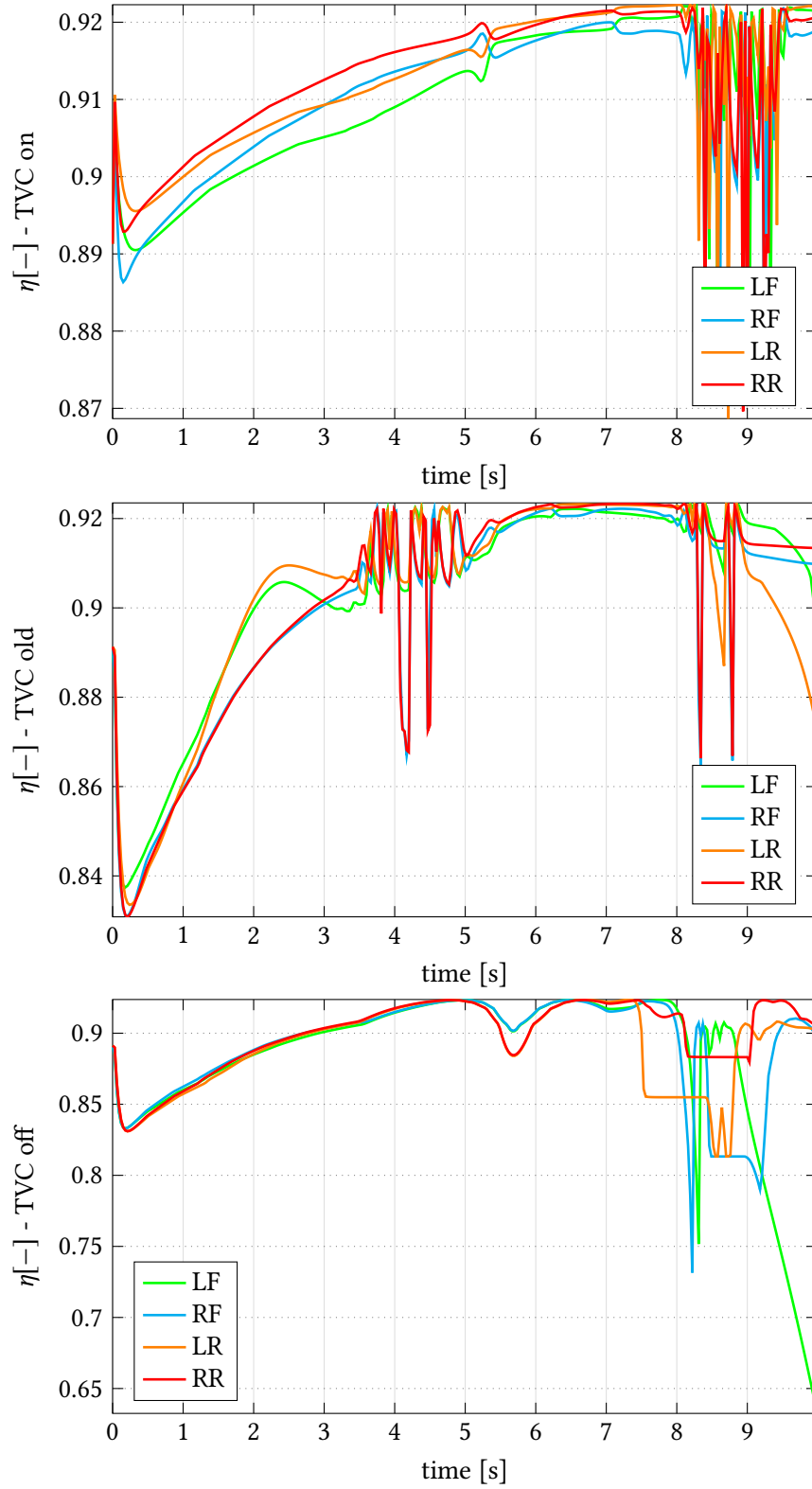


FIGURE 5.39: Sinusoidal steering angle input - Electric motor efficiencies for the three different cases: the oscillatory behaviour in the first two plots is due to the TVC intervention

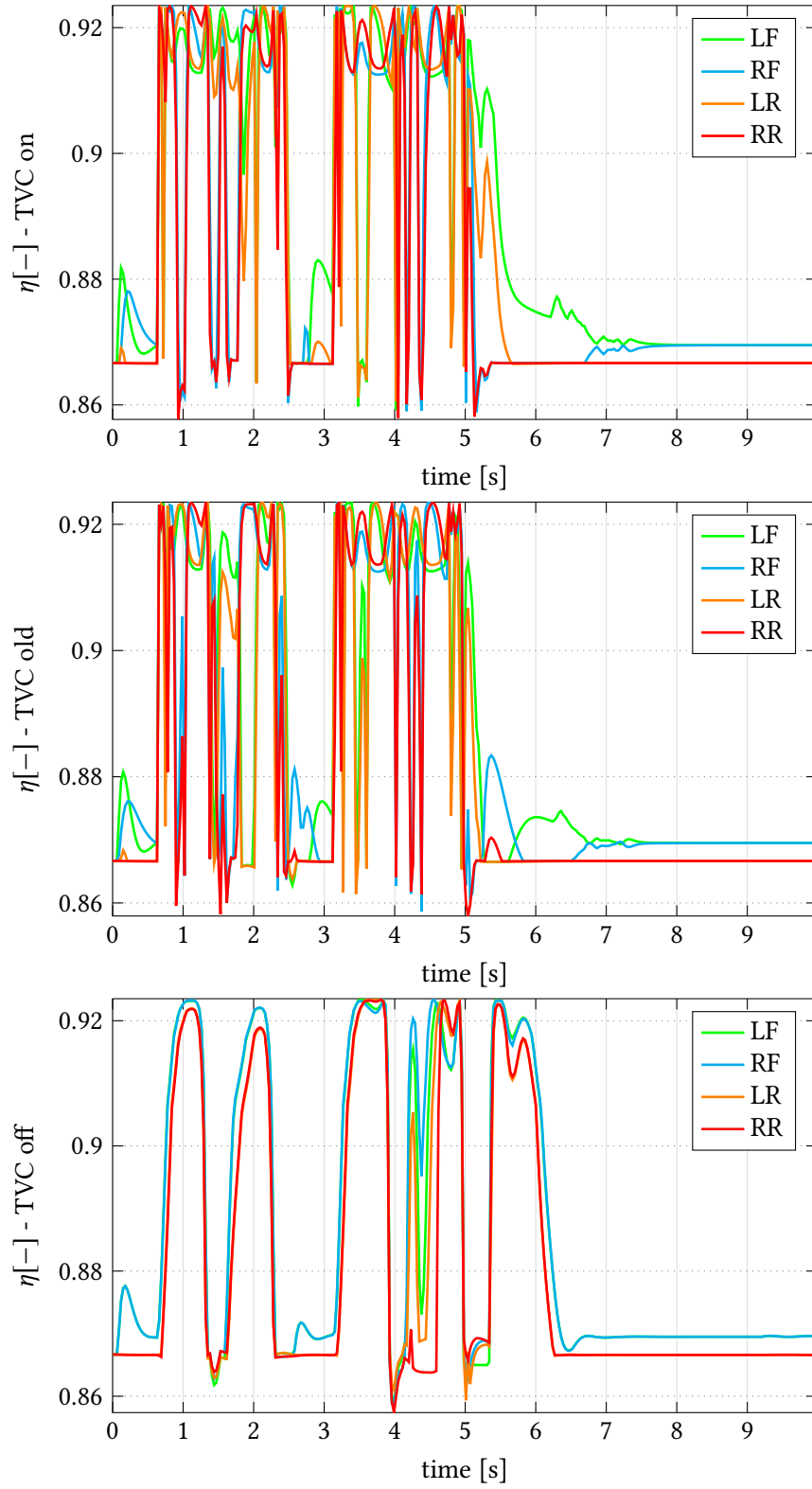


FIGURE 5.40: Double Lane-Change with cruise control at $v_x = 79.4$ km/h - Electric motors efficiencies for the three different cases: the oscillatory behaviour in the first two plots is due to the TVC intervention

5.9 Contributions of the different terms to the yaw acceleration prediction

This section explores the relative weight of the different terms inside the yaw acceleration prediction formula of Equation 4.28. The three different contributions, here referred as “contr₁”, “contr₂” and “contr₃”, are defined as follows:

$$\text{contr}_1 = \frac{\delta \dot{v}_x}{l + k_{us} \frac{v_x^2}{g}} \quad (5.1)$$

$$\text{contr}_2 = \frac{v_x \dot{\delta}}{l + k_{us} \frac{v_x^2}{g}} \quad (5.2)$$

$$\text{contr}_3 = \frac{-\delta \frac{2v_x^2 \dot{v}_x}{g}}{\left(l + k_{us} \frac{v_x^2}{g}\right)^2} \quad (5.3)$$

Since the denominator is in common among the three, the differences are in the numerators only. The first term considers steering angle and longitudinal acceleration, the second term has longitudinal speed and rate of change of steering angle, and the third features steering angle, and longitudinal velocity and acceleration. Three driving scenarios are considered in order to study their effects over a broad range of conditions: the Double Lane-Change when coasting in Section 5.3.1, the step-steer test when braking in Section 5.5 and the standing start while cornering in Section 5.6. The first one is characterized by important steering angle changes, the second one has hard decelerations and an abrupt steering angle change, and the third one features acceleration and a smooth steering angle trend. Figure 5.41 exhibits the yaw acceleration obtained from Equation 4.28 with its three contributions for the three different maneuvers. As expected, the second term in the formula is by far the predominant one in the Double Lane-Change and in the step-steer tests. Indeed, that contribution has the steering angle derivative, which is significant whenever large steering angle changes are applied. Besides, by looking carefully at the first plot (the Double Lane-Change) the sum of the three contributions is not equal to the total yaw acceleration because all their values are bounded between $-4^\circ/\text{s}^2$ and $4^\circ/\text{s}^2$. Besides, the second plot reporting the step-steer test shows that after the step the first term becomes the most important since the vehicle is decelerating and has a large steering angle. Eventually, the third plot shows the standing start maneuver: the second term follows the yaw acceleration trend but a significant contribution in terms of magnitude comes from the first term, which again is responsible for longitudinal acceleration and steering angle. In each considered maneuver the third term does not add any valuable contribution. Therefore, in the case in which one wants to simplify the yaw acceleration formula, the third term could be neglected without introducing particular errors.

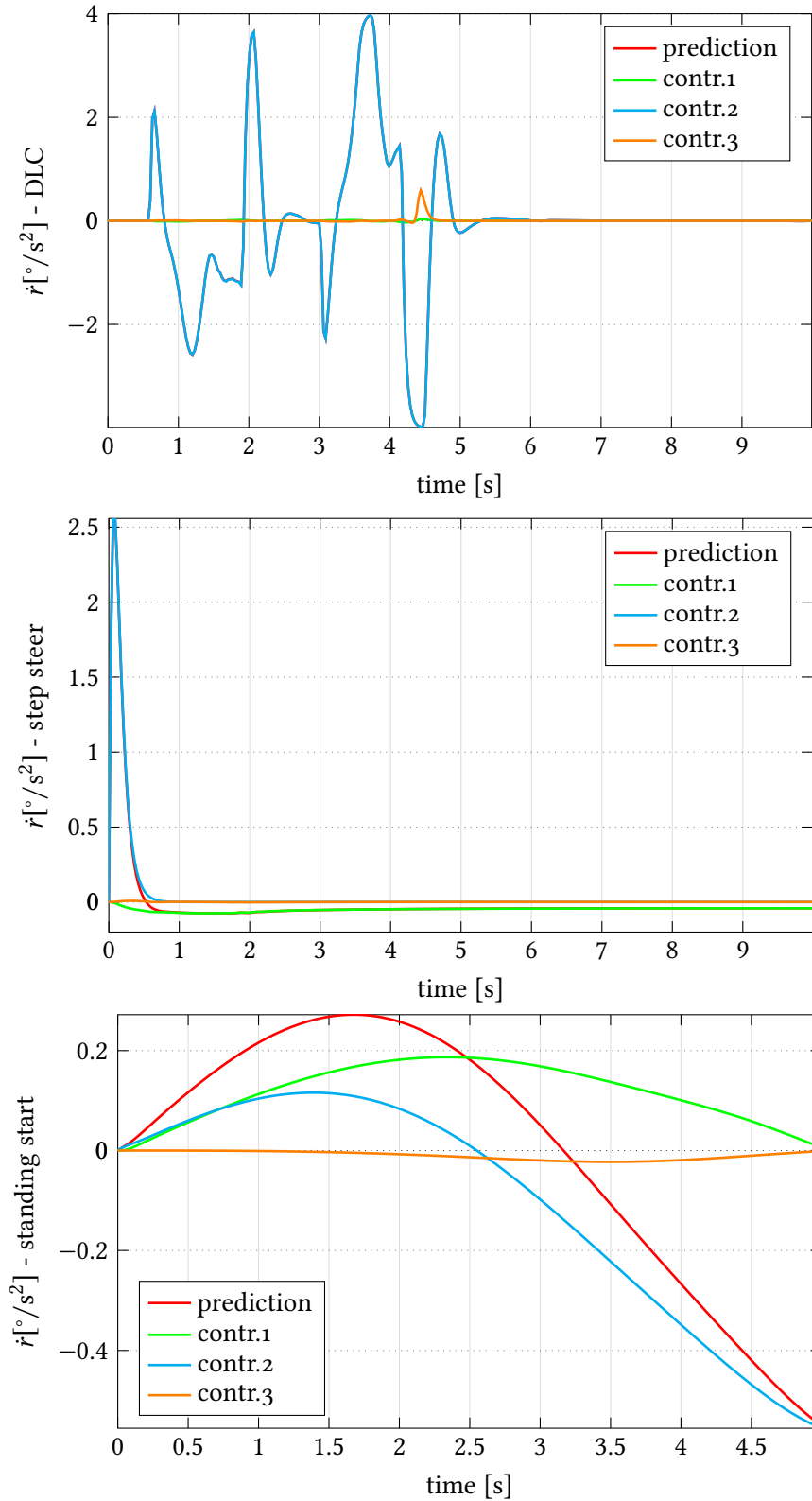


FIGURE 5.41: Contributions of the terms in the yaw acceleration prediction formula - Double Lane-Change when coasting, step-steer maneuver when braking and standing start while cornering. The second term is the predominant one in the Double Lane-Change and in the step-steer maneuver, since it contains the rate of change of steering angle; in the standing start case the second term is still relevant, but a significant contribution comes from the first term, which is responsible for longitudinal acceleration and steering angle

5.10 Controller robustness

The developed integrated and modular controller is designed for the four in-wheel motor electric vehicle whose specifications have been reported in Table 3.1 and that travels on road with $\mu = 1$. However, in most practical cases the vehicle has other load conditions that reflect also on the position of the centre of gravity. Besides, road-adhesion conditions can be far from the design point $\mu = 1$, e.g. when raining or driving off-road. As already discussed in the literature review in Section 2.2.4, the sliding mode control is claimed to be very robust against model and parameters uncertainties. Nevertheless, the overall behaviour of the proposed Torque Vectoring Controller has to be verified in off-design conditions too. Even though several changes could be tested, two situations will be analyzed: in the first one, vehicle load conditions are changed; in the second one, a different friction coefficient is considered. For the first case, the reference maneuver is chosen to be the Double Lane-Change at 84.1 km/h when coasting, already introduced in Section 5.3.1. For the second off-design situation, a Double Lane-Change at a lower speed is considered.

5.10.1 Double Lane-Change for off-design vehicle load conditions

Vehicle load conditions are affected by passengers and cargo weights and positions, which can modify handling, longitudinal performance and ride quality. Weight standards are defined considering a conventional passenger weight of 70 kg and 10 kg for luggage. From the curb weight, called Standard A, a mass of 80 kg is added per each passenger. Starting from the Standard B, which is the design condition considering one passenger, two off-design conditions will be considered: Standard C, with one additional passenger on the front seat row, and Standard E, with two further additional passengers on the rear seat row (four in total). When the passenger is seated on the front row (Standard C), the centre of gravity position is assumed to move more toward the front; by contrast, in Standard E the CG is moved towards the rear. Furthermore, it is assumed that the height of the vehicle centre of gravity is slightly increased when adding passengers, since the centre of gravity of a human body in seated posture lies just above the hip [61], which can be reasonably considered higher than 0.511 m from the ground. Table 5.6 recaps the design and off-design vehicle data.

TABLE 5.6: Vehicle mass and centre of gravity position for design and off-design conditions

	design	off-design	
	standard B	standard C	standard E
m	1510 kg	+80 kg	+240 kg
a	1.130 m	- 0.03 m	+ 0.03 m
b	1.470 m	+ 0.03 m	- 0.03 m
h	0.511 m	+ 0.004 m	+ 0.007 m

Figure 5.42 reports the three vehicle trajectories with the respective steering angles: quite surprisingly, the proposed controller manages to keep all the three vehicles within the track bounds, thus passing the test. Vehicle state errors and yaw moment correction are presented in Figure 5.43. The errors are calculated considering the reference states of the controller, which correspond to the design conditions. The TVC behaves well in off-design, as the error trend is the same as the design case. Indeed, at time $t = 4.3$ s the vehicle in Standard B requires a slightly larger steering angle, which leads to bigger side slip angle and yaw rate that in turn reflects on the state errors too. The third plot shows the allocated yaw moment: the three situations are very similar and just minor changes apply overall. Figure 5.44 confirms that the yaw acceleration does not undergo relevant modifications and thus the predicted value is still effective.

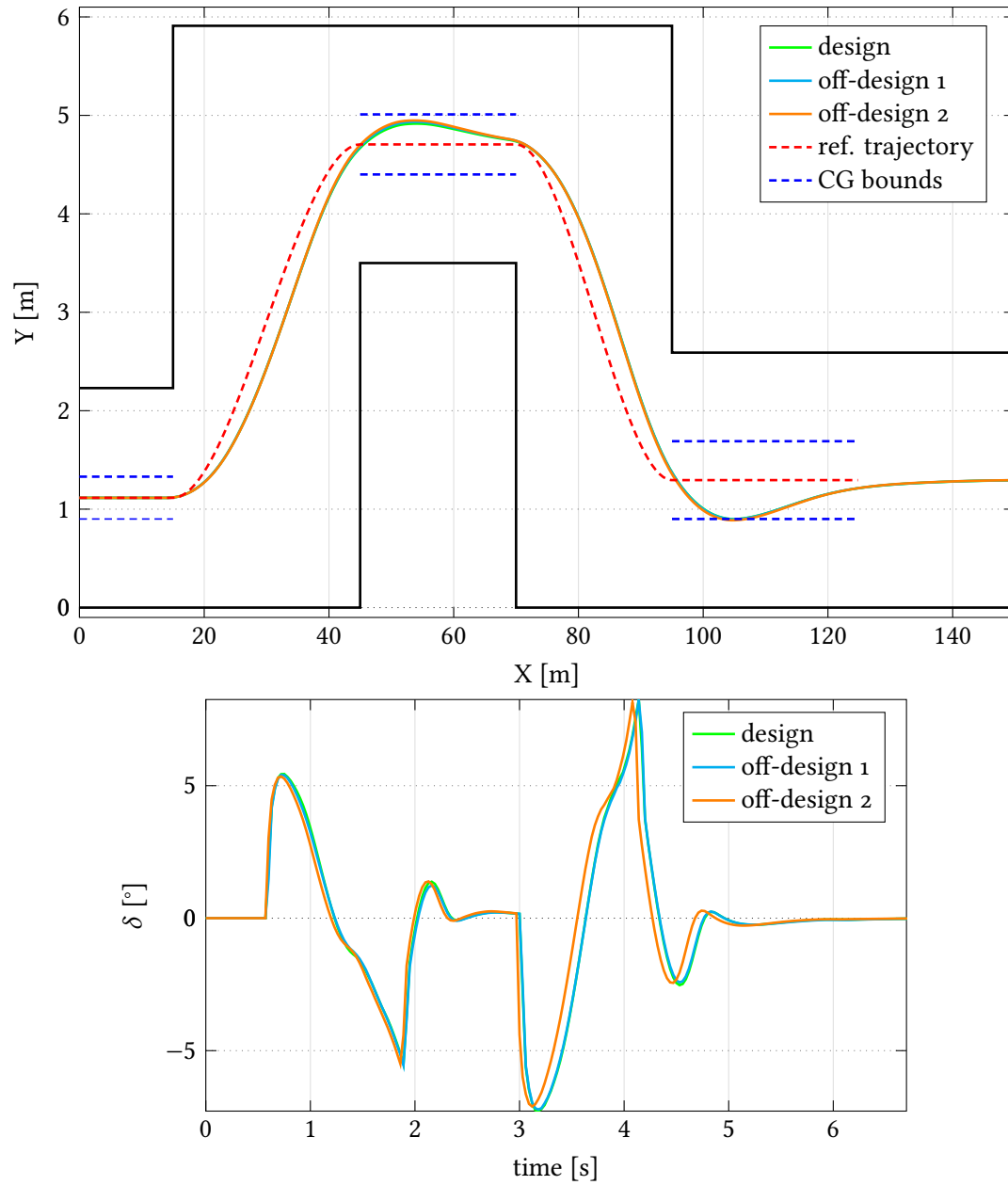


FIGURE 5.42: Double Lane-Change for off-design vehicle load conditions - Trajectories and steering angles: the proposed TVC manages to keep all the vehicles within the bounds

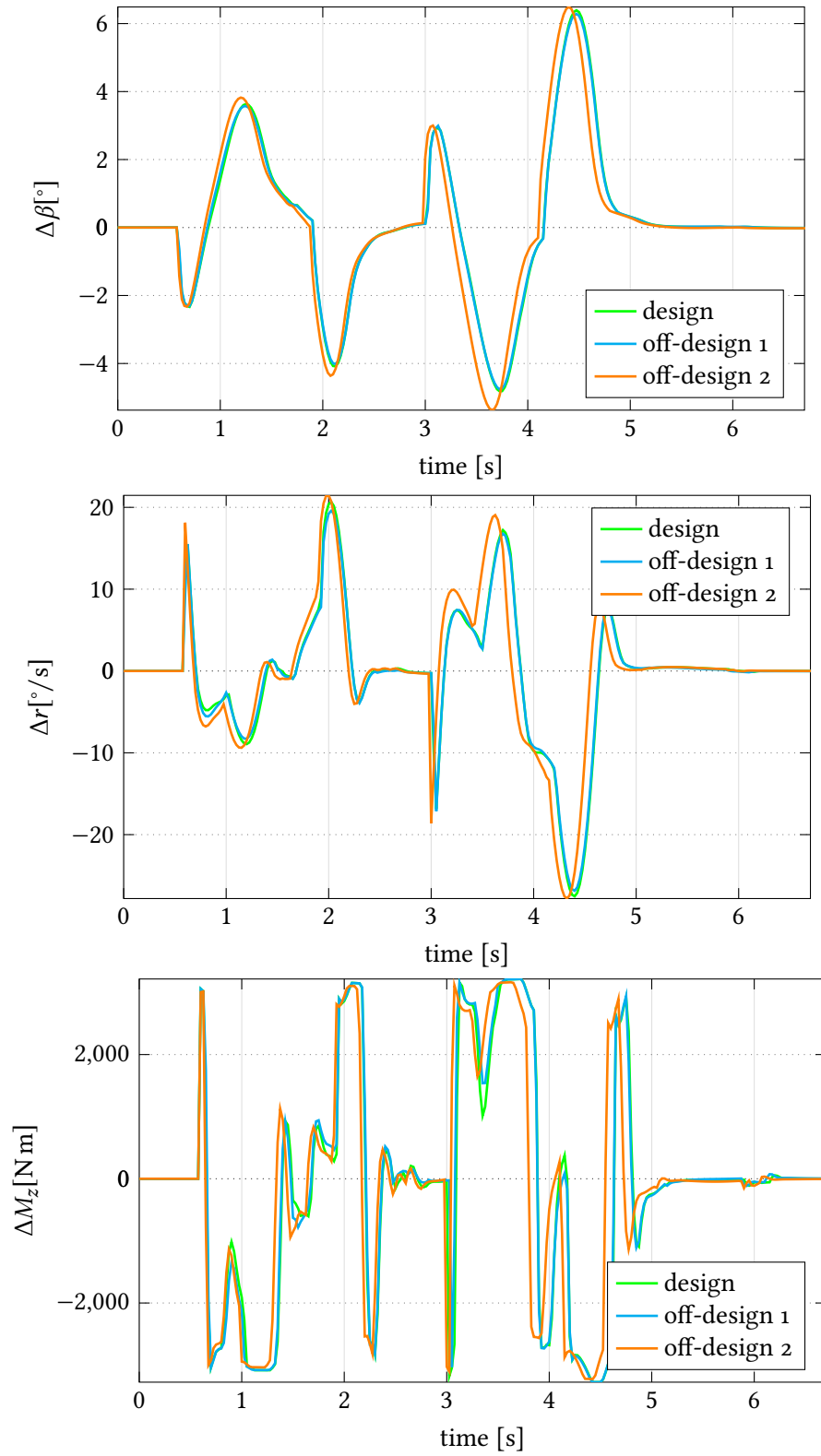


FIGURE 5.43: Double Lane-Change for off-design vehicle load conditions - Vehicle state errors and corrective yaw moment: the error trends for off-design and design conditions are the same

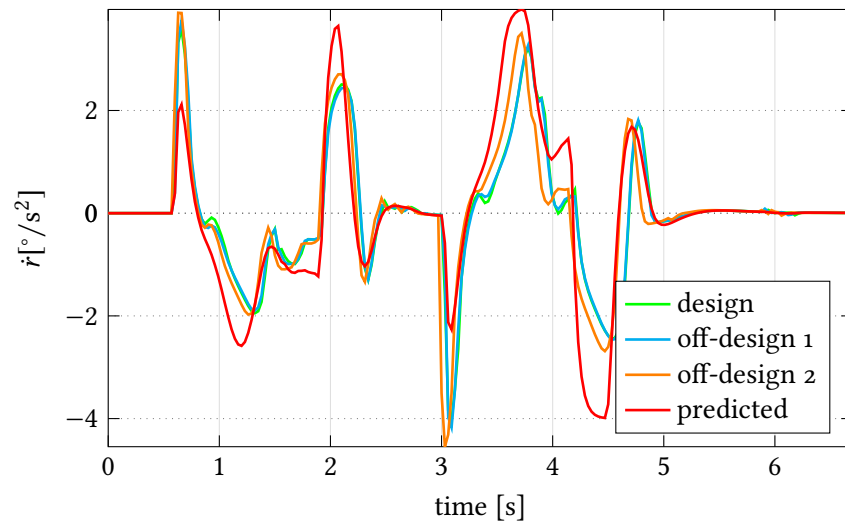


FIGURE 5.44: Double Lane-Change for off-design vehicle load conditions - Yaw acceleration: the yaw acceleration prediction is still effective

Table 5.7 reports the norm-2 of vehicle side slip angle, yaw rate, cross-track error and heading error for the three different load conditions. Overall, the controller behaviour is more than satisfactory also in off-design situations, as β and r are very close to the design conditions. Cross-track and heading errors do allow all three vehicles to pass the test, which is the clear goal of the controller.

TABLE 5.7: Double Lane-Change for off-design vehicle load conditions - Results: vehicle side slip angle and yaw rate values in off-design conditions are close to the design ones

	$\ \beta\ _2$ [rad]	$\ r\ _2$ [rad/s]	e_{ct} [m]	e_h [rad]	note
design	1.3256	9.4854	8.4394	1.2282	pass
off-design 1	1.3212	9.4462	8.4989	1.2132	pass
off-design 2	1.3925	9.7075	8.3502	1.2082	pass

5.10.2 Double Lane-Change under low road-adhesion conditions

The controller has been designed considering a well-paved road with $\mu = 1$, but in practical cases road-adhesion conditions may differ due to rain, snow, ice or gravel. For this reason, the controller has to be tested in those conditions too in order to understand its behaviour. Three different cases are compared here: the proposed controller when $\mu = 0.5$, a controller designed specifically for $\mu = 0.5$ and the proposed controller when $\mu = 1$. The reference maneuver is always the Double Lane-Change when coasting, the initial speed is set at 62.5 km/h and the vehicle is equipped with four in-wheel motors.

Figure 5.45 shows the trajectories and the steering angles of the three different vehicles. The vehicle with the proposed controller (referred as “design when $\mu = 0.5$ ”) fails the test, while a controller designed for this specific condition allows the vehicle to pass it. Quite obviously, the proposed controller easily keeps the vehicle within the track limits when $\mu = 1$, as the speed is much lower than the maximum admissible one (that is 84.1 km/h as seen in Section 5.3.1). The required steering angles are clearly lower when there are advantageous road conditions, while larger values are required when $\mu = 0.5$. The vehicle state errors reported in Figure 5.46 clearly show that the designed controller does not manage to keep the errors low, as the vehicle behaves for $\mu = 0.5$ but the controller is designed for $\mu = 1$. The situation would improve if the controller were designed for $\mu = 0.5$. The third plot reports the allocated corrective yaw moment: the designed controller when $\mu = 0.5$ is the most active one, as it struggles to force the vehicle to follow the behaviour that it would have had on a well-paved road. Eventually, Figure 5.47 plots the yaw acceleration trends: the designed controller when $\mu = 0.5$ tries to follow the predicted value, whose calculation is accurate also in this condition.

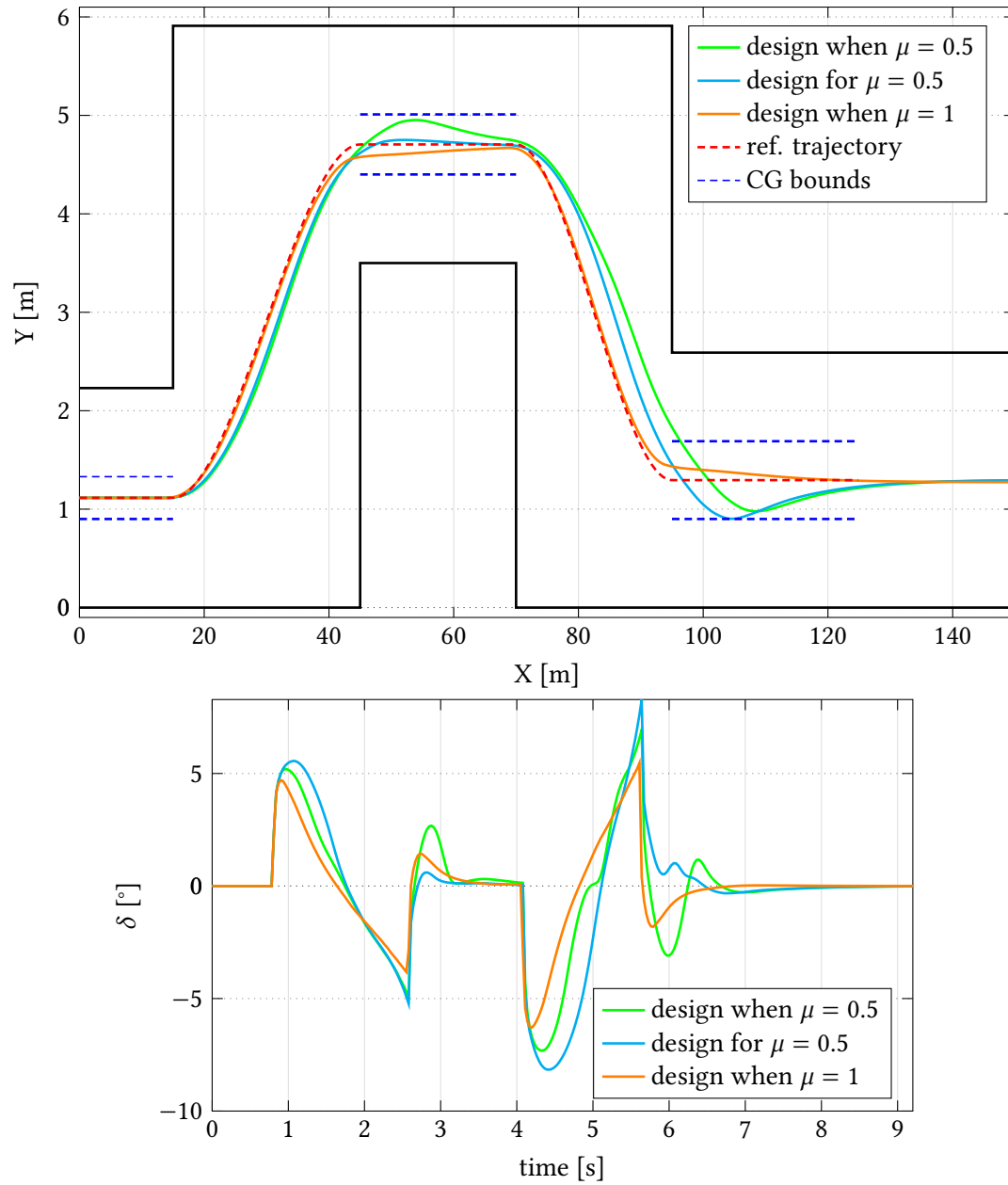


FIGURE 5.45: Double Lane-Change under low road-adhesion conditions - Trajectories and steering angles: the vehicle with the proposed controller fails the test when $\mu = 0.5$ but it passes when $\mu = 1$; a controller specifically designed for $\mu = 0.5$ would allow the vehicle to pass the test

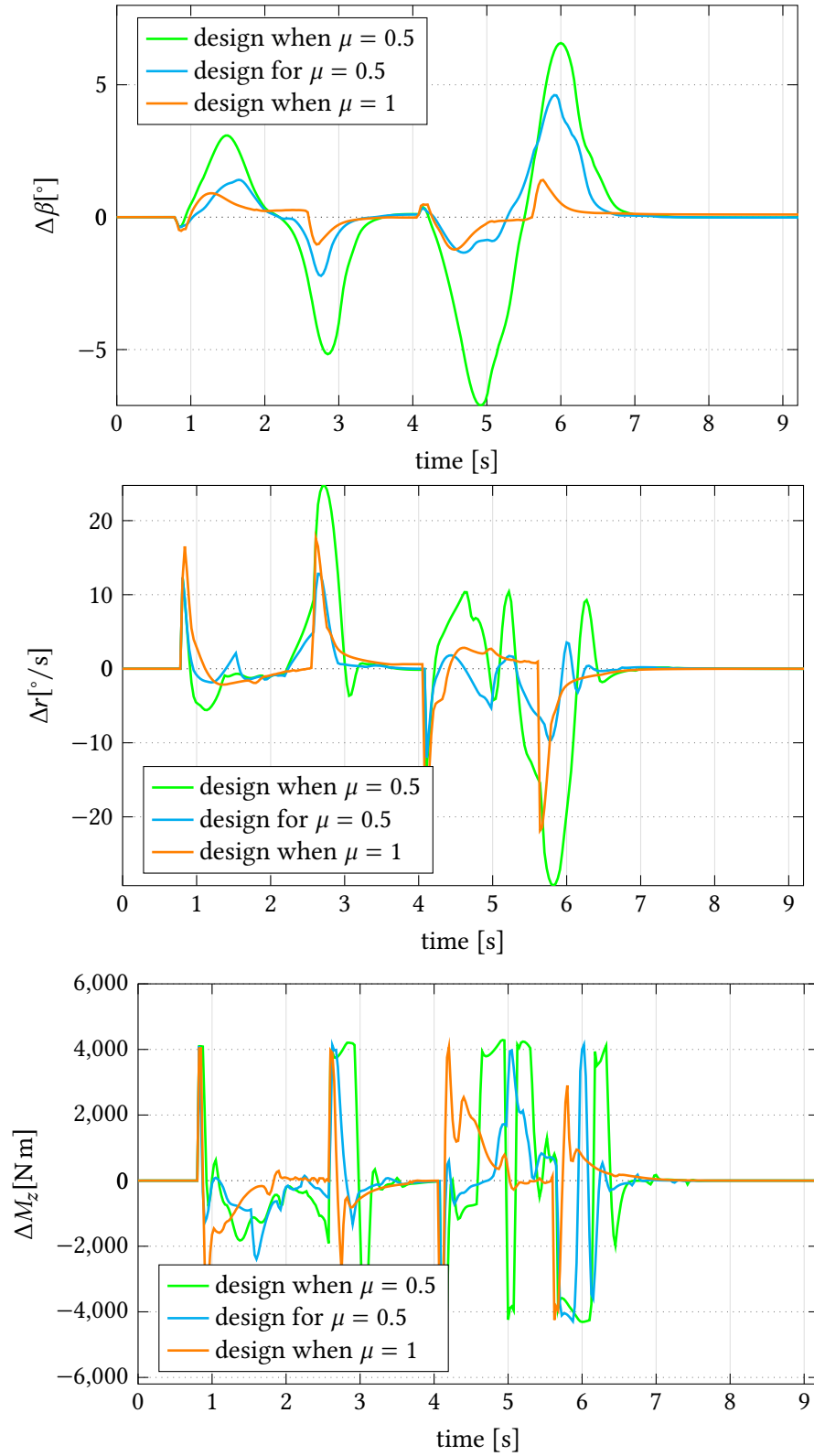


FIGURE 5.46: Double Lane-Change under low road-adhesion conditions - Vehicle state errors: the proposed controller does not manage to keep low state errors when $\mu = 0.5$, and it also require the highest control action

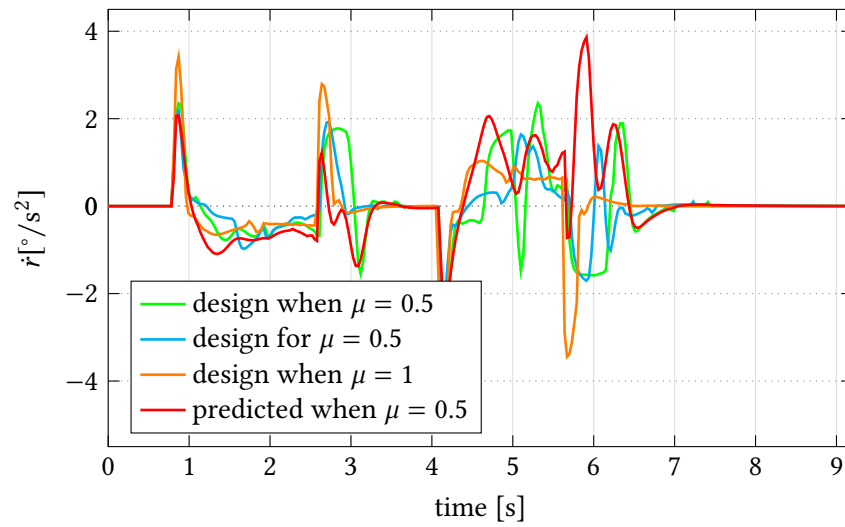


FIGURE 5.47: Double Lane-Change under low road-adhesion conditions - Yaw acceleration: the predicted yaw acceleration is quite accurate also when $\mu = 0.5$

Table 5.8 shows the norm-2 values of the vehicle side slip angle, yaw rate, cross-track error and heading error. Clearly, the proposed controller under low road-adhesion conditions has the highest values because the references are calculated for a well-paved road, and the test is failed because the vehicle's trajectory is outside the defined boundaries. A controller specifically designed for $\mu = 0.5$ makes the vehicle pass the test with overall lower vehicle state magnitudes with respect to the previous case. As a final comparison, the proposed controller tested on $\mu = 1$ conditions shows the lowest vehicle side slip angle, indicating more stability, and higher yaw rate, which is a symptom of a higher maneuverability.

TABLE 5.8: Double Lane-Change under low road-adhesion conditions - Results: the proposed controller has the highest values; a controller specifically designed for $\mu = 0.5$ would make the vehicle passing the test with lower states magnitudes

	$\ \beta\ _2$ [rad]	$\ r\ _2$ [rad/s]	e_{ct} [m]	e_h [rad]	note
design when $\mu = 0.5$	1.8925	8.2427	12.6899	1.3908	fail
design for $\mu = 0.5$	0.6175	6.4880	8.7082	1.1905	pass
design when $\mu = 1$	0.3188	7.0737	2.4974	0.4314	pass

Chapter 6

Conclusions and recommendations

The final chapter of this dissertation has the aim to provide the reader with the conclusions of this research, also clarifying its limitations and analyzing possible future work.

6.1 Summary

The proposed integrated and modular vehicle dynamics controller features a Torque Vectoring Controller, a Traction Control System and a cruise control. The TVC is based on a hierarchical approach and has been developed starting from the Sliding Mode Control equations available in the literature. It has been enhanced with the derivative feedback that links longitudinal vehicle speed and acceleration, and steering angle and its rate of change with the yaw acceleration. The torque distribution strategy, i.e., the lower-layer of the TVC, is based on tire vertical load and has been implemented in such a way that the controller can work for the four different BEV configurations considered, i.e., four in-wheel motors, two in-wheel motors on the front axle, two in-wheel motors on the rear axle and two central motors one per each axle. A seven degree-of-freedom vehicle model is built as the plant system for the controller testing. Both vehicle model and controller have been developed in MATLAB-Simulink. Besides, a driver model has been implemented in order to be able to simulate closed-loop steering maneuvers. Several tests and different combinations of driver's inputs and initial conditions have been considered to test the controller under a broad range of conditions: sinusoidal steering input, double lane-change, single lane-change, step-steer, standing start while cornering and straight μ -split. The TCS has enabled simulations under low road-adhesion situations and the cruise control has allowed constant speed maneuvers keeping longitudinal dynamics. The simulation environment is user friendly as it allows one to change the driving conditions and the general setup using knobs and switches, and it also eases the data post-processing.

6.2 Conclusions

The following conclusions can be drawn at the end of the research:

- The proposed real-time adjustment of the sliding surface dynamics parameters in the TVC according to the control surface value allows the reduction of control action magnitude and its peak value in a sinusoidal steering input maneuver. Furthermore, the norm- ∞ of the sliding surface is reduced considering the same test, and the vehicle passes a Double Lane-Change when coasting down from 81.7 km/h. Considering both maneuvers, the proposed parameters tuning is the best compromise between low control action and sliding surface minimization. It also manages to partially attenuate chattering phenomena.
- The chattering issue intrinsic of the sliding mode control is solved replacing the three sgn functions in the TVC control equation with a saturation function.
- It is possible to link the longitudinal acceleration with the yaw acceleration simply knowing vehicle constructive parameters such as mass, wheelbase and centre of gravity position. In the obtained formula other variables came into play, i.e., vehicle speed, steering angle and its rate of change.
- The proposed TVC featuring derivative feedback in addition to the SMC has proven to be effective and overall better than the SMC controllers available in the literature over a broad range of conditions. Small improvements are brought in cases where longitudinal acceleration, steering angle and its derivative are small, such as in the sinusoidal steering angle input test realized at 40% throttle: the yaw rate is anticipated closer to the reference and its oscillations are slightly reduced. Since the derivative feedback affects the yaw rate only, it is clear that the vehicle side slip angle is barely affected. The full potential of the developed controller is expressed in more severe maneuvers like the Double Lane-Change, where high steering angles and their derivatives are present. In the first test, conducted when coasting down, the controller allows the vehicle to pass it at a speed of 84.1 km/h, against 81.7 km/h for the controller with only the SMC contribution: a 2.4 km/h improvement is quite impressive. In addition to path error reduction, the new controller overall reduces yaw rate error and side slip angle error with respect to the reference values. This is also the case in the common scenario of standing start while steering: although no significant changes in the vehicle trajectories are observed, the small yaw rate error reduction highlights the merit of the proposed control strategy. When considering the Double Lane-Change at constant speed, i.e., with the cruise control activated, the benefits of the controller are slightly reduced because the longitudinal acceleration is close to zero (small oscillations due coupling of longitudinal-lateral dynamics) and thus the yaw acceleration prediction misses that link. In any case, the vehicle endowed with the proposed controller passes the test at a speed of 79.4 km/h, which is 1.5 km/h higher with respect to the vehicle with the old controller. The merit of the developed controller is also appreciable when a step-steer test is conducted: as expected, the derivative feedback allows the smoothing of yaw rate oscillations immediately after the step event. Although the pros of the new controller are clearly evident in the

above-mentioned maneuvers, some scenarios hinder its capabilities. In particular, whenever the electric motors are close to saturation due to their intrinsic constructive limits and there is a severe driving condition, the proposed controller does not manage to allocate the further corrective yaw moment contribution. For instance, this is the case of the Single Lane-Change at 60% braking. Overall, the SMC provides a solid base to start with when developing a TVC, but the yaw acceleration prediction with derivative feedback allows an even more effective action of the integrated vehicle dynamics controller, with reduction of path errors and state errors.

- The implemented TVC tested under several driving scenarios does not penalize the efficiencies of the electric motors. Indeed, the corrective yaw moment generating an additional torque contribution allows the motors to work in a higher efficiency area with respect to the uncontrolled vehicle in most of the conditions.
- The developed TVC, in combination with the TCS, allows the vehicle to deal with μ -split conditions. Besides, the controller is robust enough against vehicle parameter uncertainties and road condition changes.
- The vertical-load-based torque distribution strategy is implemented in such a way that it can work for the four considered BEV architectures. In addition to having a unique controller that could be installed in different electric vehicles configurations, this also enables the comparison among them with the objective to choose the best layout for a particular application. This TVC does not work when there is a central motor on the axle. Besides, the two in-wheel motors front axle configuration is preferable to the rear axle one, as in the second case over-steering is increased. Lastly, the 4IWM EV has more flexibility and the resulting torque distribution strategy is more effective.
- The SMC cruise control parameters tuned in real-time according to the velocity error make the controller responsive and robust at the same time. When lateral dynamics is involved too (as in the case of the Double Lane-Change at constant speed), the developed cruise control is effective and keeps the vehicle speed within less than 1 km/h from the target value.

6.3 Limitations and recommendations

Although the reader may appreciate the amount of work that has been done in this thesis, still some limitations are present. First, the vehicle model features only seven degrees of freedom plus roll and pitch that are considered in the load transfers. It is clear that suspension modelling is missing and should probably be the first component to be added in a future work in order to understand sprung and unsprung mass behaviours. The natural choice would be the use of a Multi-Body Dynamics software like CarSim, ADAMS or MotionView and the consequent setting of a co-simulation environment with MATLAB-Simulink where the controller is implemented.

Lastly, the proposed controller should be implemented in a real Electronic Control Unit and tested on a real vehicle to verify its merit in practical applications.

Besides, the Torque Vectoring Controller needs the knowledge of the vehicle side slip angle since that is one of the two control variables. Its measurement with an optical sensor can be as expensive as the whole vehicle itself, thus estimation methods are available to solve this problem. However, an important assumption made in this research is that β is exactly known, since the development of an observer would have been too time consuming. The next step would be clearly the implementation of a vehicle side slip angle estimation method for testing the controller in the real situation in which β is subjected to uncertainties.

Another limitation of the present work consists in the lack of electric powertrain modelling beyond the electric motors, i.e., the inverter and battery. The study has focused on vehicle dynamics and torque vectoring controllers, and the electric motors have been treated just as the actuators. However, the torque allocation does not consider the battery State of Charge (SoC) or the thermal limitations of the inverter. Adding inverter and battery models would be beneficial in order to take into account the remaining state of charge of the battery and possibly modify the torque distribution according to the battery status.

6.4 Research contributions

The present thesis focused on the development of an integrated and modular vehicle dynamics controller for Battery Electric Vehicles. A real-time tuning procedure for the parameters of the Sliding Mode Control applied to the TVC has been shown, and no articles about that were found in the literature. Besides, the yaw acceleration formula was obtained and it proved to be well representative of the vehicle yaw acceleration. Its usage in the derivative feedback term inside the TVC allowed improvements in path errors and state errors under a huge variety of driving scenarios, even though the proposed controller did not outperform some available in literature with the SMC only.

Another important contribution is that the developed controller can work for different BEV architectures, i.e., a unique control structure can deal with several electric motors configurations. Although the parameters optimization was carried out considering the 4IWM EV, the same TVC is able to allocate the torque when one of the other three configurations implemented here is chosen. Besides, this feature allows the benchmarking of different EV architectures without the need to develop a new controller each time.

Lastly, the SMC-based cruise control has the distinguishing feature of tuning parameters in real-time. No articles in literature were found with such a design choice. There is no overshoot when reaching the target speed and good responsiveness for high velocity errors is achieved.

References

- [1] Romeo Danielis, Mariangela Scorrano, and Marco Giansoldati. “Decarbonising transport in Europe: Trends, goals, policies and passenger car scenarios”. In: *Research in Transportation Economics* (2021), p. 101068.
- [2] Romana Čížinská and Jana Chládková. “Selected Impacts of Regulation (EU) 2019/631 On Value Creation in the Automotive Industry”. In: *Financial Internet Quarterly* 17.3 (2021), pp. 76–87.
- [3] Florian Kellner, Bernhard Lienland, and Sebastian Utz. “A multi-criteria decision-making approach for assembling optimal powertrain technology portfolios in low GHG emission environments”. In: *Journal of Industrial Ecology* 25.6 (2021), pp. 1412–1429.
- [4] Lin Zhang et al. “Model predictive control for integrated longitudinal and lateral stability of electric vehicles with in-wheel motors”. In: *IET Control Theory & Applications* 14.18 (2020), pp. 2741–2751.
- [5] Society of Automotive Engineers. *Automotive Stability Enhancement Systems*. Information Report. SAE J2564. 2017.
- [6] Junya Yamakawa and Keiji Watanabe. “A method of optimal wheel torque determination for independent wheel drive vehicles”. In: *Journal of Terramechanics* 43.3 (2006). 7th Asia-Pacific Conference of the International Society of Terrain Vehicle-Systems (ISTVS), pp. 269–285.
- [7] Lu Xiong et al. “Vehicle dynamics control of four in-wheel motor drive electric vehicle using gain scheduling based on tyre cornering stiffness estimation”. In: *Vehicle System Dynamics* 50.6 (2012), pp. 831–846.
- [8] Leonardo De Novellis, Aldo Sorniotti, and Patrick Gruber. “Wheel Torque Distribution Criteria for Electric Vehicles With Torque-Vectoring Differentials”. In: *IEEE Transactions on Vehicular Technology* 63.4 (2014), pp. 1593–1602.
- [9] Cheng Lin and Zhifeng Xu. “Wheel Torque Distribution of Four-Wheel-Drive Electric Vehicles Based on Multi-Objective Optimization”. In: *Energies* 8.5 (2015), pp. 3815–3831.
- [10] Hongliang Zhou et al. “Coordinated Longitudinal and Lateral Motion Control for Four Wheel Independent Motor-Drive Electric Vehicle”. In: *IEEE Transactions on Vehicular Technology* 67.5 (2018), pp. 3782–3790.
- [11] Jianjun Hu et al. “An Optimal Torque Distribution Control Strategy for Four-Wheel Independent Drive Electric Vehicles Considering Energy Economy”. In: *IEEE Access* 7 (2019), pp. 141826–141837.

- [12] Iman Eman Mousavinejad, Yong Zhu, and Ljubo Vlacic. "Control strategies for improving ground vehicle stability: State-of-the-art review". In: *2015 10th Asian Control Conference (ASCC)*. 2015, pp. 1–8.
- [13] Cheng Lin et al. "A multi-objective optimal torque distribution strategy for four in-wheel motor drive electric vehicles". In: *IEEE Access* 7 (2019), pp. 64627–64640.
- [14] Lin Zhang et al. "An adaptive backstepping sliding mode controller to improve vehicle maneuverability and stability via torque vectoring control". In: *IEEE Transactions on Vehicular Technology* 69.3 (2020), pp. 2598–2612.
- [15] Dean Karnopp. *Vehicle Dynamics, Stability, and Control: Second Edition*. Apr. 2016, pp. 1–304.
- [16] Yong Li et al. "Review on torque distribution strategies for four in-wheel motor drive electric vehicles". In: *IOP Conference Series: Materials Science and Engineering*. Vol. 394. 4. IOP Publishing. 2018, p. 042041.
- [17] Kaibin Cao et al. "All-Wheel-Drive Torque Distribution Strategy for Electric Vehicle Optimal Efficiency Considering Tire Slip". In: *IEEE Access* 9 (2021), pp. 25245–25257.
- [18] Naouress Fatfouta and Julie Stal Le-Cardinal. "An ontology-based knowledge management approach supporting simulation-aided design for car crash simulation in the development phase". In: *Computers in Industry* 125 (2021), p. 103344.
- [19] Gregor Sievers et al. "Driving Simulation Technologies for Sensor Simulation in SIL and HIL Environments". In: *DSC 2018 Europe* (2018).
- [20] Cláudio Gomes et al. "Co-simulation: State of the art". In: (Feb. 2017).
- [21] Li Zhai, Tianmin Sun, and Jie Wang. "Electronic Stability Control Based on Motor Driving and Braking Torque Distribution for a Four In-Wheel Motor Drive Electric Vehicle". In: *IEEE Transactions on Vehicular Technology* 65.6 (2016), pp. 4726–4739.
- [22] Runlin He et al. "Optimal torque distribution strategy considering energy loss and tire adhesion for 4WD electric vehicles". In: *2017 IEEE Transportation Electrification Conference and Expo, Asia-Pacific (ITEC Asia-Pacific)*. 2017, pp. 1–6.
- [23] Shengqin Li and Le He. "Co-simulation study of vehicle ESP system based on ADAMS and MATLAB". In: *JSW* 6 (May 2011), pp. 866–872.
- [24] Dong Hyun Kim, Sung Ho Hwang, and Hyun Kim. "Advanced Active Safety System Using Separated Front and Rear Motor Control for a 4WD Hybrid Electric Vehicle". In: *Solid State Phenomena* 120 (Feb. 2007), pp. 223–228.
- [25] Jennifer Leslie Johrendt. "Optimizing road test simulation using neural network modeling techniques". In: (2005).
- [26] Bruce P Minaker. *Fundamentals of vehicle dynamics and modelling: A textbook for engineers with illustrations and examples*. John Wiley & Sons, 2019.
- [27] Giancarlo Genta and Lorenzo Morello. *The automotive chassis: volume 2: system design*. Springer Nature, 2019.
- [28] R Rajamani. *Vehicle Dynamics and Control*. Jan. 2006.

- [29] Giancarlo Genta and Lorenzo Morello. *The Automotive Chassis: Vol. 1: Components Design*. Jan. 2009.
- [30] Andrea Tonoli. *Tires*. Course material for Motor Vehicle Design - Project 1. Politecnico di Torino, November 2019.
- [31] H. Pacejka. *Tire and Vehicle Dynamics*. Jan. 2012.
- [32] Bo Leng et al. "Robust variable structure anti-slip control method of a distributed drive electric vehicle". In: *IEEE Access* 8 (2020), pp. 162196–162208.
- [33] Xudong Zhang and Dietmar Göhlich. "Integrated traction control strategy for distributed drive electric vehicles with improvement of economy and longitudinal driving stability". In: *Energies* 10.1 (2017), p. 126.
- [34] Marco Gadola et al. "Development and validation of a Kalman filter-based model for vehicle slip angle estimation". In: *Vehicle System Dynamics* 52.1 (2014), pp. 68–84.
- [35] Daniel Chindamo, Basilio Lenzo, and Marco Gadola. "On the vehicle sideslip angle estimation: a literature review of methods, models, and innovations". In: *applied sciences* 8.3 (2018), p. 355.
- [36] Takao Kobayashi et al. "Direct yaw moment control and power consumption of in-wheel motor vehicle in steady-state turning". In: *Vehicle System Dynamics* 55.1 (2017), pp. 104–120.
- [37] Takao Kobayashi et al. *Efficient direct yaw moment control during acceleration and deceleration while turning (first report)*. Tech. rep. SAE Technical Paper, 2016.
- [38] Michele Vignati, Edoardo Sabbioni, and Federico Cheli. "A torque vectoring control for enhancing vehicle performance in drifting". In: *Electronics* 7.12 (2018), p. 394.
- [39] Andoni Medina, Guillermo Bistue, and Angel Rubio. "Comparison of typical controllers for direct yaw moment control applied on an electric race car". In: *Vehicles* 3.1 (2021), pp. 127–144.
- [40] Hiroshi Himeno, Etsuo Katsuyama, and Takao Kobayashi. *Efficient direct yaw moment control during acceleration and deceleration while turning (second report)*. Tech. rep. SAE Technical Paper, 2016.
- [41] Dongmei Wu et al. "Torque distribution of a four in-wheel motors electric vehicle based on a PMSM system model". In: *Proceedings of the Institution of Mechanical Engineers, Part D: Journal of Automobile Engineering* 232.13 (2018), pp. 1828–1845.
- [42] Lu Xiong and Zhuoping Yu. "Control allocation of vehicle dynamics control for a 4 in-wheel-motored EV". In: *2009 2nd International Conference on Power Electronics and Intelligent Transportation System (PEITS)*. Vol. 2. IEEE. 2009, pp. 307–311.
- [43] Yu Zhao and Chengning Zhang. "Electronic stability control for improving stability for an eight in-wheel motor-independent drive electric vehicle". In: *Shock and Vibration* 2019 (2019).
- [44] *All technical specs in one car database*. <https://www.cars-data.com/en/>. Accessed: 2022-04-19. 2021.

- [45] Claudio Maino. *Modeling hybrid and electric vehicles for energy optimization*. Course material for Energy Management in Hybrid and Electric Vehicles - Applied Lecture 2. Politecnico di Torino, May 2021.
- [46] Kadir Cumali and Ersin Armagan. “Steering Control of a Vehicle Equipped with Automated Lane Centering System”. In: *2019 11th International Conference on Electrical and Electronics Engineering (ELECO)*. 2019, pp. 820–824.
- [47] Bruce Minaker. *Driver Model*. Personal communication. University of Windsor, April 2022.
- [48] Carlo Novara. *Lane Keeping Assist*. Course material for Driver Assistance System Design - Part A. Politecnico di Torino, April 2021.
- [49] Juyong Kang, Jinho Yoo, and Kyongsu Yi. “Driving control algorithm for maneuverability, lateral stability, and rollover prevention of 4WD electric vehicles with independently driven front and rear wheels”. In: *IEEE Transactions on vehicular technology* 60.7 (2011), pp. 2987–3001.
- [50] Kanghyun Nam, Hiroshi Fujimoto, and Yoichi Hori. “Design of an adaptive sliding mode controller for robust yaw stabilisation of in-wheel-motor-driven electric vehicles”. In: *International Journal of Vehicle Design* 67.1 (2015), pp. 98–113.
- [51] Eman Mousavinejad et al. “Integrated control of ground vehicles dynamics via advanced terminal sliding mode control”. In: *Vehicle System Dynamics* 55.2 (2017), pp. 268–294.
- [52] Hasan Alipour, Mohammad Bagher Bannae Sharifian, and Mehran Sabahi. “A modified integral sliding mode control to lateral stabilisation of 4-wheel independent drive electric vehicles”. In: *Vehicle System Dynamics* 52.12 (2014), pp. 1584–1606.
- [53] Kyoungseok Han et al. “Development of a traction control system using a special type of sliding mode controller for hybrid 4WD vehicles”. In: *IEEE transactions on vehicular technology* 67.1 (2017), pp. 264–274.
- [54] Bosch Motorsport. *Steering Wheel Angle Sensor LWS*. https://www.bosch-motorsport.com/content/downloads/Raceparts/Resources/pdf/DataSheet_191153675_Steering_Wheel_Angle_Sensor_LWS.pdf. Accessed: 2022-06-27. 2021.
- [55] Angelo Bonfitto. *Sensors, control devices and signal processing for assisted driving*. Course material for Driver Assistance System Design - Part B. Politecnico di Torino, April 2021.
- [56] Ajinkya Chandratre, Ajit Bhatjire, and Pankaj Chaudhary. “Study of cruise control system used vehicle”. In: *International Journal of Advance Research in Science and Engineering* 5 (2016).
- [57] Steven C Chapra, Raymond P Canale, et al. *Numerical methods for engineers*. Vol. 1221. Mcgraw-hill New York, 2011.
- [58] Luca Pugi et al. “Brake blending and torque vectoring of road electric vehicles: a flexible approach based on smart torque allocation”. In: *IJEHV* 12.2 (2020), p. 87.
- [59] *Passenger cars — Test track for a severe lane-change manoeuvre*. <https://cdn.standards.iteh.ai/samples/67973/daa839ed4aca420788d9b4a51cd6cc95/ISO-3888-1-2018.pdf>. Accessed: 2022-04-12. 2018.

-
- [60] D Korzeniowski and G Ślaski. “Method of planning a reference trajectory of a single lane change manoeuver with Bezier curve”. In: *IOP Conference Series: Materials Science and Engineering*. Vol. 148. 1. IOP Publishing, 2016, p. 012012.
- [61] Cataldo Guaragnella. *Center of gravity of a person in sitting posture*. https://www.researchgate.net/figure/Center-of-gravity-of-a-person-in-sitting-posture-Body-segmental-Lengths-are-reported-in_fig2_256203106. Accessed: 2022-06-13. 2013.

Appendix A

Equations of the Sliding Mode Control for TVC

$$s = \frac{\rho}{|\Delta r|_{\max}} |r - r_d| + \frac{1 - \rho}{|\Delta \beta|_{\max}} |\beta - \beta_d| \quad (\text{A.1})$$

$$\dot{s} = -\epsilon \operatorname{sgn}(s) - k_d s \quad (\text{A.2})$$

Keeping in mind the following differentiation rule for the module of a function:

$$\frac{d\|f(x)\|}{dx} = \operatorname{sgn} f(x) \frac{df(x)}{dx} \quad (\text{A.3})$$

it is possible to differentiate Equation A.1 and combine the result with Equation A.2:

$$\frac{\rho}{|\Delta r|_{\max}} \operatorname{sgn}(r - r_d)(\dot{r} - \dot{r}_d) + \frac{1 - \rho}{|\Delta \beta|_{\max}} \operatorname{sgn}(\beta - \beta_d)(\dot{\beta} - \dot{\beta}_d) = -\epsilon \operatorname{sgn}(s) - k_d s \quad (\text{A.4})$$

Reminding the following property of the sgn function:

$$\operatorname{sgn} f(x) \cdot \operatorname{sgn} g(x) = \operatorname{sgn}(f(x) \cdot g(x)) \quad (\text{A.5})$$

the calculations below are performed to obtain \dot{r}_c as in Equation 4.16:

$$\dot{r} = \dot{r}_d + \frac{|\Delta r|_{\max}}{\rho \operatorname{sgn}(r - r_d)} \left[-\epsilon \operatorname{sgn}(s) - k_d s - \frac{1 - \rho}{|\Delta \beta|_{\max}} \operatorname{sgn}(\beta - \beta_d)(\dot{\beta} - \dot{\beta}_d) \right] \quad (\text{A.6})$$

$$\dot{r} = \dot{r}_d - \frac{\epsilon |\Delta r|_{\max}}{\rho \operatorname{sgn}(r - r_d)} - \frac{k_d |\Delta r|_{\max}}{\rho \operatorname{sgn}(r - r_d)} s - \frac{1 - \rho}{|\Delta \beta|_{\max}} \frac{|\Delta r|_{\max}}{\rho \operatorname{sgn}(r - r_d)} \operatorname{sgn}(\beta - \beta_d)(\dot{\beta} - \dot{\beta}_d) \quad (\text{A.7})$$

$$\dot{r}_c = \dot{r}_d - \frac{|\Delta r|_{max}}{\rho} \{ \epsilon \operatorname{sgn}[(r - r_d)s] + k_d s \operatorname{sgn}(r - r_d) \} - \frac{1 - \rho}{\rho} \frac{|\Delta r|_{max}}{|\Delta \beta|_{max}} \operatorname{sgn}[(r - r_d)(\beta - \beta_d)](\dot{\beta} - \dot{\beta}_d) \quad (\text{A.8})$$

Appendix B

Equation of the yaw acceleration prediction for TVC

$$v_x = rR \quad (\text{B.1})$$

Differentiating Equation B.1, \dot{r} is eventually obtained:

$$\dot{v}_x = \dot{r}R + r\dot{R} \quad (\text{B.2})$$

$$\dot{r} = \frac{\dot{v}_x - r\dot{R}}{R} = \frac{\dot{v}_x - \frac{v_x}{R}\dot{R}}{R} = \frac{\dot{v}_x R - v_x \dot{R}}{R^2} \quad (\text{B.3})$$

Now, the curvature gain equation is introduced to get the radius of curvature and its derivative:

$$\frac{1}{R\delta} = \frac{1}{l + k_{us} \frac{v_x^2}{g}} \quad (\text{B.4})$$

$$R = \frac{1}{\delta} l + \frac{1}{\delta} k_{us} \frac{v_x^2}{g} \quad (\text{B.5})$$

$$\dot{R} = -\frac{1}{\delta^2} \dot{\delta} l - \frac{1}{\delta^2} \dot{\delta} k_{us} \frac{v_x^2}{g} + \frac{1}{\delta} k_{us} \frac{2v_x \dot{v}_x}{g} \quad (\text{B.6})$$

Equations B.5 and B.6 are substituted into B.3 to get the final result showing the yaw acceleration prediction:

$$\dot{r}_{pred} = \frac{\dot{v}_x \frac{1}{\delta} \left(l + k_{us} \frac{v_x^2}{g} \right) - v_x \left(-\frac{1}{\delta^2} \dot{\delta} l - \frac{1}{\delta^2} \dot{\delta} k_{us} \frac{v_x^2}{g} + \frac{1}{\delta} \frac{2v_x \dot{v}_x}{g} \right)}{\left(\frac{1}{\delta} \left(l + k_{us} \frac{v_x^2}{g} \right) \right)^2} \quad (\text{B.7})$$

$$\dot{r}_{pred} = \frac{\dot{v}_x \delta \left(l + k_{us} \frac{v_x^2}{g} \right) - v_x \left(-\dot{\delta} \left(l + k_{us} \frac{v_x^2}{g} \right) + \delta \frac{2v_x \dot{v}_x}{g} \right)}{\left(l + k_{us} \frac{v_x^2}{g} \right)^2} \quad (\text{B.8})$$

Appendix C

MATLAB scripts

C.1 Extract of the main script

```

1 %% vehicle data
2 a=1.130; % front wheelbase [m]
3 b=1.470; % rear wheelbase [m]
4 l=2.6; % wheelbase [m]
5 h=0.511; % CG height [m]
6 tf=1.575; % front track [m]
7 tr=1.584; % rear track [m]
8 Jz=2045; % moment of inertia about z [kg m^2]
9 S=1.85; % frontal area [m^2]
10 Cx=0.290; % drag coefficient [-]
11 R=0.2891; % wheel radius [m]
12 m=1510; % curb weight + passenger [kg]
13 g=9.81;
14 Re=0.98*R; % effective radius
15 Rl=0.94*R; % loaded radius
16
17 %% initial conditions
18 ts=10; % simulation time [s]
19 v0=85.2/3.6; % initial speed [m/s]
20
21 drivermodel=2; % 0 no driver model, 1 single lane change, 2
    double lane change
22 refPoses=[0;0;0]; % initialization of the reference poses vector
23 y_dd=0; % initialization of the trajectory curvature
24
25 if drivermodel==1 % single lane change SLC
26 x=[0 15 45 70]';

```

```

27 y=[1.115 1.115 4.705 4.705]'; % reference points for vehicle CG
28 Xr=[0:0.1:70]';
29 Yr=pchip(x,y,Xr); % reference trajectory for vehicle CG
30 Xr_low=[0 15 45 70];
31 Yr_low=[0.9 0.9 4.4 4.4]; % lower limit reference trajectory for
    vehicle CG
32 Xr_high=[0 15 45 70];
33 Yr_high=[1.33 1.33 5.01 5.01]; % upper limit reference trajectory
    for vehicle CG
34 X_low=[0 45 45 70];
35 Y_low=[0 0 3.5 3.5]; % lower limit track
36 X_high=[0 15 15 70];
37 Y_high=[2.23 2.23 5.91 5.91]; %upper limit track
38
39 else if drivermodel==2 % double lane change DLC
40 x=[0 15 45 70 95 125]';
41 y=[1.115 1.115 4.705 4.705 1.295 1.295]'; % reference points for
    vehicle CG
42 Xr=[0:0.1:125]';
43 Yr=pchip(x,y,Xr); % reference trajectory for vehicle CG
44 Xr_low=[0 15 45 70 95 125];
45 Yr_low=[0.9 0.9 4.4 4.4 0.9 0.9]; % lower limit reference
    trajectory for vehicle CG
46 Xr_high=[0 15 45 70 95 125];
47 Yr_high=[1.33 1.33 5.01 5.01 1.69 1.69]; % upper limit reference
    trajectory for vehicle CG
48 X_low=[0 45 45 70 70 125];
49 Y_low=[0 0 3.5 3.5 0 0]; % lower limit track
50 X_high=[0 15 15 95 95 125];
51 Y_high=[2.23 2.23 5.91 5.91 2.59 2.59]; % upper limit track
52
53 else if drivermodel==0 % no driver model
54 Xr=zeros(100,1); % Simulink needs these vectors anyway
55 Yr=zeros(100,1);
56 psir=zeros(100,1);
57 refPoses=[Xr,Yr,psir];
58 y_dd=zeros(100,1);
59 end
60 end

```

```

61 end
62
63
64 x0=[v0;0;0]; % initial vehicle states vx0,vy0,r0
65 w0=ones(4,1)*v0/Re; % initial wheel angular velocity [rad/s]
66 X0=[0;0;0]; % vehicle initial coordinates X,Y,PSI
67 T_brake_max=-400; % maximum torque from one single brake [Nm]
68
69 if drivermodel==1 || drivermodel==2
70 pp=pchip(x,y); % trajectory polynomial
71 p_der=fnder(pp,2); % polynomial of the trajectory's second-order
    derivative
72 y_dd=ppval(p_der,Xr); % trajectory curvature at the query points
73 psir=[atan2(diff(Yr),diff(Xr));0]; % reference yaw angle
74 refPoses=[Xr,Yr,psir]; % vehicle reference poses
75 psi0=refPoses(1,3); % initial yaw angle
76 X0=[0,1.115,psi0];
77 end
78 if drivermodel==0
79 psi0=0;
80 X0=[0,0,psi0];
81 end
82
83
84 %% plots tracking ability
85 e_ct_yawacceleration_norm=norm(e_ct_yawacceleration.data); %
    cross track error norm-2
86 e_h_yawacceleration_norm=norm(e_h_yawacceleration.data); %
    heading error norm-2
87 beta_yawacceleration_norm=norm(yawacceleration_state.data(:,2));
    % vehicle side slip angle norm-2
88 yawrate_yawacceleration_norm=norm(yawacceleration_state.data(:,3)
    ); % yaw rate norm-2
89 betaerror_yawacceleration_norm=norm(state_error.data(:,1)); %
    vehicle side slip angle error norm-2
90 yawrateerror_yawacceleration_norm=norm(state_error.data(:,2)); %
    yaw rate error norm-2

```

C.2 Vehicle model functions

C.2.1 Three main DOF

```

1      function xdot = threeDOFmodel(delta ,Fx,Fy,x)
2
3      a=1.130; % front wheelbase [m]
4      b=1.470; % rear wheelbase [m]
5      l=2.6; % wheelbase [m]
6      h=0.511; % CG height [m]
7      tf=1.575; % front track [m]
8      tr=1.584; % rear track [m]
9      Jz=2045; % moment of inertia about z [kg m^2]
10     S=1.85; % frontal area [m^2]
11     Cx=0.290; % drag coefficient [-]
12     R=0.2891; % wheel radius [m]
13     m=1510; % curb weight + passenger [kg]
14     Cf=60000; % cornering stiffness of a single front wheel [
        N/rad]
15     Cr=60000; % cornering stiffness of a single rear wheel [N
        /rad]
16     rho=1.225; %air density [kg/m^3]
17     f=10^-2; %rolling resistance coefficient
18     g=9.81;
19
20     v=x(1);
21     vy=x(2);
22     psidot=x(3);
23
24     Fx1=Fx(1);
25     Fx2=Fx(2);
26     Fx3=Fx(3);
27     Fx4=Fx(4);
28     Fy1=Fy(1);
29     Fy2=Fy(2);
30     Fy3=Fy(3);
31     Fy4=Fy(4);
32
33     vdot=vy*psidot -1/m*(0.5*rho*S*Cx*v^2+f*m*g)+1/m*(( Fx1+Fx2
        )*cos(delta) -(Fy1+Fy2)*sin(delta)+Fx3+Fx4); %
        longitudinal DOF

```

```

34     vydot=-v*psidot+1/m*((Fy1+Fy2)*cos(delta)+(Fx1+Fx2)*sin(delta)+Fy3+Fy4); % lateral DOF
35     psidotdot=1/Jz*((Fx1+Fx2)*sin(delta)*a+(Fy1+Fy2)*cos(delta)*a-(Fy3+Fy4)*b+(Fx2-Fx1)*cos(delta)*tf/2+(Fx4-Fx3)*tr/2+(Fy1-Fy2)*sin(delta)*tf/2); % yaw DOF

```

C.2.2 Wheel dynamics

```

1     function wdot=wheel_dyn(Tw,Fx)
2
3     %% vehicle data (Ford Escort 1985)
4     R=0.2891; % wheel radius [m]
5     Re=0.98*R;
6     Rl=0.94*R;
7     Jw=0.6; % wheel inertia [kg/ m^2]
8     Jm=0.3; % electric motor inertia [kg m^2]
9
10    Tw1=Tw(1);
11    Tw2=Tw(2);
12    Tw3=Tw(3);
13    Tw4=Tw(4);
14    Fx1=Fx(1);
15    Fx2=Fx(2);
16    Fx3=Fx(3);
17    Fx4=Fx(4);
18
19    %% wheel dynamics
20    wdot1=Tw1/(Jw+Jm)-1/(Jw+Jm)*Fx1*Rl;
21    wdot2=Tw2/(Jw+Jm)-1/(Jw+Jm)*Fx2*Rl;
22    wdot3=Tw3/(Jw+Jm)-1/(Jw+Jm)*Fx3*Rl;
23    wdot4=Tw4/(Jw+Jm)-1/(Jw+Jm)*Fx4*Rl;

```

C.2.3 Tire vertical loads

```

1     function Fz=vertical_forces(ax,ay)
2
3     a=1.130; % front wheelbase [m]
4     b=1.470; % rear wheelbase [m]
5     l=2.6; % wheelbase [m]
6     h=0.511; % CG height [m]

```

```

7      tf=1.575; % front track [m]
8      tr=1.584; % rear track [m]
9      Jz=2045; % moment of inertia about z [kg m^2]
10     S=1.85; % frontal area [m^2]
11     Cx=0.290; % drag coefficient [-]
12     R=0.2891; % wheel radius [m]
13     m=1510; % curb weight + passenger [kg]
14     g=9.81;
15
16     Fz=zeros(4,1);
17     Fz(1)=m*g/2*b/l -m*ax/2*h/l -m*ay*b/l*h/tf; % left front
18     Fz(2)=m*g/2*b/l -m*ax/2*h/l +m*ay*b/l*h/tf; % right front
19     Fz(3)=m*g/2*a/l +m*ax/2*h/l -m*ay*a/l*h/tr; % left rear
20     Fz(4)=m*g/2*a/l +m*ax/2*h/l +m*ay*a/l*h/tr; % right rear
21
22     for i=1:4
23         if Fz(i)<1
24             Fz(i)=1; % to avoid negative vertical loads when a wheel
                       % lifts from the ground
25         end
26     end

```

C.2.4 Pacejka's Magic Formula

```

1      function [Fx,Fy] = fcn(alpha,Fz,sigma,scalingx,scalingy,
2                               mux,muy)
3
4      Fx=zeros(4,1);
5      Fy=zeros(4,1);
6
7      Fz=Fz/10^3; % Pacejka's formula wants Fz in kN
8      sigma=sigma*100; % sigma in percentage (-100,+100)
9      alpha=alpha*180/pi; % alpha in degrees
10     gamma=0; % camber angle is not considered (assumption)
11
12     % Pacejka's coefficients for longitudinal forces
13     b0=1.6500;
14     b1=-7.61;
15     b2=1122.60;
16     b3=-7.3600E-03;

```



```

16         b4=144.82;
17         b5=-7.6614E-02;
18         b6=-3.8600E-03;
19         b7=8.5055E-02;
20         b8=7.5719E-02;
21         b9=2.3655E-02;
22         b10=2.3655E-02;
23
24         % computation of tire longitudinal forces
25         for i=1:4
26             C=b0;
27             D=mux(i)*1000*Fz(i);
28             BCDx=(b3*Fz(i)^2+b4*Fz(i))*exp(-b5*Fz(i));
29             B=BCDx/(C*D);
30             E=b6*Fz(i)^2+b7*Fz(i)+b8;
31             Sh=b9*Fz(i)+b10;
32             Sv=0;
33             Fx(i)=scalingx(i)*D*sin(C*atan(B*(1-E)*(sigma(i)+Sh)+E*
                 atan(B*(sigma(i)+Sh))))+Sv;
34         end
35
36         % Pacejka's coefficients for lateral forces
37         a0=1.7;
38         a1=-55.2;
39         a2=1271.3;
40         a3=1601.8;
41         a4=6.4946;
42         a5=0.0;
43         a6=-0.3875;
44         a7=1.0;
45         a8=0.0;
46         a9=0.0;
47         a10=0.1;
48         a11=-8.0;
49         a112=0.0;
50         a12=0.0;
51         a13=0.0;
52
53         % computation of tire lateral forces

```

```

54     for i=1:4
55         C=a0;
56         D=muy(i)*1000*Fz(i);
57         BCDy(i)=a3*sin(2*atan2(Fz(i),a4))*(1-a5*abs(gamma));
58         B=BCDy(i)/(C*D);
59         E=a6*Fz(i)+a7;
60         Sh=a8*gamma+a9*Fz(i)+a10;
61         a11=a111*Fz(i)+a112;
62         Sv=a11*gamma*Fz(i)+a12*Fz(i)+a13;
63         Fy(i)=-scalingy(i)*D*sin(C*atan(B*(1-E)*(alpha(i)+Sh)+E*
           atan(B*(alpha(i)+Sh))))+Sv;
64     end

```

C.2.5 Tire side slip angles

```

1     function alpha = fcn(delta,x)
2
3     a=1.130; % front wheelbase [m]
4     b=1.470; % rear wheelbase [m]
5     l=2.6; % wheelbase [m]
6     h=0.511; % CG height [m]
7     tf=1.575; % front track [m]
8     tr=1.584; % rear track [m]
9     Jz=2045; % moment of inertia about z [kg m^2]
10    S=1.85; % frontal area [m^2]
11    Cx=0.290; % drag coefficient [-]
12    R=0.2891; % wheel radius [m]
13    m=1510; % curb weight + passenger [kg]
14
15    v=x(1);
16    vy=x(2);
17    psidot=x(3);
18
19    alpha=zeros(4,1);
20    alpha(1)=atan2((vy+psidot*a),(v-tf/2*psidot))-delta;
21    alpha(2)=atan2((vy+psidot*a),(v+tf/2*psidot))-delta;
22    alpha(3)=atan2((vy-psidot*b),(v-tr/2*psidot));
23    alpha(4)=atan2((vy-psidot*b),(v+tr/2*psidot));

```

C.2.6 Tire slip ratio and scaling factors

```

1      function [sigma , vsx , vsy , scalingx , scalingy] = sigma_eval(
        delta , v , vy , psidot , w)
2
3      R=0.2891;
4      Re=0.98*R;
5      a=1.130; % front wheelbase [m]
6      b=1.470; % rear wheelbase [m]
7      l=2.6; % wheelbase [m]
8      h=0.511; % CG height [m]
9      tf=1.575; % front track [m]
10     tr=1.584; % rear track [m]
11     Jz=2045; % moment of inertia about z [kg m^2]
12     S=1.85; % frontal area [m^2]
13     Cx=0.290; % drag coefficient [-]
14     m=1510; % curb weight + passenger [kg]
15
16     % wheel hub velocities in vehicle reference frame
17     vxw=zeros(4,1);
18     vxw(1)=v-psidot*tf/2;
19     vxw(2)=v+psidot*tf/2;
20     vxw(3)=v-psidot*tr/2;
21     vxw(4)=v+psidot*tr/2;
22
23     vyw=zeros(4,1);
24     vyw(1)=vy+psidot*a;
25     vyw(2)=vy+psidot*a;
26     vyw(3)=vy-psidot*b;
27     vyw(4)=vy-psidot*b;
28
29     % wheel hub velocities in tire reference frame
30     vlong_tire=zeros(4,1);
31     vlong_tire(1)=vxw(1)*cos(delta)+vyw(1)*sin(delta);
32     vlong_tire(2)=vxw(2)*cos(delta)+vyw(2)*sin(delta);
33     vlong_tire(3)=vxw(3);
34     vlong_tire(4)=vxw(4);
35
36     vlat_tire=zeros(4,1);
37     vlat_tire(1)=-vxw(1)*sin(delta)+vyw(1)*cos(delta)+10^-6;

```

```

38     vlat_tire(2)=-vxw(2)*sin(delta)+vyw(2)*cos(delta)+10^-6;
39     vlat_tire(3)=vyw(3)+10^-6;
40     vlat_tire(4)=vyw(4)+10^-6;
41
42     % tire slip velocities
43     vsx=zeros(4,1);
44     vsy=zeros(4,1);
45     for i=1:4
46         vsx(i)=abs(w(i)*Re-vlong_tire(i))+10^-6;
47         vsy(i)=abs(vlat_tire(i))+10^-6;
48     end
49
50     % scaling factors
51     scalingx=zeros(4,1);
52     scalingy=zeros(4,1);
53     for i=1:4
54         scalingx(i)=vsx(i)/(sqrt(vsx(i)^2+vsy(i)^2));
55         scalingy(i)=vsy(i)/(sqrt(vsx(i)^2+vsy(i)^2));
56     end
57
58     % longitudinal tire slip ratio
59     w1=w(1);
60     w2=w(2);
61     w3=w(3);
62     w4=w(4);
63     sigma1=(w1*Re-vlong_tire(1))/vlong_tire(1);
64     sigma2=(w2*Re-vlong_tire(2))/vlong_tire(2);
65     sigma3=(w3*Re-vlong_tire(3))/vlong_tire(3);
66     sigma4=(w4*Re-vlong_tire(4))/vlong_tire(4);
67
68     sigma=[sigma1 sigma2 sigma3 sigma4]';

```

C.2.7 Steering angle correction from driver model

```

1     function delta_error= fcn(e_ct,e_h,y_dd,im)
2
3     l=2.6; % wheelbase [m]
4
5     delta_error = l*y_dd(im)+1.1*e_h + 0.1*e_ct;

```

C.3 Controller functions

C.3.1 Reference values from bicycle model

```

1 function [beta_desired,psidot_desired] = fcn(v,delta)
2
3 a=1.130; % front wheelbase [m]
4 b=1.470; % rear wheelbase [m]
5 l=2.6; % wheelbase [m]
6 h=0.511; % CG height [m]
7 tf=1.575; % front track [m]
8 tr=1.584; % rear track [m]
9 Jz=2045; % moment of inertia about z [kg m^2]
10 S=1.85; % frontal area [m^2]
11 Cx=0.290; % drag coefficient [-]
12 m=1510; % curb weight + passenger [kg]
13 R=0.2891; % wheel radius [m]
14 rho=1.225; %air density [kg/m^3]
15 f=10^-2; % rolling resistance coefficient
16 g=9.81;
17
18 Cf=120000; % front axle cornering stiffness [N/rad]
19 Cr=120000; % rear axle cornering stiffness [N/rad]
20
21 k_us=m*g/l*(b*Cr-a*Cf)/(Cf*Cr); % understeering coefficient
22 beta_desired=(b-(a*m*v^2)/(Cr*l))/(l+k_us*v^2/g)*delta; % desired
    vehicle side slip angle
23 psidot_desired=v/(l+k_us*v^2/g)*delta; % desired yaw rate

```

C.3.2 Reference value limits

```

1 function state_des = fcn(x_des,v,mux)
2
3 g=9.81; % [m/s^2]
4
5 beta_des=x_des(1); % desired vehicle side slip angle
6 psidot_des=x_des(2); % desired yaw rate
7
8 mu_avg=(mux(1)+mux(2)+mux(3)+mux(4))/4; % average friction
    coefficient on the four wheels
9

```

```

10 yawrate_lim=0.85*mu_avg*g/v; % yaw rate limit
11 beta_lim=atan(0.02*mu_avg*g); % vehicle side slip angle limit
12 if abs(beta_des)>beta_lim
13     beta_des=beta_lim*sign(beta_des);
14 end
15 if abs(psidot_des)>yawrate_lim
16     psidot_des=yawrate_lim*sign(psidot_des);
17 end
18
19 state_des=[beta_des;psidot_des]; % final desired vehicle states

```

C.3.3 Yaw acceleration prediction formula

```

1 function [psidotdot_pred,contr] = fcn(xdot,v,delta,deltadot)
2
3 a=1.130; % front wheelbase [m]
4 b=1.470; % rear wheelbase [m]
5 l=2.6; % wheelbase [m]
6 h=0.511; % CG height [m]
7 tf=1.575; % front track [m]
8 tr=1.584; % rear track [m]
9 Jz=2045; % moment of inertia about z [kg m^2]
10 S=1.85; % frontal area [m^2]
11 Cx=0.290; % drag coefficient [-]
12 R=0.2891; % wheel radius [m]
13 m=1510; % curb weight + passenger [kg]
14 g=9.81;
15
16 Cf=120000;
17 Cr=120000;
18 Kus=m*g/l*(b/Cf-a/Cr);
19
20 vdot=xdot(1);
21 psidotdot_pred=(vdot/delta*(1+Kus*v^2/g)-v*(-1/delta^2*deltadot*1
    -1/delta^2*deltadot*Kus*v^2/g+1/delta*Kus^2*v*vdot/g))/(1/
    delta*(1+Kus*v^2/g))^2; % yaw acceleration prediction
22
23 contr1=vdot/delta*(1+Kus*v^2/g)/((1/delta*(1+Kus*v^2/g))^2);
24 contr2=-v*(-deltadot*(1/delta^2*l+1/delta^2*Kus*v^2/g))/((1/delta
    *(1+Kus*v^2/g))^2);

```

```

25  contr3=(-v/delta*Kus*2*v*vdot/g)/((1/delta*(1+Kus*v^2/g))^2);
26
27  % boundaries for yaw acceleration values
28  if psidotdot_pred > 4
29  psidotdot_pred=4;
30  end
31  if psidotdot_pred < -4
32  psidotdot_pred=-4;
33  end

```

C.3.4 TVC upper-layer controller

```

1
2  function [deltaMz,sy] = fcn(state_des,statedot_des,state,statedot
   ,delta,Fx,Fy,psidotdot_pred)
3
4  a=1.130; % front wheelbase [m]
5  b=1.470; % rear wheelbase [m]
6  l=2.6; % wheelbase [m]
7  h=0.511; % CG height [m]
8  tf=1.575; % front track [m]
9  tr=1.584; % rear track [m]
10 Jz=2045; % moment of inertia about z [kg m^2]
11 S=1.85; % frontal area [m^2]
12 Cx=0.290; % drag coefficient [-]
13 R=0.2891; % wheel radius [m]
14 m=1510; % curb weight + passenger [kg]
15 Cf=60000; % cornering stiffness of a single front wheel [N/rad]
16 Cr=60000; % cornering stiffness of a single rear wheel [N/rad]
17 rho=1.225; %air density [kg/m^3]
18 f=10^-2; %rolling resistance coefficient
19 g=9.81;
20
21 beta_des=state_des(1);
22 psidot_des=state_des(2);
23 betadot_des=statedot_des(1);
24 psidotdot_des=statedot_des(2);
25 beta=state(1);
26 psidot=state(2);
27 betadot=statedot(1);

```

```

28 | psidotdot=statedot(2);
29 |
30 | Fx1=Fx(1);
31 | Fx2=Fx(2);
32 | Fx3=Fx(3);
33 | Fx4=Fx(4);
34 | Fy1=Fy(1);
35 | Fy2=Fy(2);
36 | Fy3=Fy(3);
37 | Fy4=Fy(4);
38 |
39 | rho=0.6; % weight factor between psidot and beta
40 | deltar_max=0.1; % SMC parameter
41 | deltabeta_max=0.01; % SMC parameter
42 |
43 | sy=rho/deltar_max*abs((psidot-psidot_des))+(1-rho)/deltabeta_max*
    |     abs((beta-beta_des)); % sliding surface definition
44 | eps=1.5*abs(sy); % SMC parameter
45 | kd=abs(sy); % SMC parameter
46 |
47 | % saturation for first sgn function
48 | sgn1=(psidot-psidot_des)*sy;
49 | if abs(sgn1)<0.1
50 |     sgn1=sgn1/0.1;
51 | else
52 |     sgn1=sgn1/abs(sgn1);
53 | end
54 |
55 | % saturation for second sgn function
56 | sgn2=psidot-psidot_des;
57 | if abs(sgn2)<0.05
58 |     sgn2=sgn2/0.05;
59 | else
60 |     sgn2=sgn2/abs(sgn2);
61 | end
62 |
63 | % saturation for third sgn function
64 | sgn3=(psidot-psidot_des)*(beta-beta_des);
65 | if abs(sgn3)<0.1

```



```

66 sgn3=sgn3/0.1;
67 else
68 sgn3=sgn3/abs(sgn3);
69 end
70
71 psidotdot_c=psidotdot_des - eps*deltar_max/rho*sgn1+...
72 -kd*deltar_max/rho*sy*sgn2+...
73 -(1-rho)/rho*deltar_max/deltabeta_max*(betadot - betadot_des)*sgn3;
    % commanded yaw acceleration from SMC
74 deltaMz=Jz*(psidotdot_c+(psidotdot_pred - psidotdot)) - ((Fx1+Fx2)*
    sin(delta)*a+(Fy1+Fy2)*cos(delta)*a - (Fy3+Fy4)*b+(Fx2-Fx1)*cos(
    delta)*tf/2+(Fx4-Fx3)*tr/2+(Fy1-Fy2)*sin(delta)*tf/2); %
    corrective yaw moment with sum of SMC and derivative feedback
    contribution

```

C.3.5 Cruise Control

```

1      function [deltaFx , T_long] = fcn(psidot , vy , sv , v)
2
3      R=0.2891; % wheel radius [m]
4      Rl=0.94*R;
5      a=1.130; % front wheelbase [m]
6      b=1.470; % rear wheelbase [m]
7      l=2.6; % wheelbase [m]
8      h=0.511; % CG height [m]
9      tf=1.575; % front track [m]
10     tr=1.584; % rear track [m]
11     Jz=2045; % moment of inertia about z [kg m^2]
12     S=1.85; % frontal area [m^2]
13     Cx=0.290; % drag coefficient [-]
14     m=1510; % curb weight + passenger [kg]
15     Cf=60000; % cornering stiffness of a single front wheel [
        N/rad]
16     Cr=60000; % cornering stiffness of a single rear wheel [N
        /rad]
17     rho=1.225; %air density [kg/m^3]
18     f=10^-2; %rolling resistance coefficient
19     g=9.81;
20
21     % real-time tuned parameters

```

```

22     eps=0.9*abs(sv)+1;
23     kd=0.8*abs(sv);
24
25
26     deltaFx=m*(eps*(sv/(abs(sv)+0.1))+kd*sv)-m*vy*psidot
           +(0.5*rho*S*Cx*v^2+f*m*g); % corrective longitudinal
           force
27     T_long=deltaFx*Rl;

```

C.3.6 TVC lower-layer controller

Torque distribution coefficient

```

1     function k = fcn(Fz,conf)
2
3     Fz1=Fz(1);
4     Fz2=Fz(2);
5     Fz3=Fz(3);
6     Fz4=Fz(4);
7
8     if conf==0 % 4WM configuration
9         k1=Fz1/(Fz1+Fz2+Fz3+Fz4);
10        k2=Fz2/(Fz1+Fz2+Fz3+Fz4);
11        k3=Fz3/(Fz1+Fz2+Fz3+Fz4);
12        k4=Fz4/(Fz1+Fz2+Fz3+Fz4);
13    else if conf==1 % 2WM front axle
14        k1=(Fz1)/(Fz1+Fz2);
15        k2=(Fz2)/(Fz1+Fz2);
16        k3=0;
17        k4=0;
18    else if conf==2 % 2WM rear axle
19        k1=0;
20        k2=0;
21        k3=(Fz3)/(Fz3+Fz4);
22        k4=(Fz4)/(Fz3+Fz4);
23    else % 2 central motors one per each axle
24        k1=0.5*(Fz1+Fz2)/(Fz1+Fz2+Fz3+Fz4);
25        k2=0.5*(Fz1+Fz2)/(Fz1+Fz2+Fz3+Fz4);
26        k3=0.5*(Fz3+Fz4)/(Fz1+Fz2+Fz3+Fz4);
27        k4=0.5*(Fz3+Fz4)/(Fz1+Fz2+Fz3+Fz4);

```

```

28         end
29     end
30 end
31
32     k=[k1;k2;k3;k4];

```

Torque distribution strategy

```

1     function T = load_torque_distribution_EM(T_long,T_yaw,
2         T_throttle,T_brake_EM,k)
3
4     a=1.130; % front wheelbase [m]
5     b=1.470; % rear wheelbase [m]
6     l=2.6; % wheelbase [m]
7     h=0.511; % CG height [m]
8     tf=1.575; % front track [m]
9     tr=1.584; % rear track [m]
10    Jz=2045; % moment of inertia about z [kg m^2]
11    S=1.85; % frontal area [m^2]
12    Cx=0.290; % drag coefficient [-]
13    m=1510; % curb weight + passenger [kg]
14    R=0.2891; % wheel radius [m]
15    Rl=0.94*R;
16
17    T=zeros(4,1);
18    k1=k(1);
19    k2=k(2);
20    k3=k(3);
21    k4=k(4);
22
23    % load torque distribution
24    T1=k1*(T_long+T_throttle+T_brake_EM);
25    T2=k2*(T_long+T_throttle+T_brake_EM);
26    T3=k3*(T_long+T_throttle+T_brake_EM);
27    T4=k4*(T_long+T_throttle+T_brake_EM);
28    T_yaw_eff=T_yaw-(T2+T4-T1-T3);
29    T(1)=T1-k1*T_yaw_eff; % left front
30    T(2)=T2+k2*T_yaw_eff; % right front
31    T(3)=T3-k3*T_yaw_eff; % left rear
32    T(4)=T4+k4*T_yaw_eff; % right rear

```

Torque adjustment

```

1      function T_new = fcn(T_sat,T_nonsat,T_yaw)
2
3      T_new=T_sat;
4
5      if T_yaw>0 && T_new(1)>0
6      T_new(1)=T_sat(1)-((T_nonsat(2)-T_sat(2))-(T_nonsat(1)-
          T_sat(1)));
7      T_new(3)=T_sat(3)-((T_nonsat(4)-T_sat(4))-(T_nonsat(3)-
          T_sat(3)));
8      end
9      if T_yaw>0 && T_new(2)<0
10     T_new(2)=T_sat(2)+((T_nonsat(2)-T_sat(2))-(T_nonsat(1)-
          T_sat(1)));
11     T_new(4)=T_sat(4)+((T_nonsat(4)-T_sat(4))-(T_nonsat(3)-
          T_sat(3)));
12     end
13     if T_yaw<0 && T_new(2)>0
14     T_new(2)=T_sat(2)+((T_nonsat(2)-T_sat(2))-(T_nonsat(1)-
          T_sat(1)));
15     T_new(4)=T_sat(4)+((T_nonsat(4)-T_sat(4))-(T_nonsat(3)-
          T_sat(3)));
16     end
17     if T_yaw<0 && T_new(1)<0
18     T_new(1)=T_sat(1)-((T_nonsat(2)-T_sat(2))-(T_nonsat(1)-
          T_sat(1)));
19     T_new(3)=T_sat(3)-((T_nonsat(4)-T_sat(4))-(T_nonsat(3)-
          T_sat(3)));
20     end

```

Electric motor torque limits

```

1      function [torque_lim_motw_sat,torque_lim_motw,
          torque_lim_brakew] = fcn(w,Fz,mux,conf)
2
3      R=0.2891; % wheel radius [m]
4      Rl=0.94*R; % loaded radius

```

```

5
6     if conf==0 % 4WM
7         omega=1/8.604*[0    21.99    104.72    274.76    414.21    495.10
            523.65    578.38    630.72    678.30    719.53    773.44    836.85
            878.08    938.32    1001.73    1060.38    1126.96    1185.61
            1256.93    1347.28    1417.02    1518.44];
8         tor_mot=2.5*[176.59    176    175.5    175    174.5
            158.64    151.88    137.86    126.84    116.83    110.32
            102.31    94.31    88.31    82.31    76.32    71.33    66.34
            62.35    58.36    52.88    49.90    46.93];
9
10        ww=1/8.604*[412.3:0.1:1518.44]'; % query points
11        A=[ones(length(ww),1) ww 1./ww 1./ww.^2 1./ww.^3];
12        T=interp1(omega,tor_mot,ww,'linear');
13        k=inv(A'*A)*A'*T; % polynomial coefficients for torque
            limit curve after base speed
14
15        torque_lim_motw=zeros(4,1);
16        torque_lim_motw_sat=zeros(4,1); %from motor limit curves
17        torque_lim_motw_slip=zeros(4,1); %from road adhesion
            conditions
18        torque_lim_brakew=zeros(4,1);
19        for i=1:4
20            if w(i)<1/8.604*412.3 % below base speed
21                torque_lim_motw_sat(i)=2.5*176.59; % constant torque
                    region
22            else % above base speed
23                torque_lim_motw_sat(i)=[1 w(i) 1/w(i) 1/w(i)^2 1/w(i)^3]*
                    k; % constant power region
24            end
25            torque_lim_motw_slip(i)=Fz(i)*mux(i)*Rl;
26            torque_lim_motw(i)=min(torque_lim_motw_sat(i),
                torque_lim_motw_slip(i));
27            torque_lim_brakew(i)=-torque_lim_motw(i);
28        end
29
30        else if conf==1 % 2IWM front axle

```

```

31     tor_mot2=2*2.5*[176.59  176.59  176.59  176.59  176.59
    158.64  151.88  137.86  126.84  116.83  110.32  102.31
    94.31   88.31   82.31   76.32   71.33   66.34
    62.35   58.36   52.88   49.90   46.93];
32     omega2=1/8.604*[0  21.99  104.72      274.76  414.21
    495.10  523.65  578.38  630.72  678.30  719.53  773.44
    836.85  878.08  938.32  1001.73 1060.38 1126.96
    1185.61 1256.93 1347.28 1417.02 1518.44];
33
34     ww2=1/8.604*[412.3:0.1:1518.44]';
35     A2=[ones(length(ww2),1) ww2 1./ww2 1./ww2.^2 1./ww2.^3];
36     T2=interp1(omega2,tor_mot2,ww2,'linear');
37     k2=inv(A2'*A2)*A2'*T2;
38
39     torque_lim_motw=zeros(4,1);
40     torque_lim_motw_sat=zeros(4,1); %from motor limit curves
41     torque_lim_motw_slip=zeros(4,1); %from road adhesion
    conditions
42     torque_lim_brakew=zeros(4,1);
43     for i=1:2
44         if w(i)<1/8.604*412.3
45             torque_lim_motw_sat(i)=2*2.5*176.59;
46         else
47             torque_lim_motw_sat(i)=[1 w(i) 1/w(i) 1/w(i)^2 1/w(i)^3]*
    k2;
48         end
49         torque_lim_motw_slip(i)=Fz(i)*mux(i)*Rl;
50         torque_lim_motw(i)=min(torque_lim_motw_sat(i),
    torque_lim_motw_slip(i));
51         torque_lim_brakew(i)=-torque_lim_motw(i);
52     end
53
54     else if conf==2 % 2IWM rear axle
55     tor_mot2=2*2.5*[176.59  176.59  176.59  176.59  176.59
    158.64  151.88  137.86  126.84  116.83  110.32  102.31
    94.31   88.31   82.31   76.32   71.33   66.34
    62.35   58.36   52.88   49.90   46.93];

```

```

56     omega2=1/8.604*[0    21.99   104.72           274.76   414.21
        495.10   523.65   578.38   630.72   678.30   719.53   773.44
        836.85   878.08   938.32   1001.73  1060.38  1126.96
        1185.61  1256.93  1347.28  1417.02  1518.44];

57
58     ww2=1/8.604*[412.3:0.1:1518.44]';
59     A2=[ones(length(ww2),1) ww2 1./ww2 1./ww2.^2 1./ww2.^3];
60     T2=interp1(omega2,tor_mot2,ww2,'linear');
61     k2=inv(A2'*A2)*A2'*T2;
62
63     torque_lim_motw=zeros(4,1);
64     torque_lim_motw_sat=zeros(4,1); %from motor limit curves
65     torque_lim_motw_slip=zeros(4,1); %from road adhesion
        conditions
66     torque_lim_brakew=zeros(4,1);
67
68     for i=3:4
69         if w(i)<1/8.604*412.3
70             torque_lim_motw_sat(i)=2*2.5*176.59;
71         else
72             torque_lim_motw_sat(i)=[1 w(i) 1/w(i) 1/w(i)^2 1/w(i)^3]*
                k2;
73         end
74         torque_lim_motw_slip(i)=Fz(i)*mux(i)*Rl;
75         torque_lim_motw(i)=min(torque_lim_motw_sat(i),
                torque_lim_motw_slip(i));
76         torque_lim_brakew(i)=-torque_lim_motw(i);
77     end
78
79     else % 2 central motors one per each axle
80     tor_mot2=2*2.5*[176.59   176.59   176.59   176.59   176.59
        158.64   151.88   137.86   126.84   116.83   110.32   102.31
        94.31    88.31    82.31    76.32    71.33    66.34
        62.35    58.36    52.88    49.90    46.93];
81     omega2=1/8.604*[0    21.99   104.72           274.76   414.21
        495.10   523.65   578.38   630.72   678.30   719.53   773.44
        836.85   878.08   938.32   1001.73  1060.38  1126.96
        1185.61  1256.93  1347.28  1417.02  1518.44];
82

```

```

83     ww2=1/8.604*[412.3:0.1:1518.44]';
84     A2=[ones(length(ww2),1) ww2 1./ww2 1./ww2.^2 1./ww2.^3];
85     T2=interp1(omega2,tor_mot2,ww2,'linear');
86     k2=inv(A2'*A2)*A2'*T2;
87
88     torque_lim_motw=zeros(4,1);
89     torque_lim_motw_sat=zeros(4,1); %from motor limit curves
90     torque_lim_motw_slip=zeros(4,1); %from road adhesion
91     conditions
92
93     torque_lim_brakew=zeros(4,1);
94
95     for i=1:4
96         if w(i) < 1/8.604*412.3
97             torque_lim_motw_sat(i)=2.5*176.59;
98         else
99             torque_lim_motw_sat(i)=0.5*[1 w(i) 1/w(i) 1/w(i)^2 1/w(i)
100                ^3]*k2;
101         end
102         torque_lim_motw_slip(i)=Fz(i)*mux(i)*Rl;
103         torque_lim_motw(i)=min(torque_lim_motw_sat(i),
104                                torque_lim_motw_slip(i));
105     end
106 end
107 end
108 end
109 end

```

Total limit torque

```

1     function [torque_lim_motw_total,torque_lim_brakew_total]=
2         fcn(torque_lim_motw,conf)
3
4     if conf==0 || conf==3 % 4WM or 2 central motors
5         configurations
6         torque_lim_motw_total=torque_lim_motw(1)+torque_lim_motw
7             (2)+torque_lim_motw(3)+torque_lim_motw(4);
8         torque_lim_brakew_total=-torque_lim_motw_total;
9     else if conf==1 % 2WM front axle
10         torque_lim_motw_total=torque_lim_motw(1)+torque_lim_motw
11             (2);
12     end
13 end

```



```
8      torque_lim_brakew_total=-torque_lim_motw_total;  
9      else % 2WM rear axle  
10     torque_lim_motw_total=torque_lim_motw(3)+torque_lim_motw  
        (4);  
11     torque_lim_brakew_total=-torque_lim_motw_total;  
12     end  
13     end
```

Vita Auctoris

Riccardo Ninfa was born in 1999 in Chieti, Abruzzo, Italy. He graduated from “I.I.S Luigi di Savoia” high school in Chieti with a 100/100 score in 2017. From there, he moved to Torino to pursue his dream since he was a child of becoming an automotive engineer. He took the Bachelor’s Degree cum laude in Automotive Engineering from Politecnico di Torino, Piemonte, Italy, in 2020. His thesis “E-clutches and their usage on mild-hybrid vehicles” focused on fuel consumption savings for a compact mild-hybrid city car. During those three years he was also part of the “Young Talent Project”, an elite program reserved to the best students in Politecnico di Torino. After the first achieved goal, he continued his studies in Automotive Engineering with a Master of Science at Politecnico di Torino. He is currently part of the Dual International Master Degree program between Politecnico di Torino and University of Windsor in Ontario, Canada, with the guidance of Stellantis. His new research topic on “Torque Vectoring Controls for Multi-architecture Battery Electric Vehicles” clearly indicates his interests for future developments in the automotive field. He also presented his project at the Canadian Society for Mechanical Engineering International Congress held in Edmonton, Alberta, Canada, in June 2022. He is expected to graduate from University of Windsor in August 2022 and from Politecnico di Torino in October 2022.